

Structure-activity relationship of gallium nitride for the direct non-oxidative methane coupling to ethylene.

Presented by

Kanchan Dutta

Department of Chemical Engineering



McGill University Montreal, Canada

June 2020

A thesis submitted to McGill University in partial fulfillment of the requirements of the degree of
Doctor of Philosophy

Supervisor:

Prof. Dr. Sc. Jan Kopyscinski (McGill University, Chemical Engineering).

Examiners:

Prof. Dr. Ali Seifitokaldani (McGill University, Chemical Engineering).

Prof. Dr. Audrey Moores (McGill University, Chemistry).

Prof. Dr. Sheima Jatib Khatib (Texas Tech University, Chemical Engineering).

© Kanchan Dutta

2020

The years of anxious searching in the dark, with their intense longing, their alternations of confidence and exhaustion, and final emergence into light—only those who have experienced it can understand that.

Albert Einstein

Acknowledgments

While writing the acknowledgment, I thought of the quote by Ursula K. Le Guin (*The Left Hand of Darkness*), “*it is good to have an end to journey toward; but it is the journey that matters, in the end.*” My journey of four years in Dr. Kopyscinski’s CPE lab was not just academically and professionally enriching, but also was personally moving.

I thank Dr. Jan Kopyscinski for believing in me, trusting me with a very complex and challenging project. I sincerely thank him for his guidance, patience, encouragement, willingness to help always, and leading by example. You were always there as a leader, not a boss. Thank you for that.

I also thank Dr. C. -J. Li, from McGill Chemistry, our collaborator for the project, for discussing the experiments designed, and directing me to the right resources for finding answers to complex questions.

I extend my sincere gratitude to the technical and administrative staff at McGill chemical engineering department. Thanks to Frank Caporuscio, Lou Cousmich, Andrew Golsztajn, Gerald Lepkyj, and Ranjan Roy for the technical assistance, and characterization techniques presented within this dissertation. Also, thanks to Lisa Vopalto and Louise Miller-Aspin for your help in the administrative duties.

I thank Pranjal Gupta, Daniel Pacheco Gutierrez, and Obinna Uwa for their help when I started synthesizing the catalysts for this dissertation.

I thank Elmira Pajootan for her insights on the FTIR findings. I also thank Nathan Paul Fargier and Xavier Solimando for helping me with the French abstract.

I can never forget the times I shared with my colleagues in the CPE group, sharing ups and downs of life, supporting each other. Thank you, Jose, Jennifer, Ali, Jingsi, Vishnu, Garance, Pranjal, Daniel, Obinna, Pak, Varun, Liz, and Roham. A special thanks to my first colleague of methane activation, Mohsen, patiently getting trained, and performing required experiments at the same time. I enjoyed being your mentor and friend.

I thank my Mom, brother, and sister-in-law, who constantly supported me during gloomy times when nothing seemed to work. I miss you, Dad, I wish you were there to see this moment.

I take a moment to thank Jiten, who flew thousands of miles with me to Canada, leaving everything behind. Thanks for your trust and love. We have witnessed so many personal and professional changes in our lives, thanks for being patient with me.

Also, I would like to thank NSERC, FRQNT, and McGill MEDA for providing financial support to complete my Ph.D. studies.

Abstract

Canada is one of the world's top chemicals and plastics manufacturing countries. In the feedstock for the petrochemical industry, ethylene constitutes about 52%, while the aromatic compounds such as benzene are at 30%. The highly volatile price of crude oil makes it essential for the refiners to get a reliable feed source for optimum revenue and stable pricing of petrochemicals for the consumers. Abundantly available methane in natural and shale gases is a promising feed. Direct non-oxidative conversion of methane to petrochemical feedstocks like ethylene and aromatics, is not only greenhouse gas emission-free but also produces valuable hydrogen gas. High C–H bond strength, thermodynamic limitations, kinetics constraints, and coking of catalysts are the major technological challenges. As of now, most work has been done on molybdenum-containing zeolites and other metal and metal oxide catalysts. However, this research project focuses on an emerging class of nitride catalysts, specifically gallium nitride (GaN).

The main objective of this dissertation was to understand the structure-activity relationship of gallium nitride for the direct non-oxidative methane coupling to ethylene. For that purpose, the proof of

concept with commercial GaN in a packed bed reactor was established, followed by the GaN catalyst development, elucidation of the underlying reaction mechanisms, and catalyst regeneration study.

Direct non-oxidative methane activation was investigated for the first time in a fixed bed reactor under continuous operation over commercially available gallium nitride powder. High reaction temperatures (650–710 °C) were needed to initiate the activation due to the small surface area ($8 \text{ m}^2 \text{ g}^{-1}$) of the gallium nitride material, thermodynamic constraints, and the low residence time (1–4 s). The C_2 species (ethylene) was the main product, and besides C_2 , benzene and toluene were the minor components. The catalyst gets deactivated by carbon (coke deposition). Unlike the batch reactor where the residence time was in the order of hours, benzene was not the main product in a continuous reactor.

Using commercially available GaN powder is not economical even though it has methane activation capability. Because of commercial viability, the focus was directed towards the nitride catalyst development. A new stable supported GaN/SBA15 catalyst from an emerging class of nitride catalysts was reported for the direct non-oxidative methane coupling to ethylene. Additionally, unsupported GaN catalysts were also synthesized. An important step in the catalyst synthesis was the conversion of gallium oxide with ammonia to gallium nitride. In detail, the effect of nitridation temperatures, as well as ammonia exposure time on the morphology and activity of the catalyst, have been investigated. The optimum nitridation temperatures were 700 °C and 750 °C for the GaN/SBA15 and the unsupported GaN catalyst, respectively. Supported catalysts were more stable and had 5–10 times higher product (ethylene) formation rates per gram of gallium than the unsupported catalysts due to the higher surface area (>320 vs. $<20 \text{ m}^2 \text{ g}^{-1}$) and Ga-dispersion inside the pores. Compared to the oxide precursors, the nitrides exhibited a higher atom conversion efficiency for the CH_4 carbon leading to higher ethylene selectivity (71% for GaN/SBA15, $<58\%$ for $\text{Ga}_2\text{O}_3/\text{SBA15}$) and lower coke selectivity (27% for GaN/SBA15, 40% for $\text{Ga}_2\text{O}_3/\text{SBA15}$). Unsupported nitride catalysts deactivated within 3 hours and had much higher coke selectivity of up to 70%. Methane activation over not and partially nitridated catalysts resulted in the formation of H_2O , CO_2 , and CO as the CH_4 reacted with the lattice oxygen from Ga_2O_3 , which did not occur over GaN catalyst. Both nitride content and availability of active sites were important for methane activation. The supported catalyst was not just economical but had higher and stable ethylene selectivity, and lower coke selectivity than the unsupported (commercial) one.

An important step in the catalyst development work is understanding the reaction mechanism. Both theoretical and experimental approaches were made to elucidate the underlying mechanism.

Comprehensive DFT modeling was conducted to investigate the reaction mechanism of (1) gallium oxide (Ga_2O_3) surface nitridation to gallium nitride (GaN) and (2) methane coupling to ethylene over GaN as well as Ga_2O_3 . For the former, it was assumed that the nitridation involved the formation of gallium oxynitrides species ($\text{GaO}_x\text{N}_y\text{H}_z$) in which oxygen was stepwise replaced with nitrogen via adsorbed NH_2^* , NH^* , and H^* intermediates obtained through NH_3^* dissociation. The NH_2^* dissociation to NH^* was calculated to be the rate-limiting step. For the second study, the calculation indicated that the C–H bond cleavage of the adsorbed CH_3^* species had the highest activation barrier for both catalysts. The results illustrated that the most feasible pathway among the GaN (or Ga_2O_3) surfaces for the ethylene formation was via two CH_2^* species adsorbed on adjacent Ga–N (or Ga–O) hollow sites. DFT modeling also confirmed the formation of H_2O , CO , and CO_2 through the reaction with lattice oxygen, creating an oxygen vacancy on the Ga_2O_3 surface.

Diffuse reflectance infrared Fourier transform spectroscopy, ^{13}C solid-state nuclear magnetic resonance, and isotope labeling experiments validated the DFT results and clearly showed the existence of Ga– CH_3 species as well as confirmed that the rate-determining step is the formation of CH_2^* (or CD_2^*) from CH_3^* (or CD_3^*). Other surface species like alkene and aromatic $\text{C}=\text{C}$, $>\text{CH}_2$, CH_3 , $\text{N}-\text{H}$, $\text{O}-\text{H}$ were detected as well. Also, the kinetic isotope exchange experiments showed that the C–D bond was stronger than the C–H bond.

The regeneration capability and reusability of gallium nitride (GaN) catalysts for the direct non-oxidative methane activation was studied. Each catalyst was subjected to two different regeneration methods. In the first method, the used catalysts were regenerated with air at 500–550 °C and reused several times. Due to the slight oxidation of the surface GaN to Ga_2O_3 , the ethylene yield decreased by 16% after 5 cycles. The second method included an intermediate re-nitridation step after air regeneration to convert the surface Ga_2O_3 back to GaN. By doing so, the ethylene yield remained constant over multiple cycles. Multiple regenerating agents were tested, and the air was found to be the optimum one. The supported catalyst can not only be reused but also had long-term stability in terms of CH_4 conversion and ethylene yield.

Résumé

Le Canada est l'un des principaux pays producteurs de produits chimiques et de plastiques au monde. L'éthylène constitue environ 52 % de la matière première de l'industrie pétrochimique, tandis que les composés aromatiques tels que le benzène en représentent 30 %. Le prix très fluctuant du pétrole brut fait qu'il est essentiel pour les raffineurs de disposer d'une source d'alimentation fiable afin d'optimiser leurs revenus et de garantir aux consommateurs des prix stables pour les produits pétrochimiques. Le méthane disponible en abondance dans les gaz naturels et les gaz de schiste est une source d'alimentation prometteuse. La conversion directe non oxydante du méthane en matières premières pétrochimiques, comme l'éthylène et les composés aromatiques, ne produit non seulement pas d'émissions de gaz à effet de serre, mais génère aussi un précieux gaz, l'hydrogène. Cette méthode fait néanmoins face à des défis technologiques, tels qu'une thermodynamique défavorable, des contraintes cinétiques importantes, la cokéfaction des catalyseurs à haute température et la force élevée de la liaison C-H. À ce jour, la plupart des travaux ont été réalisés sur les zéolithes contenant du molybdène et sur d'autres catalyseurs à base de métaux et d'oxydes métalliques. Toutefois, ce projet de recherche se concentre sur une nouvelle classe de catalyseurs à base de nitrure, en particulier le nitrure de gallium (GaN).

L'objectif principal de cette thèse était de comprendre la relation entre la structure et l'activité du nitrure de gallium pour le couplage direct non oxydant du méthane à l'éthylène. À la fin de ces travaux, un concept de réacteur à lit tassé avec du GaN commercial a été établi, suivi par le développement du catalyseur GaN, la compréhension des mécanismes des réactions sous-jacentes et enfin l'étude de la régénération du catalyseur.

L'activation directe non oxydante du méthane a été étudiée pour la première fois dans un réacteur à lit fixe en fonctionnement continu sur de la poudre de nitrure de gallium disponible dans le commerce. Des températures de réaction élevées (650–710 °C) ont été nécessaires pour déclencher l'activation en raison de la faible surface ($8 \text{ m}^2 \text{ g}^{-1}$) du nitrure de gallium, des contraintes thermodynamiques et du faible temps de séjour (1–4 s). L'espèce C_2 (éthylène) était le composé principal, et le C_2 , le benzène et le toluène étaient les composants mineurs. Le catalyseur est désactivé par le carbone (dépôt de coke). Contrairement au cas du réacteur discontinu où le temps de séjour était de l'ordre de quelques heures, le benzène n'était pas le produit principal dans le cas d'un réacteur continu.

Bien qu'elle eût la capacité d'activer le méthane, l'utilisation de poudre de GaN disponible dans le commerce n'était pas économiquement viable. C'est pour cette raison que l'accent a été mis sur le développement d'un catalyseur de nitrure. Un nouveau catalyseur GaN/SBA15 stable, issu d'une classe émergente de catalyseurs à base de nitrure, a été rapportée pour le couplage direct du méthane non oxydant à l'éthylène. En outre, des catalyseurs GaN non supportés ont également été synthétisés. Une étape importante de la synthèse des catalyseurs a été la conversion de l'oxyde de gallium en nitrure de gallium avec de l'ammoniac. Plus précisément, l'effet des températures de nitruration, ainsi que le temps d'exposition à l'ammoniac sur la morphologie et l'activité du catalyseur ont été étudiés. Les températures de nitruration optimales étaient respectivement de 700 °C et 750 °C pour le catalyseur GaN/SBA15 et le catalyseur GaN non supporté. Les catalyseurs sur support étaient plus stables et présentaient des rendements de formation de produit (éthylène) par gramme de gallium 5 à 10 fois plus élevés que les catalyseurs non supportés, en raison de la surface plus importante (>320 contre $<20 \text{ m}^2 \text{ g}^{-1}$) et de la dispersion du Ga à l'intérieur des pores. Par rapport aux précurseurs d'oxydes, les nitrures présentaient un rendement de conversion atomique plus élevé pour le carbone CH_4 , ce qui se traduit par une plus grande sélectivité de l'éthylène (71 % pour le GaN/SBA15, <58 % pour le $\text{Ga}_2\text{O}_3/\text{SBA15}$) et une plus faible présence de coke (27 % pour le GaN/SBA15, 40 % pour le $\text{Ga}_2\text{O}_3/\text{SBA15}$). Les catalyseurs à base de nitrure non supportés se désactivaient en 3 heures et présentaient une déposition de coke beaucoup plus importante, allant jusqu'à 70 %. L'activation du méthane sur des catalyseurs

non ou partiellement nitrurés a entraîné la formation de H_2O , CO_2 et CO , car le CH_4 a réagi avec l'oxygène du réseau du Ga_2O_3 , ce qui ne s'est pas produit lors de l'utilisation du catalyseur au GaN. La teneur en nitrures et la disponibilité des sites actifs sont deux paramètres importants pour l'activation du méthane. Le catalyseur supporté est donc viable économiquement, tout en possédant à la fois une sélectivité plus élevée et plus stable pour l'éthylène et en accumulant moins de coke que le catalyseur non supporté (commercial).

Une étape importante dans le travail de développement du catalyseur a été la compréhension du mécanisme de réaction. Des approches à la fois théoriques et expérimentales ont été adoptées pour élucider le mécanisme sous-jacent. Des calculs basés sur la théorie de la fonctionnelle de la densité (DFT, sigle pour *Density Functional Theory*) ont été réalisés pour étudier le mécanisme de réaction (1) de la nitruration de surface de l'oxyde de gallium (Ga_2O_3) en nitrure de gallium (GaN) et (2) du couplage du méthane à l'éthylène sur GaN ainsi que sur Ga_2O_3 . Pour le premier, nous avons supposé que la nitruration implique la formation d'espèces d'oxynitrures de gallium ($\text{GaO}_x\text{N}_y\text{H}_z$), dans lesquelles l'oxygène était progressivement remplacé par l'azote via des intermédiaires NH_2^* , NH^* et H^* adsorbés obtenus par dissociation de NH_3^* . La dissociation de NH_2^* en NH^* a été calculée comme étant l'étape limitant la conversion. Pour la deuxième étude, le calcul a indiqué que le clivage de la liaison C–H des espèces CH_3^* adsorbées était la barrière d'activation la plus élevée pour les deux catalyseurs. Les résultats ont montré que le mécanisme le plus probable pour la formation de l'éthylène sur les surfaces de GaN (ou Ga_2O_3) passait par deux espèces de CH_2^* adsorbées sur des sites creux adjacents de Ga–N (ou Ga–O). La modélisation utilisant la DFT a également confirmé la formation de H_2O , CO et CO_2 par la réaction avec l'oxygène du réseau, créant une lacune d'oxygène sur la surface de Ga_2O_3 .

Des expériences de réflectance diffuse, de spectroscopie infrarouge à transformée de Fourier, de résonance magnétique nucléaire à l'état solide ^{13}C et de marquage isotopique ont validé les résultats de la DFT et ont clairement montré l'existence d'espèces de Ga– CH_3 , tout en confirmant que l'étape cinétiquement déterminante est celle de la formation de CH_2^* (ou CD_2^*) à partir de CH_3^* (ou CD_3^*). D'autres espèces de surface comme les alcènes et les aromatiques $\text{C}=\text{C}$, $>\text{CH}_2$, CH_3 , $\text{N}-\text{H}$, $\text{O}-\text{H}$ ont également été détectées. De plus, les expériences d'échange cinétique d'isotopes ont montré que la liaison C–D était plus forte que la liaison C–H.

La capacité de régénération et de réutilisation des catalyseurs au nitrure de gallium (GaN) pour l'activation directe non oxydante du méthane a aussi été étudiée. Chaque catalyseur a été soumis à deux

méthodes de régénération différentes. Dans la première méthode, les catalyseurs utilisés ont été régénérés avec de l'air à 500–550 °C et réutilisés plusieurs fois. En raison de la légère oxydation du GaN de surface en Ga₂O₃, le rendement en éthylène a diminué de 16 % après 5 cycles. La deuxième méthode comprend une étape intermédiaire de renitridation après la régénération de l'air pour reconvertir le Ga₂O₃ de surface en GaN. Ce faisant, le rendement en éthylène est resté constant sur plusieurs cycles. Plusieurs agents de régénération ont été testés, et l'air s'est avéré être le meilleur. Le catalyseur supporté peut non seulement être réutilisé, mais il est également stable à long terme en matière de conversion du CH₄ et de rendement en éthylène.

Table of Content

Acknowledgments.....	i
Abstract	iii
Résumé	vi
1 Introduction	1
1.1 Motivation.....	1
1.2 Objectives	3
1.3 Organization of the thesis	4
2 Theoretical background.....	6
2.1 Chemistry and thermodynamics.....	6
2.2 Catalyst	8
2.3 Reaction mechanism	10
2.4 Reactor concepts.....	12
3 Methodology	14
3.1 Catalyst preparation.....	14
3.1.1 Unsupported catalysts.....	14

3.1.2	Supported catalysts.....	15
3.1.3	Synthesized catalyst nomenclature.....	16
3.2	Catalyst characterization.....	17
3.2.1	Inductively coupled plasma – optical emission spectroscopy.....	17
3.2.2	Total nitrogen analysis.....	17
3.2.3	X-ray diffraction (XRD).....	18
3.2.4	Nitrogen adsorption/desorption measurements.....	18
3.2.5	Chemisorption.....	18
3.2.6	Scanning electron microscopy (SEM).....	19
3.2.7	Transmission electron microscopy (TEM).....	19
3.2.8	Solid-state nuclear magnetic resonance (SS-NMR).....	19
3.2.9	Temperature-programmed oxidation (TPO).....	20
3.2.10	Temperature-programmed desorption (TPD).....	20
3.3	Experimental setup.....	21
3.3.1	Fixed bed reactor (FBR).....	21
3.3.2	Diffuse reflectance infrared Fourier transform spectroscopy (DRIFTS).....	24
3.3.3	Methane activation through thermogravimetric analysis (TGA).....	26
3.4	Experimental conditions and procedure.....	26
3.4.1	Fixed bed reactor.....	26
3.4.2	Diffuse reflectance infrared Fourier transform spectroscopy (DRIFTS).....	28
3.4.3	Thermogravimetric analysis (TGA).....	29
3.5	Kinetic parameter estimation and model discrimination.....	29
4	Commercial gallium nitride (GaN).....	32
4.1	Introduction.....	32
4.2	Characterization of fresh catalyst.....	33
4.3	Activity measurements.....	36
4.3.1	Effect of temperature.....	36
4.3.2	Effect of catalyst amount.....	38
4.3.3	Effect of methane partial pressure.....	39
4.3.4	Temperature programmed surface reaction (TPSR).....	39
4.4	Characterization of spent catalyst.....	40
4.5	Conclusions.....	42
5	Gallium nitride catalyst development.....	43
5.1	Introduction.....	44
5.2	Characterization of fresh catalyst.....	45
5.2.1	Unsupported catalysts.....	45
5.2.2	Supported catalysts.....	49
5.2.3	Temperature-programmed desorption.....	53

5.3	Activity measurements.....	54
5.3.1	Unsupported catalysts.....	54
5.3.2	Supported catalysts.....	59
5.3.3	Thermogravimetric analysis for carbon deposition.....	64
5.4	Characterization of spent catalyst.....	65
5.4.1	Temperature-programmed oxidation.....	66
5.5	Conclusions.....	71
6	Reaction mechanism and kinetics.....	72
6.1	Introduction.....	73
6.2	Density functional theory (DFT) modeling.....	74
6.2.1	Ga ₂ O ₃ nitridation.....	74
6.2.2	Methane activation.....	78
6.3	Experimental results.....	86
6.3.1	Kinetic isotope effect.....	86
6.3.2	Nuclear magnetic resonance (NMR).....	101
6.3.3	Diffuse reflectance infrared Fourier transform spectroscopy (DRIFTS).....	102
6.4	Kinetic study.....	111
6.4.1	Approach to equilibrium.....	112
6.4.2	Influence of the pore diffusion.....	113
6.4.3	Apparent activation energy.....	114
6.4.4	Apparent reaction order.....	116
6.4.5	Effect of space velocity.....	117
6.4.6	Kinetic modeling.....	118
6.5	Conclusions.....	124
7	Catalyst regeneration.....	126
7.1	Introduction.....	127
7.2	Regeneration cycles.....	128
7.2.1	Regeneration medium.....	128
7.2.2	Reference activation/regeneration cycle.....	130
7.2.3	Optimized activation/regeneration cycle.....	134
7.3	Thermogravimetric analysis for carbon deposition.....	138
7.4	Long-term test.....	139
7.5	Catalyst characterization: fresh and spent.....	140
7.6	Conclusions.....	146
8	Conclusion and future work.....	148
8.1	Proof of concept with commercial GaN.....	148
8.2	Catalyst development and influence of nitridation.....	148

8.3	Reaction mechanism and kinetics	149
8.4	Catalyst stability and regeneration.....	151
8.5	Future work	151
8.5.1	Other metal nitrides	151
8.5.2	Effect of catalyst supports and support parameters	152
8.5.3	Kinetics study.....	153
8.5.4	Other metal pnictogenides (group 15 anions) catalysts.....	153
9	Originality	154
9.1	Proof of concept with commercial GaN	154
9.2	Catalyst development and structure-activity relationship.....	155
9.3	Optimized catalyst activation/regeneration cycle.....	155
	Nomenclature.....	157
	Latin symbols	157
	Greek symbols	158
	Other	159
	Subscripts and superscripts.....	159
	Abbreviation	159
	Gas species (mass-to-charge ratio, m/z)	160
	References	162
	Appendix	170
	Published contributions	204
	Oral contributions	205
	Curriculum Vitae.....	206

Chapter **1**

1 Introduction

1.1 Motivation

In 2019, the Canadian plastic and resin manufacturing industry achieved a total revenue of \$9.7 billion [1]. Ethylene is the most crucial building block for the production of plastic and resin precursors such as polyethylene (50%), ethylene oxide (10%) other derivatives like ethylene glycol. It is estimated to be the world's most widely used petrochemical in terms of worldwide production volume. It also is used to produce vinyl acetate, polyvinyl chloride, polyester fiber, and film and a range of alcohols and solvents. Ethylene is produced in Alberta, Ontario, and Quebec and accounts for 58.6% of industry revenue in 2019 [2]. Ethylene is produced commercially by the steam cracking of a wide range of hydrocarbon feedstocks (from cracking naphtha, gas oil and condensates with the coproduction of propylene, C₄ olefins, and aromatics, pyrolysis gasoline). The cracking of ethane and propane primarily carried out in the US, Canada, and the Middle East. In short, the primary source is crude oil. Crude oil price is highly volatile, and this is significantly affecting the price of petrochemicals and hence revenue. Refiners need a reliable and preferably indigenous feed source for an optimum revenue and growth rate, to ensure higher profit margins. This also stabilizes the selling price offered to the end-users of petrochemicals. Thus, the focus should be on a reliable alternate feed for petrochemicals and clean technology to meet the market demand. Much effort has been made to replace petroleum feedstock

with natural gas and shale gas. Thus, the valorization of methane (CH_4), which is the main component in natural and shale gases into useful chemicals (i.e., olefins and aromatic), is a hot topic and pursued by many scientists and engineers through catalytic processes. Globally, Canada is the fourth-largest producer and fifth largest exporter of natural gas [3]. Canada's natural gas reserves are estimated to be 35 trillion cubic meters, of which 10 trillion cubic meters are conventional gas, and the rest is unconventional, including coal-bed methane, shale, and tight gas [3]. For comparison, the world's reserves are estimated at 798 trillion cubic meters, with 429 trillion cubic meters being conventional [3]. With the declining export of natural gas to the US, new ways of utilizing natural gas need to be explored. In Quebec, it is in the Utica Shale formation in a region called the St. Lawrence Lowlands found in the corridor between Montreal and Quebec City and on the Gaspé Peninsula [4]. Early assessments suggest it could contain more than 600 billion cubic meters of recoverable natural gas. This reserve is enough to meet Quebec's natural gas demand for more than 100 years [4]. These reserves make Canada self-sufficient for a reliable, indigenous source of natural gas for several years to come.

Processes that catalytically convert CH_4 into chemicals are (1) indirect oxidative, (2) direct oxidative, and (3) direct non-oxidative dehydrogenation [5–7]. Partial oxidation or reforming to syngas (CO , H_2) followed by coupling reactions (Fischer Tropsch, Methanol synthesis) are typical indirect processes that have low efficiency, high capital cost, and high CO_2 emissions. However, they are the dominant industrial practice. Direct oxidative coupling of methane (OCM) to olefins and methanol, and non-oxidative methane aromatization, as well as non-oxidative methane coupling to ethylene, are the more challenging routes and far from commercialization. The non-oxidative routes have significant thermodynamic ($\Delta G > 0 \text{ kJ mol}^{-1}$, low CH_4 conversion) and kinetic (low product selectivity and high coking) constraints. Due to the stable C–H bond, CH_4 is difficult to convert directly into ethylene or benzene; therefore, high temperature (700–1000°C), an efficient catalyst and reactor engineering concept is needed [6,8]. In the last two decades, direct non-oxidative methane conversion has been extensively studied over metal oxides, the most investigated catalyst materials [7–15]. For example, Profs. Kapteijn [15], Spivey [13], Hensen [10], Lobo [12], Dumesic [16], Varma [17], Khatib [18], and many more are working on conventional bifunctional metal-modified zeolites. The reaction mechanism involves C–H bond cleavage to a reactive CH_x surface species. The subsequent C–C coupling and cyclization are assumed to occur on the Brønsted acid site of the zeolites or at temperatures higher than 950 °C in the gas phase. The Brønsted acid site is also responsible for the severe coking of the catalysts [11,13]. Direct oxidative coupling of methane, is not limited by

thermodynamics ($\Delta G < 0 \text{ kJ mol}^{-1}$); however, the intermediates and products are more reactive than CH_4 and can oxidize to CO_2 resulting in low product yield [7,19]. Again, most catalyst systems are based on metal oxides [7,20,21]. It is widely accepted that the acidity/basicity of the catalyst (Lewis acid-base pairs) plays an essential role in the C–H bond activation.

In this dissertation, I departed from metal and metal oxide catalysts and investigated the applicability of metal nitride catalysts (GaN) for the C–H activation under thermocatalytic conditions towards the formation of value-added chemicals. Metal nitrides are an interesting class of heterogeneous catalysts that exhibit catalytic activity similar or even better than precious metals [22]. For example, metal nitrides are active for ammonia synthesis, hydrotreating, and selective hydrogenation [23]. Li et al. [24] carried out direct methane activation in a batch reactor with commercial gallium nitride (GaN) powder at temperatures of up to $450 \text{ }^\circ\text{C}$ with a residence time of up to 8 h. They obtained a high benzene selectivity ($\sim 90\%$). This finding led to the start of a collaboration between Dr. Li's and Dr. Kopyscinski's research groups for the gallium nitride catalyst development. Gallium nitride has been touted as silicon of the future in the semiconductor industry due to its superior properties over silicon [25]. No study has been reported on using the GaN catalyst in a flow reactor and its synthesis as a highly dispersed catalyst (on support).

1.2 Objectives

It was established that gallium nitride (GaN) was active for the C–H activation as it consists of Lewis acid-base pairs, in which the metal-nitride has stronger basicity than the corresponding metal-oxide (Ga_2O_3) that enhances C–H bond dissociation. The objective of this dissertation is to gain a deeper fundamental understanding of the role of the active catalyst sites (metal-nitrogen) and surface intermediates to design better catalysts and processes. To shed light and understand the structure-activity relationship, the following four sub-objectives and tasks were defined:

- 1) Proof of concept with commercial GaN catalyst in a fixed-bed reactor.** It has been shown that under batch conditions with residence times of up to 8 h, methane can be converted over commercially available GaN. However, residence times in catalyzed packed bed reactors are usually in the order of seconds. Therefore, I aimed at investigating the non-oxidative methane conversion over commercial GaN material at low gas residence times.
- 2) GaN catalysts synthesis:** An important aspect of the development of metal-nitride catalysts is the nitridation step in which the metal oxide is converted through a high-temperature process to

metal-nitride. Therefore, the aim was to synthesize unsupported and supported GaN catalysts and understand the effect of nitridation condition on the catalyst structure and activity towards methane conversion.

- 3) What are the underlying reaction mechanism and their kinetic descriptions?** Understanding the reaction mechanism and the reaction kinetics are two important aspects of catalyst and process development. Task III follows a framework of modeling and experimental procedures. The former consists of density functional theory (DFT) modeling to investigate and compare various reaction mechanisms. The latter includes a variety of experiments to validate the models, such as Diffuse reflectance infrared Fourier transform spectroscopy (DRIFTS), ^{13}C solid-state Nuclear magnetic resonance (SS-NMR), and isotope labeling experiment. Based on the experiments, the kinetic assessment was carried out.
- 4) Catalyst stability and regeneration:** All catalysts operated under non-oxidative methane conditions are prone to carbon deposition and thus catalyst deactivation. Therefore, the goal of task IV was to establish a catalyst regeneration procedure that would enable a long lifetime. The questions to answer were: What is the best regeneration medium (gas)? What are the optimum conditions?

1.3 Organization of the thesis

This thesis is organized in seven chapters from the introduction to catalyst development and direct non-oxidative methane activation experiments to the catalyst regeneration and stability study:

Chapter 2 provides a short theoretical background on direct non-oxidative methane activation (section 2.1) and reaction mechanism reported for the methane activation (section 2.1).

Chapter 3 presents a comprehensive overview of the materials and experimental methods used in the dissertation. In detail, sections 3.1 and 3.2 deal with catalyst synthesis and catalyst characterization, respectively. Sections 3.3 and 3.4 describe the experimental setup as well as the experimental procedures. Section 3.5 describes the DFT calculations approach.

Chapter 4 summarizes the results of methane activation over commercial GaN catalyst. The effect of temperatures, catalyst amount, and the methane partial pressures are presented and discussed.

Chapter 5 presents the results of the supported and unsupported GaN catalyst development. This chapter summarizes the effect of synthesis parameters (nitridation temperatures) on the catalyst activity. Results of detailed catalyst characterization techniques have been presented, including the spent catalyst analysis.

Chapter 6 covers results from experimental and theoretical approaches for understanding the reaction mechanism. It also presents the kinetics in terms of the global reaction rate for methane activation over the GaN catalyst.

Chapter 7 presents the results on the reusability of the catalysts and its long-term use (catalyst stability) perspective.

Chapter 8 concludes this work and provides some recommendations for future work.

Chapter 9 states the novelties of the work presented in this dissertation.

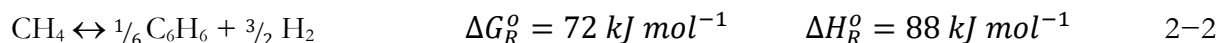
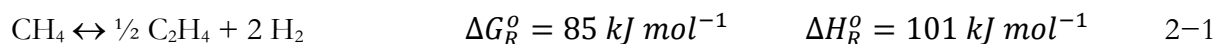
Chapter 2

2 Theoretical background

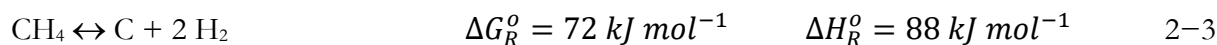
Methane from natural gas, shale gas, and even biogas is going to become one of the most important hydrocarbon feedstock for the synthesis of chemicals and its building blocks. Therefore, the heterogeneously catalyzed direct non-oxidative conversion of methane has the potential to be an important industrial application. In the last two decades, a tremendous amount of research has been carried out with emphasis on the catalyst, reactor, and process development for the production of aromatic compounds, as summarized in many review articles [5–7,13,26–29]. However, research on the direct coupling of methane to ethylene is very scarce. This chapter provides a short overview of its chemistry, thermodynamics, catalysts, reaction mechanism, and reactor concepts.

2.1 Chemistry and thermodynamics

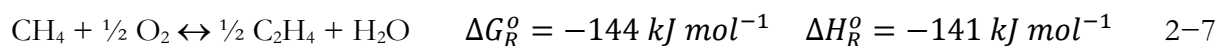
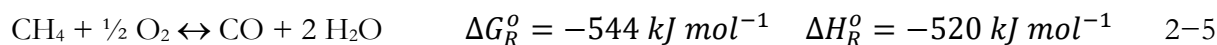
The direct non-oxidative methane coupling to ethylene and benzene is presented by eqs. 2–1 and 2–2:



Besides these two ideal reactions, methane can be pyrolyzed to H₂ and carbon via eq. 2–3:



The oxidative coupling of methane (OCM) can be represented by eqs. 2–4 to 2–7:



The Gibbs free energy and enthalpy changes for the non-oxidative conversion are positive, which indicates that the reaction is thermodynamically unfavorable and endothermic, respectively. Thermodynamically, the maximum CH₄ conversions and C₂H₄ yields (without coke) are 4.1% and 3.5% at 700 °C, 9.1%, and 8.1% at 800 °C and 17.0% and 15.5% at 900 °C, respectively (Fig. 2–1A). If benzene is included (Fig. 2–1B), it becomes the main product ($Y_{\text{C}_6\text{H}_6}$ at 700 °C = 12.4 %), while ethylene yield is much lower ($Y_{\text{C}_2\text{H}_4}$ at 700 °C = 0.18 %). This can be explained as benzene is more stable due to resonance and π -electron cloud delocalization [30].

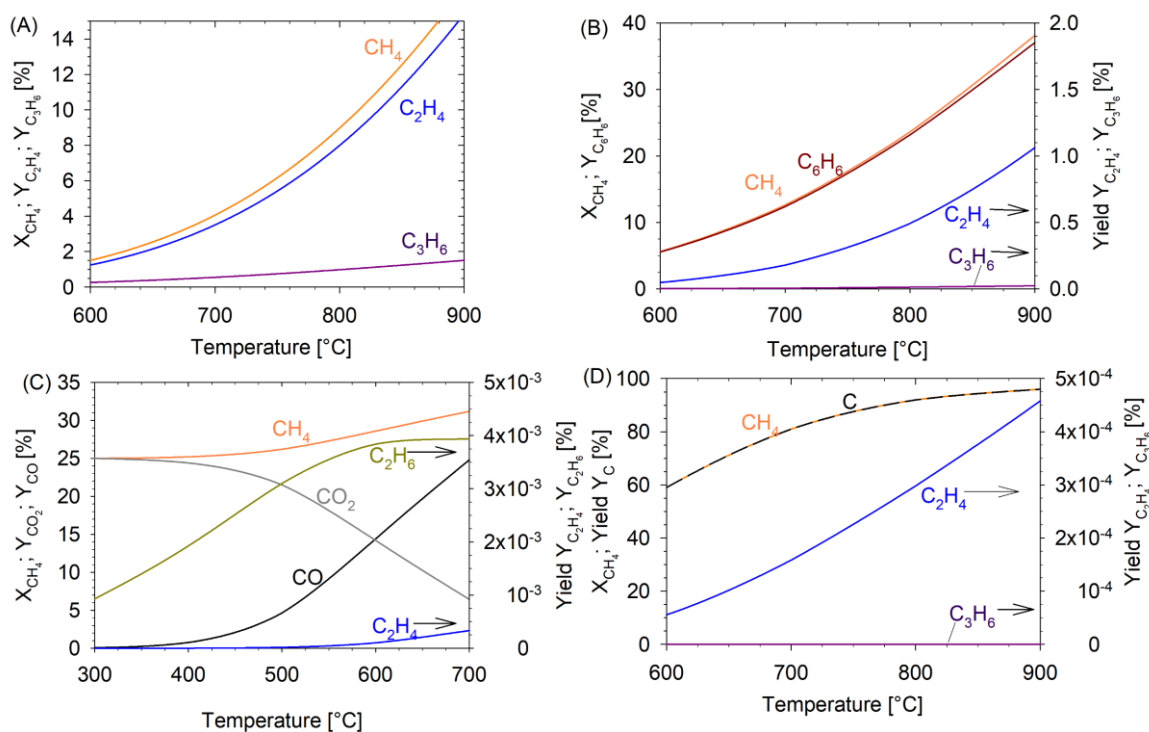


Fig. 2–1 (A) CH₄ equilibrium conversion and C₂H₄, C₃H₆ yields, (B) CH₄ equilibrium conversion and C₆H₆, C₂H₄, and C₃H₆ yields, (C) CH₄ equilibrium conversion and CO, CO₂, C₂H₆, and C₂H₄ yields for the oxidative coupling of methane (OCM with CH₄/O₂ = 2) as a function of temperature at 1 bar, and (D) CH₄ equilibrium conversion (non-oxidative) and C₂H₄, C₃H₆ yields with carbon as one of the products.

The calculations were done with the software tool HSC Chemistry v9. For the non-oxidative methane activation, two scenarios were calculated. One where H_2 , C_2H_4 , and C_3H_6 were the products (Fig. 2–1A), and the other where C_6H_6 was added (Fig. 2–1B).

For the oxidative pathway (OCM), all the reactions represented by equations 2–4 to 2–7 are thermodynamically favorable. A CH_4 to O_2 ratio of 2 [25] and CO , CO_2 , H_2O , C_2H_6 , and C_2H_4 as possible products were assumed for the thermodynamic equilibrium calculations (Fig. 2–1C). While the methane conversion was higher than for the non-oxidative conversion, but the main products were carbon oxides (CO being the main), while C_2H_4 and C_2H_6 were negligible ($Y < 0.01\%$). The formation of carbon oxides decreases the carbon conversion efficiency, and also the CO_2 production is undesirable.

The direct non-oxidative pathway is more environmentally friendly, as no CO_2 is produced. However, direct conversion has its limitations and drawbacks, as discussed above. In addition to the formation of other hydrocarbons, catalyst coking, and hence the deactivation occurs at higher temperatures. Carbon deposition is one of the biggest challenges. Thus, if carbon is added in the equilibrium calculation, practically all methane is converted to coke, and the hydrocarbons yields are negligible, as shown in Fig. 2–1D. The carbon formation could be either due to methane pyrolysis to carbon and hydrogen or through the formation of H_2 from the adsorbed surface intermediates like C_xH_y . The surface intermediates and hence methane activation mechanism has been discussed in the subsequent section.

2.2 Catalyst

At first glance, the reaction seems very simple. However, its reaction mechanism, surface intermediates, and rate-limiting steps over metal-nitride catalysts are unknown and still debatable over metals and metal-oxides. To best of my knowledge, gallium nitride material has not been used as a catalyst besides the reported batch experiment [24]. GaN has been touted as silicon of the future in the semiconductor industry due to its superior properties over silicon [25].

The advantage of non-oxidative conversion of methane is that it prevents irreversible overoxidation of the products, which leads to undesired products, such as CO_2 and H_2O (Fig. 2–1C). However, methane has a very stable C–H bond, which is difficult to activate under non-oxidative conditions [8]. Methane aromatization is the most studied pathway for direct non-oxidative methane activation. Review articles from Ma et al. [11], Spivey and Hutchings [13], and Karakaya and Kee [6] summarize the research work that has been conducted with an emphasis on metal-modified zeolites. Metals such

as Mo, Zn, W, Re, Cu, Mn, Ni, and Cr have been investigated, with molybdenum-containing zeolites exhibiting the highest activity in terms of methane conversion (3–16%) with benzene (50–75%) as the main product [8]. It is assumed that Mo-zeolites are bifunctional catalysts. The basic reaction mechanism involves several steps. In the initial reduction period, molybdenum oxide (MoO_2 , MoO_3)

is reduced by CH_4 to Mo-carbide (Mo_2C) on which the C–H bond in CH_4 is broken to a reactive $-\text{CH}_x$. The reactive $-\text{CH}_x$ surface intermediate dimerizes to C_2H_y that further oligomerizes and cyclizes to C_6H_6 with the formation of H_2 (Fig. 2–2). Oligomerization and cyclization are presumed to occur on the Brønsted acid site of the zeolites. The detailed mechanism, the specific configuration and oxidation state of the Mo-carbide as well as the interaction with the Brønsted

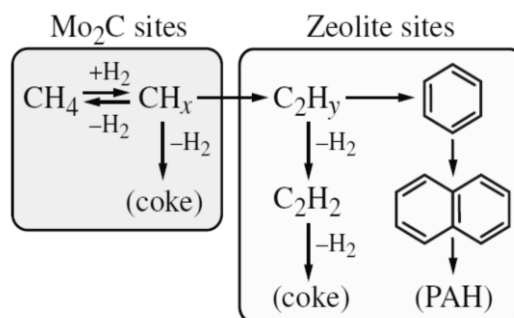


Fig. 2–2 Reaction mechanism for non-oxidative CH_4 aromatization, adapted from [6].

acid site and kinetic description of the dimerization and oligomerization are still not well understood [6,11]. The $-\text{CH}_x$ and C_2H_y complexes lead to coke deposition, which is inevitable for most catalysts (zeolites) in a methane-rich atmosphere at high temperature and in the absence of oxygen. A combination of benzene and the active species like CH_2 and CH_3 can form toluene. Two phenyl species (active aryl rings) can form naphthalene [16]. Further combination of phenyl species can lead to the formation of polynuclear aromatic compounds (i.e., coke) that deactivates the catalysts, which is the main drawback of this reaction. Adding promoters such as transition metals in Period 4 (Fe, Co, Ni, and Cr) and metals in Group 13 (Ga and Al) show the best improvement in terms of methane conversion, product selectivity, and catalyst stability [11]. It has been shown that Ga containing zeolites are highly active for the dehydrogenation of light alkane [31,32]. But the nature of the active gallium species, as well as the gallium alkane intermediates, is still under debate. While non-oxidative coupling of methane does not form greenhouse gas CO_2 , coke formation on the catalyst surface and the relatively high reaction temperatures as compared to oxidation processes are still a challenge.

The number of studies focusing on the non-oxidative conversion of methane to light hydrocarbons and olefins is relatively scarce compared with the number of studies on aromatization [33]. Recently, Dumesic's group developed PtSn/zeolite catalysts that achieved high ethylene selectivities (70–90% at 700 °C, coke not included); yet coking was still a huge problem [16]. They obtained methane conversions (in terms of fraction converted to the products) less than 0.5%, typically 0.25% at 700 °C. Xiao and Varma [17] used bimetallic PtBi/zeolite catalysts and reported ethane (C_2H_6) selectivity of

90% (coke not included) at 700 °C, with methane conversion between 1–5%. However, they had 40–50% coke selectivity with up to 10% ethylene (C_2H_4) selectivity on 1% Pt–0.2% Bi catalyst at 650 °C and 0.1 atm CH_4 partial pressure. They suggested that carbon deposition occurs during the initial activation period. Bajec et al. [33] used Fe/HZSM-5, Mo/HZSM-5, and FeMo/HZSM-5 catalysts for methane activation and coupling to ethane and ethylene. They obtained 1–6% methane conversion, up to 50% ethylene selectivity, and 11–35 wt% coke. Their reaction conditions were $T = 700$ °C, $WHSV = 2$ h⁻¹, $p_{tot} = 1.5$ bar. Sheng et al. [12] used a less acidic boron-based [B]ZSM-5 catalyst for methane activation and obtained 90% ethylene selectivity (gas phase) with less than 1% methane conversion at 700 °C with an average rate of 0.3 mmol_{CH₄} h⁻¹ g_{cat}⁻¹. The low acidity of the support produced more ethylene than benzene and lower coke. Guo et al. [9] synthesized single iron sites embedded in a silica matrix. They reported minimum carbon deposition, maximum ethylene selectivity of 48%, and maximum methane conversion of 48% at 1090 °C. Lee et al. [34] used Ga/HZSM-5 catalysts for converting a mixed feed of methane and ethane. They used 0–7 wt% gallium loadings at 650 °C and a GHSV of 6000 ml g_{cat}⁻¹ h⁻¹. Their ethylene selectivity was between 25–30%, aromatics between 15–30%, and coke between 45–65 %. Methane and ethane conversions were 0.3–6% and 13–59%, respectively. Dipu et al. [35] controlled catalysis by Ni for methane activation by adding a second element. They found silica-supported nickel phosphide (NiP/SiO₂) materials as an active catalyst for the reaction at 900 °C. Ethylene selectivity was around 60%, with methane conversion of 3% for NiP catalyst at 900 °C. Products were C_2H_4 (ethylene), C_2H_6 (ethane), C_2H_2 (acetylene), C_3H_6 (propylene), C_6H_6 (benzene), C_7H_8 (toluene) and $C_{10}H_8$ (naphthalene).

2.3 Reaction mechanism

An elementary step-based kinetic model was developed by Wong et al. [36] for the ‘steady-state’ reaction of methane to aromatics over Mo/HMCM-22, and Mo/HZSM-5 (Fig. 2–3).

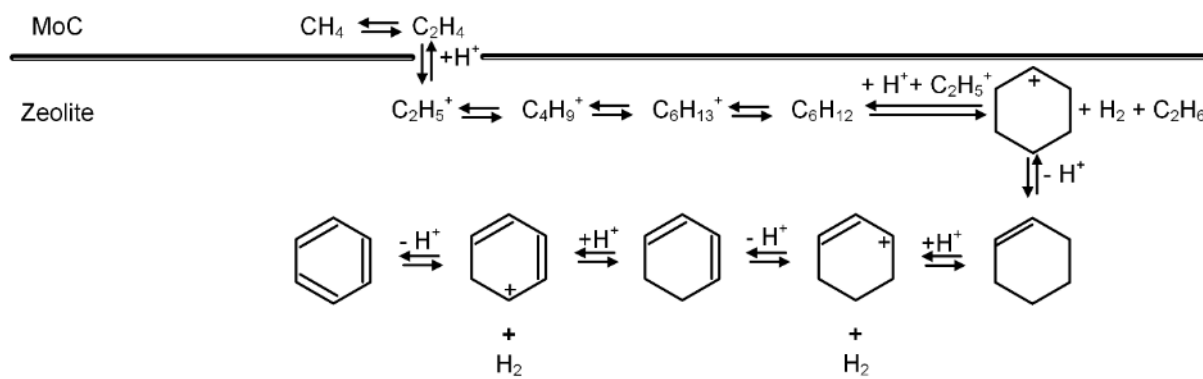


Fig. 2–3 Elementary steps for CH_4 activation over the Mo/HZSM5 catalyst, adapted from [36].

Methane is first dimerized into ethene on Mo sites, followed by ethene oligomerization into benzene on acid sites [36]. The ethene formation rate was second order with respect to the methane partial pressure, including the approach to equilibrium (refer to section 6.4.1). The acid-catalyzed elementary steps are grouped into chemisorption, desorption, oligomerization, β -scission, hydride transfer, protolytic dehydrogenation and hydrogenation, protolysis, alkylation and dealkylation of toluene and naphthalene. They used Langmuir-Hinshelwood equations for these elementary steps for the conversion of ethene to aromatics. Karakaya et al. assumed that C_2H_4 is formed over Mo_2C sites via adsorbed C_2H_6 (Fig. 2–4) [37]. In detail, they consider that CH_4 adsorbed first as a molecule over $Mo_2C-CH_4^*$, which leads to the C-H bond cleavage and formation of $Mo_2C-CH_2^*$. Ethylene formation is then assumed via the reaction of new CH_4 with the CH_2^* surface intermediate [37]. The reactions proceed on the zeolite acid site, following C_2H_4 desorption from the Mo_2C site to the gas phase. The ethylene mainly reacts to form surface species $C_2H_5^+$, $C_4H_9^+$, and $C_6H_{13}^+$, as discussed above. A small fraction of the methane is converted to methyl-carbenium ion (CH_3^+) on the acid site of the zeolite support, $CH_4 + H-ZSM(s) \rightarrow CH_3(s) + H_2(g)$.

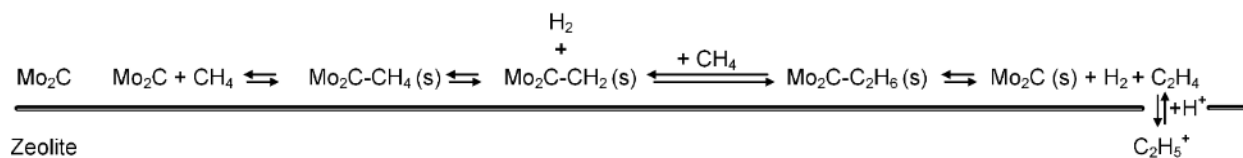


Fig. 2–4 Elementary steps for CH_4 activation to ethylene over the Mo/HZSM-5 catalyst, adapted from [37].

Gerceker et al. [16] did microkinetic modeling supported by DFT calculations to elucidate the underlying mechanism over Pt(433) and $Pt_3Sn(211)$ sites. The activation of adsorbed CH_4^* was calculated to be the rate determining step. Additionally, desorption of H_2 and C_2H_4 was also rate controlling over Pt, respectively. The fastest C–C coupling was $CH^* + CH^* \rightarrow CHCH^* + *$ on all sites except on $Pt_3Sn(211)$ terrace sites. On the $Pt_3Sn(211)$ terrace sites, the fastest C–C coupling was $CH_2^* + C^* \rightarrow CH_2C^* + *$. The addition of Sn increased the ethylene turnover frequency (TOF), and after 5 h on stream, when ethylene TOF achieved a steady value. The $PtSn/SiO_2$ catalyst had approximately 3 times higher ethylene TOF than Pt/SiO_2 . The addition of Sn to Pt/SiO_2 increased the initial benzene activity, and the steady-state benzene TOF over $PtSn/SiO_2$ was approximately 2 times higher than that over Pt/SiO_2 . The $PtSn/SiO_2$ catalyst yielded a higher methane conversion and a higher ethylene selectivity in comparison to Pt/SiO_2 . Also, both catalysts showed low selectivity toward ethane and benzene [16].

Luzgin et al. [32] used Ga-modified zeolites, and they reported that methane undergoes dissociative adsorption on Ga_2O_3 species of the zeolite via the “alkyl” pathway to form gallium-methyl ($\text{Ga}-\text{CH}_3$) species and/or via the “carbenium” mechanism with the formation of gallium-methoxy ($\text{Ga}\cdot\text{O}-\text{CH}_3$) species. Gallium-methyls are the primary species, while gallium-methoxy groups represent the minor species of the methane activation. The addition of molecular oxygen favors the generation of gallium-methoxy species by the reaction of partial oxidation.

Li et al. [24] first reported the CH_4 adsorption model on gallium nitride using density functional theory (DFT). They suggested that the most stable adsorption configuration for the methane molecule on the exposed m -plane ($1\bar{1}00$) of GaN through the alkyl adsorption way. The m -plane of GaN is a non-polar plane composed of equal numbers of Ga and N atoms, tetrahedrally coordinated with each other. The carbon atom in methane is attracted by the lattice Ga^{3+} cation, wherein one H atom in methane is adsorbed on N^{3-} anion, and the other three hydrogen atoms are situated on the opposite side. The next step to the formation of ethylene and subsequently aromatics on GaN has not been reported yet, either experimentally or theoretically.

2.4 Reactor concepts

Although this dissertation focuses on catalyst development, it is worth discussing the membrane reactors concept in the context of the non-oxidative methane conversion. While the catalyst can be improved to increase conversion and selectivity and reduce coking, it does not affect the position of the chemical equilibrium. One way to increase methane conversion and product selectivity is in-situ coupling with other reactions that consume hydrogen. Yet another approach is the use of membranes that selectively remove H_2 and shift the equilibrium towards hydrocarbon formation. For example, equilibrium calculations by the minimization of the free energy approach showed that at 600 °C, the equilibrium conversion of methane increases from 3.5% to 24% if 90% of the H_2 is removed in a batch reactor. Several studies claim the equilibrium advantage for different dehydrogenation reactions using membrane reactors [38–41]. A suitable membrane must be kinetically compatible, i.e., the H_2 permeation rate should ideally be equal to the H_2 formation rate.

Two common types of membrane reactors were used: packed bed tubular and planar catalytic membrane reactors. The former comprises of an inert permselective membrane with conventional catalyst particles or pellets present in a packed bed. The latter, on the other hand, consists of a catalytically active and permselective membrane. Limitations of the membrane reactor include the membrane’s chemical and mechanical stability at high temperature and permeation rate. The hydrogen

permeance is inversely proportional to membrane thickness, while for the mechanical strength, a higher thickness is needed.

Palladium based membranes are highly selective towards hydrogen. Natesakhawat et al. used a tubular membrane reactor to remove hydrogen from the methane dehydroaromatization system [42]. Mo/HZSM-5 catalyst was used, a significant improvement in methane conversion and total aromatic yield were observed when compared to conventional fixed bed reactors. Iliuta et al. [43] reported an increase in methane conversion over equilibrium value by 173% with RuMo/HZSM-5 catalyst in a membrane reactor at 600 °C, as compared to 73% of the equilibrium conversion in a conventional fixed bed reactor. For the methane aromatization with a zeolite-based catalyst, the in-situ removal of H₂ via a membrane is not practical as the coking problem becomes even worse [44]. For catalysts, however, that show little or no coking, membrane reactors may be a better solution to increase benzene yield. Caro et al. [45] applied a different approach by using a reactor with an oxygen-permeable membrane allowing in-situ oxidation of the hydrogen under controlled conditions. The produced steam helped in avoiding/reducing coke formation.

In the membrane (permeable to H₂) reactor, hydrogen permeation entrained first a significant increase in benzene conversion (1.7 times the equilibrium value). But the conversion decreased sharply due to the accumulation of carbonaceous species under very low hydrogen pressure. The coke could be removed by re-hydrogenation using H₂ (in a regeneration step after the activation step), leading to the restoration of the active sites.

Chapter 3

3 Methodology

This chapter summarizes the materials and methods used for catalyst synthesis, their characterization, catalyst activity testing in various reactors and setups, and the testing conditions.

3.1 Catalyst preparation

Two types of catalysts were synthesized; one group was unsupported GaN, the second one was GaN supported on SBA-15 with Ga target loading of 16 wt%. A proof of principle was also performed using commercial GaN (refer to Chapter 4), which had 99.9% GaN.

3.1.1 Unsupported catalysts

Unsupported catalysts were prepared by the Evaporation Induced Self Assembly (EISA) technique adapted from Chaudhari et al. [46]. Around 1 g of a triblock copolymer (Pluronic P-123, Sigma Aldrich) was dissolved in 16 mL of pure anhydrous ethanol (Greenfield Global Inc.) until a homogeneous solution was obtained. This was followed by the addition of 1.7 mL of nitric acid (67–70 wt%, Fisher Scientific) and stirring for complete mixing with the acid. Another solution was prepared in 5 mL DI-water and 5 mL of ethanol with 4.5 g of dry gallium (III) nitrate hydrate powder (99.9998 wt% trace metal basis, ACROS Organic, Thermo Fisher Scientific). DI-water was used to get a homogeneous solution as the nitrate is only slightly soluble in ethanol. The hygroscopic nitrate was always stored under dry inert gas (Ar with < 5 ppm moisture, Praxair) desiccator to prevent moisture absorption.

The nitrate bottle was also flushed with Ar after every use. This ensured that the weight of the nitrate was consistent and not influenced by absorbed moisture. The copolymer solution was then added to the gallium precursor solution and stirred for 5 h at 600 rpm at room temperature. The homogeneous, colorless mixture was kept inside a drying oven at 60 °C for 48 h. After that, the dried copolymer-gallium mixture was calcined at 650 °C for 6 h at a heating rate of 1 °C min⁻¹ in which the copolymer was burned, and the gallium-precursor was converted to Ga₂O₃.

Before nitridation, the catalysts were dried for 4.5 h in Ar (99.999%, MEGS Specialty Gases, 15–20 mL_N min⁻¹) at 300 °C with a heating rate of 1 °C min⁻¹ (subscript *N* denotes normal condition with *T* = 0 °C and 1 bar). The nitridation was carried out in a fixed bed reactor with anhydrous ammonia (NH₃, 99.99%, MEGS Specialty Gases, 20 mL_N min⁻¹) flowing top-down through the catalyst bed (around 1 g). A quartz tube (7 mm ID × 275 mm long) with a 15–40 μ frit at one end was used as the reactor inside a vertical tube furnace (Mellen Company). At the reactor outlet, the gas was mixed and diluted with Ar. A slipstream was analyzed via mass spectrometry (Pfeiffer Omnistar GSD 301 O1), while the rest was sent through a 10 L hydrochloric acid bubbler (36.5–38 wt%, Fisher Scientific) to absorb unreacted ammonia. Nitridation was carried out at five nitridation temperatures (600, 650, 700, 750 and 800 °C at a heating rate of 1.5 °C min⁻¹ and 24 h NH₃ exposure from the start of heating to cool down), and ammonia exposure time (3–9 h at 750 °C at a heating rate of 1.5 °C min⁻¹). After cooling to room temperature under the NH₃ atmosphere, the reactor was purged with Ar, and the catalyst sample was stored for further use under inert gas in a desiccator. Refer to Fig. 3–1 for the schematic.

3.1.2 Supported catalysts

Supported gallium catalysts were prepared as follows. Ordered mesoporous silica (SBA–15) was synthesized as described in Zhao et al. [47]. Around 4 g of a triblock copolymer (Pluronic P-123, Sigma Aldrich) was dissolved by stirring (600 rpm for 5 h) in 95 mL of deionized water until a homogeneous solution was obtained. To this solution, 4 mL of hydrochloric acid (HCl, 37 wt%, Fisher Scientific) was added and stirred for about 15 min at a temperature of 38.5 °C. Then 9.5 mL of tetraethoxysilane (TEOS, 99.9%, Alfa Aesar) was added. The resulting mixture was stirred at 600 rpm for an additional 24 h at 38.5 °C for completing TEOS hydrolysis and precipitation of silica. The above mixture was placed inside a closed polypropylene digestion DigiTUBEs (SCP science) and kept inside an oven at 100 °C for 48 h for hydrothermal treatment. After cooling down, the white powder was separated by filtration and washed with deionized water several times, followed by overnight

drying at 60 °C. Finally, SBA-15 was obtained by calcining the dried solid at 550 °C for 5 h at a heating rate of 1 °C min⁻¹.

Supported catalysts were synthesized by incipient wetness impregnation of SBA-15 with gallium containing precursor. Typically, 1 g of SBA-15 was impregnated with 1 g of gallium (III) nitrate hydrate in 4.5 mL aqueous solution. The almost wet solid was left for 24 h at room temperature followed by drying overnight at 70 °C. The dried solid was then calcined at 550 °C for 5 h at a heating rate of 1 °C min⁻¹ to produce gallium oxide inside SBA-15. Refer to Fig. 3-1 for the schematic.

Nitridation of the supported catalysts was carried out in the same manner as described above for the unsupported catalysts. Due to the small bulk density (0.26 g cm⁻³), around 200 mg supported gallium oxide (Ga₂O₃/SBA15) was nitridated at temperatures of 650, 700, 750, and 800 °C from 3 to 24 h. Finally, the supported catalysts were stored in Ar filled vials inside the desiccator.

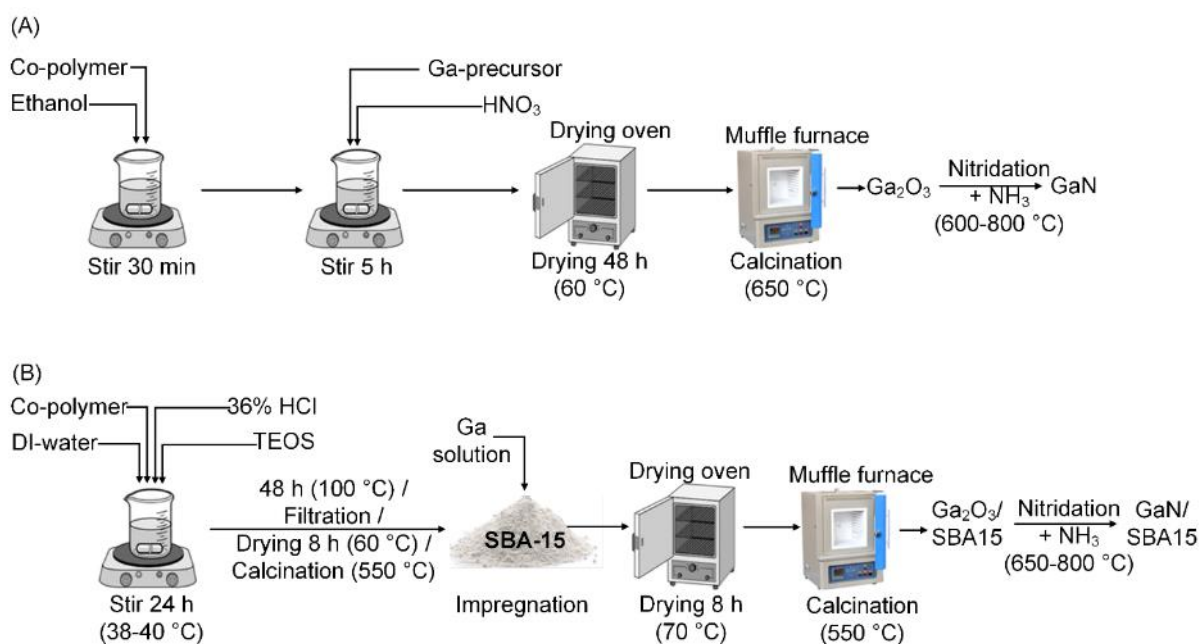


Fig. 3-1 Schematic for the synthesis of (A) unsupported GaN and (B) supported GaN/SBA15.

3.1.3 Synthesized catalyst nomenclature

The produced unsupported catalysts were named Ga₂O₃, GaN-750, or GaN-750-03, referring to the calcined and nitridated samples, respectively. In detail, for GaN-750, the 750 denotes the nitridation temperature in degree Celsius (°C) with a total NH₃ exposure of 24 h, while for GaN-750-03, the 03 refers to the nitridation time in hours (e.g., 3, 6 or 9 h). The produced supported catalysts were named Ga₂O₃/SBA15 and GaN/SBA15-750, referring to the calcined and nitridated

samples, respectively. In detail, for GaN/SBA15–750, the 750 denotes the nitridation temperature in degree Celsius (°C). N–SBA15–800 refers to a nitridated SBA–15 (without Ga₂O₃) with a nitridation temperature of 800 °C. Catalyst nomenclature without the mention of nitridation temperature (e.g., GaN and GaN/SBA15), correspond to nitridation temperatures of 750 and 700 °C for unsupported and supported catalysts, respectively.

Catalyst synthesis (both unsupported and supported) and the subsequent analyses (BET, XRD, ICP) were repeated for confirming repeatability and reproducibility.

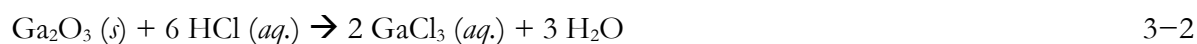
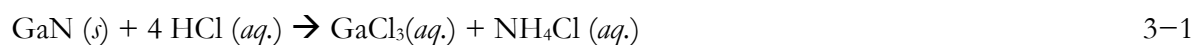
3.2 Catalyst characterization

3.2.1 Inductively coupled plasma – optical emission spectroscopy

The gallium content in the supported catalysts was determined using Inductively Coupled Plasma – Optical Emission Spectroscopy (ICP-OES, iCAP 6500 dual view Thermo Scientific). The supported catalyst was fused with twice the amount (by weight) of lithium tetraborate (SCP science) in a 9 mL graphite crucible (SCP science). The fusion was carried out in a muffle furnace ramping to 950 °C, where it was held for 30 min. A glassy bead was obtained after cooling down, and the fusion flux was carried out in triplicate. Two different solutions were prepared from the bead; one in 10% HNO₃ (trace metal grade) and another one in 3:1 HCl to HNO₃ concentrated solution (aqua regia). These solutions were digested in polypropylene DigiTUBEs (SCP science) at 95 °C for 2 h until the bead was completely dissolved. After cooling down, the solutions were filtered through 45 μ filter and diluted appropriately for ICP analysis. Unsupported catalysts were either GaN or Ga₂O₃ or a mix of both, and no other metals were present in them.

3.2.2 Total nitrogen analysis

The total nitrogen content of unsupported gallium nitride catalysts was determined by Shimadzu TOC-Vcph with TNM-1 Total Nitrogen Module. Before the analysis, around 25–50 mg of the sample was dissolved in 6M hydrochloric acid (HCl) overnight at 80 °C. The gallium nitride was converted to gallium chloride and ammonium chloride, while gallium oxide was converted to gallium chloride and water, as shown in equations 3–1 and 3–2, respectively.



The homogenous and clear solution was cooled down, diluted with deionized water to adjust the pH between 2–3. The diluted solution was analyzed for the total nitrogen content. The instrument was always calibrated before the analysis using ammonium standard (Sigma Aldrich) containing 1000 mg L⁻¹ of N as NH₄⁺ in water. The pH of the calibration solutions was adjusted between 2–3 by using HCl. Ga₂O₃ conversion ($X_{\text{Ga}_2\text{O}_3}$) was calculated based on equation 3–3 below.

$$X_{\text{Ga}_2\text{O}_3} = \frac{n_{\text{Ga}_2\text{O}_3}^0 - n_{\text{Ga}_2\text{O}_3}}{n_{\text{Ga}_2\text{O}_3}^0} \quad 3-3$$

Where, $n_{\text{Ga}_2\text{O}_3}^0 = \frac{(1 - n_N \cdot M_{\text{GaN}})}{M_{\text{Ga}_2\text{O}_3}} + \frac{n_N}{2}$ and $n_{\text{Ga}_2\text{O}_3} = \frac{(1 - n_N \cdot M_{\text{GaN}})}{M_{\text{Ga}_2\text{O}_3}}$, are mol of Ga₂O₃ before and after nitridation (unconverted), respectively. n_N denotes the mol of nitrogen in 1 g of unsupported catalyst determined by total nitrogen analysis, M_{GaN} and $M_{\text{Ga}_2\text{O}_3}$ denote the molar mass of GaN (83.73 g mol⁻¹) and Ga₂O₃ (187.44 g mol⁻¹), respectively. $n_N = \frac{N}{M_N}$, with N as the total nitrogen content in g_N g_{cat}⁻¹ and M_N as the molecular weight of nitrogen (14.01 g mol⁻¹).

This method, however, could not be applied for the supported catalysts because HCl could not leach out gallium salt from the SBA-15 support. During fusion flux, the silica structure was wholly disintegrated, and gallium was extracted entirely, but the nitrogen was lost as ammonia gas.

3.2.3 X-ray diffraction (XRD)

X-Ray Diffraction (XRD) was used to identify the crystallinity of the catalyst. Analyses were conducted on a Bruker D8 Discovery X-Ray Diffractometer with a two-dimensional VANTEC-500 detector and CuK_α ($\lambda = 1.5406 \text{ \AA}$) radiation source. The tube voltage was 40 kV, tube current 20 mA, and scan rate 5° min⁻¹.

3.2.4 Nitrogen adsorption/desorption measurements

Nitrogen adsorption/desorption measurements (-196 °C) were conducted using Micromeritics Tristar 3000 BET or Gemini VII or Quantachrom Autosorb iQ analyzer to determine total surface area, pore size distribution, and pore volume. Before the analysis, the samples were degassed under vacuum for 12 h at 250 °C. Surface areas of the catalyst were calculated following the BET method, while the BJH method was used to determine the pore size distribution.

3.2.5 Chemisorption

Methane chemisorption was carried out at 40–45 °C, to determine the number of active sites on the catalysts. Two methods were used; in one method, the fresh catalyst (200 mg for unsupported or 20

mg for supported) was first activated at 700 °C under Ar, and then it was cooled down to 45 °C. A CH₄-Ar mixture containing 80% CH₄ was flown (12.5 mL_N min⁻¹) through the catalyst bed for 1 h. This was followed by outgassing with Ar (15 mL_N min⁻¹) for 1 h to remove the physisorbed, loosely bound CH₄. After outgassing, the Ar continued at the same rate while the bed temperature was increased to 850 °C at 5 °C min⁻¹. The exit gas from the reactor was monitored for methane (m/z = 15) utilizing mass spectrometry (MS).

In the second method, the CH₄ uptake measurement was conducted in an Autosorb iQ gas sorption (Quantachrome) instrument. The fresh catalyst was placed in a U-shaped quartz tube. It was purged with He for 30 min at room temperature, and then it was heated to 700 °C (under He) with a heating rate of 10 °C min⁻¹. The sample was held at 700 °C for 30 min. After cooling down to 40 °C under He, CH₄ chemisorption measurement was carried out; all measurements were taken at pressures ranging from 40 to 600 Torr.

3.2.6 Scanning electron microscopy (SEM)

Scanning Electron Microscopy (SEM) analysis for the unsupported catalyst (Ga₂O₃) was performed using a FEI Inspect F-50 field emission scanning electron microscope. Also, Energy-Dispersive X-ray Spectroscopy (EDS) experiments were performed for elemental analysis (Ga, N, O, and C).

3.2.7 Transmission electron microscopy (TEM)

High-resolution transmission electron microscopy (HRTEM) of fresh and spent catalysts was carried out on FEI Tecnai G2 F20 with 200 kV. Before the analysis, a catalyst suspension in ethanol was prepared by sonicating 1–2 mg of the catalyst in 2 mL anhydrous ethanol. Energy-dispersive X-ray spectroscopy (EDS) was also carried out for detecting the elements present in the catalyst (qualitative).

3.2.8 Solid-state nuclear magnetic resonance (SS-NMR)

The NMR spectra were acquired on a Varian VNMRs spectrometer operating at 399.8 MHz for ¹H and 100.5 MHz for ¹³C using a 4 mm double-resonance Varian Chemagnetics T3 probe (now Agilent, Santa Clara, CA, USA). Approximately 15 mg of sample were center-packed into rotors using boron nitride inserts and spun at between 10 and 15 kHz. The recycle delay used was 5 s for all experiments, and a contact time of 1500 μs of approximately 60 kHz was used for the cross-polarization (CP) experiments. Between 6000 and 12000 scans were acquired for each experiment. SPINAL-64 decoupling at a rf-field of 45 kHz was applied during acquisition. The samples were spent catalysts obtained by CH₄ activation (at least 2 h run at 700 °C) using CH₄ and ¹³CH₄ over GaN/SBA15 and GaN. Post CH₄ activation, the spent catalyst in the reactor was first purged with Ar (5 mL_N min⁻¹) for

30 min at 700 °C. After that, the reactor was cooled down to room temperature overnight under Ar (15 mL_N min⁻¹). Mass spectrometry analysis confirmed the complete removal of methane (CH₄ or ¹³CH₄) from the gas stream (Ar). The spent catalysts were collected and stored in an Ar filled vial inside an Ar filled desiccator before they were used for collecting the NMR spectra.

3.2.9 Temperature-programmed oxidation (TPO)

Temperature-programmed oxidation coupled with mass spectrometry (TPO-MS) was carried out for the fresh and spent catalysts to determine the carbon either deposited during methane activation or catalyst synthesis. Around 50 mg of supported catalyst or 250 mg of unsupported catalyst was placed in a quartz tube (7 mm ID × 275 mm long and 15–40 μ frit) and heated in the presence of air (Ultra Zero Air, MEGS Specialty Gases, 22 mL_N min⁻¹) to 950 °C with a heating rate of 5 °C min⁻¹. The product gas at the reactor outlet was electrically heated to 200 °C, mixed with Ar (MEGS Specialty Gases, 10 mL_N min⁻¹), and then subsequently analyzed by a mass spectrometer (Pfeiffer Omnistar GSD 301) calibrated for CO₂ (m/z = 44), see below for details. The gas flow rates were controlled by respective calibrated Vögtlin red-y smart controllers (± 0.3 % accuracy, Switzerland).

Also, temperature-programmed oxidation with thermogravimetric analysis (TPO-TGA) was carried out for both fresh and spent catalysts (Q500 TA Instrument). 20–25 mg of catalyst was first purged for 30 min with N₂ at room temperature to remove air from the system and then heated at the rate of 5 °C min⁻¹ to 120 °C to remove the moisture. After a holding for 30 min at 120 °C, the sample was then heated to 950 °C at 5 °C min⁻¹ in the presence of air and held at 950 °C for 30 min, while the weight change was recorded.

3.2.10 Temperature-programmed desorption (TPD)

Temperature-programmed desorption (TPD) was carried out on the fresh supported (and also the metal-free supports) and unsupported catalysts under Ar (10 mL_N min⁻¹). The catalysts were dried for 2 h at 150 °C. This was followed by TPD, where the temperature was increased to 1000 °C at a heating rate of 2.5 °C min⁻¹. The temperature was held at 1000 °C for 30 min before cooling down. The reactor outlet was monitored qualitatively by a mass spectrometer. The monitoring was done by an analog scan from mass 1 to 50 amu.

3.3 Experimental setup

3.3.1 Fixed bed reactor (FBR)

3.3.1.1 Methane activation

The catalyst performance was measured in a vertical packed bed reactor at 650–710 °C and 1 bar_{abs} in a conventional fixed bed reactor (Fig. 3–2). A quartz tube (7 mm ID × 335 mm long) with a 15–40 μ frit at one end was used as the reactor inside a vertical tube furnace (Mellen Company). The inlet gas contained 10–80 vol% CH₄ (99.999%, Praxair) in Ar (99.999%, MEGS Specialty Gases), which were mass flow controlled (MFC) using calibrated Vögtlin red-y smart controller (± 0.3% accuracy, Switzerland, FC–1 and 2 in Fig. 3–2). The reactor outlet and transfer lines were electrically heated (TIC–1, TI–2, TIC–3 in Fig. 3–2) at 200 °C to avoid condensation of the organic components (i.e., C₆H₆, C₇H₈, C₁₀H₈).

A quadrupole mass spectrometer (Pfeiffer Omnistar GSD 301 with Prisma ion source and yttria coated iridium cathode) was used for gas analysis. The instrument acquires mass spectra from 0 to 200 amu (atomic mass units). The MS was used in secondary electron multiplier (SEM) mode. This enabled measuring concentrations as low as 0.5 ppmV. The shape of the peaks at the mass to charge ratio (*m/z*) of interest was optimized by adjusting ion-source voltage to get the accurate maximum ion-current for a *m/z*. The following instrument parameters were set: Ion-ref (150 V), Cathode (80 V), Focus (7.00 V), Field axis (5.88 V), and Extract (31 V), Mode (Scan-F), Speed (0.5 s), Resolution (50).

The MS was calibrated for methane (CH₄, 15 amu), ethylene (C₂H₄, 28 amu), propylene (C₃H₆, 42 amu), benzene (C₆H₆, 78 amu), toluene (C₇H₈, 91 amu), naphthalene (C₁₀H₈, 128 amu), carbon dioxide (CO₂, 44 amu), hydrogen (H₂, 2 amu) and argon (Ar, 40 amu). Argon was used as the internal standard with a calibration factor of 1. The calibration factors of the other species (*Cf_i*) were calculated based on the intensity ratio as follows:

$$Cf_i = \frac{I_i}{I_{Ar}} \frac{C_{Ar}}{C_i} \quad 3-4$$

Where the intensity was measured in ion-current (*I*, unit ampere [A]), while the concentration (*C*) refers to the concentration of the calibration mixture in vol%. By doing so, a calibration matrix was designed using 4 different calibration gas cylinders (primary standards with ±1% accuracy) and standard ethanol solutions for benzene (1–1000 ppmV), toluene (1–100 ppmV), and naphthalene (1–10 ppmV). The relative standard deviations for the calibration factors (from multiple calibration

cycles) were less than 1% for the major components and less than 5% for the minor components (for naphthalene, it was < 10%).

The ion-current associated with a product component (e.g., $m/z = 2$ for H_2) was corrected for the ion-current contribution from the feed, to get the net production during the reaction.

The calibration of the mass spectrometer was verified by a calibrated gas chromatograph (SRI GC 8610) for CH_4 , H_2 , and C_6H_6 . The internal reactor temperature (i.e., within the catalyst bed) was measured by a K-type thermocouple (Omega, TIC-9 in Fig. 3-2), which was used to control the furnace.

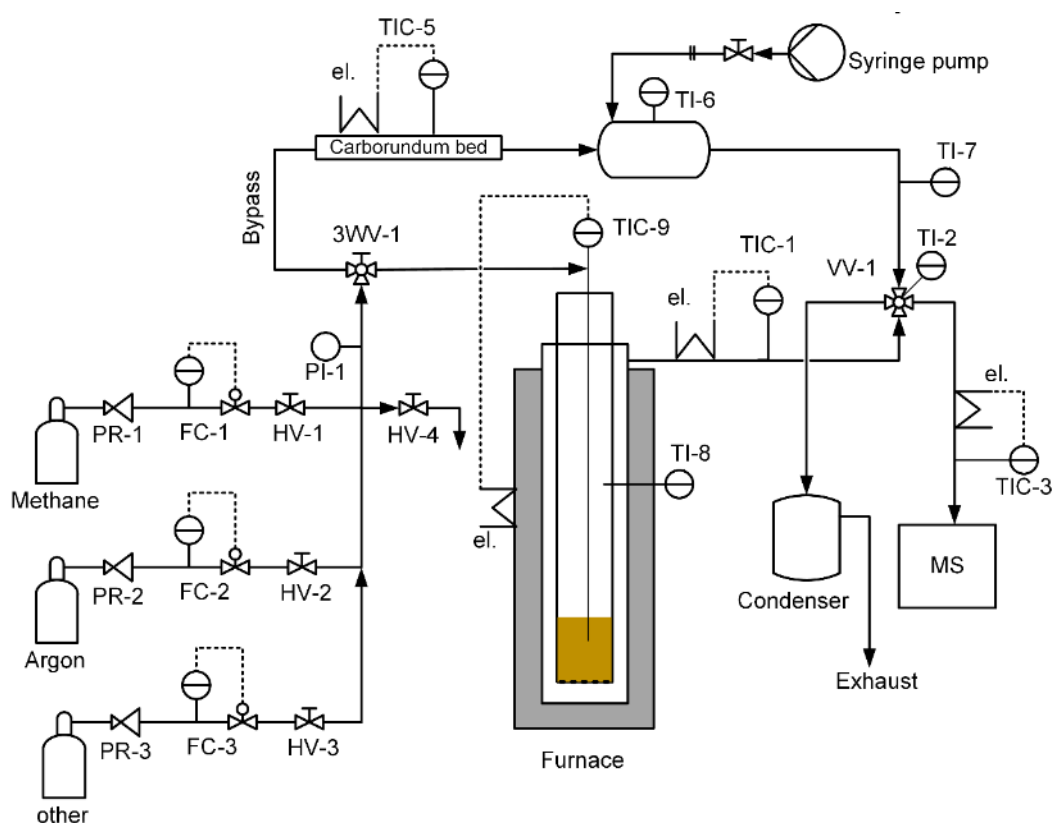


Fig. 3-2 Simplified P&ID of the packed bed reactor setup. (PR pressure regulator; FC = mass flow controller; HV = hand valve; PI = pressure indicator; TI = temperature indicator; TIC = temperature indicator control; 3WV = 3 way valve; VV = Vici valve).

The MS can only handle a gaseous mixture, therefore the gas lines and MS inlet capillary were heated between 180–200 °C to avoid condensation. The ethanolic solution mentioned above was evaporated completely before sending it to the MS. The cold liquid solution (inside a 50 mL gas-tight syringe) was pumped (0.5 mL min^{-1}) using a syringe pump (New Era NE-1000) into a heated line (120–150 °C)

followed by a heated vessel (200–250 °C). The hot vapor was then mixed with hot Ar (120–130 °C, 25 mL_N min⁻¹ using Ar MFC) by expansion inside the heated vessel (200–250 °C). The hot calibration mixture (130–150 °C) then flowed through the MS, and an analog scan was performed from mass to charge ratio of $m/z = 1-130$. Multiple analog scans (50–100) were performed in the MS for one calibration mixture, to achieve statistically significant results (achieving acceptable RSD's, and calculating average calibration factor for each component).

The thermal mass flow controllers for measuring methane and argon flow rates have an accuracy of $\pm 0.3\%$. In the beginning, some experimental results were verified with a gas chromatograph (SRI GC 8610) calibrated for H₂, CH₄, and C₆H₆. The GC was equipped with a capillary column MXT-1 for organic compounds and two packed columns for permanent gases (H₂ and CH₄) Haye Sep-D and Molecular Sieve 13X in series, with flame ionization detector (FID) and thermal conductivity detector (TCD). The GC was calibrated with the MS simultaneously. The same calibration mixture flowed through the GC and the MS at the same time. Unlike the MS, the GC calibration was based on a component's peak area, which depends on its concentration. For the same calibration mixture, at least 3 (up to 5) peak areas were recorded for each component. The comparison between GC and MS are shown in Fig. 3–3.

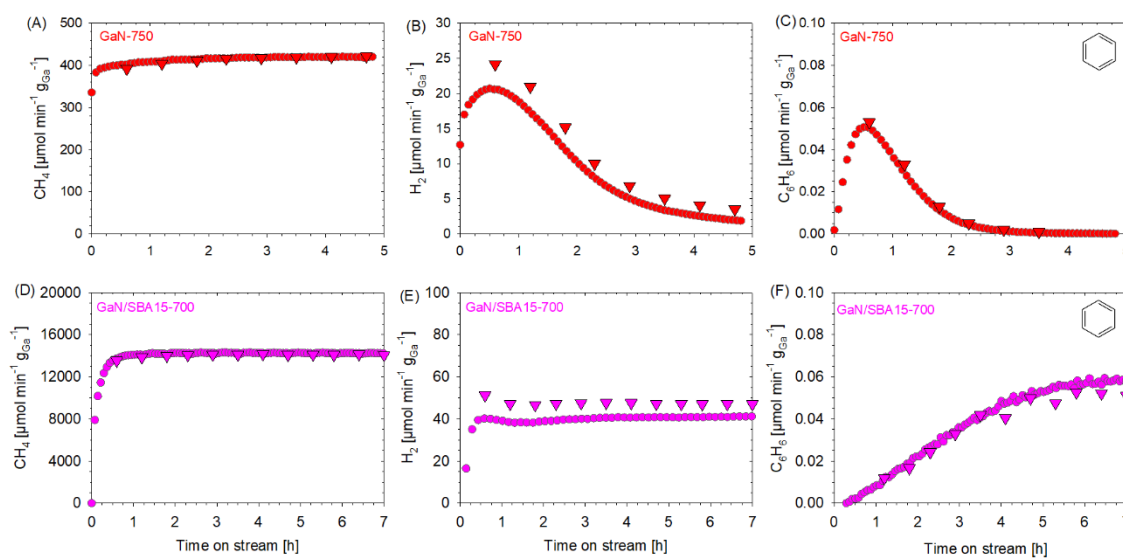


Fig. 3–3 Comparison for GC (∇) and MS (●) results for (A) and (C) CH₄, (B) and (E) H₂, and (C) and (F) C₆H₆ for GaN–750 and GaN/SBA15–700, respectively

3.3.1.2 Catalyst regeneration

Catalyst regeneration (Chapter 7) was performed in two different ways; (1) regeneration with air and (2) regeneration with air followed by re-nitridation with NH_3 . The unsupported samples were named GaN-R or GaN-RN, while the supported samples were named GaN/SBA15-R or GaN/SBA15-RN. In this notation, -R and -RN stands for regeneration and regeneration/re-nitridation, corresponding to methods 1 and 2, respectively.

Regeneration was carried out in a separate but identical reactor setup as described above (Fig. 3-2) to avoid exposing the stainless steel to alternate reducing and oxidizing atmospheres. Preliminary tests showed that when multiple activation regeneration cycles were conducted in the same reactor, the iron oxide of the reactor housing reacted with methane (not shown).

3.3.2 Diffuse reflectance infrared Fourier transform spectroscopy (DRIFTS)

Diffuse reflectance infrared Fourier transform spectroscopy (DRIFTS) spectra were recorded on a Thermo Scientific™ Nicolet™ iS50 FTIR Spectrometer equipped with a standard diffuse-reflectance attachment in the range of $400\text{--}6000\text{ cm}^{-1}$, with a resolution of 4 cm^{-1} and 250 scans for signal accumulation. For high temperature ($\geq 700\text{ }^\circ\text{C}$) methane activation, a Harrick Praying Mantis™ high-temperature reaction chamber (with ZnSe window) was used, and the data was analyzed using OMNIC 9.11.706 software (Fig. 3-4). For an optimum analysis, the particle size, sample packing, and dilution must be carefully controlled. The following precautions were taken to obtain the highest quality DRIFT spectrum [48]; particle size should be small and uniform ($\leq 50\text{ }\mu\text{m}$). Dilute sample in a non-absorbing matrix powder such as KBr. This ensures deeper penetration of the incident light into the sample, which increases the diffused scattered light [48]. The samples should be well mixed, and the sample should be loosely packed in the cup to maximize the IR beam penetration [48].

Fig. 3-5 illustrates the P&ID for carrying out the DRIFTS experiments. The setup is very similar to what has been depicted in Fig. 3-2. The gas flows from the *top of the sample* in the chamber, and the product gas leaves from the *bottom of the sample*. The outlet transfer lines are heated to prevent condensation of any condensable ($130\text{--}150\text{ }^\circ\text{C}$). The outlet gas was monitored utilizing a MS (Fig. 3-5). The thermocouple in the chamber (TIC-1, Fig. 3-5) measures and control the sample temperature. The mass flow controllers discussed in section 3.3.1 were used for controlling the gas flow.

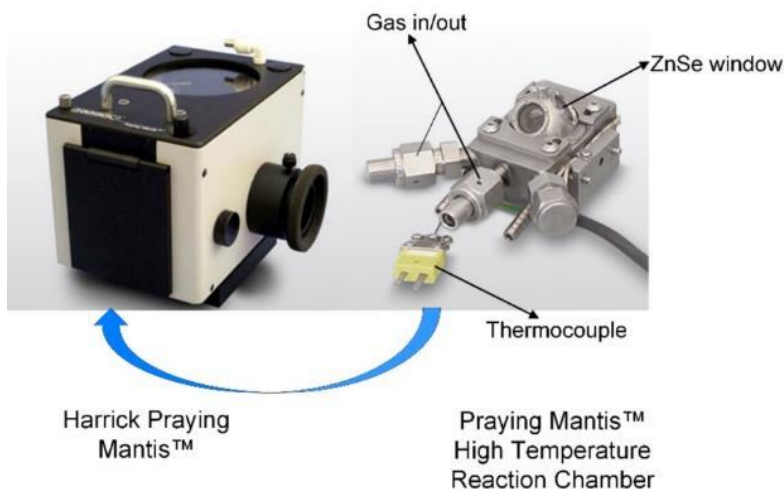


Fig. 3-4 The Harrick Praying Mantis™ into which the high-temperature reaction chamber is installed. The praying mantis is installed inside the spectrometer.

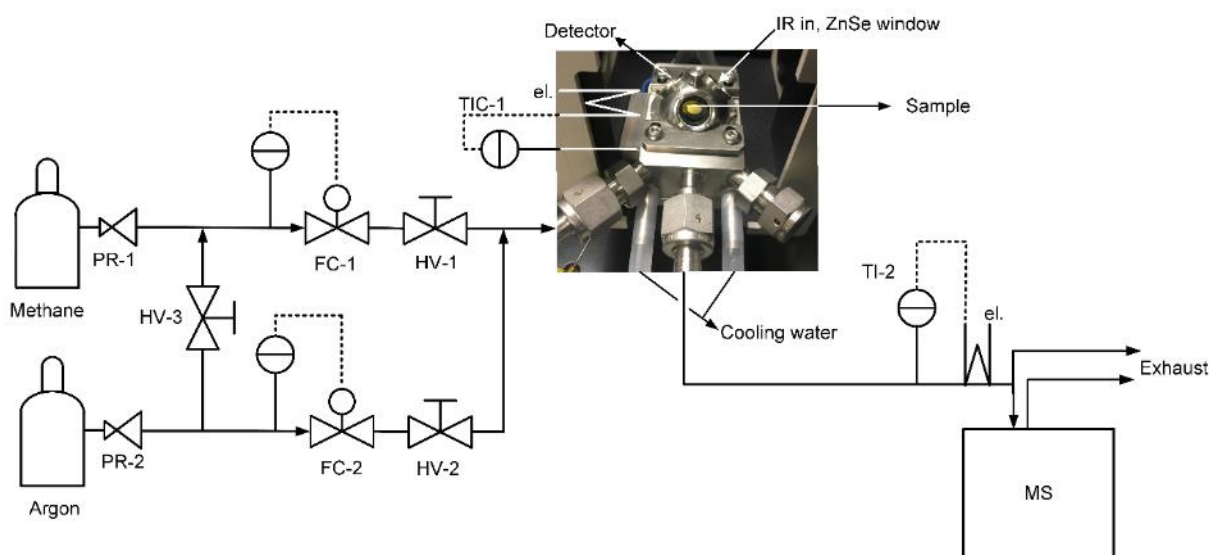


Fig. 3-5 Diffuse reflectance infrared Fourier transform spectroscopy (DRIFTS) setup for direct non-oxidative methane activation.

How does the catalyst bed in DRIFTS high-temperature chamber compare with the catalyst bed in a fixed bed reactor (Fig. 3-2)? For supported GaN/SBA15, the total GaN loading (in SBA-15 and KBr) was 1.5 mg (versus 19 mg in fixed bed reactor). The bed height was around 3 mm (versus 15 mm in fixed bed reactor). Also, 60 wt% of <5mm bed was KBr (versus 0% KBr in 15 mm bed in the fixed bed reactor). The residence time (at 700 °C) in the catalyst bed inside the DRIFTS chamber was <0.5s (versus <2s in the fixed bed reactor).

3.3.3 Methane activation through thermogravimetric analysis (TGA)

Methane activation followed by regeneration (with air) over GaN/SBA15 catalyst was also conducted employing TGA experiments (Netzsch TA 209 F1 Libra). The purpose was to determine the evolution of the adsorbed surface carbonaceous species (on the catalyst) as a function of time. A single activation cycle was also carried out with unsupported GaN without regeneration.

3.4 Experimental conditions and procedure

3.4.1 Fixed bed reactor

3.4.1.1 Methane activation

Around 500 mg of unsupported (250–1000 mg of commercial GaN) or 100 mg of supported catalysts were loaded to achieve the same bed height of 11 ± 1 mm and the same residence times of 1.3 s (superficial gas velocity at 700 °C) for both catalysts. The bulk densities of the GaN and GaN/SBA15 were 1300 kg m^{-3} and 260 kg m^{-3} , respectively. The resulting CH₄-based gas hourly space velocities (GHSV) were the same for both GaN and GaN/SBA15 with a value of 567 h^{-1} . Prior to heating, the catalyst was purged with Ar ($25 \text{ mL}_N \text{ min}^{-1}$) for 1 h, then heated to reaction temperature (600–750 °C) at a rate of 5 °C min^{-1} , and subsequently, CH₄ was added. For isotope labeling experiments, CH₃D (98 atom%, Sigma-Aldrich), ¹³CH₄ (99 atom%, Sigma-Aldrich), and CD₄ (99 atom%, Sigma-Aldrich) were used. The commonly used operating conditions were 700 °C, 80% CH₄ in Ar (0.8 bar CH₄ partial pressure, $4 \text{ mL}_N \text{ min}^{-1}$), 100 mg supported catalyst (or 500 mg unsupported catalyst), and 1 bar pressure. For the parametric study, the temperature was varied from 650–710 °C, and the CH₄ partial pressure was varied from 0.1–0.8 bar (total flow rate $5 \text{ mL}_N \text{ min}^{-1}$), the CH₄ flow rate was varied from 1–4 $\text{mL}_N \text{ min}^{-1}$ (0.8 bar partial pressure), the catalyst amount was varied from 100–1000 mg (0.8 bar CH₄ partial pressure, $4 \text{ mL}_N \text{ min}^{-1}$).

Based on a detailed mass spectrum analysis and calibration factors, the CH₄ conversion, the product molar flow rates ($\mu\text{mol min}^{-1} \text{ g}_{\text{Ga}}^{-1}$) as a function of time on stream, were determined. Besides ethylene (C₂H₄), other hydrocarbons such as propylene (C₃H₆), benzene (C₆H₆), toluene (C₇H₈) and naphthalene (C₁₀H₈) were detected and quantified. The CH₄ conversion [%] was calculated based on the gaseous carbon products (equation 3–4).

$$x_{CH_4} = \frac{\sum v_i \cdot \dot{n}_i}{\dot{n}_{CH_4, in}} \cdot 100 \quad 3-4$$

Where \dot{n}_i denotes the molar flow rate in $\mu\text{mol min}^{-1}$, while ν_i denotes the number of carbon atoms in the i^{th} species in the product stream (i.e., C_2H_4 , C_3H_6 , CO_2 , C_6H_6 , C_7H_8 , and C_{10}H_8). The denominator represents the molar flow of methane in the feed ($\mu\text{mol min}^{-1}$). The conversion closely represents the percentage (%) of carbon (C) converted to hydrocarbons and not coke. Results reported in this work for the methane activation were consistent within 5% of C and H elemental balances.

3.4.1.2 Isotope labeling experiments

The setup for the isotope labeling experiments was the same, as shown in Fig. 3–2. The only addition was a three-way valve (seamless switch between CH_4 and the isotope gas, and one outlet to the reactor) between FC–1 and HV–1. For all isotope labeling experiments, the temperature was set at 700 °C, and the isotope flow rate was 4 $\text{mL}_N \text{min}^{-1}$ (FC–1) calibrated for CH_4 and 1 $\text{mL}_N \text{min}^{-1}$ Ar as internal standard, the total duration for each isotope was 0.5–2 h. Since the MS was not calibrated for the isotope products (e.g., D_2 , HD, C_2D_4 , C_3D_6 , C_6D_6), the results are presented as the normalized MS signal with respect to the internal standard Ar (e.g., for C_2H_4 it was $[\text{A}]_{m/z=28}/[\text{A}]_{m/z=40}$). The same MS calibration factors were not assumed for the products and their isotopes (e.g., C_2H_4 vs. C_2D_4).

3.4.1.3 Catalyst regeneration

The quartz tube containing the spent catalyst, which was distinctly black (Fig. A3–6), was removed from the activation setup and installed in the regeneration setup. Then spent catalyst was first purged with Ar for 1 h ($20 \text{ mL}_N \text{min}^{-1}$) at room temperature, and then the temperature was increased under Ar to the regeneration temperature (500 °C for GaN, and 550 °C for GaN/SBA15) at a heating rate of 5 °C min^{-1} . The GaN and GaN/SBA15 catalysts were regenerated with air for 4.25 h and 3.25 h, respectively. After the regeneration step, the samples were purged under Ar for 20 h at 700 °C to remove any physisorbed species such as CO_2 , O_2 , and N_2 from the catalyst and reactor. For method 1, the reactor was then cooled to room temperature under Ar. The quartz tube with the regenerated catalyst was reinstalled in the activation setup for the second activation cycle, and this process was repeated for each subsequent cycle. A total of five activation and four intermediate regeneration cycles were carried out. Once completed, the spent catalysts (last cycle) were designated as GaN–R or GaN/SBA15–R.

For method 2, after regeneration with air and purging with Ar (for 20 h), the catalysts were re-nitridated with NH_3 ($20 \text{ mL}_N \text{min}^{-1}$) for 12 h. The unsupported catalysts were re-nitridated at 750 °C, while the supported catalysts were re-nitridated at 700 °C. After cooling down, the catalysts were purged with Ar ($20 \text{ mL}_N \text{min}^{-1}$) for 1 h to remove any remaining NH_3 . The quartz tube was then reinserted into

the activation setup. The spent catalyst at the end of 3 activation cycles (with 2 intermediate regenerations/re-nitridations) was designated as GaN–RN or GaN/SBA15–RN.

For H₂ as a regenerating agent, 100 mg of spent unsupported GaN catalyst was heated from room temperature to 950 °C at 2.5 °C min⁻¹ under 40% H₂ (balance 10 mL_N min⁻¹ of Ar); while the product gas was qualitatively analyzed for CH₄ (m/z =15), NH₃ (m/z=17), N₂ (m/z = 28) via mass spectrometry. For CO₂ regeneration, the sample was heated to 1000 °C under pure CO₂ (Praxair, 99.999%), while the mass signal corresponding to CO (m/z = 28) was monitored.

3.4.2 Diffuse reflectance infrared Fourier transform spectroscopy (DRIFTS)

DRIFTS experiments were carried out with both supported and unsupported catalysts. The supported catalyst was GaN/SBA15–700, and the unsupported was GaN–750. Henceforth, they are referred to as GaN/SBA15 and GaN in chapter 6. The catalysts were diluted with potassium bromide (KBr, Infrared grade, Fisher Chemical), the catalyst content in the KBr mixture was 40 wt% for the supported and 12.5 wt% for the unsupported. Before mixing with the catalyst, KBr was crushed in a glass mortar-pestle (< 20 μm) and dried overnight in a drying oven at 150 °C. After drying, KBr was cooled to room temperature and stored inside a desiccator. Around 9.5 mg of supported GaN/SBA15 (2.5 mg of unsupported GaN) was mixed thoroughly with 14 mg (17.5 mg KBr for GaN) of dried KBr. The loading of GaN in the DRIFTS sample of GaN/SBA15 was around 8 wt% (balance is SBA–15 and KBr). On the other hand, it was 12.5 wt% GaN in the DRIFTS sample of unsupported GaN. Also, GaN/SBA15 is well dispersed inside the SBA–15 support (refer to chapter 5, Fig. 5–6), which, in addition to higher dilution, helped in achieving a better peak resolution in the spectra (Chapter 6). Around 80% of the catalyst-KBr mixture was loaded in the high-temperature reaction chamber (Fig. 3–4).

The catalyst-KBr sample was placed on quartz wool (previously dried overnight at 150 °C, cooled and stored inside the desiccator) inside the high-temperature reaction chamber (Fig. 3–5). The chamber was purged with Ar (10 mL_N min⁻¹) for 1 h at room temperature. The sample was heated under Ar (10 mL_N min⁻¹) to 650 °C (10 °C min⁻¹) to remove moisture and adsorbed CO₂. It was then cooled down (or heated) under Ar (10 mL_N min⁻¹) to the initial temperature of analysis. The background was collected at this temperature. Two studies were carried out after the purging mentioned above and drying, (1) isothermal DRIFTS at 700 °C, and (2) temperature-programmed DRIFTS (TP–DRIFTS) from 400–700 °C were carried out. In the second approach, the experiment was started at 400 °C. The CH₄ was started at 2.0 mL_N min⁻¹, and the Ar flow rate was reduced to 0.5 mL_N min⁻¹. After 30 min,

CH₄ was stopped, and the Ar flow rate was gradually increased to 15 mL_N min⁻¹. The Ar flow was held for about 25 min to assure that CH₄ has been removed completely (confirmed via MS and the IR spectra). After that, the temperature was increased by 50 °C (20 °C min⁻¹) under Ar atmosphere. Around 10 min of stabilization time was given before starting CH₄ again, as discussed above. During this whole time (starting from the background collection), the IR spectra were being automatically collected continuously. To confirm that the surface intermediates were forming on the catalysts, the support (SBA-15 and N-SBA-15) were also tested undiluted, at 700 °C with 80% CH₄ in Ar (2.0 mL_N min⁻¹ CH₄ and 0.5 mL_N min⁻¹ Ar).

3.4.3 Thermogravimetric analysis (TGA)

For the TGA experiments (Netzsch TA 209 F1 Libra), ~20 mg of catalyst was loaded in the alumina crucible and dried prior at 150 °C (under Ar 20 mL_N min⁻¹). Methane activation was carried out at 700 °C for 24 h, followed by a 4.25 h regeneration step with air (20 mL_N min⁻¹, in a 1:1 air-Ar mixture) at 550 °C. In between the activation and regeneration, the sample was flushed for 5 h with Ar (20 mL_N min⁻¹). The single activation cycle with the unsupported GaN (120 mg) without regeneration was also carried out for 17 h.

3.5 Kinetic parameter estimation and model discrimination

The parameters to be estimated were the pre-exponential factors of the reaction rate and adsorption coefficients as well as the corresponding activation energies and heats of adsorptions, which can be described by Arrhenius' and van't Hoff's equations, respectively:

$$k_j = k_j^0 \cdot \exp\left\{-\frac{E_{A,j}}{\mathfrak{R} \cdot T}\right\} \quad 3-5$$

$$K_i = K_i^0 \cdot \exp\left\{-\frac{\Delta H_i}{\mathfrak{R} \cdot T}\right\} \quad 3-6$$

As this form of the equations often has very high magnitudes of k_j^0 and K_i^0 , since k_j^0 and K_i^0 refer to infinite temperature, a modified form based on a finite reference temperature T_{ref} , set to 973.15 K (700 °C), was used:

$$k_j = \exp\{\theta_{k,j}\} \cdot \exp\left\{\theta_{E,j} \left(1 - \frac{T_{ref}}{T}\right)\right\} \quad 3-7$$

$$K_i = \exp\{\theta_{K,i}\} \cdot \exp\left\{\theta_{H,i} \left(1 - \frac{T_{ref}}{T}\right)\right\} \quad 3-8$$

The parameters were chosen to be $\theta_{k,j} = \ln(k_{j,T_{ref}})$ and $\theta_{K,i} = \ln(K_{i,T_{ref}})$ to assure non-negative values of the pre-exponential factors according to the chemical theory. Activation energies and heat of adsorptions are estimated by introducing a dimensionless energy parameter $\theta_{E,j} = \frac{E_{A,j}}{\mathfrak{R} \cdot T_{ref}}$ and $\theta_{H,i} = \frac{\Delta H_i}{\mathfrak{R} \cdot T_{ref}}$, respectively.

For the determination of the kinetic parameters, data points at all temperature and pressure levels have been evaluated simultaneously by Bayesian estimation using the GREGPLUS solver within the software package Athena Visual Studio[®] v 14.2, developed by Stewart and Caracotsios [49]. For one response, Bayesian estimation essentially becomes the least square regression. The single response measured and estimated for this work is the rate of ethylene formation ($r_{C_2H_4}$).

The Bayesian probability theory presents a reasonable degree of belief and gives the best estimate from the available data and prior probability [50]. This was developed based on the Bayes Theorem[51]:

$$p((\theta_k, \varphi)|D) \propto L(D|\theta_k, \varphi) p(\theta_k, \varphi) \quad 3-9$$

Some knowledge of the values comprising the parameter vector θ_k is known a priori, e.g., the boundaries of activation energy E_A that lie between 0 and 450 kJ mol⁻¹ and reaction rate constants are positive.

The observed data D acknowledges the existence of error in these data and accounts for it explicitly through an error model function $\varepsilon_i(\varphi)$ associated with an error model parameter vector φ . This knowledge is included in the *prior* distribution $p(\theta_k, \varphi)$. The prior distribution is confirmed or modified by new data D , and this new knowledge about the parameters is represented by the *posterior* distribution $p((\theta_k, \varphi)|D)$.

The third term is the *likelihood* function $L(D|\theta_k, \varphi)$, which is the likelihood that the model k with its kinetics parameters θ_k generates the data D . The likelihood function reflects the discrepancy between the data and the model prediction. Through it, all the experimental data enter the Bayesian inference formulation along with the reactor numerical model. For the general case, the postulated models are related to N experimental data points data by:

$$M_k: r_i = f_k(\theta_k, u_k) + \varepsilon_i(\varphi) \quad 3-10$$

Where r_i is the rate of reaction for the i -th experimental condition, $f_k(\theta_k, u_k)$ is the k -th model with the parameters θ_k and experimental condition u_i . The experimental error is described by the error model $\varepsilon_i(\varphi)$. In the present case, the error space is determined by replicate experimental data points and does not assume to be normally distributed as commonly assumed in many studies. For the multiresponse parameter estimation, the GREGPLUS solver within the Athena Visual Studio software [49] minimizes the objective function $S(\theta_k)$ and calculates the maximum posterior probability density of the parameters θ_k and the posterior distribution of the proposed model k [52].

$$S(\theta_k) = (n + m + 1) \cdot \ln|v(\theta_k)| \quad 3-11$$

In most kinetic studies, the objective function is equal to the sum of the squares of the residuals, whereas in this study the objective function takes into account the number of responses m , the number of events per response n , and the determinant of the covariance matrix of the responses $|v(\theta_k)|$. Each element in the covariance matrix $v(\theta_k)$ is defined as:

$$v_{yj}(\theta_k) = \sum_{y=1}^n [Y_{yu} - f_{yu}(\varepsilon_u, \theta_k)] \cdot [Y_{ju} - f_{ju}(\varepsilon_u, \theta_k)] \quad 3-12$$

where Y_{yu} is the experimental observation and $f_{ju}(\varepsilon_u, \theta_k)$ is the predicted value for response y and event u . Each element is the sum of the product of the deviation of observed y and predicted j responses. The size of the square $v_{yj}(\theta_k)$ matrix is determined by the number of responses. The model discrimination is based on the posterior probability; once it is known, the preference for the different models is quantified. In a single response parameter estimation, the model with the smallest sum of the squares of the residuals may be the best. Model discrimination is based on the posterior probability share of model M_k :

$$\pi(M_k | D, \varepsilon) = \frac{p(M_k | D, \varepsilon)}{\sum_k p(M_k | D, \varepsilon)} \quad 3-13$$

Where $p(M_k | D, \varepsilon)$ is the posterior probability. A detailed description can be found in [50,53].

Chapter 4

4 Commercial gallium nitride (GaN)

The direct non-oxidative methane activation over commercially available gallium nitride powder has been investigated for the first time in a fixed bed reactor under continuous operation. High reaction temperatures (650–710 °C) are needed to initiate benzene formation due to the small surface area ($8 \text{ m}^2 \text{ g}^{-1}$) of the gallium nitride material, thermodynamic constraints, and the low residence time (1–4 s). Besides benzene and toluene, C_2 species and coke were formed. Part of the results presented in this chapter has been published: ‘Dutta, K., Li, L., Gupta, P., Gutierrez, D. P., Li, C-J., Kopyscinski, J., *Direct non-oxidative methane aromatization over gallium nitride catalyst in a continuous flow reactor*. Catal. Commun. 106 (2018) 16–19 [54]. Kanchan Dutta designed the setups and conducted the experiments, analyses, and wrote the manuscript. Daniel Gutierrez and Pranjal Gupta (undergrad summer students) assisted in carrying out the experiments and making GaN crystal structure on VESTA – JP–Minerals. Chao-Jun Li (collaborator, Chemistry McGill) provided feedback on the manuscript, while Jan Kopyscinski provided feedback on the methodology, analysis, and manuscript as well as was responsible for funding.

4.1 Introduction

Almost all the catalysts studied so far were bifunctional precious metals and metal oxides. Our manuscript focuses on metal nitrides, which are gaining interests as heterogeneous catalysts [23].

Nitride catalysts have been used for ammonia synthesis (Co, Mo, Ru nitrides), ammonia decomposition to obtain CO₂ free H₂ (Ru nitride), and for hydrotreating process (Mo nitride) [23]. Nitrides of Si, B have also been used as catalysts support. Compared to the conventional alumina and silica supports, the nitrides can have greater thermal conductivity, increased inertness, modified basicity, and enhanced hydrophobicity [23]. Gallium nitride, a material used in the semiconductor industry, was tested for the first time for methane activation in a batch reactor. The tests were carried out under Ultraviolet (UV) irradiation at room temperature, and also under thermocatalytic conditions at 450 °C and 5–8 h residence time [24,55]. They demonstrated a high selectivity for benzene ($S_{C_6H_6} = 97\%$ under UV and $S_{C_6H_6} = 89.8\%$, at 450 °C, respectively). However, due to low temperature and thermodynamic limitations, the methane conversion was less than 0.5%. Considering these promising results, the objective of this work has been to investigate the applicability of commercially available GaN powders (99.99%, Sigma Aldrich) for direct methane activation under flow conditions with much shorter residence time (~2 s). The quantification of the reaction product stream was done using a gas chromatogram (SRI GC 8610). The GC was calibrated for CH₄, H₂, C₆H₆, and C₇H₈ based on the work of Li et al. [24]. However, it could not be said with certainty that the product profile will be the same in a flow reactor having a residence time 3000 times less than the batch reactor [24]. Hence, to detect the formation of any additional component(s), the reactant effluent was analyzed *qualitatively* via online quadrupole mass spectrometry (Pfeiffer GSD 301). The work in this chapter laid the foundation for subsequent study of catalyst synthesis methods, activity testing procedures, and catalyst characterization techniques used. The methodologies have been discussed in chapter 3.

4.2 Characterization of fresh catalyst

Nitrogen adsorption/desorption measurement of the GaN powder showed type-II isotherm according to the IUPAC classification, indicating non-porous or macroporous particles (Fig. 4–1). The determined BET surface area was around 8 m² g⁻¹, which was considerably smaller than surface areas reported for the catalysts used in aromatization studies (i.e., $S_{BET} = 300\text{--}400$ m² g⁻¹ for Mo/ZSM-5 [45]). Gerceker et al. [16] used Pt and PtSn catalysts supported on SiO₂ and H-ZSM-5, with surface areas between 300–400 m² g⁻¹.

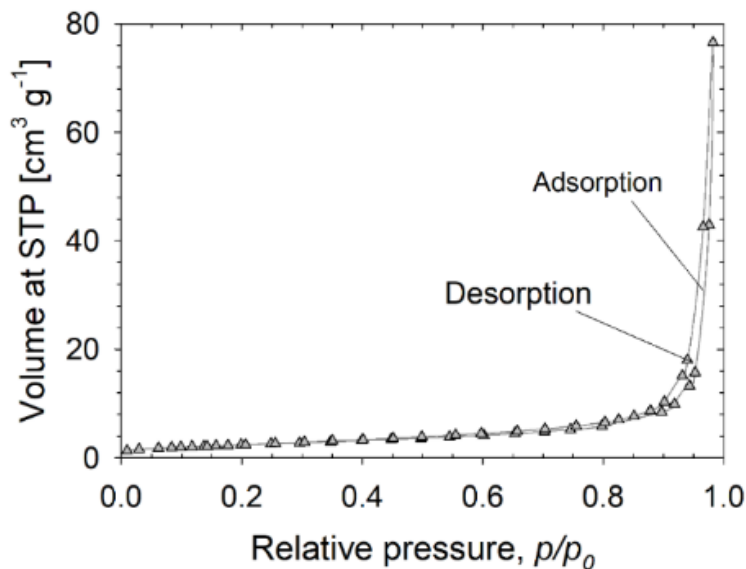


Fig. 4-1 Adsorption/desorption isotherm for the fresh commercial GaN powder

A transmission electron microscope (TEM) was used to identify the crystal structure of the fresh catalyst. Fig. 4-2A illustrates the GaN nanoparticles of the fresh catalyst, with crystal planes (Fig. 4-2B and C). Gallium nitride has a regular wurtzite structure (Fig. 4-2D) with both c - and m -planes (Fig. 4-2B and C). The m -plane is non-polar and made of alternating gallium and nitrogen ions, with 5.5 Å as the smallest width ($\sqrt{3}$ times the lattice constant a depicted in Fig. 4-2B and D) of the hexagonal lattice system of the wurtzite structure. On the other hand, the polar c -plane consists of either Ga or N atoms, with a bilayer thickness of 5.2 Å along the c -axis (lattice constant c , as depicted in Fig. 4-2C and D). Based on density functional theory (DFT) calculations [24], it has been suggested that m -planes are active for aromatization where the carbon atom of methane is oriented towards the Ga^{3+} , while one hydrogen atom towards the N^{3-} anion (alkyl adsorption model).

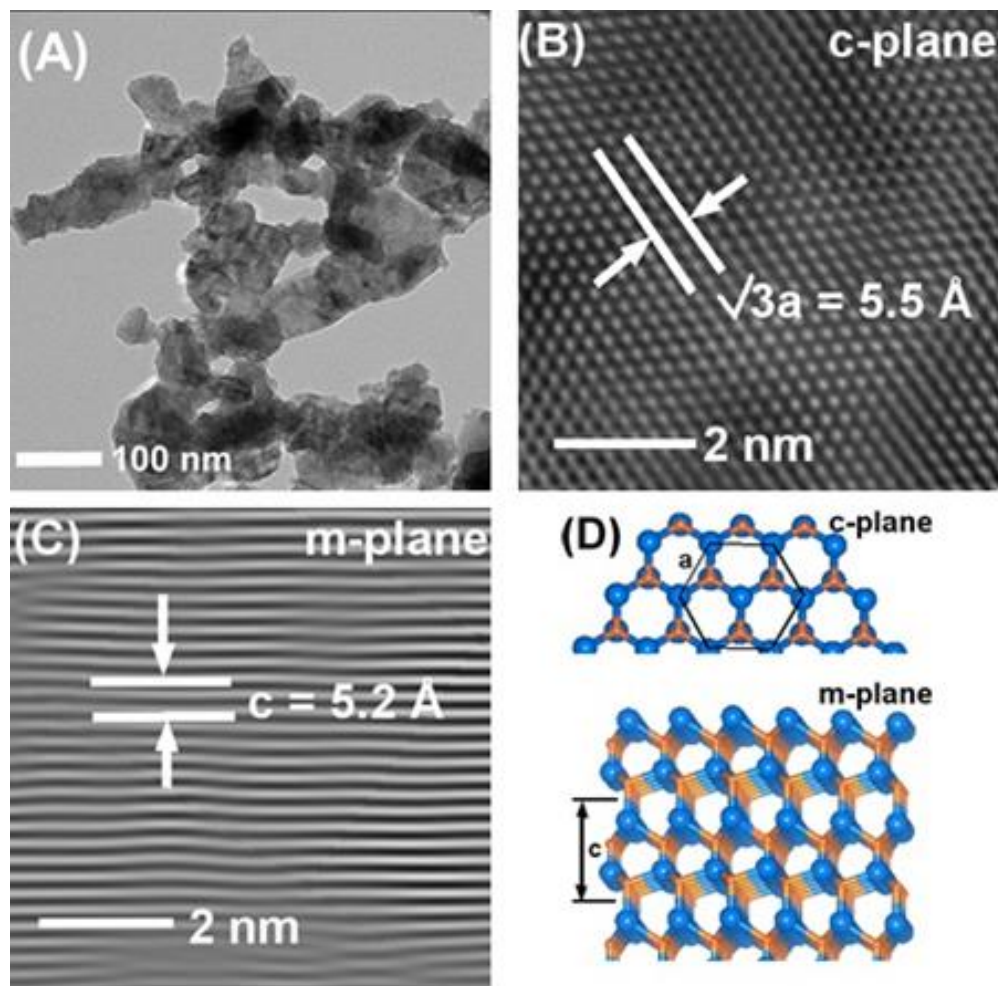


Fig. 4-2 (A) TEM image of the GaN nanoparticles (B) HRTEM images of the c -plane and (C) m -plane (D) wurtzite structure of GaN, showing c and m -planes, orange, and blue spheres represent N and Ga atoms, respectively.

X-ray diffraction analysis result on the fresh catalyst is illustrated in Fig. 4-3. The catalyst diffractograms matched with the reference gallium nitride XRD patterns (International Centre for Diffraction Data ICDD PDF # 04-013-1733).

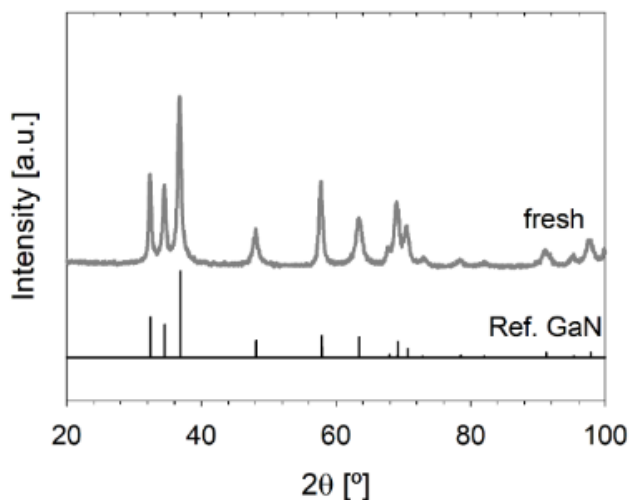


Fig. 4–3 XRD for fresh GaN in comparison with the reference (PDF #04–013–1733)

4.3 Activity measurements

4.3.1 Effect of temperature

The effect of reaction temperature was studied with a GHSV of $360 \text{ ml}_N \text{ h}^{-1} \text{ g}_{\text{cat}}^{-1}$ (1247 h^{-1}). Methane conversion (x_{CH_4}) was calculated per equation 4–1. Equation 3–4 could not be used because not all products could not be quantified by the GC. The subsequent runs were switched to MS for gas analysis (refer to section 4.3.4 for details).

$$x_{CH_4} = \frac{\dot{n}_{CH_4,in} - \dot{n}_{CH_4,out}}{\dot{n}_{CH_4,in}} \cdot 100 \quad 4-1$$

Theoretically, CH_4 conversion exceeds 8% only above $600 \text{ }^\circ\text{C}$ (Fig. 2–3B) with hydrogen, benzene, and toluene as the assumed products as per the minimization of free energy calculations. Experiments conducted between $250 \text{ }^\circ\text{C}$ and $600 \text{ }^\circ\text{C}$ did not show any benzene formation. CH_4 conversion was detectable above $500 \text{ }^\circ\text{C}$ with hydrogen as the only gaseous product. Benzene was formed at temperatures $> 650 \text{ }^\circ\text{C}$. The results are illustrated in Fig. 4–4 A, B, and C, showing CH_4 conversion, H_2 , C_6H_6 , and C_7H_8 product flow rates as a function of reaction time, respectively. The C_7H_8 product flow rates were approximately 10 times smaller compared to benzene.

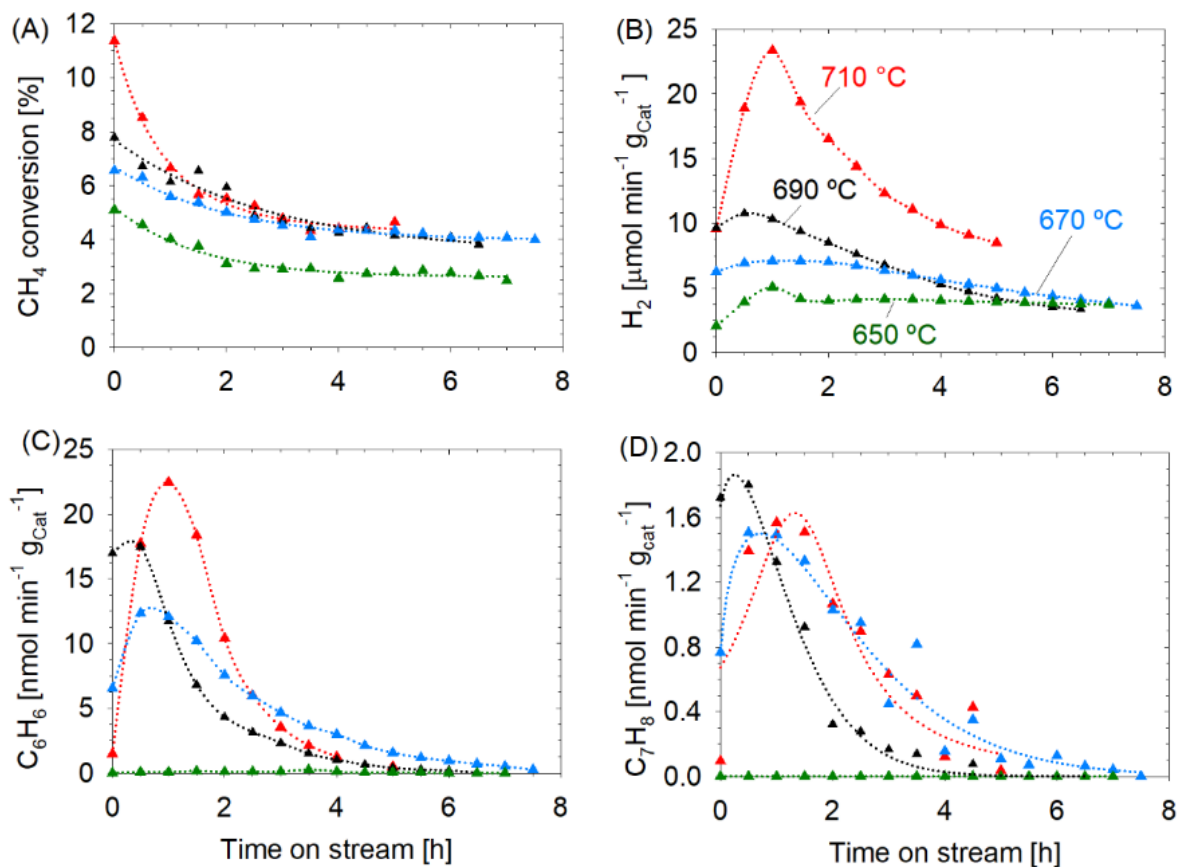


Fig. 4–4 Influence of temperature on (A) CH_4 conversion, (B) H_2 , (C) C_6H_6 , and (D) C_7H_8 formation rates (CH_4 GHSV: $360 \text{ mL}_\text{N} \text{ h}^{-1} \text{ g}_{\text{cat}}^{-1}$). Note. Symbols represent experimental data points, and dotted lines are for guidance only.

The mean residence time based on the inlet flow rate, catalyst volume, porosity, and the temperature was around 2.1 s, which was 7200 times shorter than the residence time used in the batch experiments (4 h). As expected, methane conversion increased with the increasing temperature but declined faster with time. The initial methane conversion increased from 5% to 11.5% for 650 °C to 710 °C. At all temperatures, an induction time was observed (0.5–1.5 h), in which the product flow rates increased, reached a maximum, and then declined (Fig. 4–4). This induction period is probably due to the formation of active species (C_xH_y), and once formed, they react with each other to produce benzene and toluene but also lead to coke formation. In the case of Mo-containing zeolites, an induction period is also observed but is associated with the reduction of Mo^{6+} to Mo_2C structures [11].

Under the current operating conditions, the commercial gallium nitride material deactivated rather fast; within 4 to 7 h, the C_6H_6 and C_7H_8 rates dropped to zero. The H_2 , on the other hand, reached a

constant flow rate, and the CH₄ conversion approached a value of 2%, indicating continuous coke formation. For comparison purposes, batch reactor experiments conducted at 450 °C resulted in a methane conversion of 0.56% after 4 h and no sign of carbon deposition [24]. However, due to the small catalyst surface area (8 m² g⁻¹) and short residence time (2.1 s) in the flow reactor, higher temperatures were needed, which favored a fast coke formation and low product yields. The maximum CH₄ conversion, C₆H₆, and H₂ formation rates at 710 °C (methane GHSV of 360 ml_N g_{cat}⁻¹ h⁻¹) were 11.5%, 22.5 nmol min⁻¹ g_{cat}⁻¹, and 23.5 μmol min⁻¹ g_{cat}⁻¹, respectively. Metal modified zeolites achieved similar methane conversions, but much higher benzene yields (e.g., X_{CH₄} = 8–14 %, r_{C₆H₆} = 1800–2400 nmol min⁻¹ g_{cat}⁻¹ at 700 °C with a GHSV of 1500 ml_N g_{cat}⁻¹ h⁻¹ [56]). However, the zeolite catalysts had BET surface areas of > 300 m² g⁻¹.

4.3.2 Effect of catalyst amount

Experiments with different amounts of catalyst were conducted at 670 °C and methane GHSV of 180–360 ml_N h⁻¹ g_{cat}⁻¹. This not only changed the total surface area (2, 4 to 8 m²) but also increased the residence time from 1.0, 2.1 to 4.3 s for 250, 500, and 1000 mg GaN, respectively. The product molar flow rates were almost proportional to the catalyst amount. The maximum benzene rates (Fig. 4–5B) were 13.0 nmol min⁻¹ g_{cat}⁻¹ for 1000 and 500 mg catalyst, respectively. In the same sequence, the maximum hydrogen flow rates were 6 to 7 μmol min⁻¹ g_{cat}⁻¹ (Fig. 4–5C). For the run with 250 mg of catalyst, benzene was only formed during the first hour. Higher catalyst mass led to slower deactivation, which was evident from benzene and hydrogen flow rates at the end of the run (Fig. 4–5B and C). Unlike the product flow rates, the conversion of methane was not directly proportional to the catalyst mass (Fig. 4–5A).

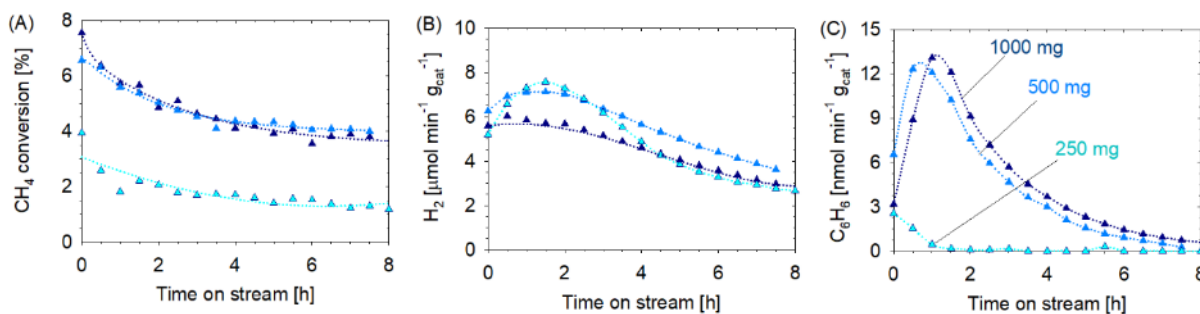


Fig. 4–5 Influence of catalyst mass at 670 °C on (A) CH₄ conversion, (B) H₂, and (C) C₆H₆ formation rates (methane flow rate: 180 ml_N h⁻¹). Note. Symbols represent experimental data points, and dotted lines are for guidance only.

4.3.3 Effect of methane partial pressure

The effect of CH₄ feed concentration is also an important parameter, as it is directly proportional to the amount of active species (C_xH_y). Two different feed gas compositions were used: 40 vol% and 60 vol% methane with balance Ar. The temperature was set at 670 °C with a methane GHSV of 228 and 360 mL_N h⁻¹ g_{cat}⁻¹. The CH₄ conversion, H₂, and C₆H₆ molar flow rates as a function of time are illustrated in Fig. 4–6 (note; curve labeled with 500 mg refers to 60 vol%). The CH₄ conversion was about 3.5 times higher for the higher partial pressure. This was most likely due to an increased formation of reactive surface intermediates (C_xH_y), which in turn results in a higher C₆H₆ and H₂ formation rates. The maximum C₆H₆ and H₂ rates were 2.3 times and 1.5 times higher for the experiment conducted with 60 vol% methane compared to the experiment conducted with 40 vol% CH₄. Nevertheless, carbon deposition was still dominant, given the black appearance of the spent catalyst and the TEM analysis (Fig. 4–9).

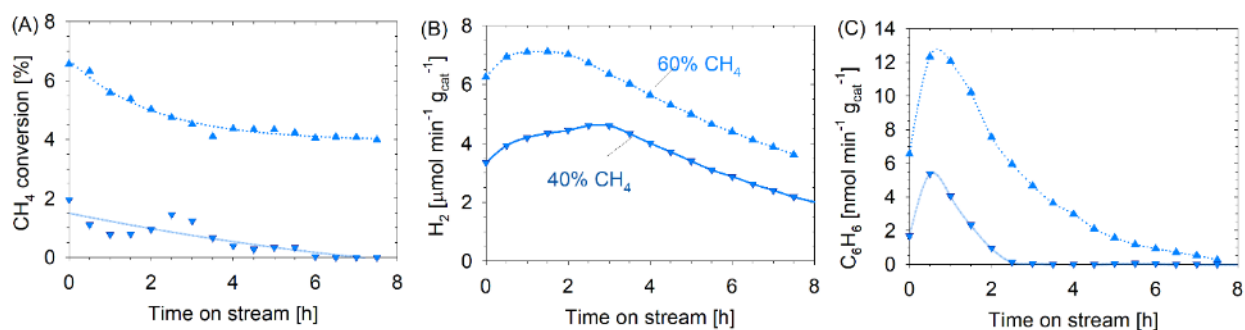


Fig. 4–6 Influence of CH₄ partial pressure at 670 °C on (A) CH₄ conversion, (B) H₂, and (C) C₆H₆ formation rates (GHSV for 40 vol% methane is 228 mL_N h⁻¹ g_{cat}⁻¹ based on CH₄). Note. Symbols represent experimental data points, and dotted lines are for guidance only.

4.3.4 Temperature programmed surface reaction (TPSR)

Temperature programmed surface reaction (TPSR) with MS was carried out with CH₄ GHSV of 360 mL_N h⁻¹ g_{cat}⁻¹ at 710 °C. Besides C₆H₆ and C₇H₈, the TPSR–MS experiment confirmed the formation of C₂ species, such as ethylene (Fig. 4–7, m/z = 28). No cyclohexane nor other aliphatic hydrocarbons were detected.

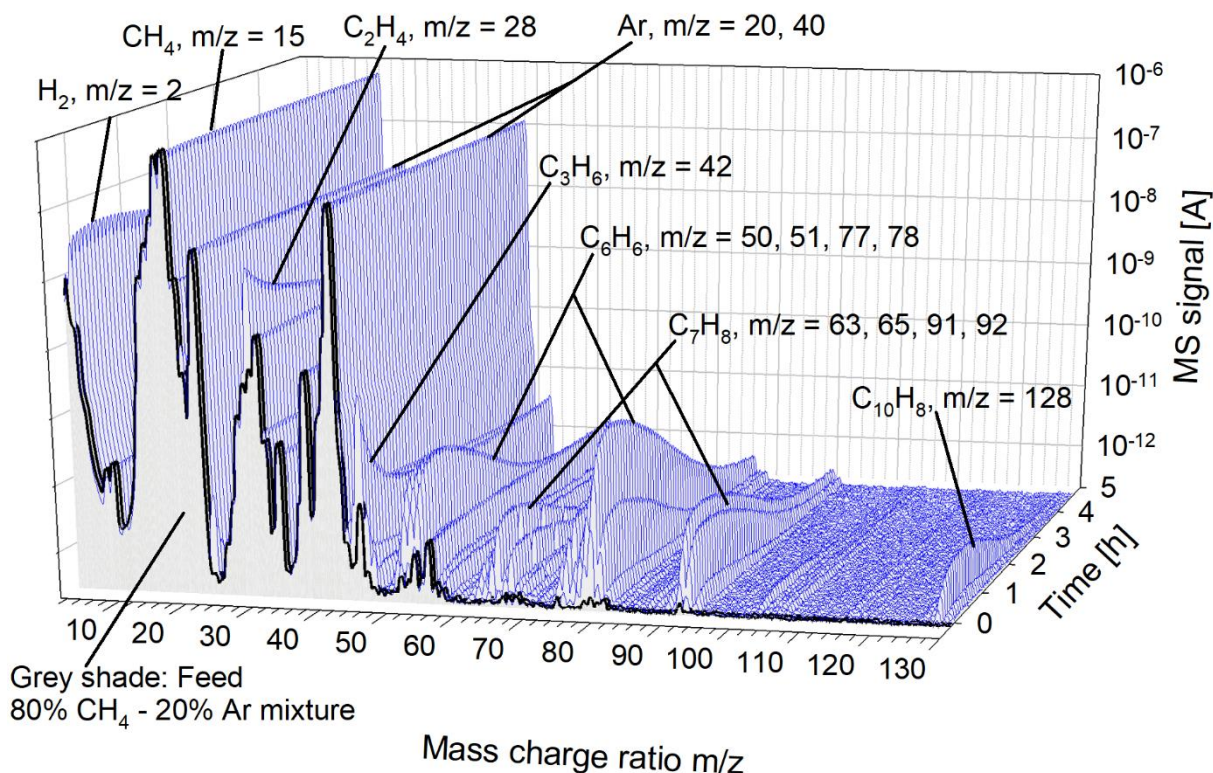


Fig. 4–7 The TPSR–MS experiment with CH₄ GHSV of 360 mL_N h⁻¹ g_{cat}⁻¹ at 710 °C. Note; the dark grey spectrum refers to the inlet representing the feed composition, while the subsequent spectra refer to the product profile as a function of time.

Additionally, naphthalene (C₁₀H₈, m/z = 128) was also detected. It became obvious that the GC could not be used for the study because with *its existing configuration* because C₂H₄ and C₃H₆ were masked by a large tailing CH₄ (80%) peak saturating the FID detector. Also, because of naphthalene, the time for the GC method was more than 30 min. Since the reaction rapidly deactivates the catalysts, and to capture the product profile, the MS was used for the subsequent studies.

4.4 Characterization of spent catalyst

Although visibly, the spent catalyst looked black due to carbon deposition (like the spent catalysts shown in Fig. A3–6), XRD did not exhibit any structural change even at 710 °C (Fig. 4–8). No peaks for carbon (coke) were observed, indicating that the carbon was probably amorphous.

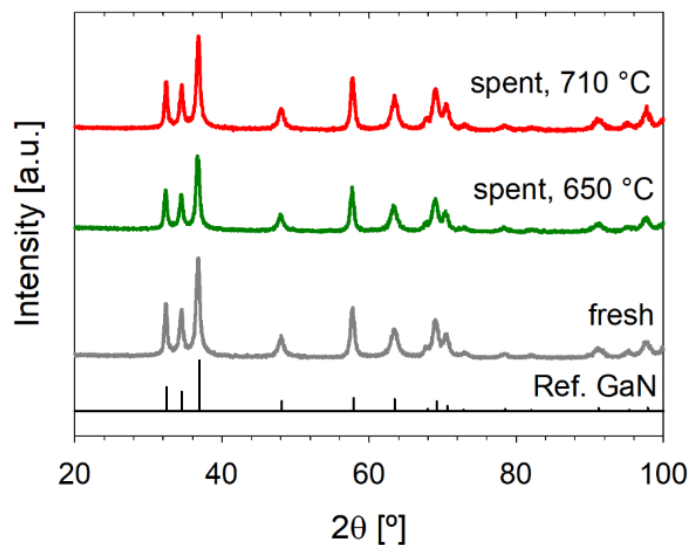


Fig. 4–8 XRD for fresh and spent GaN in comparison with the reference (PDF #04–013–1733)

TEM analysis was also carried out on the spent catalyst for detecting carbon deposition on the surface (Fig. 4–9). The spent catalyst used at 710 °C has a thin layer of carbon deposited on the surface, which was not observed on the fresh catalyst.

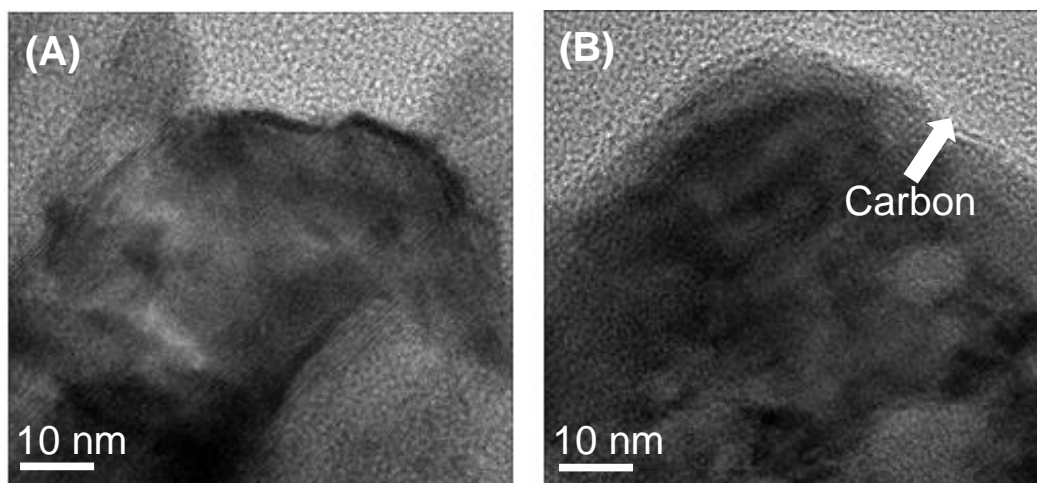


Fig. 4–9 TEM images of single (A) fresh GaN nanoparticle without any carbon deposition on the surface in comparison with (B) spent GaN nanoparticles with a thin layer of carbon on the surface.

Temperature-programmed oxidation (TPO) was carried out for both fresh and spent catalysts (Fig. 4–10). Prior to the oxidation with air, the catalysts were dried under nitrogen at 130 °C for 30 minutes, yielding a small weight decrease of 0.26 wt% for the fresh catalyst and no change in weight for the spent catalyst. This could be due to the moisture sensitivity of gallium nitride powder. A further

increase of the temperature to 400 °C resulted in an additional minimal weight loss due to the devolatilization of other species in the fresh catalyst. On the other hand, spent gallium nitride did not exhibit any weight loss until 440 °C. After that, a 0.5 wt% drop in weight was observed until a temperature of 540 °C, indicating oxidation of the coke. The temperature range confirms that the coke deposition was amorphous and not graphitic [57]. For the fresh catalyst, the weight increased at a temperature higher than 420 °C due to oxidation of gallium nitride (GaN) to gallium oxide (Ga₂O₃). Two moles of gallium nitride produce one mole of gallium oxide, which increases weight by about 12% (assuming complete oxidation). No analysis was done for the fate of nitrogen during oxidation. Weight increase was also observed for the spent catalyst after 540 °C. The oxidation of the coke deposition and gallium nitride might be overlapping, which masks the weight loss due to carbon oxidation.

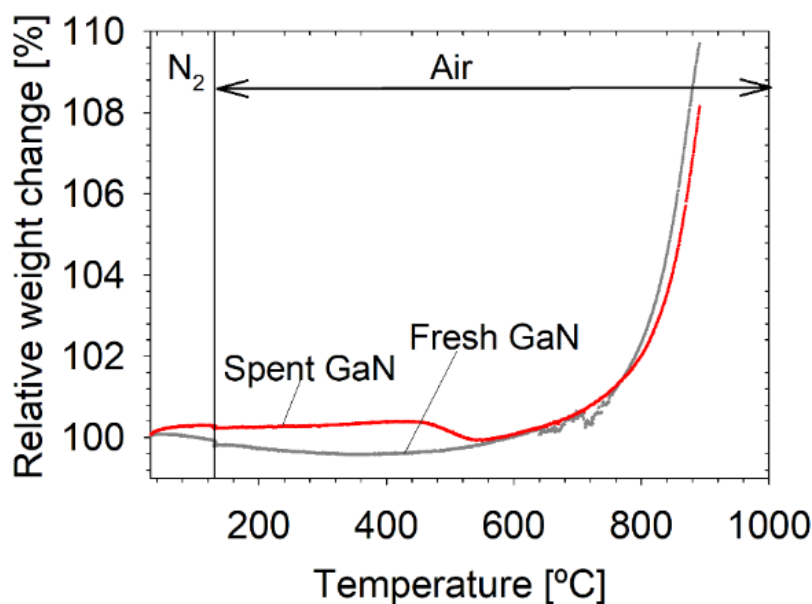


Fig. 4-10 Temperature-programmed oxidation (TPO) for fresh and spent GaN catalysts.

4.5 Conclusions

The gallium nitride exhibits a catalytic activity towards the direct non-oxidative methane activation in a continuous flow reactor. Small surface area (8 m² g⁻¹) and lower residence time (1–4 s) necessitated temperatures above 650 °C to initiate benzene formation, and at these temperatures, coke formation becomes inevitable. However, the formation of C₂ species (C₂H₄) was dominant in the flow reactor. This was attributed to lower residence time and faster deactivation of the catalyst (formation of polyaromatic compounds like naphthalene and above).

Chapter 5

5 Gallium nitride catalyst development

Using pure GaN, as discussed in Chapter 4, is not economically viable. Also, most active sites (GaN) are inaccessible due to the non-porous nature of the material. Therefore, the development of a supported GaN catalyst with a high metal dispersion is of interest. Within this chapter, a new GaN/SBA15 catalyst is reported for the direct non-oxidative methane coupling to ethylene. In detail, the effect of nitridation conditions on the catalyst properties and activity was investigated and compared to unsupported GaN as well as to parent gallium oxide catalysts (Ga_2O_3). The optimum nitridation temperatures were 700 °C and 750 °C for the GaN/SBA15 and the unsupported GaN catalyst, respectively. Supported catalysts were more stable and had 5–10 times higher product (ethylene) formation rates per gram of gallium than the unsupported catalysts due to the higher surface area (>320 vs. $<20 \text{ m}^2 \text{ g}^{-1}$) and Ga-dispersion inside the pores. Compared to the oxide precursors, the nitrides exhibited a higher atom conversion efficiency for the CH_4 carbon leading to higher ethylene selectivity (71 % for GaN/SBA15, <58 % for Ga_2O_3 /SBA15) and lower coke selectivity (27 % for GaN/SBA15, 40 % for Ga_2O_3 /SBA15).

Parts of the results presented in this chapter have been published: ‘Dutta, K., Chaudhari, V., Li, C-J., Kopyscinski, J., *Methane conversion to ethylene over GaN catalysts. Effect of catalyst nitridation*, Appl. Catal. A, Gen. 595 (2020) 117430’ [58]. Kanchan Dutta developed the catalyst synthesis methodology,

conducted the experiments and analysis, and wrote the manuscript, while Vishnu Chaudhari (Master's student) assisted with modeling and reviewed the manuscript. Chao-Jun Li (collaborator, Chemistry McGill) provided feedback on the manuscript, while Jan Kopyscinski provided feedback on the methodology, analysis, and manuscript as well as was responsible for funding.

5.1 Introduction

In chapter 4, it was established that gallium nitride is thermocatalytic active toward the methane activation. However, low surface area ($<10 \text{ m}^2 \text{ g}^{-1}$) and metal dispersion make pure GaN not economically viable. ***I hypothesize that increasing the total surface area as well as using low acidic support will increase the conversion, reaction rate, and product selectivity.*** Only a small number of Brønsted acid sites are required to accomplish the aromatization reaction for benzene formations. The additional Brønsted acid sites serve only to facilitate the retention of coking precursors inside the zeolite, which promotes their further polymerization, thereby accelerating the formation of aromatic carbonaceous deposits. Removal of these extraneous Brønsted acid sites (Dealumination, silanation of the zeolite support) suppresses the aromatic coke-forming reactions [11]. I chose SBA-15 as the first support material for synthesizing supported GaN. The SBA-15 practically does not have any Brønsted acid sites ($<0.1 \mu\text{mol g}^{-1}$ [59]). Moreover, during nitridation, SBA-15 also gets nitridated (refer to section 3.1.2 for the catalyst synthesis methodology), where Si-OH gets converted to Si-NH₂, further reducing the Brønsted acid sites. The synthesis process of SBA-15 is well established and can be modified to change the pore size and surface area.

In the optoelectronics and semiconductor industry, GaN is often synthesized in the form of nanostructures (nanotubes [60], nanowires [61], and nanorods [60]) through various procedures such as arc discharge [62], laser ablation [63], chemical vapor deposition [64], plasma-assisted molecular beam epitaxy [65], and metal-organic vapor phase epitaxy [66]. In most of these procedures, NH₃ at high temperature (nitridation) is used to produce GaN nanostructures from gallium precursors. Some of these methods might not be applicable for the preparation of the catalysts that require a large surface area and well-distributed active sites. In this work, for the first time, supported gallium nitride catalysts were synthesized (refer to Chapter 3, sec. 3.1), and the effect of the nitridation conditions on the direct non-oxidative methane conversion to value-added chemicals were investigated. Also, unsupported catalysts were synthesized, which were analogous to the commercial GaN (refer to Chapter 3, section 3.1). The methodologies have been discussed in chapter 3.

5.2 Characterization of fresh catalyst

5.2.1 Unsupported catalysts

The nitridation study for unsupported catalysts was divided into two parts, to investigate (1) the effect of nitridation temperature, and (2) the effect of NH_3 exposure time at a fixed temperature (750 °C). In the first part, the temperature was increased under the NH_3 atmosphere, while in the second study, NH_3 was added after the target temperature of 750 °C was reached (under Ar atmosphere). During the nitridation, water is produced ($\text{Ga}_2\text{O}_3 + 2 \text{NH}_3 \leftrightarrow 2 \text{GaN} + 3 \text{H}_2\text{O}$), which was recorded employing mass spectrometry (H_2O , $m/z = 18$). The first study was a combination of a temperature-programmed reaction with an extended soak time at five different temperatures to determine the onset and peak temperature for the Ga_2O_3 nitridation and the optimum condition. The results indicate that the nitridation started above 600 °C and that the maximum H_2O formation rate was close to the targeted nitridation temperature for $T_{\text{Ni}} = 650\text{--}800$ °C (Fig. 5–1A). No maximum was observed for 600 °C, indicating a prolonged nitridation rate. For nitridation temperatures of 750 and 800 °C, the water signal dropped after 8–10 h to the same level resulting in a very similar Ga_2O_3 conversion, which was confirmed by the total nitrogen analysis ($\sim 88 \pm 5\%$, Fig. 5–1A and B). For GaN–650 and GaN–700, the H_2O production rate (i.e., Ga_2O_3 conversion rate) was significantly slower, and even after a total NH_3 exposure time of 24 h, the Ga_2O_3 conversions were $46 \pm 5\%$ and $70 \pm 5\%$, respectively (Fig. 5–1B).

In the second study, the Ga_2O_3 samples were exposed to NH_3 for 3 h, 6 h, or 9 h after the desired nitridation temperature of 750 °C was achieved. The results are illustrated in Fig. 5–1D and E. The H_2O signal increased instantaneously at the onset of the nitridation and then declined rather fast with time. The longer the nitridation time, the smaller the H_2O signal, and the higher the Ga_2O_3 conversion (i.e., 64% at 3 h vs. 85% at 9 h, refer to Fig. 5–1D and E). Based on this result, a nitridation temperature of 750 °C was sufficient as complete bulk conversion might not be necessary for the methane conversion. The nitridation reaction is thermodynamically unfavorable and highly endothermic as indicated by the large positive standard Gibbs free energy and heat of reaction ($\Delta G_{R,298K} = 191.8 \text{ kJ mol}^{-1}$ and $\Delta H_{R,298K} = 238.2 \text{ kJ mol}^{-1}$) [67]. However, the significant excess of ammonia, the removal of gaseous products (water), and higher temperatures (750 and 800 °C) resulted in an 88% conversion of Ga_2O_3 to GaN (Fig. 5–1B). For lower temperatures (with the same gas flow rates), the Ga_2O_3 conversion was significantly smaller (by around 50%), indicating that more time and

higher temperature was needed. Moreover, not all Ga was accessible for NH_3 due to collapsing of the pores.

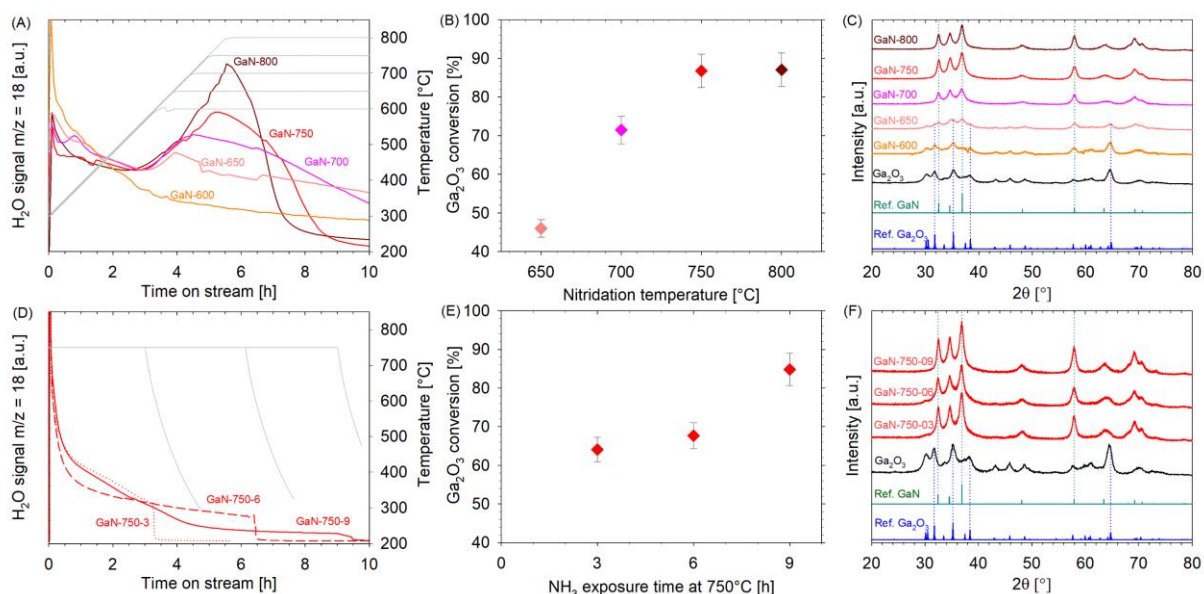


Fig. 5-1 Results for nitridation of unsupported catalysts. (A) H_2O signal as a function of nitridation time at different temperatures, (B) Conversion of Ga_2O_3 as a function of temperature (C), XRD pattern as a function of temperature. (D) H_2O signal as a function of nitridation time at 750 °C, (E) Conversion of Ga_2O_3 as a function of nitridation time at 750 °C and (F) XRD pattern as a function of nitridation time at 750 °C.

XRD analyses confirmed the trend as a distinct transition from $\beta\text{-Ga}_2\text{O}_3$ to GaN with increasing nitridation temperature was observed (Fig. 5-1C). The catalyst nitridated at 600 °C exhibited predominately broad XRD pattern of $\beta\text{-Ga}_2\text{O}_3$ ($2\theta = 31.7^\circ, 35.2^\circ, 38.4^\circ,$ and 64.7° ; PDF file #00-006-0523 from the International Centre for Diffraction Data). The XRD pattern for the samples treated at 650 °C started to show clear diffraction pattern of GaN ($2\theta = 32.5^\circ, 36.9^\circ,$ and 57.9° ; PDF file # 04-013-1733) with only minor peaks for $\beta\text{-Ga}_2\text{O}_3$. At nitridation temperatures of 700 °C and higher, the catalyst samples had only diffraction patterns corresponding to GaN, even though the Ga_2O_3 conversion was only between 70–90%.

For the second study, the XRD analyses of these three samples showed only diffraction patterns corresponding to GaN (Fig. 5-1F). Even with a Ga_2O_3 conversion of only 64% at 3 h NH_3 exposure time, the peaks corresponding to oxide ($\beta\text{-Ga}_2\text{O}_3$) were not visible. It has been suggested that the conversion of $\beta\text{-Ga}_2\text{O}_3$ to GaN proceeds either through the formation of amorphous gallium

oxynitride (GaO_xN_y) intermediates or via Ga_2O [68]. The latter Ga_2O is a gaseous intermediate (>900 °C).

Nitrogen adsorption/desorption analysis of all unsupported Ga_2O_3 and GaN catalysts exhibited type-IV isotherms with H3 and H4 type hysteresis loops with bimodal pore size distribution (Fig. 5–2). The disordered structure was also observed for Ga_2O_3 synthesized by the EISA method [69]. Table 5–1 summarizes BET surface areas and pore volumes, as well as two-pore sizes with the highest contributions. The Ga_2O_3 had a surface area of $19 \text{ m}^2 \text{ g}^{-1}$ and a pore volume of $0.08 \text{ cm}^3 \text{ g}^{-1}$ with a bimodal pore size distribution of 7.5 and 31.5 nm. More than 85% of the surface area corresponded to meso- and macropores, while the rest were micropores.

Upon nitridation at 650 °C, the surface area decreased by $\sim 20\%$ down to $15 \text{ m}^2 \text{ g}^{-1}$ with a pore volume of $0.075 \text{ cm}^3 \text{ g}^{-1}$. This was probably due to the change from the monoclinic crystal structure of $\beta\text{-Ga}_2\text{O}_3$ to the wurtzite structure of GaN. A further decrease of the surface area to $11 \text{ m}^2 \text{ g}^{-1}$ at $T_{\text{Nitridation}}$ of 800 °C could be attributed to sintering and pore structure collapse due to the crystallization of GaN at temperatures above the calcination temperatures [70]. Commercial GaN powder had a slightly smaller surface area with $S_{\text{BET}} = 8 \text{ m}^2 \text{ g}^{-1}$ (see chapter 4 and reference [54]) than catalyst prepared in this work.

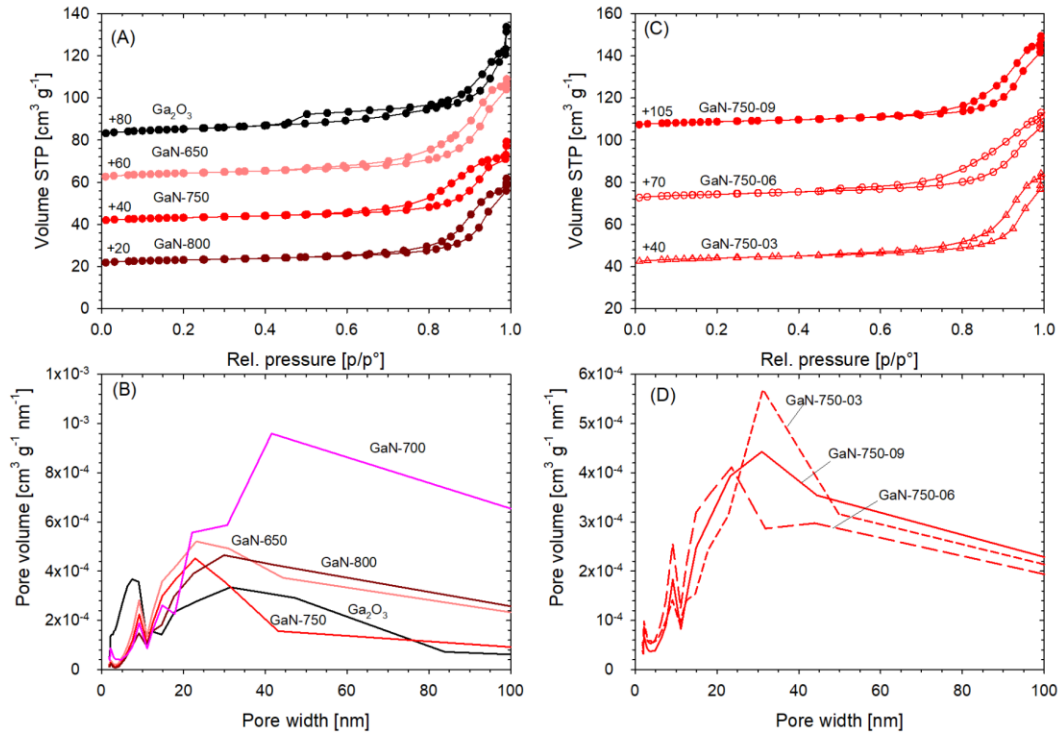


Fig. 5-2 (A) N_2 adsorption-desorption isotherms and (B) Particle size distribution for unsupported Ga_2O_3 and nitridated samples at different nitridation temperatures. Samples were under ammonia for 24 h. (C) N_2 adsorption-desorption isotherms and (D) Pore size distribution for unsupported nitridated samples at 750 °C under different ammonia exposure duration.

Table 5-1 Nitrogen adsorption and desorption results for unsupported Ga_2O_3 , GaN catalysts.

Sample	$t_{Nitridation}$ [h]	$T_{Nitridation}$ [°C]	S_{BET}^a [$m^2 g^{-1}$]	S_{Micro}^a [$m^2 g^{-1}$]	$S_{Meso+Macro}^a$ [$m^2 g^{-1}$]	V_{Pore}^b [$cm^3 g^{-1}$]	D_{Pore}^c [nm]
Ga_2O_3	—	—	18.9	0.8	18.1	0.083	7.5, 31.5
GaN-650	24	650	15.4	1.7	13.7	0.075	9.2, 23.1
GaN-750	24	750	11.6	1.0	10.6	0.060	9.2, 22.9
GaN-800	24	800	11.3	1.2	10.1	0.064	9.1, 29.9
GaN-750-03	3	750	14.5	1.8	12.7	0.067	9.1, 31.2
GaN-750-06	6	750	15.5	1.9	13.6	0.065	9.2, 23.6
GaN-750-09	9	750	13.4	1.4	12.0	0.069	9.2, 31.0

^a S_{BET} = BET total specific surface area obtained from adsorption data in the p/p^0 range from 0.06–0.2; all reported data are within $\pm 4 m^2 g^{-1}$ based on the repeated analysis. S_{Micro} = micropore; $S_{Meso+Macro}$ = meso + macropore surface areas.

^b V_{Pore} = pore volume was obtained at $p/p^0 = 0.9$

^c D_{Pore} = bimodal pore size distribution for all samples, calculated using the Barrett-Joyner-Halenda (BJH) method;

TEM and EDS analysis for Ga_2O_3 and GaN-650 are illustrated in Fig. 5-3. Both gallium catalysts are an agglomeration of nanoparticles with polycrystalline structure, as depicted with the darkfield in the top-left insets of Fig. 5-3A and B. The nanoparticle size ranges from 20 to 200 nm (Fig. A1-1). Polycrystalline Ga_2O_3 has several characteristic d -spacings representing the monoclinic structure (cell dimensions of $a = 12.23 \pm 0.02$, $b = 3.04 \pm 0.01$, $c = 5.80 \pm 0.01$ Å and $\beta = 103.7 \pm 0.3^\circ$) [71]. Fig. 5-3 and A1-2 visualizes d -spacings of 3.0 ± 0.1 and 6.0 ± 0.1 Å corresponding to the [001] plane [72] as well as 9.9 Å associated with the [010] plane [73].

The synthesized GaN-650 catalyst had a Ga_2O_3 conversion after the nitridation of around 46 %; thus, as expected, both GaN and Ga_2O_3 phases were visible in the TEM, with a possible core-shell structure of Ga_2O_3 in the center (Fig. 5-3B and A1-3). GaN has a regular wurtzite structure with both m - and c -planes. The m -plane is non-polar and made of alternating Ga and N ions, while the c -plane is polar containing either Ga or N ions. The m -plane with 5.2 Å, as well as the hexagonal structure of the c -plane with $\sqrt{3}a = 5.5$ Å could be observed, as illustrated in Fig. 5-3 B, and Fig. A1-4, respectively. For the amorphous Ga_2O_3 part, a d -spacing of 9.9 Å was measured. An amorphous gallium oxynitride (GaO_xN_y) might exist at the boundary between GaN and Ga_2O_3 .

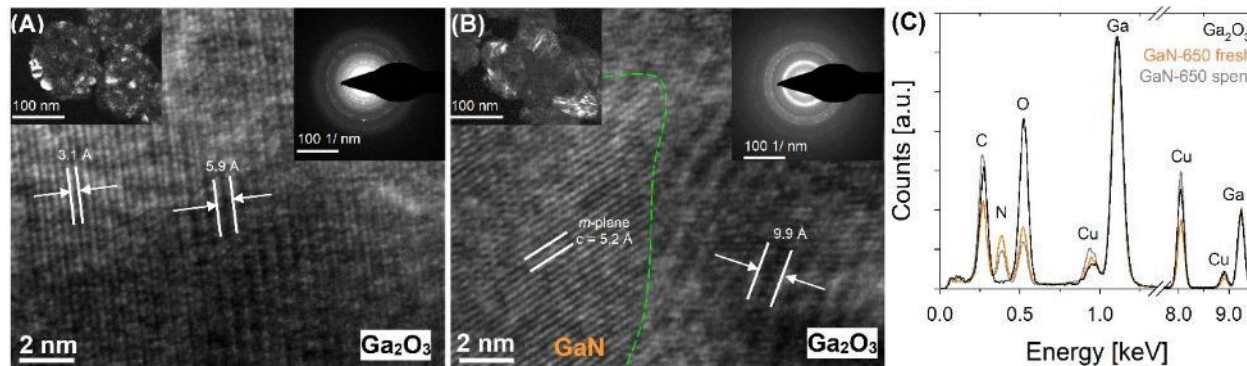


Fig. 5-3 HRTEM image of (A) fresh Ga_2O_3 and (B) fresh GaN-650 catalyst with GaN/ Ga_2O_3 intersection.

Top left inset darkfield image at low resolution and top right inset electron diffraction pattern. (C) EDS analyses (Ga normalized) for Ga_2O_3 , fresh, and used GaN-650. Note: The green dashed line indicates approximately the boundary between GaN and Ga_2O_3 . Note: Cu and some of the C signals in EDS are from the grid.

5.2.2 Supported catalysts

Supported gallium oxide ($\text{Ga}_2\text{O}_3/\text{SBA15}$) samples showed a slightly higher H_2O signal upon nitridation when compared with SBA-15 without gallium oxide (GaN/SBA15 vs. N-SBA15 in Fig. 5-4A). But

no maximum was observed, which was probably due to the lower Ga_2O_3 content (around 35 mg compared to 1000 mg for the unsupported Ga_2O_3 loaded for nitridation). As mentioned above, the degree of nitridation (i.e., Ga_2O_3 conversion) by total nitrogen analyses of the product (GaN/SBA15) could not be determined.

The nitridated gallium-containing supported catalysts showed the presence of crystalline GaN but did not exhibit any peak corresponding to $\beta\text{-Ga}_2\text{O}_3$ (Fig. 5–4B). Even for the $\text{Ga}_2\text{O}_3/\text{SBA15}$ samples, no diffraction pattern for $\beta\text{-Ga}_2\text{O}_3$ was observed, indicating very small non-crystalline particles. The XRD peak around $2\theta = 44^\circ$ (Fig. 5–4B) corresponds to the aluminum sample holder of XRD. Although the total N could not be performed for the supported catalysts, the peaks corresponding to the nitrides are sharper at all nitridation temperatures compared to the unsupported catalysts (GaN–600 and 650). Since the total Ga content in the supported catalyst was much lower, it can be assumed that the conversion of Ga_2O_3 to GaN was near completion for all samples.

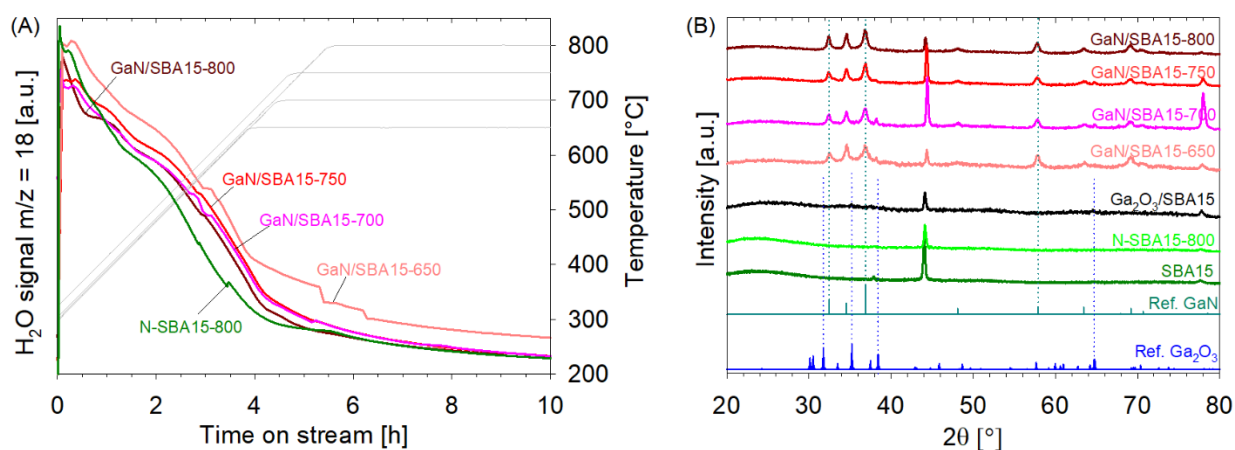


Fig. 5–4 Results for nitridation of supported catalysts. (A) H_2O signal and (B) XRD pattern as a function of nitridation temperature.

The prepared support SBA–15 had a total BET surface area of $912 \text{ m}^2 \text{ g}^{-1}$ ($\sim 20\%$ micro and $\sim 80\%$ mesopores), which decreased to $420 \text{ m}^2 \text{ g}^{-1}$ ($\sim 15\%$ micropores) when nitridated at 800°C (N–SBA15–800). This might be due to partial pore collapse at higher temperatures, as shown by the reduced pore volume (i.e., from 0.89 to $0.61 \text{ cm}^3 \text{ g}^{-1}$). Adding Ga to the support (including impregnation and calcination at 550°C) also reduced the total surface area to $426 \text{ m}^2 \text{ g}^{-1}$ and pore volume to $0.53 \text{ cm}^3 \text{ g}^{-1}$ but did not change the average pore size (Table 5–2). Moreover, the data show that the share of the micropore surface area decreased from 20% to 13% .

Compared to the unsupported catalyst (GaN), the supported catalysts (GaN/SBA15) had a unimodal pore size distribution at around 6.4 nm (Table 5–2, Fig. 5–5).

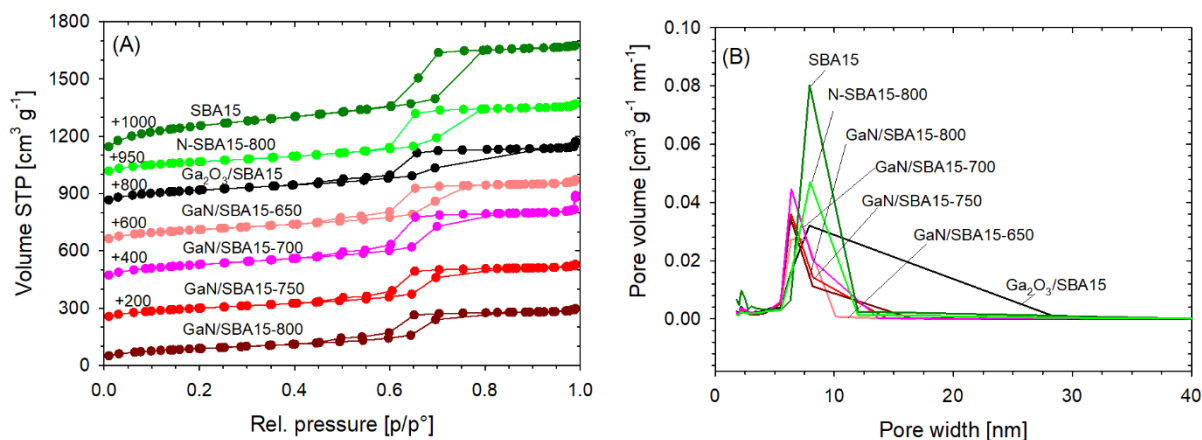


Fig. 5–5 (A) N_2 adsorption-desorption isotherms and (B) Pore size distribution for supported Ga_2O_3 and nitrated samples (on SBA–15) at different nitridation temperatures. Samples were under ammonia for 24 h.

Table 5–2 N_2 adsorption, and desorption results for supported Ga_2O_3 , GaN catalysts on SBA–15.

Sample	$T_{Nitridation}$ [°C]	S_{BET}^a [$m^2 g^{-1}$]	S_{Micro}^a [$m^2 g^{-1}$]	$S_{Meso+Macro}^a$ [$m^2 g^{-1}$]	V_{Pore}^b [$cm^3 g^{-1}$]	D_{Pore}^c [nm]
SBA15	–	912	195	717	0.89	7.9
N–SBA15	800	420	61	359	0.61	8.0
$Ga_2O_3/SBA15$	–	426	55	371	0.53	7.9
GaN/SBA15–650	650	405	41	364	0.54	6.4
GaN/SBA15–700	700	436	44	392	0.49	6.4
GaN/SBA15–750	750	361	29	331	0.48	6.4
GaN/SBA15–800	800	320	27	293	0.44	6.3

^a S_{BET} = BET total specific surface area obtained from adsorption data in the p/p^0 range from 0.05–0.2; all reported data are within $\pm 20 m^2 g^{-1}$ based on the repeated analysis. S_{Micro} = micropore; $S_{Meso+Macro}$ = meso + macropore surface areas.

^b V_{Pore} = pore volume was obtained at $p/p^0 = 0.9$

^c D_{Pore} = Unimodal pore size distribution for all samples, calculated using the Barrett-Joyner-Halenda (BJH) method;

The surface areas of $Ga_2O_3/SBA15$ was still 20 times larger than for the unsupported catalyst samples with a value of $19 m^2 g^{-1}$ (refer to Ga_2O_3 in Table 5–1). Thus, it was easier for NH_3 to access Ga_2O_3 resulting in most likely in a higher conversion during the nitridation, especially at lower temperatures.

Upon nitridation up to 700 °C, the surface area did not change much, but the average pore size decreased from 7.9 to 6.4 nm when compared to the Ga₂O₃/SBA15 sample. An increase in the nitridation temperature above 750 °C (i.e., GaN/SBA15–750 and 800) resulted in the reduction of the total surface area down to 320 m² g⁻¹. The share of micropores decreased even further to 8%. At higher nitridation temperatures, the surface area reduction was most likely due to a combination of sintering of GaN particles and pore structure collapsed [70].

Based on ICP analyses, Ga-loadings of 13 ± 1 wt% in Ga₂O₃/SBA15 (target 16 wt% Ga) and 11 ± 1 wt% in GaN/SBA15 were determined. The loss of around 3 wt% from the target loading could be attributed to the loss of gallium nitrate solution during catalyst synthesis.

No prior reference for GaN loading on SBA–15 was available. The loadings of 3–20 wt% have been reported [74,75] for molybdenum-based catalysts for non-oxidative methane activation. Furthermore, a few MoN/Al₂O₃ catalysts have been used for various reactions with a Mo loading of 7–20 wt% [76,77]. Thus, loading of 16 wt% Ga was a good starting point, which was approximately 1/5th of the Ga content in the unsupported GaN catalysts (83 wt% Ga and 17 wt% N).

HRTEM was carried out for Ga₂O₃/SBA15, GaN/SBA15–650, and GaN/SBA15–800 catalysts (Fig. 5–6). For the fresh Ga₂O₃/SBA15, no gallium nanoparticles were observed, while the ordered hexagonal pore structure of the SBA–15 was visible with a size of around 8 nm (same as determined by BET measurement, refer to Table 5–2). In EDS, however, the presence of Ga was confirmed (Fig. 5–6D). This suggests that the Ga₂O₃ nanoparticles were highly amorphous as supported by XRD results for the Ga₂O₃/SBA15 (Fig. 5–4B). GaN, on the other hand, was distinguishable from the SBA–15 in the TEM, as depicted in Fig. 5–6B and C for GaN/SBA15–650 and 800, respectively. Moreover, Fig. 5–6B and C show clearly that the GaN nanoparticles (3–5 nm, Fig. 5–6B, and C) were inside the 6–8 nm pores of the SBA–15 support. XRD measurement confirmed that GaN had a crystalline structure (refer to Fig. 5–4B).

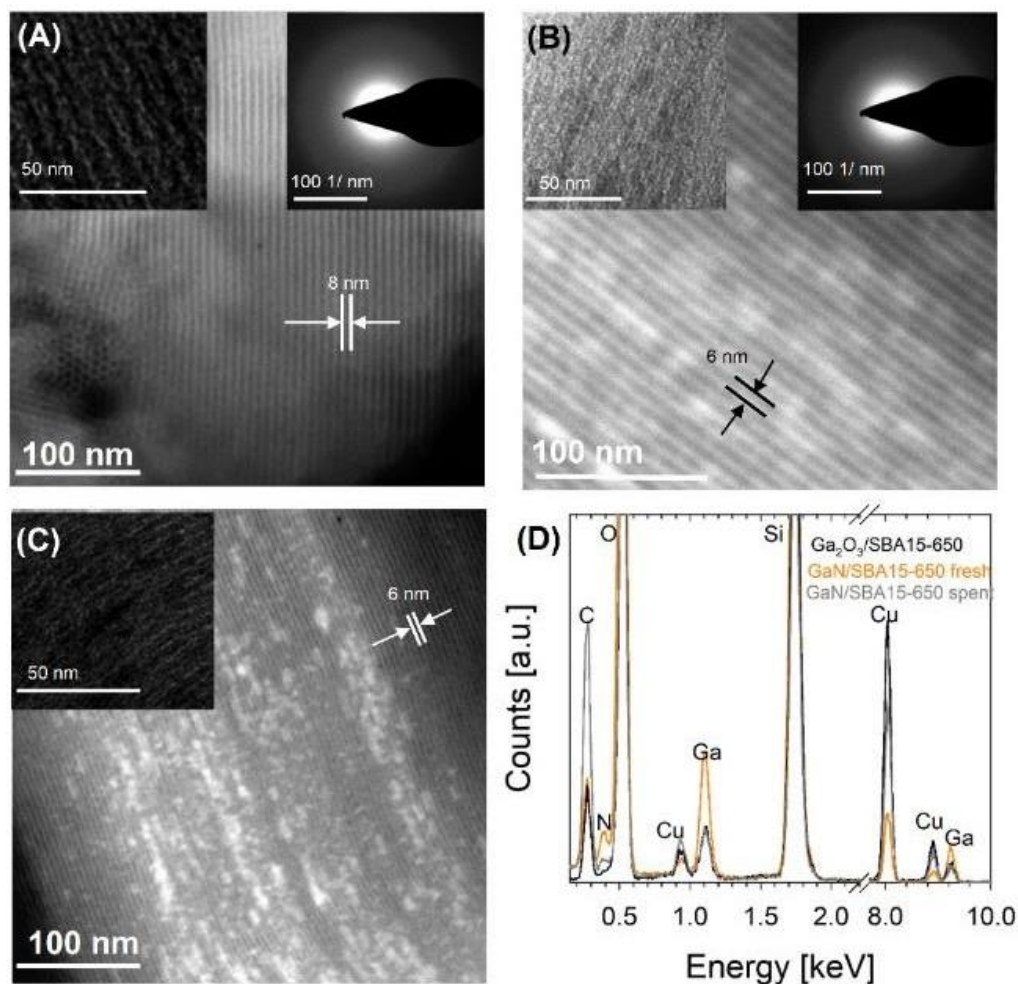


Fig. 5-6 STEM image of (A) fresh Ga₂O₃/SBA15, (B) fresh GaN/SBA15-650 catalyst. Top left inset HRTEM image and top right inset electron diffraction pattern. (C) fresh GaN/SBA15-800. Top left inset HRTEM image and top right inset electron diffraction pattern. (D) Si normalized EDS for Ga₂O₃/SBA15, fresh, and used GaN/SBA15-650. Note: Cu and some of the C signals in EDS are from the grid.

5.2.3 Temperature-programmed desorption

Temperature-programmed desorption (TPD) showed that more than 750 °C is required to decompose the catalysts (Fig. 5-7). The decomposition was tracked based on N₂ ($m/z = 28$) evolution. Unsupported GaN-750 is nearly as stable as GaN/SBA15-700 up to 750 °C. The support also undergoes nitridation, which was also seen in our DRIFTS study. The terminal silanol (Si-OH) group gets nitridated to Si-NH₂ (refer to Chapter 6, section 6.3.3). This SBA-15 nitridation was also reported in [78]. Some CO₂ ($m/z = 44$) and moisture (H₂O, $m/z = 18$) were chemisorbed on the catalyst, probably during air exposure during loading. The supported catalysts might also have trapped NH₃ ($m/z = 17$) during their synthesis, which was not significant for the unsupported one.

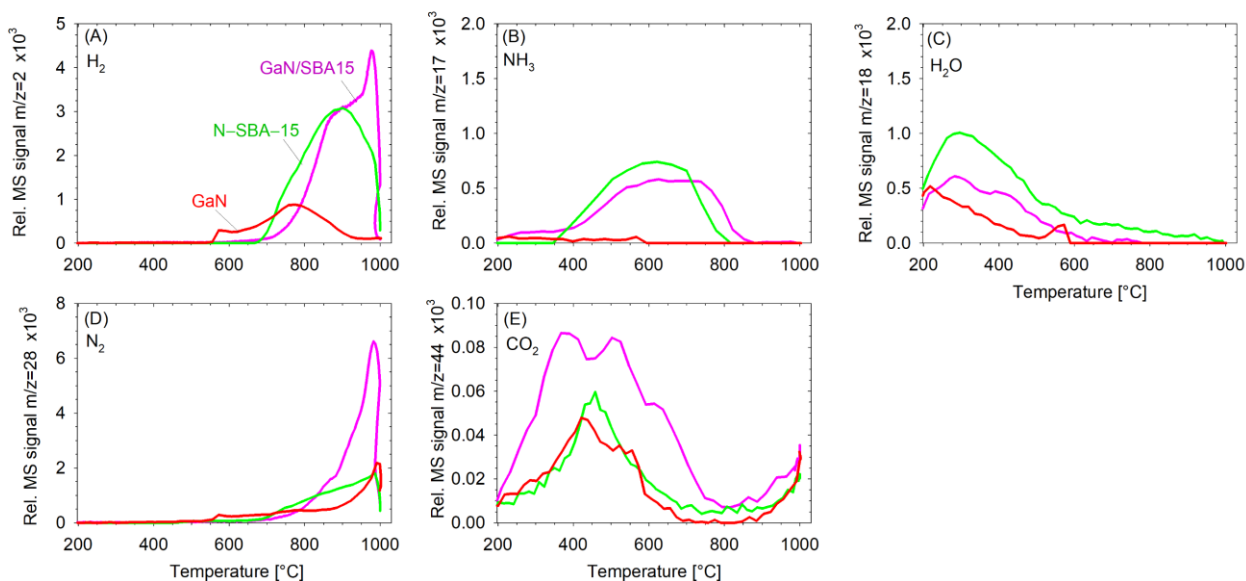


Fig. 5-7 Temperature programmed desorption (TPD) results for the support and the catalysts (supported and unsupported), showing the evolution of (A) H_2 , (B) NH_3 , (C) H_2O , (D) N_2 , and (E) CO_2 as a function of temperature.

5.3 Activity measurements

5.3.1 Unsupported catalysts

Mass spectrum analyses revealed that the Ga_2O_3 sample produced amount of H_2O ($m/z = 18$) and CO_2 ($m/z = 44$) in the first hour during the methane activation (Fig. 5-8A to D), while the nitrated catalysts did not exhibit any formation of H_2O and CO_2 (Fig. 5-8E to H). The GaN-600 sample showed an insignificant amount of H_2O and CO_2 , (refer to Fig. A3-1), even though this sample contained $\sim 65\%$ of Ga_2O_3 . This may indicate that during the nitridation, mostly the outer surface of the low porosity Ga_2O_3 was converted to GaN, while the bulk remained Ga_2O_3 (core-shell structure).

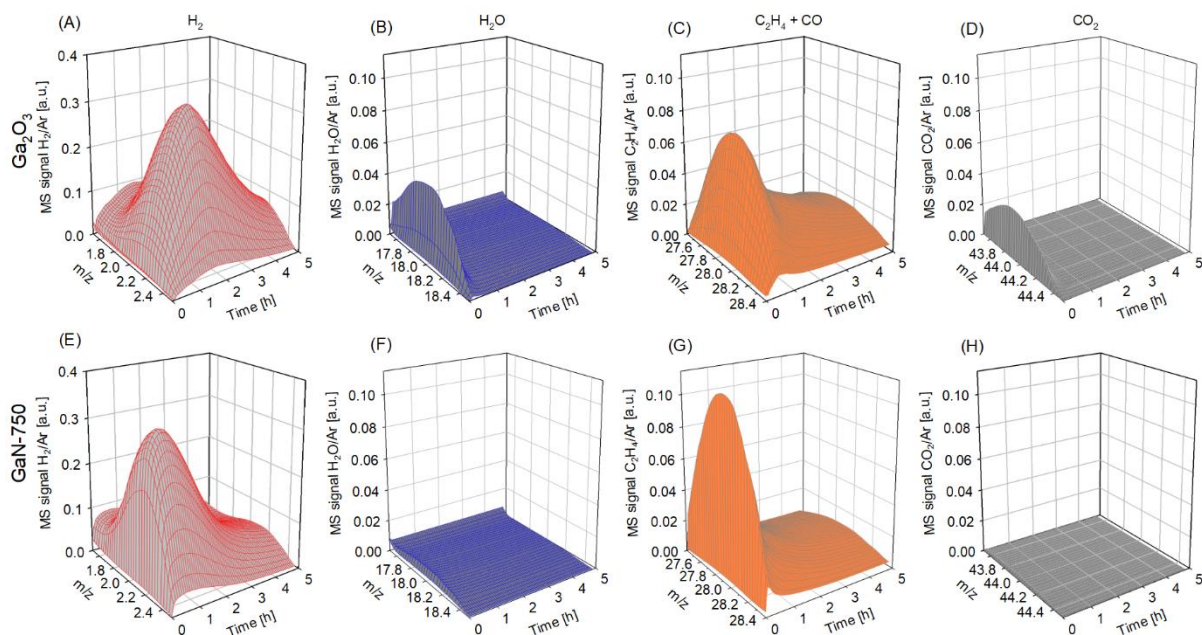


Fig. 5–8 Normalized mass spectra as function of time for Ga_2O_3 (A to D) and GaN–750 (E to H) for mass to charge ratios of $m/z = 2$ (H_2 , red), $m/z = 18$ (H_2O , blue), $m/z = 28$ ($\text{C}_2\text{H}_4 + \text{CO}$, orange) and $m/z = 44$ (CO_2 , grey).

This also explains the different behavior of the H_2 formation ($m/z = 2$) for the Ga_2O_3 (max. H_2 at 2 h) and GaN (max. H_2 at < 1 h) samples. During the induction period, CH_4 produced H_2O , CO , and CO_2 on Ga_2O_3 , creating an oxygen vacancy in the crystal lattice, also predicted by our DFT work (see chapter 6 and reference [46]). SEM-EDS analysis of fresh and used Ga_2O_3 catalysts (Fig. A3–2 and A3–3) showed only a marginal loss of oxygen within the error of estimation. Also, the XRD for fresh and spent Ga_2O_3 were practically indistinguishable, indicating no change in the crystal structure (Fig. A3–4).

Since CO and C_2H_4 have the same nominal mass ($m/z = 28$), it was impossible to distinguish between them via mass spectrometry. The GaN catalysts did not show the presence of gallium-methoxy species in ^{13}C SS-NMR (Chapter 6), which appears around 56 ppm [32]. This again verifies that GaN does not produce CO and CO_2 . CO and CO_2 might have been formed via gallium-methoxy species ($\text{Ga}\cdot\text{O}-\text{CH}_3$) that were experimentally observed via ^{13}C SS-NMR over Ga-modified zeolites [32]. However, the number of methoxy groups are assumed to be much smaller than the gallium-methyl species. The reaction pathway towards CO and CO_2 has been reported by Chaudhari et al. [46]. It has been shown that gallium oxide is active towards the reverse water-gas shift reaction during the alkane dehydrogenation in the presence of CO_2 [79]. Assuming the reverse water-gas shift reaction, at

equilibrium, the maximum CO formation and hence the minimum C₂H₄ formation rates could be determined. Since negligible amounts of H₂O and CO₂ were observed for the nitrdated samples, the mass-to-charge ratio $m/z = 28$ was associated with C₂H₄ only (Fig. 5–8E to F).

All unsupported catalyst samples exhibited similar behavior in terms of CH₄ conversion as well as product formation rate except ethylene. The ethylene rates were higher for the nitrdated catalysts when compared with the oxide precursor (Ga₂O₃), but the rates were similar within the nitrdated samples from 600–800 °C. At the onset of the reaction, CH₄ conversion values of 4% were determined, which rapidly decreased to less than 1% after 3 h on stream. The steady-state rate attained was up to $1.67 \mu\text{mol}_{\text{CH}_4} \text{min}^{-1} \text{g}_{\text{Ga}}^{-1}$.

C₂H₄ had the highest hydrocarbon-based formation rate at the beginning of the reaction with up to $5 \mu\text{mol min}^{-1} \text{g}_{\text{Ga}}^{-1}$ that was 3 to 4 orders of magnitude larger than for the other hydrocarbons. Benzene formation rates were about 100 times smaller, while the rates for propylene, toluene, and naphthalene (Fig. A3–5) were more than 1000 times lower. The maximum hydrocarbon and H₂ formation rates for the nitrdated catalysts occurred within the first hour, while the non-nitrdated catalyst (Ga₂O₃) had longer induction time with an observed the maxima between 1 and 2 h (Fig. 5–9 and 5–10).

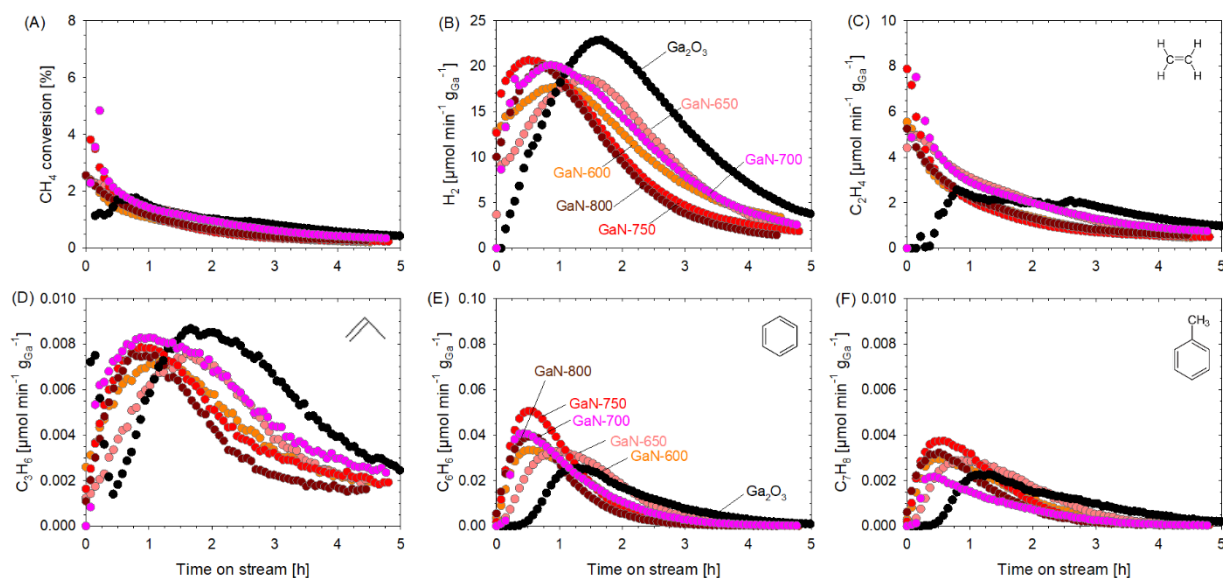


Fig. 5–9 (A) Methane conversion and product flow rates of (B) hydrogen, (C) ethylene (D) propylene (E) benzene and (F) toluene as a function of time on stream for the methane activation at 700 °C and 1 bar over unsupported Ga₂O₃ and GaN catalysts nitrdated at different temperatures.

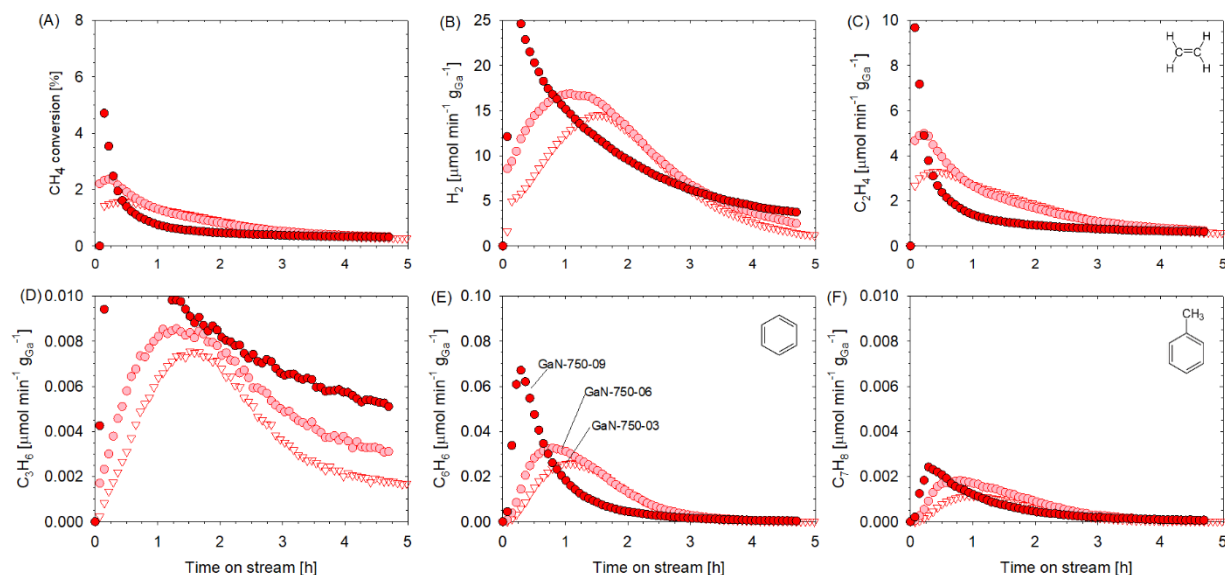


Fig. 5–10 (A) Methane conversion and product flow rates of (B) hydrogen (C) ethylene (D) propylene (E) benzene and (F) toluene as a function of time on stream for methane activation carried out using unsupported GaN catalysts nitridated at 750 °C at different ammonia exposure times (B). Methane activation conditions: 700 °C and 1 bar.

Independent of the nitridation temperature and time, all unsupported catalysts deactivated faster within 3–5 h due to coking (Fig. 5–9 and 5–10), which was evident from the color change from yellow (fresh GaN) or white (fresh Ga₂O₃) to black (spent, Fig. A3–6) as well as the temperature-programmed oxidation results (see below). The degree of nitridation influenced slightly more the formation rates of aromatic compounds (C₆H₆ and C₇H₈) than of olefins (C₂H₄ and C₃H₆). The Ga₂O₃ catalyst had the lowest C₆H₆ and C₇H₈ formation rates, followed by the catalyst nitridated 600 °C (GaN–600). GaN–700 and GaN–750 exhibited the highest C₆H₆ and C₇H₈ formation rates.

If C₂H₄ would be the only hydrocarbon product, the ratio of the observed H₂ to C₂H₄ formation rates should be 2, corresponding to the stoichiometric factor shown in equation 5–1.



For the unsupported catalysts, the ratio of hydrogen and ethylene formation rate changed with time, as illustrated in Fig. A3–7A and B. At the onset, the ratio was close to two, while it increased to a maximum of 7–12 depending on the catalyst after 1 to 2 h on stream. Afterward, the ratio attained a value of 3 at the end of the run. The ratio was higher than 2; thus, more H₂ was formed, indicating that a considerable amount of hydrocarbons were adsorbed on the catalyst surface as CH_x* or C_xH_y*

species with a yet unknown stoichiometry. Since the C_2H_4 formation rate was a factor of 100 to 1000 larger than the other gaseous hydrocarbons, they would not influence the observed H_2/C_2H_4 ratio significantly. No methane activation was observed when the reaction was carried out in an empty quartz reactor (blank run); therefore, homogeneous gas phase reactions were negligible at 700 °C.

Based on the TPO analysis (refer section 5.3.3) and product gas composition data, the overall selectivities for the adsorbed carbon as well as specific selectivities and total C_2H_4 yield were determined and summarized in Table 5–3. It is evident that the adsorbed carbon/coke, yet with an unknown C_xH_y stoichiometry, was the primary product, whereas the total hydrocarbon selectivity was between 30–50 mol%. The hydrocarbons itself were predominately C_2H_4 with selectivity values of up to 49 mol% for GaN–750–03 and 27 to 34 mol% for Ga_2O_3 . For the latter, a range was calculated indicating the minimum and maximum value for C_2H_4 selectivity depending on the influence of the reverse water-gas shift reaction and thus CO formation. C_6H_6 and C_3H_8 selectivities ranged from 0.5 to 0.9 mol% and 0.1 to 0.3 mol%, respectively.

Table 5–3 Overall and hydrocarbon (HC) selectivity, CH_4 conversion, and C_2H_4 yield for unsupported catalysts.

Catalyst	Overall selectivity [mol%]							C_{ads}^b	X_{CH_4}	Yield
	C_2H_4	C_3H_6	C_6H_6	C_7H_8	$C_{10}H_8$	CO_2	CO		[%] ^a	[%] ^a
Ga_2O_3	27–34	0.13	0.46	0.06	0.01	1.2	0–7	65.09	2.7–2.9	0.7–1.1
GaN–600	39.46	0.17	0.88	0.10	0.02	–	–	59.37	1.80	0.71
GaN–650	44.38	0.14	0.83	0.09	0.02	–	–	54.53	2.18	0.97
GaN–700	41.44	0.16	0.68	0.05	0.02	–	–	57.66	2.46	1.02
GaN–750	41.12	0.83	1.08	0.12	0.02	–	–	57.47	1.75	0.72
GaN–800	40.96	0.15	0.84	0.09	0.02	–	–	57.94	1.87	0.76
GaN–750–03	49.11	0.18	0.76	0.04	0.02	–	–	49.88	1.55	0.76
GaN–750–06	38.17	0.17	0.70	0.05	0.02	–	–	60.87	2.29	0.87
GaN–750–09	30.78	0.27	0.74	0.05	0.02	–	–	68.12	2.13	0.66

^a based on total products [mol] determined by integration of molar flow rates vs. time on stream (5 h)

^b adsorbed carbon based on TPO = temperature-programmed oxidation

To put these results in context, the equilibrium composition was calculated with the assumption of CH_4 as the only reactant and H_2 , C_2H_4 , and C_3H_6 as the only products. Aromatic compounds benzene, toluene, and naphthalene being less than 100 times than C_2H_4 had not been considered in the

calculations. Thermodynamically, the maximum CH₄ conversions and C₂H₄ yields (without coke) are 4.1% and 3.5% at 700 °C, 9.1%, and 8.1% at 800 °C and 17.0% and 15.5% at 900 °C, respectively (refer to Fig. 2–1A). Carbon deposition was excluded from the conversion calculations (Fig. 5–9, 10) as the molar rates of surface intermediates were not measured as a function of time. Methane conversion based on carbon incorporated in the products (excluding coke) can be compared with the equilibrium calculations (Fig. 2–1A). The equilibrium calculations did not include coke. The steady-state conversion (Fig. 5–9) was less than 10% of the equilibrium conversion (Fig. 2–1A).

5.3.2 Supported catalysts

Unlike unsupported Ga₂O₃ catalyst, the supported Ga₂O₃/SBA15 sample produced H₂O and CO₂ in the first hour on stream, while the nitrdated catalysts did not produce a significant amount of CO₂ and H₂O (Fig. 5–11 and Fig. A3–8). The main hydrocarbon product of the supported catalysts was again ethylene (C₂H₄), as depicted in Fig. 5–12. Supported GaN catalysts were very selective for the direct non-oxidative methane dehydrogenation and subsequent coupling to ethylene. Propylene and benzene were approximately 100 and 1000 times smaller, respectively. Unlike the unsupported catalyst, the initial CH₄ conversion was less than 1%, and then decreased to less than 0.5%, and remained steady (Fig. 5–12A). Similar CH₄ conversions (< 0.3%) were reported by Dumesic's group over PtSn/zeolite catalysts [16]. The supported GaN/SBA15 deactivates slower than the unsupported GaN, at the initial reaction stage.

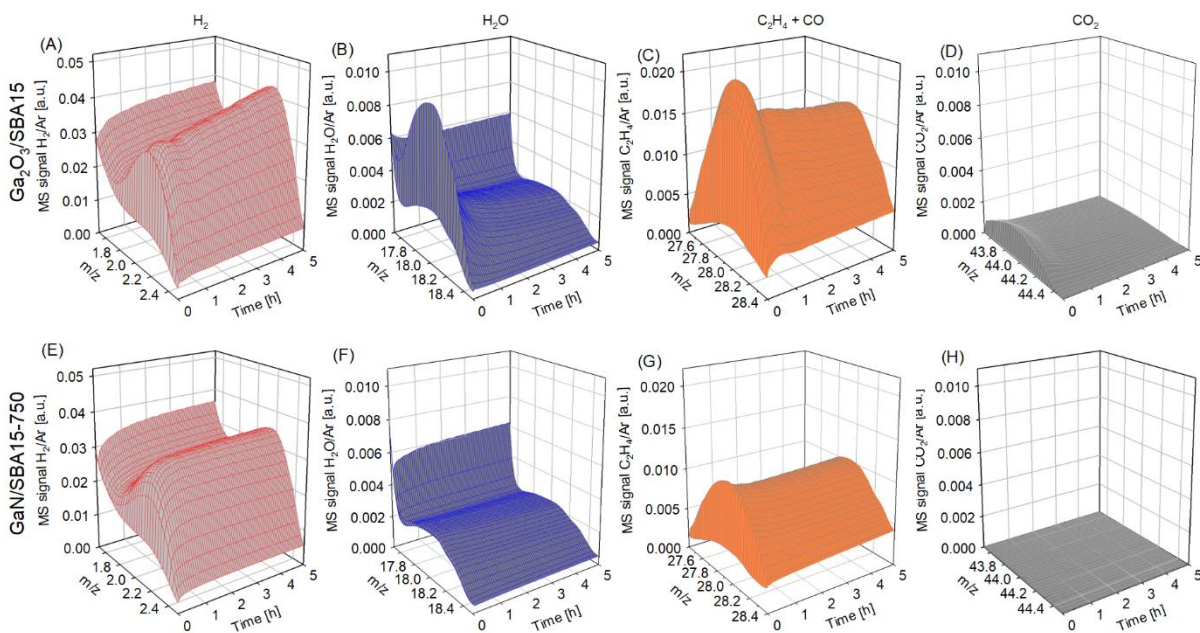


Fig. 5-11 Normalized mass spectra as function of time for Ga₂O₃/SBA15 (A to D), and GaN/SBA15-750 (E to H) for mass to charge ratios of $m/z = 2$ (H₂, red), $m/z = 18$ (H₂O, blue), $m/z = 28$ (C₂H₄ + CO, orange) and $m/z = 44$ (CO₂, grey).

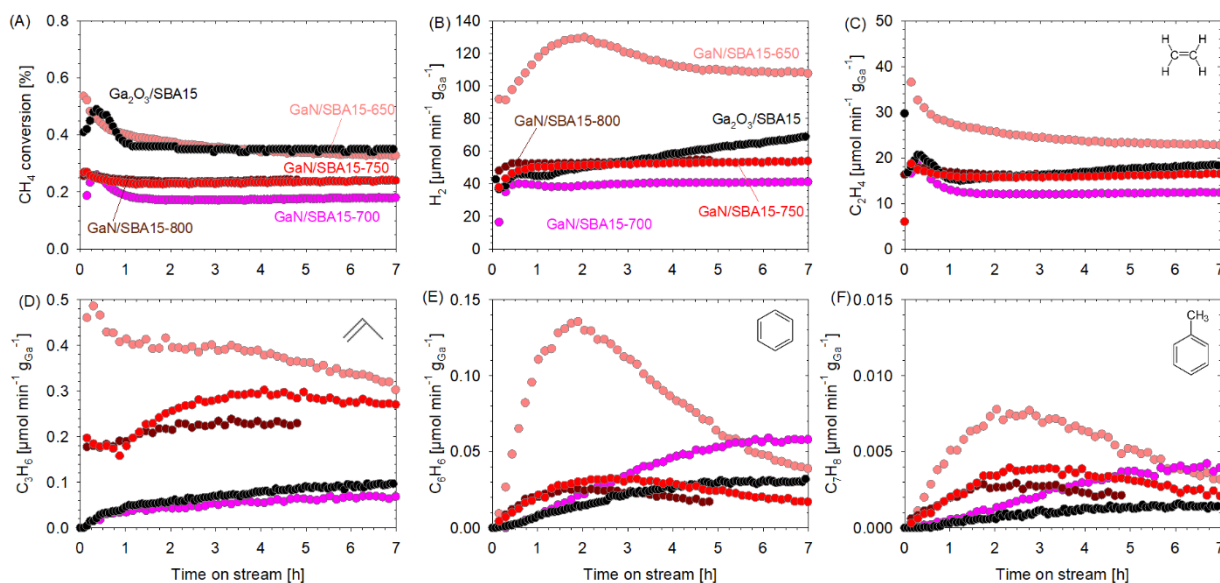


Fig. 5-12 (A) Methane conversion and product flow rates of (B) hydrogen, (C) ethylene, (D) propylene, (E) benzene, and (F) toluene formation rates as a function of time on stream over supported Ga₂O₃ and GaN catalyst at different nitridation temperatures. Methane activation conditions: 700 °C and 1 bar.

The steady-state rate attained was between 25–50 $\mu\text{mol}_{\text{CH}_4} \text{min}^{-1} \text{g}_{\text{Ga}}^{-1}$ (equivalent to 3–6 $\mu\text{mol}_{\text{CH}_4} \text{min}^{-1} \text{g}_{\text{cat}}^{-1}$), which was at least 10 times the unsupported catalysts. The rate is comparable to the rate reported by Sheng et al. [12] with 5 $\mu\text{mol}_{\text{CH}_4} \text{min}^{-1} \text{g}_{\text{cat}}^{-1}$.

The supported catalysts were more stable than the unsupported. Moreover, the C_2H_4 and C_3H_6 formation rates per gram of Ga were about 10 and 100 times higher for the supported catalyst (Fig. 5–9 vs. 5–12), respectively. The supported catalyst had more than 20 times higher porosity than the unsupported samples (refer to Tables 5–1 and 5–2). Moreover, GaN within the SBA–15 structure was very well dispersed with a crystallite size of 3–5 nm (from Fig. 5–6B and C), whereas the unsupported GaN, consists of an agglomeration of nanoparticles with 20–200 nm (Fig. A1–1). The latter had a much lower Ga dispersion and, therefore, a much lower rate per mass of gallium. It seems that methane coupling to ethylene over GaN is structure sensitive.

After approximately 1 h, the CH_4 conversions were in steady-state and corresponded to the hydrocarbon formation rates (specifically C_2H_4). This indicates that the active catalyst surface might have been covered with CH_4 during the initial phase, which has been confirmed by TGA experiments, as reported in our work [80]. This was also suggested by Xiao and Varma [17].

The $\text{Ga}_2\text{O}_3/\text{SBA15}$ and $\text{GaN}/\text{SBA15-650}$ exhibited higher CH_4 conversions compared to the samples nitrdated at 700 to 800 °C ($\text{GaN}/\text{SBA15-700}$ to $\text{GaN}/\text{SBA15-800}$, Fig. 5–12A). However, the H_2 formation rate differs significantly. For $\text{Ga}_2\text{O}_3/\text{SBA15}$, the H_2 production rate increased from 43 to 68 $\mu\text{mol min}^{-1} \text{g}_{\text{Ga}}^{-1}$ within 7 h of reaction time. At the same time, the H_2O formation decreased (Fig. A3–8). Since no water was produced over the nitrdated samples, the H_2 formation rates were constant with $\text{GaN}/\text{SBA15-650}$, achieving the fastest rate of $\sim 110 \mu\text{mol min}^{-1} \text{g}_{\text{Ga}}^{-1}$ and $\text{GaN}/\text{SBA15-700}$ the slowest rate of $\sim 40 \mu\text{mol min}^{-1} \text{g}_{\text{Ga}}^{-1}$. The C_2H_4 production rate exhibited a similar trend as observed for H_2 , highest steady-state rate of 22 $\mu\text{mol min}^{-1} \text{g}_{\text{Ga}}^{-1}$ for $\text{GaN}/\text{SBA15-650}$, and lowest of 12 $\mu\text{mol min}^{-1} \text{g}_{\text{Ga}}^{-1}$ for $\text{GaN}/\text{SBA15-700}$. Minor components such as C_3H_6 , C_6H_6 , and C_7H_8 were 100–1000 times lower than C_2H_4 , similar to their unsupported counterparts.

The ratio of the H_2 and C_2H_4 formation rates over the supported samples was close to three and did not change significantly with time on stream (Fig. A3–7). This value was much smaller than for the unsupported gallium catalysts indicating that over supported gallium catalysts less adsorbed carbon surface species (i.e., CH_x^*) were formed. Since the behavior for the unsupported and supported GaN

catalysts were different (i.e., supported catalyst was more stable compared with the unsupported), it is assumed that the adsorbed carbonaceous species was not catalytically active.

Based on the TPO results (refer section 5.3.3), the overall carbon-based selectivities (i.e., C₂H₄, C₃H₈, C₆H₆, C₇H₈, C₁₀H₈, and adsorbed carbon C_{ads}) were determined and summarized in Table 5–4 together with the overall CH₄ conversion and C₂H₄ yield.

Table 5–4 Overall and hydrocarbon selectivity for supported catalysts.

Catalyst	Overall selectivity [mol%]							X_{CH_4} [%] ^a	Yield [%] ^a	
	C ₂ H ₄	C ₃ H ₆	C ₆ H ₆	C ₇ H ₈	C ₁₀ H ₈	CO ₂	CO	C _{ads} ^b	CH ₄	C ₂ H ₄
Ga ₂ O ₃ /SBA15	43–58	0.30	0.01	0.18	0.01	1.7	0–15	39.71	0.6–0.7	0.25–0.45
GaN/SBA15–650	57.91	1.32	0.57	0.04	0.02	–	–	40.14	0.60	0.35
GaN/SBA15–700	70.18	0.42	0.60	0.05	0.01	–	–	28.74	0.26	0.18
GaN/SBA15–750	70.94	1.70	0.30	0.04	0.02	–	–	26.98	0.32	0.23
GaN/SBA15–800	67.79	1.71	0.33	0.04	0.01	–	–	30.09	0.26	0.18

^a based on total products [mol] determined by integration of molar flow rates vs. time on stream (7 h)

^b adsorbed carbon based on TPO = temperature-programmed oxidation

The nitrated support without any gallium (N–SBA15–800) did not exhibit any methane activation, which was also evident from the color of the spent catalyst, which was white same as the fresh catalyst (not shown). All supported catalysts achieved a higher C₂H₄ overall selectivity than the unsupported catalysts (43–70% vs. 30–49%). The GaN/SBA15–700 and 750 catalysts had the highest C₂H₄ selectivity with 70%, but the lowest yields due to the lower CH₄ conversion. However, the Ga₂O₃/SBA15 and GaN/SBA15–650 catalysts had a considerably higher adsorbed carbon (coke) content. Also, Ga₂O₃/SBA15 produced a significant amount of carbon oxides and water.

Less than 0.5 mol% of the total methane feed added was converted to adsorbed carbon (e.g., CH* or CH₂*) within 7 h time on stream. After 7 h on stream, the adsorbed carbon to gallium molar ratio was about $C_{ads}/Ga = 1 \pm 0.05$ for GaN/SBA15–650 and Ga₂O₃/SBA15. With increasing nitridation temperature, the ratio decreased to $C_{ads}/Ga = 0.25 \pm 0.05$ for the GaN/SBA15–700, –750, and –800 samples. For the nitrated samples, this might indicate that the adsorbed carbon species (CH* or CH₂*) are site-selective [81]. Based on this, a Ga dispersion of approximately 25% can be estimated for the supported catalyst that has GaN cluster sizes of 3–5 nm (from Fig. 5–6B and C).

Fig. A3–9 compares the results (for major product components H_2 and C_2H_4) for different runs with either multiple runs with the same catalyst batch or same catalyst synthesized as a separate batch using the same method (GaN–750 and GaN/SBA15–700).

To summarize, catalyst nitridation was needed for two reasons: (1) over gallium oxide H_2O , and CO_x were formed in addition to C_2H_4 , leading to lower C_2H_4 selectivity ($S_{C_2H_4}$, Fig. 5–13), and (2) nitridation reduced the carbon deposition (C_{ads} Fig. 5–13).

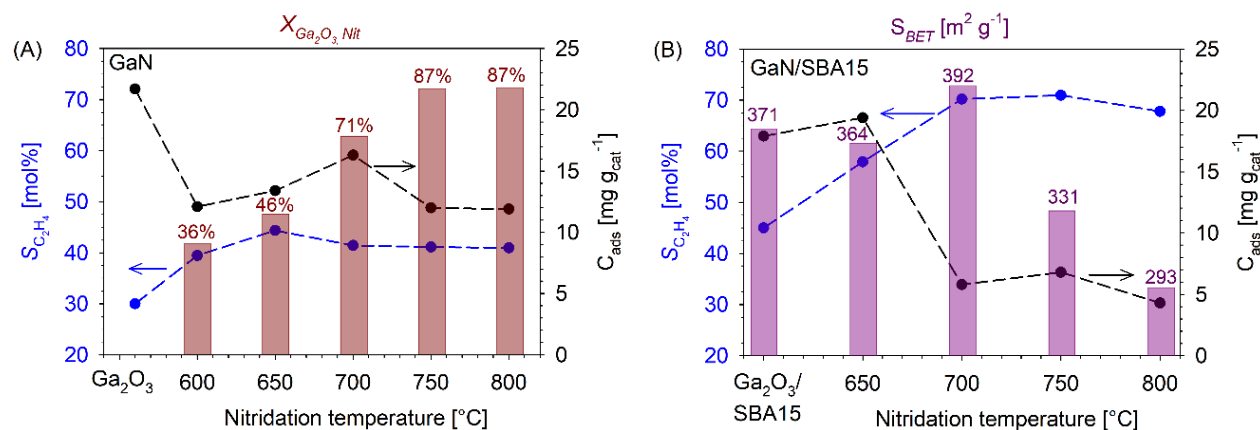


Fig. 5–13 Effect of nitridation on ethylene selectivity ($S_{C_2H_4}$) and adsorbed carbon (C_{ads}) on (A) unsupported GaN and (B) supported GaN/SBA15 catalysts. The dotted lines are for guidance only.

Hence, nitridation improved the atom conversion efficiency for CH_4 carbon, and the efficiency was higher for the supported catalyst. In the case of unsupported catalysts, the nitridation temperature affects the nitrogen content (i.e., Ga_2O_3 conversion) directly; however, the degree of nitridation did not influence the methane activity in terms of $S_{C_2H_4}$ and C_{ads} as a complete bulk nitridation was not needed (Fig. 5–13B). Surface nitridation was sufficient for improving $S_{C_2H_4}$ and reducing C_{ads} . Similar behavior was observed for the supported catalyst (except GaN/SBA15–650); in detail, with higher nitridation temperature (≥ 700 °C) the total surface area decreased, which did not influence the activity in terms of $S_{C_2H_4}$ and C_{ads} (Fig. 5–13A). There is an additional factor of support basicity in GaN/SBA15 catalysts. Huo et al. [82] have shown that nitridated N–SBA–16 support was more stable and had lower carbon deposition than non-nitridated SBA–16 for Ni/SBA–16 catalysts for methane dry reforming. Depending upon the nitridation temperature, the O atoms in SBA–16 and SBA–15 (silanol OH) are replaced by N (NH_2) [78,82]. The increased basicity in N–SBA–16 resulted in stronger metal-support interaction [82]. As reported by Chino et al. [78], in their work on SBA–15 nitridation, the nitrogen uptake by SBA–15 was negligible below 700 °C. The nitrogen content

increased from 2 wt% to 16 wt% from 700 °C to 1000 °C [78]. This explains why our GaN/SBA15-650 had the highest C_{ads} among all the supported nitride catalysts, as the SBA-15 support was not sufficiently nitrated. From Fig. 5-13, it can be concluded that the optimum nitridation temperatures were 700 °C and 750 °C for the supported and the unsupported catalysts, respectively.

5.3.3 Thermogravimetric analysis for carbon deposition

Activation experiments with unsupported GaN-750 conducted in the TGA confirmed that during the first hour, the empty catalytic sites (GaN) were covered by CH_3^* due to the dissociative adsorption of CH_4 , as depicted in Fig. 5-14. In the first hour, the rate of surface carbon formation reached a maximum and then decreased to a constant value for the remaining 15 h. The ratio of initial rate to the steady rate of carbon deposition is 24 (Fig. 5-14).

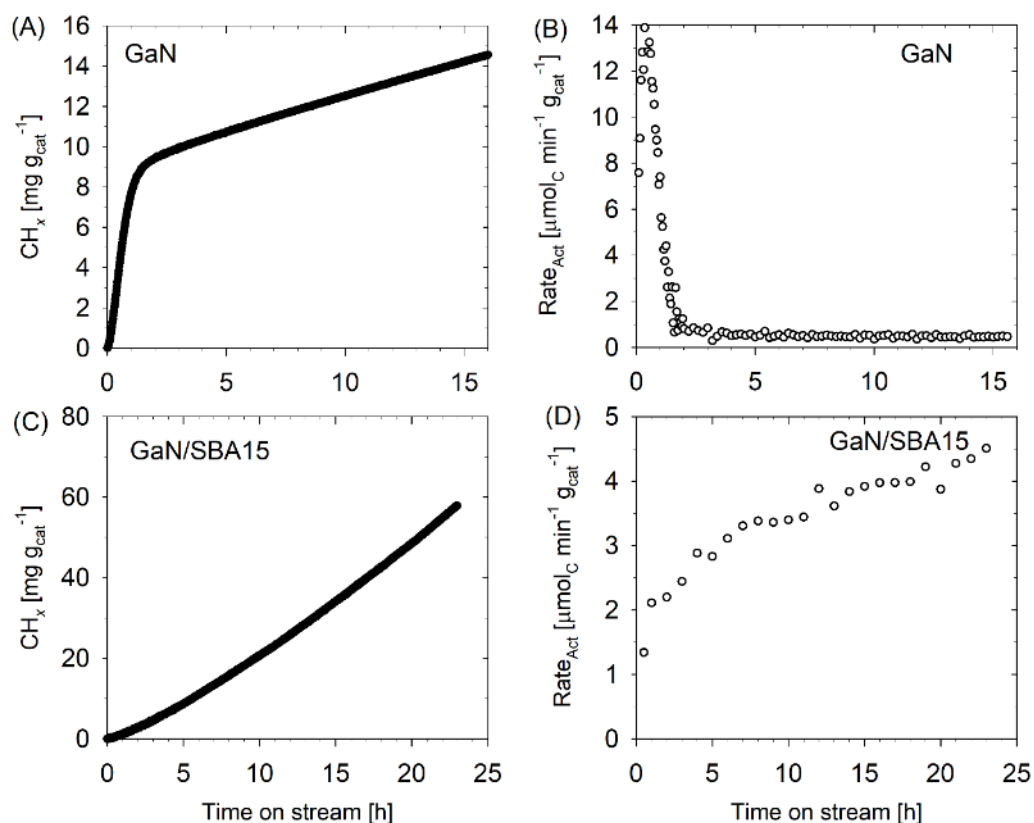


Fig. 5-14 Results for methane activation inside the TGA at 700 °C and 1 bar, surface intermediates (CH_x) formation, and rate of surface intermediates formation as a function of time over (A) and (B) 120 mg fresh unsupported catalyst GaN, and (C) and (D) 15 mg fresh supported catalyst GaN/SBA15.

The ratio of the initial rate of C_2H_4 formation to the steady-state rate (Fig. 5–9C and 5–10C) on GaN-750 is 16. The ethylene rates ratio (16) is close the half of the carbon formation rate ratio (24, maximum rate to steady-state rate in Fig. 5–14). A small difference of 4 is due to the difference in the modes of operation of the TGA (semi-batch) and the fixed bed reactor (continuous). Methane has to diffuse from the top of the bed to its bottom in TGA (slow), while it flows under pressure difference through the bed in the fixed bed reactor (fast).

A similar conclusion could be drawn for the supported GaN/SBA15-700 (Fig. 5–14B and C). Unlike GaN-750, there was no asymptotic increase, followed by an asymptotic decrease for carbon deposition rates for GaN/SBA15-700 (Fig. 7–11). The increase was with a nearly flat slope (first cycle in Fig. 7–11) over 24 h. In a fixed bed reactor also, the ratio of the initial rate of C_2H_4 formation to the steady-state rate (Fig. 5–12C) on GaN/SBA15-700 is only 1.3. Again, this comparison between TGA and FBR is qualitative because of the difference in the modes of their operation. The TGA acts as a batch reactor where CH_4 diffuses from the bulk gas at the top of the catalyst bed to the bottom (inside the crucible), and the products leave by diffusion from the bottom of the bed to the top bulk phase. In a flow reactor, this movement is facilitated by the flow of gas through the bed (top to bottom).

5.4 Characterization of spent catalyst

Morphologically the catalysts did not undergo any change after methane activation as depicted by the X-ray diffractogram of the spent catalyst (Fig. 5–15). The XRD patterns are indistinguishable with that of the fresh catalysts (Fig. 5–1 and 5–4).

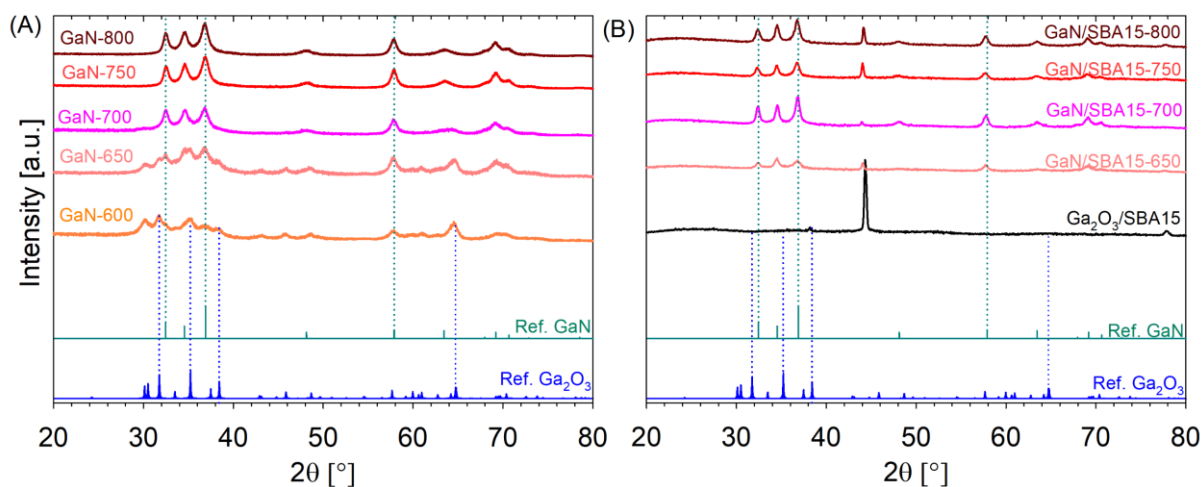


Fig. 5–15 XRD for the spent (A) unsupported catalysts and (B) supported catalysts post CH_4 activation.

Fig. 5-3C depicts the EDS for fresh Ga_2O_3 , and fresh and spent GaN-650 catalysts. As expected, the pure Ga_2O_3 sample had no peaks corresponding to nitrogen and much higher oxygen counts than both of the GaN-650 samples (fresh and spent) that contain GaN as well as Ga_2O_3 phases. The spent GaN catalyst had a higher carbon peak and, consequently, smaller peaks associated with nitrogen and oxygen, confirming the presence of carbonaceous material deposition. Some contributions to the carbon signal, and all the copper count were from the sample grid. The EDS data shown were normalized based on the gallium count and semi-quantitative.

Although the supported spent GaN/SBA15-800 did not show much change in morphology, several agglomerations of particles inside the hexagonal array of pores for the spent GaN/SBA15-650 were observed with the TEM (refer to Fig. A2-1). These agglomerations were most likely carbon deposition due to coking during the methane conversion. EDS analysis (Si normalized) confirmed that the spent GaN/SBA15-650 catalyst had a much higher carbon count than the fresh catalyst (Fig. 5-6D). Consequently, the peak corresponding to Ga was significantly smaller in the spent than in the fresh catalyst.

5.4.1 Temperature-programmed oxidation

For the unsupported catalysts, A single CO_2 peak at 467 ± 5 °C for the spent Ga_2O_3 was observed during temperature-programmed oxidation (TPO-MS), which shifted slightly to higher temperatures 480 ± 6 °C for the GaN catalysts as illustrated in Fig. 5-16. A H_2O peak ($m/z = 18$) was observed at the same temperature (Fig. A4-1A). Based on this temperature range, it can be assumed that the carbonaceous material was rather amorphous instead of graphitic carbon, which requires higher oxidation temperatures [57]. Also, the single CO_2 peak indicates a single carbon surface species that behaved similarly on the GaN and Ga_2O_3 samples under an oxidizing atmosphere. TPO-TGA measurements of the spent samples confirmed the results, as depicted in Fig. 5-18A and B. Interestingly, at temperatures above 550 °C, the weight of the used GaN samples increased due to the oxidation to Ga_2O_3 , which was also observed in our study [54]. The quantitative analysis of the spent catalyst after 5 h yielded a relative carbon amount of $22 \text{ mg g}_{\text{cat}}^{-1}$ for Ga_2O_3 and $10\text{--}16 \text{ mg g}_{\text{cat}}^{-1}$ for GaN catalysts (Table 5-5).

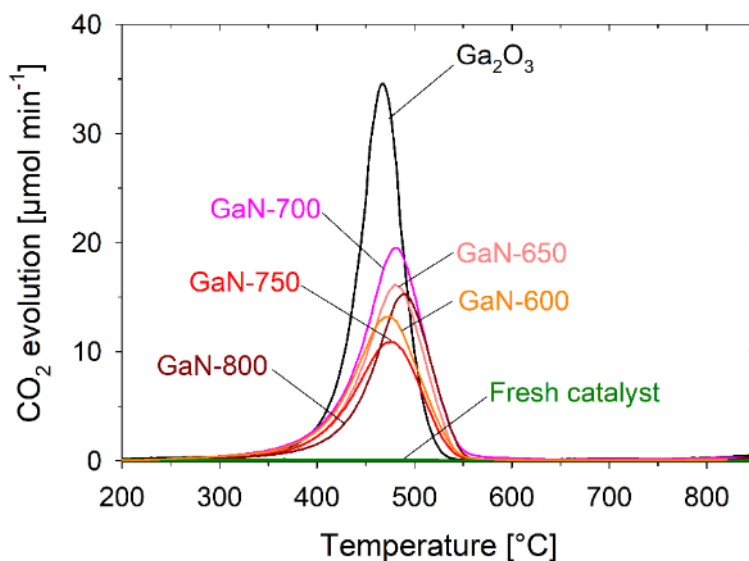


Fig. 5–16 TPO for spent unsupported GaN and Ga_2O_3 catalysts used for methane activation at 700 °C.

For the supported catalysts, the temperature-programmed oxidation - mass spectrometry (TPO-MS) analyses of the spent catalysts showed a major CO_2 peak at 600 ± 10 °C, as illustrated in Fig. 5–17. This was around 120 °C higher than for the unsupported catalysts (Fig. 5–16 vs. 5–17). The same behavior was observed in the thermogravimetric experiments (TPO-TGA, Fig. 5–18) as well as by determining the produced water via mass spectrometry (Fig. A4–1). For the latter, the H_2O signal corresponded perfectly to the CO_2 peaks. The reason for the higher temperature might be the confinement effect due to the small pore size of the supported catalysts (6 nm). A similar effect has been reported for Mo-containing zeolites [83]. A different adsorbed carbon surface species with a stronger carbon-catalyst bond than for the unsupported catalysts might be possible as well. The presence of polyaromatic compounds inside SBA–15 pores cannot be ruled out, as observed in [84]. However, in the present case, the rate of ethylene formation was by a factor of 1000 higher than the rate for benzene and toluene formation (Fig. 5–12). Thus, it is more likely that the carbon surface species were CH_x or C_xH_y instead of polyaromatic. The small CO_2 peak between 300 and 400 °C was observed in all samples, including the fresh catalysts. It most likely was a remnant of the copolymer.

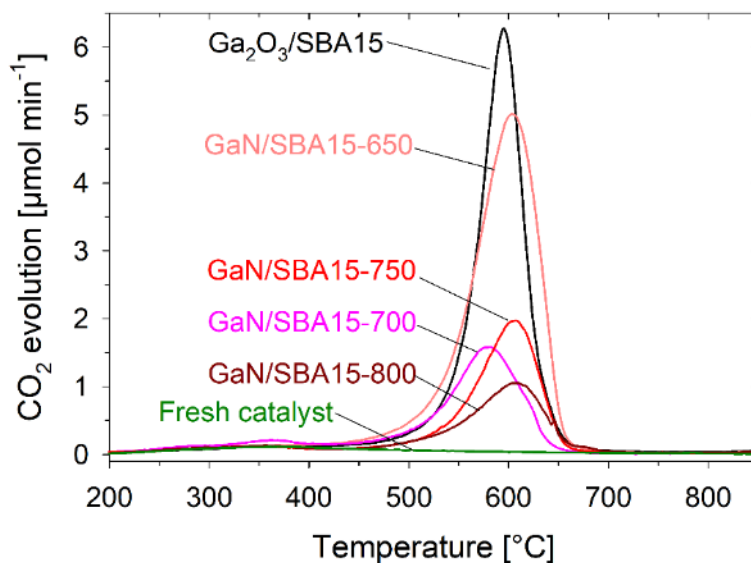


Fig. 5–17 TPO for spent supported GaN/Ga₂O₃ on SBA–15 catalyst used for methane activation at 700 °C.

For all spent catalysts, there was a noticeable decrease in weight, as illustrated in Fig. 5–18. The increase in weight above 550 °C was due to the buoyancy effect, which was verified with a blank run (not shown) and can also be observed with the fresh catalysts. However, this weight increase had a much steeper slope for spent GaN–750 (Fig. 5–18B). The weight increase was due to the formation of Ga₂O₃ from GaN oxidation above 550 °C. A theoretical increase of 12 wt% is expected when 1 g of GaN is oxidized to 1.12 g of Ga₂O₃. Since the GaN–750 catalyst contained approximately 88 wt% GaN and 12 wt% Ga₂O₃ (refer to Fig. 5–1B), the weight increase of 9 percentage points was in good agreement with the theoretical increase of about 10 wt%.

For the supported catalyst (GaN/SBA15–700), the weight increase above 550° C was slightly larger than for the Ga₂O₃/SBA15 sample, as the sample contained approx. 11 wt% gallium.

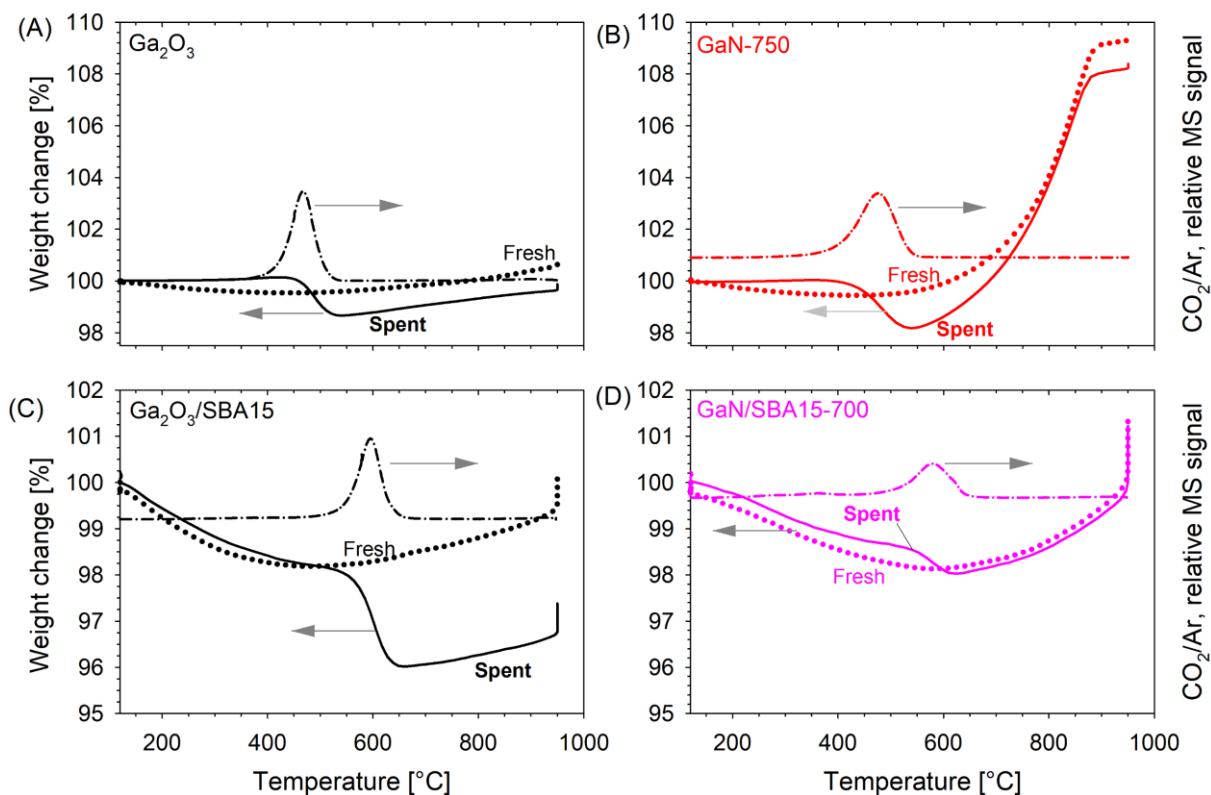


Fig. 5–18 TPO-TGA (% weight change on dry basis versus temperature), and TPO-MS results (relative CO_2/Ar MS signal versus temperature) for fresh and spent (A) unsupported Ga_2O_3 (B) GaN–750 (C) $\text{Ga}_2\text{O}_3/\text{SBA15}$ and (D) GaN/SBA15–700. Spent catalysts were obtained after methane activation for 5–7 h at 700 °C and 1 bar in a fixed bed reactor.

The weight changes determined with TPO-TGA agreed with TPO-MS analyses, as summarized in Table 5–6 and 5–7. For example, GaN/SBA15–700 had $5.8 \text{ mg}_C \text{ g}_{\text{cat}}^{-1}$ and $6.5 \text{ mg}_{\text{CH}} \text{ g}_{\text{cat}}^{-1}$ based on TPO-MS and TPO-TGA, respectively. $\text{Ga}_2\text{O}_3/\text{SBA15}$ had $17.9 \text{ mg}_C \text{ g}_{\text{cat}}^{-1}$ and $21.5 \text{ mg}_{\text{CH}} \text{ g}_{\text{cat}}^{-1}$ based on TPO-MS and TPO-TGA, respectively. The results for the TPO-MS analyses were slightly lower, as it was based on CO_2 (i.e., carbon) only, whereas TPO-TGA was based on the weight loss (i.e., carbon and hydrogen included). Gerceker et al. reported much higher carbon depositions of 43 to 120 $\text{mg}_C \text{ g}_{\text{cat}}^{-1}$ for the non-oxidative methane coupling to ethylene over PtSn/zeolite catalysts [16].

Table 5–5 Adsorbed carbon (C_{ads}) versus nitridation temperature for the unsupported catalysts. Spent catalysts were obtained after 5 h CH_4 activation at 700 °C and 1 bar.

Catalyst	C_{ads} [$\text{mg g}_{\text{cat}}^{-1}$]
Ga_2O_3	21.7
GaN–600	12.1
GaN–650	13.4
GaN–700	16.3
GaN–750	12.0
GaN–800	11.9
GaN–750–03	9.7
GaN–750–06	15.9
GaN–750–09	16.5

Table 5–6 Adsorbed carbon (C_{ads}) versus nitridation temperature for the supported catalysts. Spent catalysts were obtained after 7 h CH_4 activation at 700 °C and 1 bar.

Catalyst	C_{ads} [$\text{mg g}_{\text{cat}}^{-1}$]
$\text{Ga}_2\text{O}_3/\text{SBA15}$	17.9
GaN/SBA15–650	19.4
GaN/SBA15–700	5.8
GaN/SBA15–750	6.8
GaN/SBA15–800	4.3

Table 5–7 Adsorbed carbon (C_{ads}) from TGA for spent supported and unsupported catalysts. Spent catalysts were obtained after 5–7 h CH_4 activation at 700 °C and 1 bar.

Catalyst	C_{ads} [$\text{mg g}_{\text{cat}}^{-1}$]
Ga_2O_3	13.4
$\text{Ga}_2\text{O}_3/\text{SBA15}$	21.5
GaN/SBA15–700	6.5
GaN–750	11.2

5.5 Conclusions

For the first time, this work reported the synthesis and characterization of supported GaN/SBA15 catalysts for direct methane coupling to ethylene. Additionally, unsupported GaN catalysts were also synthesized, characterized, and tested for methane activation. The effect of synthesis parameters and catalyst type were investigated on ethylene selectivity and carbon deposition on the catalysts. The issue of carbon deposition was addressed by using less acidic support. The catalysts produced more ethylene than aromatics and less coke when compared to precious metal and metal oxide catalysts. The unsupported and SBA-15 supported gallium nitride catalysts were synthesized via a simple one-pot procedure and incipient impregnation, respectively, followed by calcination and subsequent nitridation. The influence of the nitridation condition on the catalyst structure and further on the direct non-oxidative methane activation was investigated. With higher nitridation temperature, the Ga_2O_3 conversion to GaN of the unsupported samples increased from 35 to 88%, while the surface area decreased significantly from 19 to $11 \text{ m}^2 \text{ g}^{-1}$. For the supported catalyst, the Ga_2O_3 conversion to GaN could not be determined; however, since the gallium particles inside SBA-15 pores were around 3–5 nm, high conversions can be assumed. The total surface area of the supported gallium samples was much larger, which decreased from 420 to $320 \text{ m}^2 \text{ g}^{-1}$ with increasing nitridation temperature.

The unsupported GaN catalysts deactivated rather fast within 3 h, whereas the supported GaN/SBA catalysts were stable and exhibited a steady H_2 and hydrocarbons formation rate for 7 h. The main hydrocarbon product was C_2H_4 , with selectivities of up 71 mol% for the supported and 50 mol% for the unsupported samples. The balance was predominantly adsorbed surface carbon and coke. The supported catalysts had 10 times higher C_2H_4 and H_2 formation rate per gram of Ga than the unsupported catalysts. Ga_2O_3 and $\text{Ga}_2\text{O}_3/\text{SBA15}$ samples had a smaller C_2H_4 selectivity as they produced a significant amount of H_2O and CO_2 through the reaction of the lattice oxygen with CH_4 . This was not observed for the nitridated catalysts, even for the GaN-650 sample that contained ~65 wt% Ga_2O_3 .

Higher surface area, well-dispersed GaN in the supported catalysts increased the accessibility of CH_4 to the active sites (GaN). The accessibility to GaN was much lower in practically non-porous unsupported catalysts (even with higher Ga content). In conclusion, based on $S_{\text{C}_2\text{H}_4}$ and C_{ads} , the catalyst of interest for methane activation and coupling to ethylene is the supported catalyst GaN/SBA15-700.

Chapter 6

6 Reaction mechanism and kinetics

The reaction mechanism for methane activation on GaN has not been studied so far. The only work reported was the DFT model published by Li et al. [24], as discussed in chapter 2. While this work concludes the energetically favorable position of methane adsorption on GaN, it did not delve deeper into the product formation. Two DFT studies were performed by Vishnu Chaudhari (Master's student) and Garance Gougeon (Master's student) to elucidate the mechanisms for methane activation to ethylene over GaN (and Ga₂O₃) and Ga₂O₃ nitridation, respectively. Additionally, experimental validation of the mechanism was done using isotope-labeled experiments (CD₄, ¹³CH₄, and CH₃D), solid-state nuclear magnetic resonance (SS-NMR) analysis, and in-situ Diffused Reflectance Infrared Fourier Transform Spectroscopy combined with mass spectrometry (DRIFTS-MS). The results of the first DFT work have been published: "Chaudhari, V., Dutta, K., Li, C-J., Kopyscinski, J., *Mechanistic insights of methane conversion to ethylene over gallium oxide and gallium nitride using density functional theory*, Mol. Catal. 482 (2020) 110606 [46]. Vishnu Chaudhari (Master's student) conducted the DFT modeling and wrote the manuscript, while Kanchan Dutta conducted the experiments and wrote the manuscript. Chao-Jun Li (collaborator Chemistry McGill) provided feedback, and Jan Kopyscinski provided feedback on the modeling and manuscript as well as was responsible for funding. Two more manuscripts are under preparation, one based on the nitridation DFT work (supported by experimental data), and the second one based on methane activation reaction mechanism and kinetics.

6.1 Introduction

Density functional theory (DFT) is a powerful tool for the computational study of chemical reactions. The DFT modeling can shed light on possible CH₄ conversion processes and investigate possible reaction mechanisms. In detail, these calculations allow us to determine adsorption and dissociation energies of reaction intermediates on catalyst surfaces, identify transition states and reaction pathways, and visualize the full reaction energy diagram. By doing different reaction mechanisms and catalysts, materials can be compared.

In the first DFT study, the reaction mechanisms of the direct non-oxidative methane (CH₄) coupling to ethylene (C₂H₄) over gallium-based catalysts, GaN ($\bar{1}\bar{1}00$), and Ga₂O₃ (001) was investigated. Li et al. [24] suggested that the first C–H bond activation occurs on the *m*-plane of the GaN catalyst via the alkyl mechanism. However, the detailed reaction mechanism from CH₄ to C₂H₄ and further to C₆H₆ on the GaN and Ga₂O₃ surfaces, including surface intermediates, are still unknown. Gallium–nitrogen and gallium–oxygen atom pairs are Lewis acid-base pairs that enable the dissociation of methane into an alkyl (CH₃) species and hydrogen (H) species following the alkyl pathway [24,31,32]. An alternative mechanism of methane activation known as the “carbenium” mechanism implies the hydride abstraction by gallium to form an alkyl (CH₃) species adsorbed on oxygen [32]. Computational modeling by Mayernick et al. indicated that methane activation on CeO₂(111), Pd_xCE_{1-x}O₂(111), and PdO(111) surfaces is limited by the first C–H bond activation [85]. Trinchero et al. [86] found the same with Pd(111), Pd(100), Pd(211), Pd(321), Pt(111), Pt(100), Pt(211) and Pt(321). Our DFT study is also based on the alkyl adsorption pathway suggested by our collaborator Dr. Li [24]. The adsorption energies of the reactants, the potential intermediates, and the products were calculated on both GaN and Ga₂O₃ surfaces. For each of the catalysts, different mechanistic pathways have been proposed and discussed. Reaction energies and activation energy barriers for the reactions were calculated and compared.

In the second study, DFT was used to investigate the mechanism of gallium oxide (β -Ga₂O₃ (100)) surface nitridation to gallium nitride (GaN). According to the nitridation reaction ($\text{Ga}_2\text{O}_3(\text{s}) + 2\text{NH}_3(\text{g}) \leftrightarrow 2\text{GaN}(\text{s}) + 3\text{H}_2\text{O}(\text{g})$), two gaseous ammonia (NH₃) molecules are inserted into the surface of β -Ga₂O₃ (100) to produce two GaN species with the abstraction of three water (H₂O) molecules. Ghazali et al. [87] synthesized GaN nanostructures through nitridation of Ga₂O₃ deposited on silicon (Si) in a horizontal quartz tube single zone furnace at 900 °C. They suggested that ammonia decomposes to N₂ and H₂, and then H₂ reduces Ga₂O₃ to the gaseous intermediate Ga₂O, and gallium

(I) oxide reacts with NH_3 to produce GaN , H_2 , and H_2O . Another mechanism was proposed by Jung et al. [68]. They identified gallium oxynitrides (GaO_xN_y) as amorphous solid intermediates when monitoring h-gallium oxide ($\text{h-Ga}_2\text{O}_3$) to gallium nitride (GaN) under a flow of NH_3 in the temperature range of 600–1000 °C by X-ray diffraction, infrared, and nuclear magnetic resonance spectroscopy. Since catalyst nitridation in the current work has been carried out below 800 °C, the formation of gaseous Ga_2O has been neglected, while the oxynitride pathway was assumed for the DFT study.

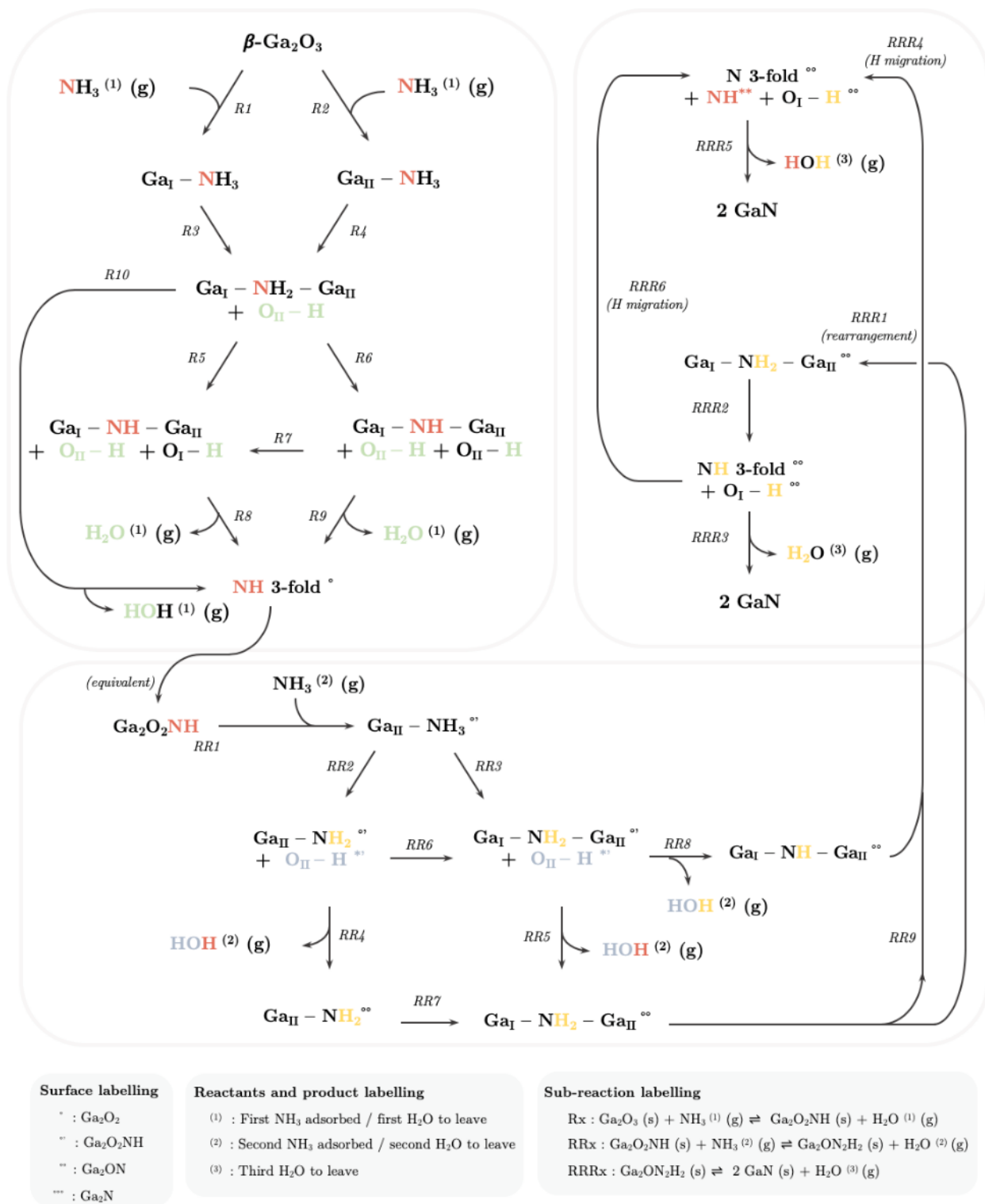
In addition to the first DFT study, experiments were carried out to validate the reaction mechanism. DRIFTS helped in identifying the intermediates which were predicted from the DFT study, and the DRIFTS also identified the onset temperature for the formation of these intermediates. The evidence for the main surface intermediate Ga-CH_3 was further established using NMR studies on the spent catalysts. These spent catalysts were activated using isotope $^{13}\text{CH}_4$, which were subjected to ^{13}C SS-NMR. The isotope study was not only conducted for SS-NMR study, but they were also used to understand how methane (as CH_4 , CD_4 , $^{13}\text{CH}_4$, and CH_3D) interacts with the catalyst, and how the strength of C–H (or C–D) bond changes the product profile.

A parametric study was conducted over GaN/SBA15 catalysts to determine reaction rate dependency on temperature, methane partial pressure, and contact (residence) time. The results from these studies were used to determine the apparent activation energy and order of the reaction. Based on the elementary steps from our DFT study, a forward rate expression was developed and correlated with the experimental findings.

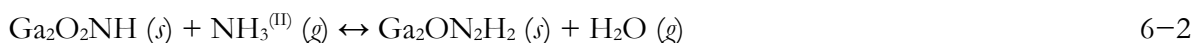
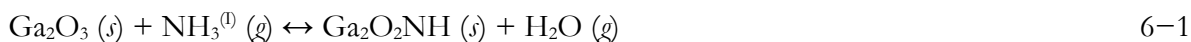
6.2 Density functional theory (DFT) modeling

6.2.1 Ga_2O_3 nitridation

This section was adapted from the Master's thesis of Garance Gougeon [88] and summarized the findings of the $\beta\text{-Ga}_2\text{O}_3$ nitridation DFT study. The crystallographic unit cell of $\beta\text{-Ga}_2\text{O}_3$ is composed of four Ga_2O_3 units and counts three oxygen (O^{2-}) types (O_I , O_II , and O_III) and two gallium (Ga^{3+}) types (Ga_I and Ga_II). Both O_I and O_II are 3-fold coordinated, while O_III is 4-fold coordinated [71]. Ga_I is tetrahedral, and Ga_II is octahedral. The reaction could be represented by the gradual addition of N (from NH_3) and removal of O (from Ga_2O_3) as H_2O , as illustrated in Fig. 6–1.

Fig. 6-1 Proposed pathways for β -Ga₂O₃ surface nitridation [88].

The insertion of the first NH_3 to the Ga_2O_3 (100) surface leads to the formation of the first H_2O and a nitrogenous structure (equation 6-1). This is followed by the insertion of the second NH_3 to the aforementioned nitrogenous structure with the release of the second H_2O (equation 6-2). Finally, the second nitrogenous structure loses H_2O (third) and form GaN (equation 6-3). The nitridation reaction is represented by a set of three equations 6-1 to 6-3.



NH_3^* bonds strongly to the octahedral Ga_{II} than the tetrahedral Ga_{I} (more negative adsorption energy on Ga_{II} , -1.73 vs. -0.73 eV (-167 vs. -70 kJ mol $^{-1}$), and shorter $\text{Ga}_{\text{II}}-\text{N}$ bond length, 2.08 vs. 2.12 Å). NH_3 was more likely to adsorb on exposed Ga top sites (see Fig. 6-2). It was assumed that NH_3^* dissociated stepwise to NH_2^* , NH^* , and H^* on perfect and imperfect Ga_2O_3 (100) surfaces. Imperfect Ga_2O_3 (100) surfaces are characterized by O vacancy arising from H_2O formation during nitridation (e.g., nitrogenous structures in equations 6-1, 6-2). As NH_3 loses H gradually, the adsorption energy becomes more negative, which implies stronger adsorption. Just like NH_3 , NH_2 also adsorbs on the Ga-top site.

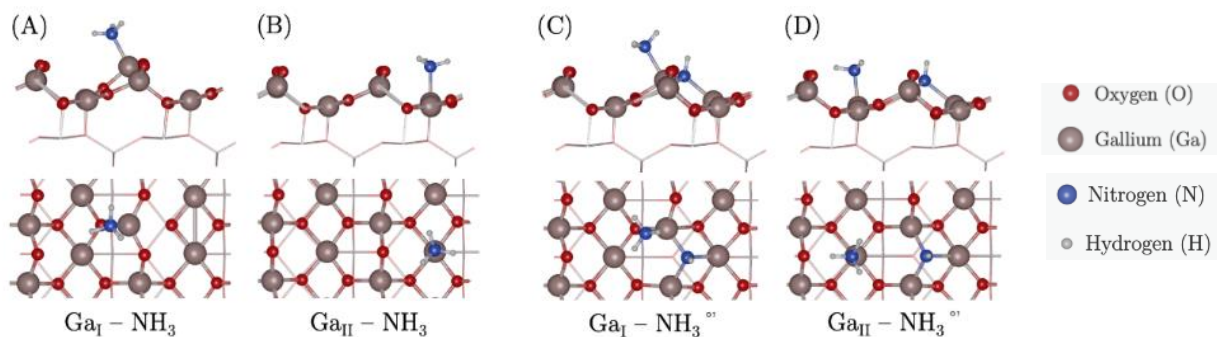


Fig. 6-2 Side (top) and top (bottom) views of NH_3 adsorbed on gallium [88].

From the cross-analysis of the most stable adsorbed structures, energy barriers and kinetics, and thermodynamics parameters of the elementary steps of $\beta\text{-Ga}_2\text{O}_3$ (100) surface nitridation, the most likely pathway is $\text{R1} \rightarrow \text{R3} \rightarrow \text{R6} \rightarrow \text{R9} \rightarrow \text{RR1} \rightarrow \text{RR3} \rightarrow \text{RR8} \rightarrow \text{RRR4} \rightarrow \text{RRR5}$ (Fig. 6-3). The two main rate-limiting steps were found to be the NH_2^* dissociation (R6) to NH^* and the desorption of the last H_2O^* (RRR5).

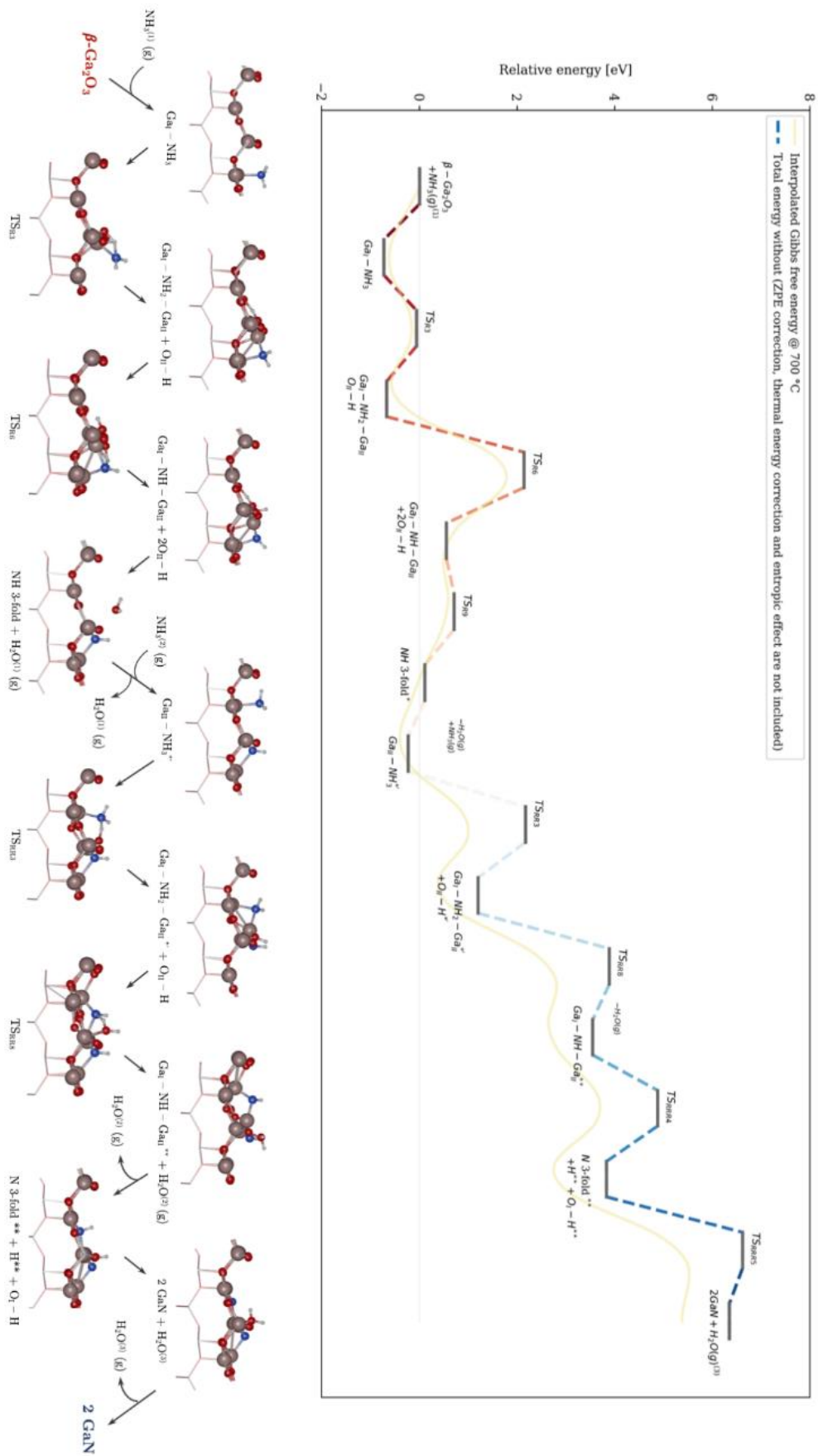


Fig. 6-3 Energy diagram, Gibbs free energy (ΔG) at 700 °C and side view of main structures of the optimal β -Ga₂O₃(100) surface nitridation reaction pathway [88].

The growth of the first GaN layer on the $\beta\text{-Ga}_2\text{O}_3(100)$ surface achieved through consecutive nitridation reactions was also studied. One nitridation corresponds to the insertion of two N atoms into the $\beta\text{-Ga}_2\text{O}_3(100)$ surface for three H_2O molecules formation. To replace the 24 O atoms of modeled $\beta\text{-Ga}_2\text{O}_3(100)$ surface by sixteen N atoms, a total of eight consecutive nitridations were required. For each nitridation, the following surface species were used in the model:

1. Ga_2O_3 : unit cell of $\beta\text{-Ga}_2\text{O}_3(100)$ surface being the reactant of the nitridation unit reaction.
2. Ga_2O_2 : intermediate with one O vacancy coming from the first H_2O leaving from perfect Ga_2O_3 .
3. $\text{Ga}_2\text{O}_2\text{N}$: intermediate with the first N atom, coming from gaseous NH_3 , inserted into the Ga_2O_2 surface. This species was obtained by adding an N atom into the Ga_2O_2 structure.
4. Ga_2N : intermediate with two O vacancies coming from the two additional H_2O molecules leaving the $\text{Ga}_2\text{O}_2\text{N}$ surface.
5. 2GaN : nitridation product arising from the second N insertion into Ga_2N .

By repeating this procedure eight times, the first GaN layer was constructed. Obtained Ga_2O_3 and 2GaN structures, which are nitridation reactants and products, for each of the eight nitridations are displayed in Fig. 6–4 (and also TEM in Fig. 5–3B, where coexisting GaN and Ga_2O_3 can be seen):

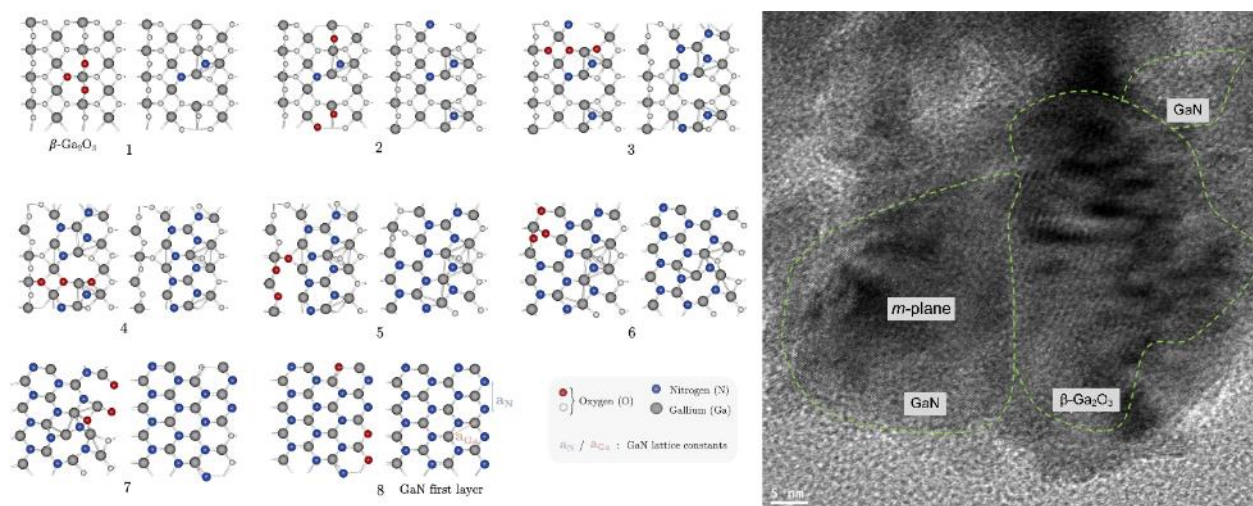


Fig. 6–4 Top view of optimized GaN structures with highlighted leaving O and inserted N atoms for each nitridation reaction along with the first GaN layer build-up, 1,2 ... 8 denoted the nitridation index or the number of consecutive nitridation reactions already occurred [88].

6.2.2 Methane activation

This section was adapted from the Master's project work of Vishnu Chaudhary (and the associated publication [46]) and summarized the findings of CH_4 activation on GaN and Ga_2O_3 DFT study. The

turnover frequency (TOF) could not be calculated as the active surface area (number of active sites per gram of catalyst) could not be determined via standard chemisorption (CH_4) and CH_4 -TPD techniques (chemisorption methodology, section 3.3.5). CH_4 did not chemically adsorb at low temperatures (25–45 °C). To shed more light on the methane adsorption as well as on the reaction pathway to ethylene over Ga_2O_3 and GaN, molecular modeling via density functional theory (DFT) was conducted using the Quantum ESPRESSO package [89]. Three different reaction pathways for each catalyst were proposed and evaluated.

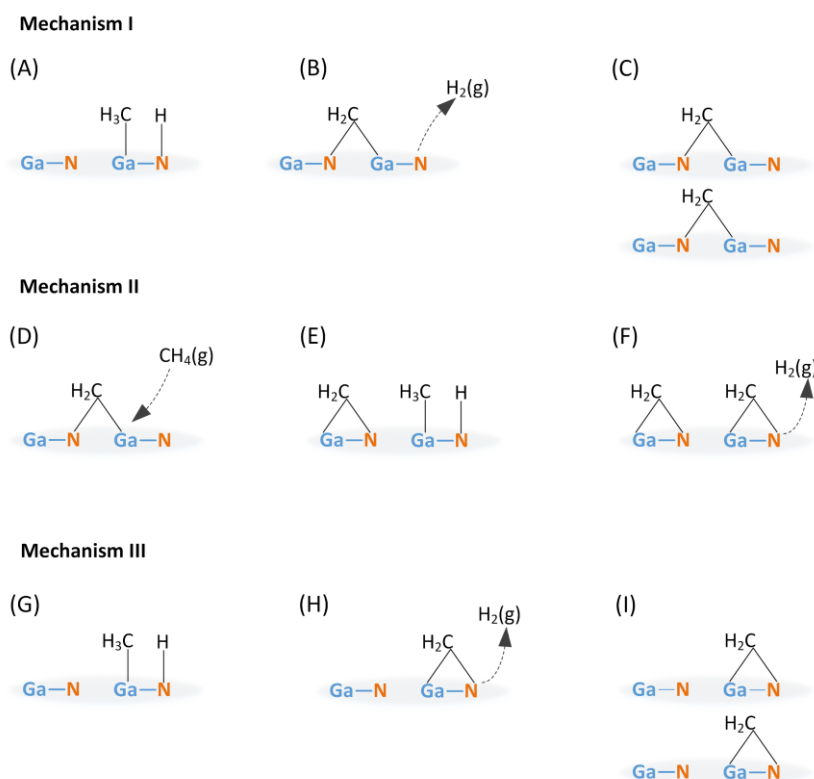


Fig. 6-5 The adsorbed surface intermediates hypothesized in the three mechanisms proposed by the DFT study for CH_4 activation over GaN. Adapted from [46].

The step common to all pathways is adsorption of CH_3^* on Ga and H^* on adjacent N (formation of $\text{H}_3\text{C}-\text{Ga}\cdot\text{N}-\text{H}$). In one mechanism (I), the H^* ($\text{H}-\text{N}$) forms $\text{H}_2(\text{g})$ (Fig. 6-5B) with a H from CH_3^* . The resulting CH_2^* forms a *hollow* bridge-like structure with N on the other side (Fig. 6-5A). In another mechanism (III), the CH_2^* bridge formation took place with the same N from which H^* was lost as $\text{H}_2(\text{g})$ (Fig. 6-5H). In both mechanisms, I and III, the two adjacent CH_2^* on two parallel Ga·N (Fig. 6-5C and I), results in the formation of C_2H_4 . The mechanism II considers chemisorption of another CH_4 on the same Ga, which is the part of CH_2^* bridge in mechanism I (Fig. 6-5B and D). The CH_2^*

spills over from the hollow to the solid GaN on the other side (Fig. 6-5E). Just like in mechanism I, the H* in N-H forms H₂(g) with H from CH₃*. The final two CH₂* bridges (Fig. 6-5F), form C₂H₄. The results indicate that the first step of CH₄ activation involves weak adsorption on the *m*-plane of the GaN with carbon weakly bonded to Ga with a Ga-C bond length of 2.08 Å following the alkyl mechanism (Fig. 6-6A)[24,46]. Upon structure optimization, a H atom is being attracted to N³⁻ anion, which results in stretching of the C-H bond from 1.08 Å to 1.23 Å (Fig. 6-6B). Due to this, the C-H bond is weakened and cleaved with the formation of N-H (bond length of 1.02 Å; adsorption energy = 4.57 eV, 441 kJ mol⁻¹) and Ga-CH₃ (bond length of 1.98 Å, adsorption energy = 1.55 eV, 150 kJ mol⁻¹) bonds (Fig. 6-6C). Therefore, an active site consists of both a Ga and an adjacent N.

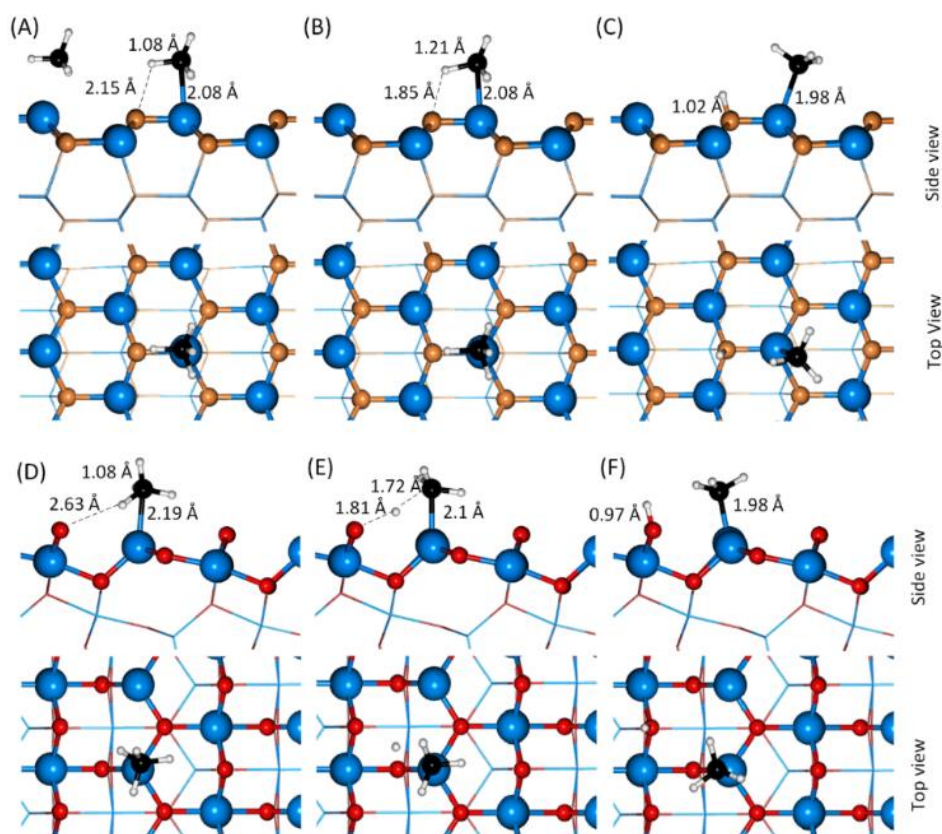


Fig. 6-6 Side view (top) and top view (bottom) of the dissociative adsorption following the alkyl mechanism of CH₄ on (A-C) *m*-plane GaN surface and (D-F) monoclinic Ga₂O₃. Blue (Ga), orange (N), red (O), white (H), and black (C).

A similar result was obtained for Ga₂O₃, as illustrated in Fig. 6-6D to F. Carbon from CH₄ is bonded to Ga (2.19 Å), while one H is attracted to O (alkyl mechanism), which stretched and weakened the C-H bond (1.08 to 1.72 Å). O-H (bond length of 0.97 Å, adsorption energy = 5.46 eV, 527 kJ mol⁻¹)

and Ga-CH₃ (bond length of 1.98 Å, adsorption energy = 2.43 eV, 234 kJ mol⁻¹) bonds are formed (Fig. 6-6C), which further reacts to form H₂ and hydrocarbons (C₂H₄, C₃H₆). CH₄ can also adsorb via the carbenium mechanism to form a methoxy group, Ga-O-CH₃, which has ~1.8 eV higher energy. Based on the DFT calculation, the alkyl mechanism is more likely than the carbenium mechanism, which is in agreement with our in-situ ¹³C solid-state NMR spectroscopy experiments (see chapter 6.3.3) and findings in the literature for a Ga/H-BEA catalyst [32]. Furthermore, our detailed DFT study confirmed that CO₂, CO, and H₂O are formed when CH₄ interacts with lattice oxygen from Ga₂O₃ [46].

The DFT calculations findings are summarized in Fig. 6-7 below. Only mechanism I has been discussed, which is the energetically favorable pathway. Other possible pathways (II and III), have been explained in [46]. As per mechanism I, an H atom present in the CH₃* species is attracted towards nitrogen atom on which an H* species is adsorbed. This induces the stretching of the C-H bond in CH₃* species and N-H bond of H* species adsorbed at the N-top site, as seen in the R2-I of Fig. 6-7A. The activation barrier is 4.68 eV (452 kJ mol⁻¹), and the reaction energy is 3.92 eV (378 kJ mol⁻¹). The final state of this elementary step is a CH₂* species adsorbed on the Ga-N hollow site forming a bridge and H₂ molecule in the gas phase. Similar to the formation of a CH₂* species on the Ga-N hollow site, another species of CH₂* was considered adsorbed on the adjacent Ga-N hollow site, as shown in Fig. 6-7A. The two CH₂* species turn towards each other to form C₂H₄ with an activation barrier of 4.51 eV (435 kJ mol⁻¹). This step is a highly exothermic reaction (-3.98 eV, -384 kJ mol⁻¹). The desorption energy of C₂H₄ from GaN is -0.03 eV (-3 kJ mol⁻¹).

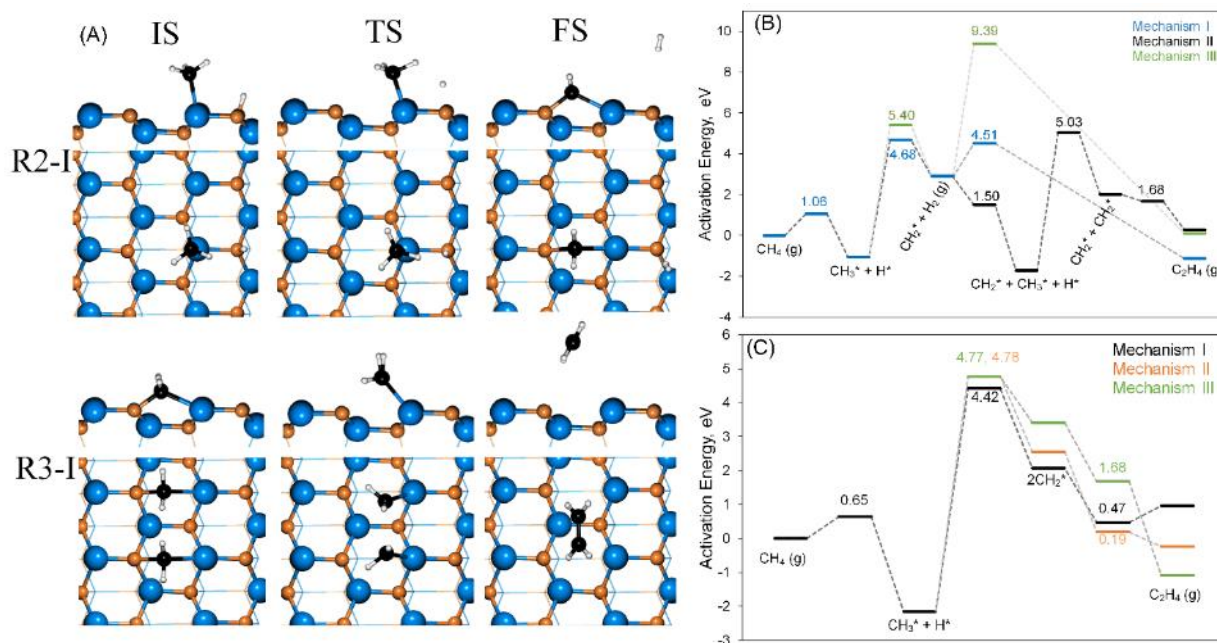


Fig. 6-7 (A) Side (top) and top view (bottom) of the initial state (IS), transition state (TS) and final state (FS) involved in mechanism II on GaN (1100) surface, (B) Calculated activation energy profile of mechanism I (blue line), II (black line), and III (green line) for the non-oxidative methane coupling to ethylene on GaN (1100) surface, and (C) Calculated activation energy profile of mechanism I (black), II (orange), and III (green) for the methane non-oxidative coupling to ethylene on G₂O₃ (001) surface. Ga, N, C, and H atoms are represented by blue, orange, black, and white balls.

The calculations showed that the cleavage of the C–H bond in the CH₃* species adsorbed on the Ga-top site (i.e., R2-I, Fig. 6-7A) is the rate-limiting step in mechanism I. Whereas in mechanism II [46], the reaction $\text{CH}_3^* + \text{CH}_2^* + \text{H}^* \rightarrow 2 \text{CH}_2^* + \text{H}_2$ resulting in co-adsorption of two CH₂* species on the Ga–N hollow and Ga–N bridge site is the rate-limiting step with an activation barrier of 5.03 eV (485 kJ mol⁻¹). The CH₂* species can also be formed on the Ga–N bridge site via mechanism III [46]; however, this required activation energy of 5.40 eV (521 kJ mol⁻¹), which is significantly higher than required on the Ga–N hollow sites (i.e., 4.68 eV, 452 kJ mol⁻¹) as suggested in mechanisms I and II. As for the formation of C₂H₄, activation barriers of 4.51, 1.68, and 9.39 eV (435, 162, and 906 kJ mol⁻¹) were determined for mechanisms I, II, and III, respectively. The analysis showed that the most likely pathway for CH₄ dehydrogenation to C₂H₄ follows the reaction pathway of mechanism I (Fig. 6-7B in blue). This finding is in agreement with the experimental results that suggest a fast

CH₄ dissociation and a rather slow CH₂* and subsequent C₂H₄ formation. Table 6–1 summarizes the activation and reaction energies for all elementary steps on the GaN (1 $\bar{1}$ 00) surface.

Table 6–1 Calculated activation barriers (E_a), and reaction energy (ΔE) for the elementary steps of the CH₄ to C₂H₄ conversion over GaN (1 $\bar{1}$ 00). Roman numerals **I**, **II**, and **III** represent mechanisms I, II, and III [46].

Elementary step	Activation barrier (E_a)	Reaction Energy (ΔE)
	eV (kJ mol ⁻¹)	eV (kJ mol ⁻¹)
I. CH ₄ (g) → CH ₄ *	–	–0.04 (–4)
I. CH ₄ * → CH ₃ * + H*	1.06 (102)	–1.02 (–96)
I. CH ₃ * + H* → CH ₂ * + H ₂ (g)	4.68 (452)	3.92 (378)
I. 2CH ₂ * → C ₂ H ₄ (g)	4.51 (435)	–3.98 (–384)
II. CH ₃ * + H* → CH ₂ * + H ₂ (g)	4.68 (452)	3.92 (378)
II. CH ₄ (g) + CH ₂ * → CH ₃ * + CH ₂ * + H*	1.50 (145)	–4.57 (–441)
II. CH ₃ * + CH ₂ * + H* → 2CH ₂ * + H ₂ (g)	5.03 (485)	3.73 (360)
II. 2CH ₂ * → C ₂ H ₄ (g)	1.68 (162)	–1.74 (–168)
III. CH ₃ * + H* → CH ₂ * + H ₂ (g)	5.40 (521)	3.97 (383)
III. 2CH ₂ * → C ₂ H ₄ (g)	9.39 (906)	–2.80 (–270)

Unlike GaN, Ga₂O₃ contains oxygen that can react with adsorbed hydrogen and carbon to form H₂O, CO, and CO₂ besides the desired C₂H₄, which has been shown in chapter 5. Fig. 6–7C illustrates the activation energy profile for methane to ethylene conversion on Ga₂O₃ for mechanisms I, II, and III [46]. The first step in this conversion involves the dissociative adsorption of methane, which requires an activation barrier of 0.65 eV (63 kJ mol⁻¹) where the CH₃* species is adsorbed on the Ga–top site, and H* species is adsorbed on O–top site of O(I) atom. The cleavage of the C–H bond from CH₃* species is found to be rate-limiting step with the highest activation energy 4.42, 4.77, and 4.78 eV (426, 460, and 461 kJ mol⁻¹) in mechanisms I, II, and III, respectively. The rate-limiting step is found to be highly endothermic as for all three mechanisms with 4.22, 4.70, and 5.56 eV (407, 453, and 536 kJ mol⁻¹). The last step in ethylene formation is the coupling of two CH₂* species, which has an activation barrier of 0.47 and 0.19 eV (45 and 18 kJ mol⁻¹) for the mechanisms I and II [46]. Whereas for mechanism III [46], a much higher activation barrier of 1.68 eV (162 kJ mol⁻¹) is required. In general, this step is found to be highly exothermic for all three mechanisms. H₂O and CO₂ are undesired products, which are formed on the Ga₂O₃ surface when CH₄ is oxidized. H₂O creates a single oxygen

atom vacancy on the Ga_2O_3 surface, whereas CO_2 creates two oxygen vacancies. The formation of H_2O , CO_2 , and CO (mechanism I) could be represented by equations 6-4 to 6-8. Their formation goes through CH_2^* formation from CH_3^* .



○ represents oxygen vacancy

DFT result is summarized in the schematic shown in Fig. 6-8. The CH_4 does not adsorb on GaN and Ga_2O_3 as a molecule but undergoes dissociative adsorption. This confirms that CH_4 -TPD and CH_4 chemisorption techniques failed to determine the number of active sites. The active CH_3 surface intermediate is further dehydrogenated to CH_2 with the release of H_2 and then dimerized to C_2H_4 , which are much slower than the CH_4 adsorption. The rate determining step is the dehydrogenation to CH_2 (R4, R5). The CH_2 surface intermediate can further dehydrogenate to CH and C (R7), which might lead to undesired coke. For the Ga_2O_3 catalysts, H_2O is formed via R3' leaving a vacant site (Fig. 6-8). The carbon oxides are produced from the interaction of adsorbed CH_2 (on Ga) with neighboring top layer O atoms [46]. It is not known yet whether the creation of O vacancy in β - Ga_2O_3 alters the mechanism.

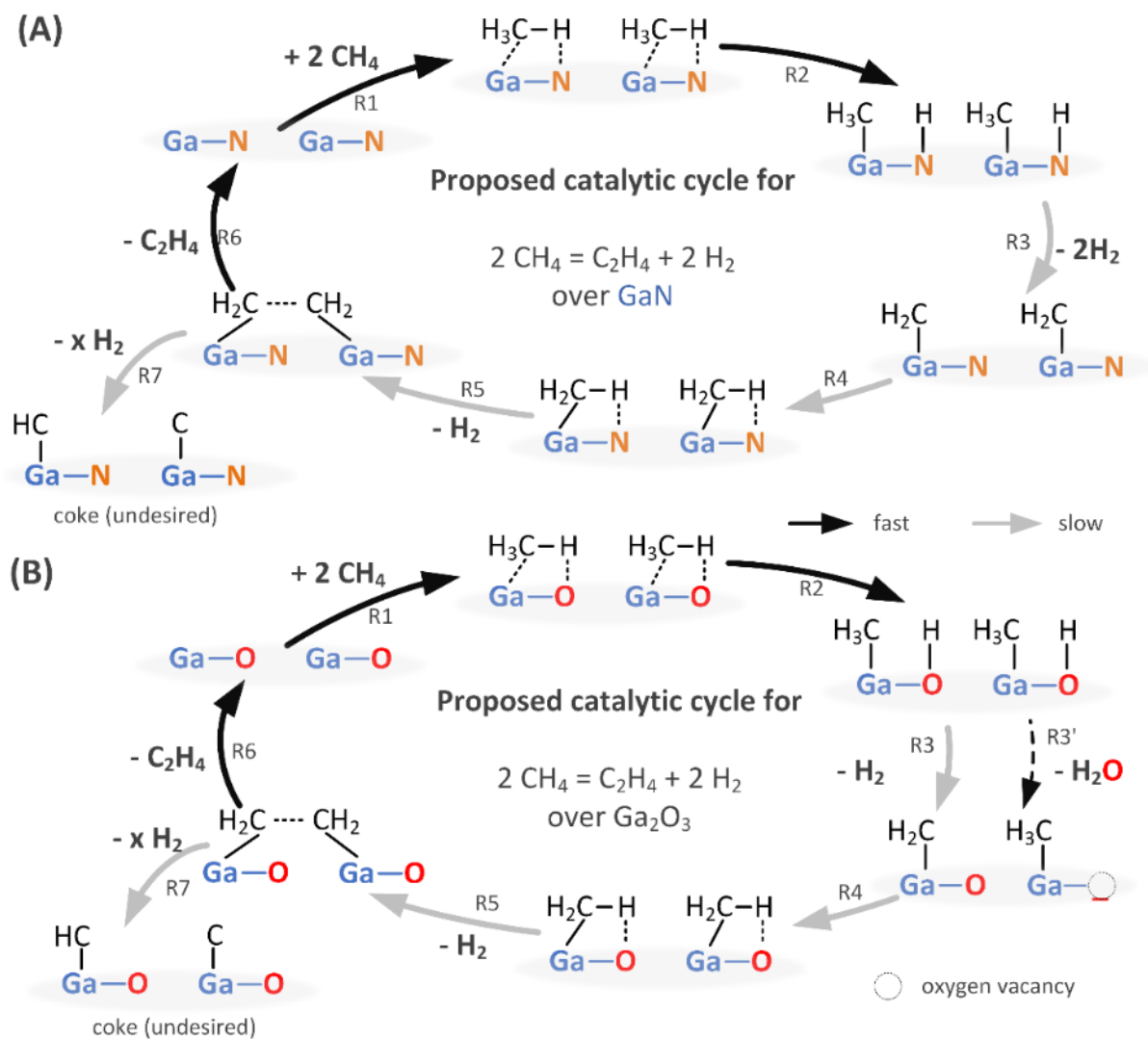


Fig. 6–8 Schematic of the non-oxidative methane dehydrogenation mechanism to ethylene over (A) GaN and (B) Ga_2O_3 .

6.3 Experimental results

6.3.1 Kinetic isotope effect

As described in chapter 5, lattice oxygen in Ga₂O₃ and partially nitrated GaN led to CO_x and H₂O formation during the non-oxidative methane activation. Since CO and C₂H₄ have the same nominal mass ($m/z = 28$), isotope labeling experiments with carbon labeled (¹³CH₄) and deuterated methane (CD₄) were conducted to distinguish between them. For ¹³CH₄, the formed carbon monoxide ¹³CO has a mass-to-charge ratio of $m/z = 29$, while ethylene ¹³C₂H₄ has $m/z = 30$. For CD₄, the formed carbon monoxide CO has a mass-to-charge ratio of $m/z = 28$, while ethylene C₂D₄ has $m/z = 32$.

Also, partially deuterated methane (CH₃D) was used to study the kinetic isotope effect (KIE) during the methane activation over both commercial GaN and supported GaN/SBA15. The commercial (GaN) powder was partially oxidized by exposure to air at room temperature for 4 weeks (2 GaN + 3 H₂O ↔ Ga₂O₃ + 2 NH₃). The supported catalyst, on the other hand, were synthesized by in-situ nitridation (at 700 °C using 15 ml_N min⁻¹ NH₃ and 1 ml_N min⁻¹ Ar for 11 h) of Ga₂O₃/SBA15 (110 mg containing 16 wt% Ga) before the methane activation experiments in the same reactor. By doing so, exposure to air was avoided, and no surface oxygen was present.

6.3.1.1 Partially oxidized commercial GaN

Fig. 6–9 illustrates and compares the results of the hydrogen group ($m/z = 2-3$, H₂, HD, and D₂) for partially oxidized commercial GaN powder exposed to different methane isotopes. The absence of mass spectra signal within the initial 5 min was due to the residence time (low flow rate). For both CH₄ and ¹³CH₄ experiments, the H₂ ($m/z = 2$) formation rates were similar, while for the partially and fully deuterated methane (CH₃D and CD₄) the hydrogen group consisted of H₂ ($m/z = 2$), HD ($m/z = 3$) and D₂ ($m/z = 4$) with different normalized intensities. The H₂ ($m/z = 2$) formation rate obtained for the CH₃D experiment was about half when compared to CH₄ and ¹³CH₄ experiments. The D₂ ($m/z = 4$) signal intensity ($[A]/[A]$) from the CD₄ runs did not correspond to the H₂ signal from CH₄. In detail, the H₂ formation rates from CH₄ were around 40% higher than the D₂ formation. This kinetic isotope effect (KIE) indicates that it is easier to break the C–H bond than to break the C–D bond, with a corresponding rate constant ratio of $k_{C-H}/k_{C-D} = 1.7$. A similar ratio of $k_{C-H}/k_{C-D} = 1.80$ was calculated based on the CH₃D experiments as illustrated in Fig.6–9B, which shows H₂ ($m/z = 2$) and HD ($m/z = 3$) formation rates. These values are in agreement with the literature that reports ratios between 1.60–1.89 for the chlorination of CH₄ and CD₄ at 700 °C (in a low-pressure, high-velocity discharge-flow system without any catalyst) [90]. The measured signal of $m/z = 3$ (HD) for the CD₄

experiments was most likely due to the H in <1% CH₄ and 30 ppmV C₂H₆ impurities in CD₄ (refer to Appendix A5–1).

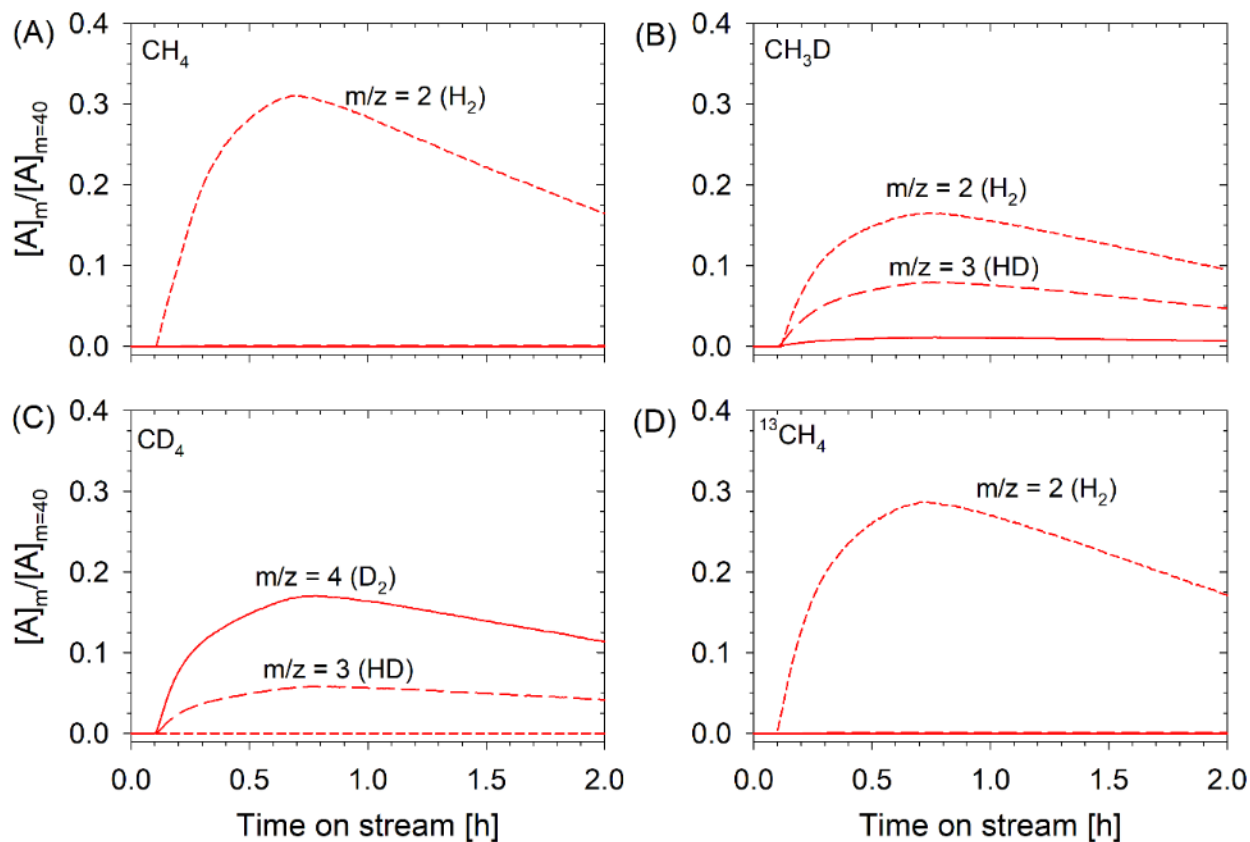


Fig. 6–9 Normalized MS signals for the products of methane activation from the hydrogen group (H₂, m/z = 2, HD, m/z = 3, and D₂, m/z = 4), over partially oxidized commercial GaN powder with CH₄ isotopes (A) CH₄, (B) CH₃D, (C) CD₄, and (D) ¹³CH₄ (experiments were done at 700 °C and 1 bar).

The kinetic isotope effect (KIE) was also demonstrated by the characteristic mass spectra from the feed gas, as illustrated in Fig. 6–10A, B, C, and D for CH₄, CH₃D, CD₄, and ¹³CH₄, respectively. These species are CH₃ and CH₄ with m/z = 15 and 16 in CH₄; species with m/z = 15 (CHD, CH₃), 16 (CH₂D), 17 (CH₃D, CHD₂) and 18 (CHD₃) in CH₃D; species CD₃ and CD₄ with m/z = 18 and 20, respectively in CD₄; and species ¹³CH₃ and ¹³CH₄ with m/z = 16 and 17, respectively in ¹³CH₄. The lines in the left grey shaded area represent the feed gas without any catalyst, while the plots in the right white space are in the presence of the catalyst.

All these ions involve breaking of C–H or C–D bonds. Fig. 6–10 (the grey area) depicts that the cleavage of the ¹³C–H and the C–D bonds become more difficult from CH₄ to ¹³CH₄ to CD₄,

(decreasing MS signals for $m/z = 15, 16,$ and 18 as illustrated in grey areas Fig. 6–10A, C, and D). This was also illustrated for two feed ions (CH_3 , $m/z = 15$ and CH_2D , $m/z = 16$) for CH_3D , where the mass 15 (CH_3) had the lowest MS signal (normalized) that involves C–D bond cleavage (the grey area in Fig. 6–10B).

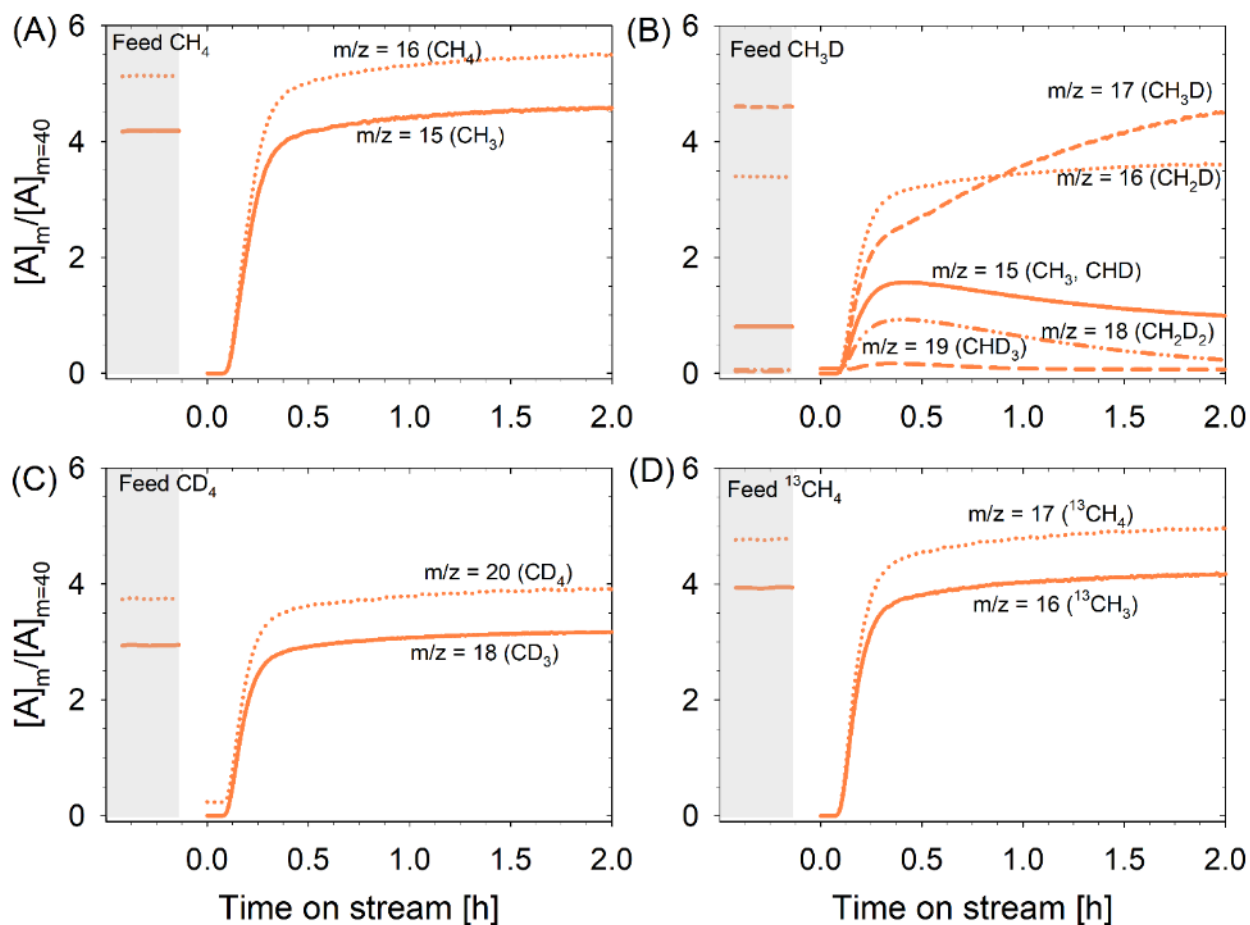


Fig. 6–10 Normalized MS signals for the characteristic feed ions of different CH_4 isotopes during activation over partially oxidized commercial GaN powder (A) CH_4 , (B) CH_3D , (C) CD_4 , and (D) $^{13}\text{CH}_4$. The shaded area on the left represents the plot without any catalysts.

For all isotopes except CH_3D , the MS ion-current intensities of the characteristic species during the reaction approached the intensities without any catalyst (grey shaded areas in Fig. 6–10). The behavior of the isotope CH_3D was unique and indicating the H and D exchange over the catalyst. This phenomenon of proton exchange was also reported by Sattler et al. [91]. The following elementary steps were hypothesized for CH_3D :

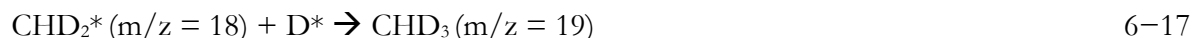
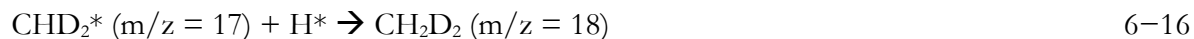
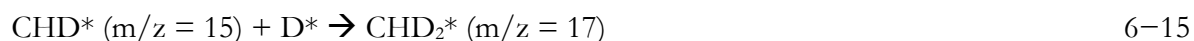
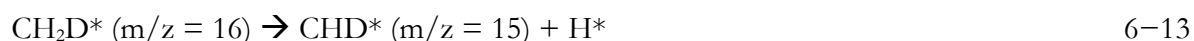
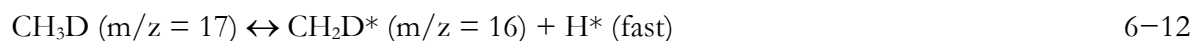
Normal ionization in the quadrupole mass spectrometer without catalyst (grey shaded area in Fig. 6-10).



The following reaction (equation 6-11) is less probable (in the absence of catalyst) because all m/z from 15 to 17 were constant.



Since $m/z = 16$ remained unchanged in the presence of a catalyst (Fig. 6-10), it was assumed that CH_2D (equation 6-12) attains faster equilibrium. The following elementary steps are being postulated in the presence of the catalyst:



Equations 6-12 and 13 illustrate the pathway which explains why ion-current intensity for the main fed species (CH_3D , $m/z = 17$) was increasing slowly. The more CH_2D^* was converted to CHD^* (equation 6-13), the more CH_2D^* was produced from CH_3D to maintain the equilibrium (equation 6-12). The C-D bond cleavage in CH_3D is shown by equation 6-14. The maxima for $m/z = 15$ and 18 were due to series reactions (equations 6-14 and 6-15, and equations 6-16 and 6-17). A small shoulder for $m/z = 17$ at 0.5 h (Fig. 6-10) could be attributed to the series reactions represented by equations 6-15 and 6-16. It was near 0.5 h (Fig. 6-10), where $m/z = 15$ and 18 reached maximums.

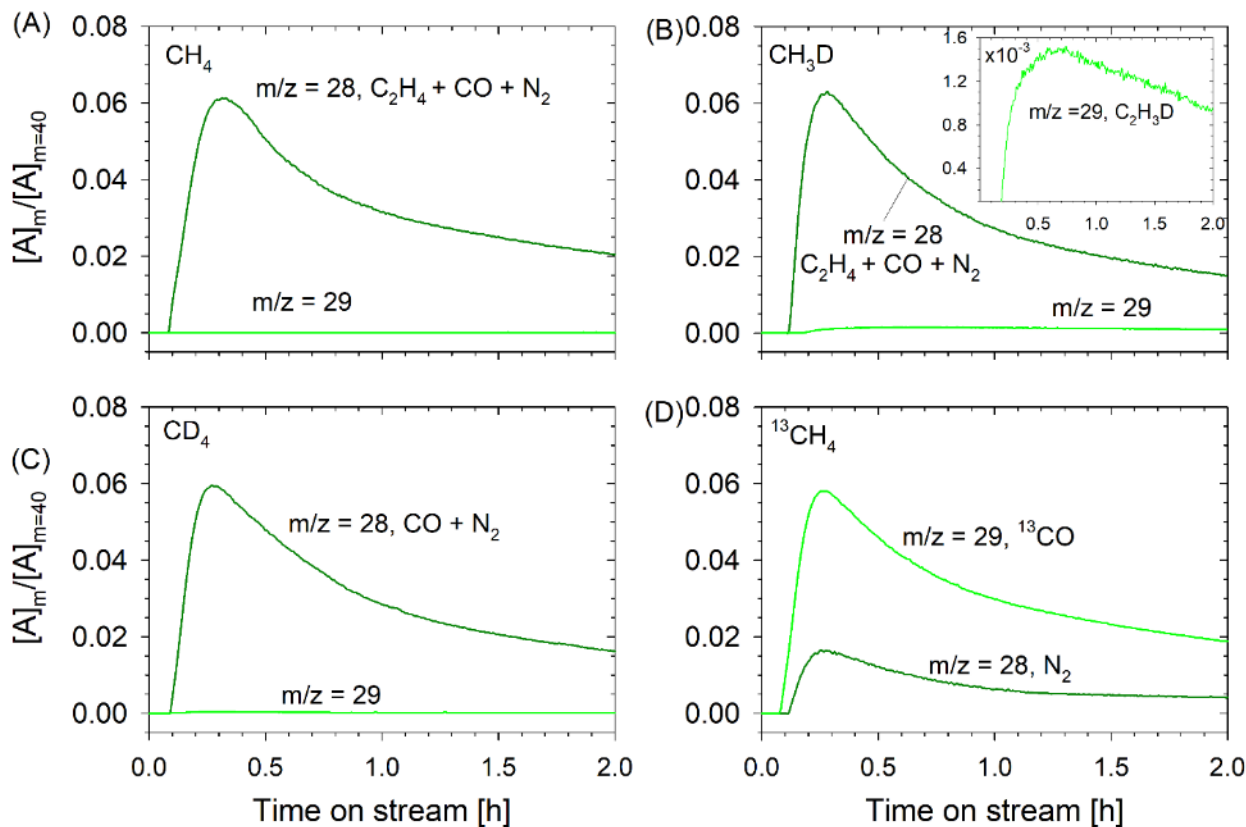


Fig. 6-11 Normalized MS signals for the products of methane activation from the ethylene group $m/z = 28$ and 29 over partially oxidized commercial GaN powder with (A) CH_4 , (B) CH_3D , (C) CD_4 , and (D) $^{13}\text{CH}_4$. (experiments were done at 700 °C and 1 bar).

The normalized mass spectra signal for the C_2 -group (ethylene) is illustrated in Fig. 6-11. The mass to charge ratio of $m/z = 28$ for the different feeds can be associated to C_2H_4 , CO and/or N_2 . Since (and $m/z = 29$ for ^{13}CO with $^{13}\text{CH}_4$) were nearly same. The $m/z = 28$ with $^{13}\text{CH}_4$ corresponds to N_2 , produced by the decomposition of NH_3 produced during partial oxidation of GaN. The ammonia produced during partial oxidation of GaN was adsorbed on the catalyst (DFT suggests that ammonia adsorption on Ga_2O_3 is instantaneous, refer to section 6.2.1). Hence, $m/z = 28$ includes C_2H_4 , CO , and N_2 for all methane isotopes except $^{13}\text{CH}_4$. This proves our DFT findings and supports that nitridation was essential for a better carbon atom conversion economy in CH_4 .

While $m/z = 29$ was nil for CH_4 and CD_4 , it corresponded to $\text{C}_2\text{H}_3\text{D}$ with CH_3D , as shown in the inset of Fig. 6-11B. The KIE was pronounced for the product of interest ethylene (Fig. 6-11B inset, and Fig. 6-12, C_2H_4 , $^{13}\text{C}_2\text{H}_4$, and mixed ethylene isotopes from CH_3D like $\text{C}_2\text{H}_3\text{D}$ with $m/z = 29$, $\text{C}_2\text{H}_2\text{D}_2$ with $m/z = 30$). These were measured respectively using $m/z = 28$, 30, and 32. With $^{13}\text{CH}_4$

and CD_4 , masses 32 ($^{13}\text{C}_2\text{H}_6$) and 36 (C_2D_6) were not detected, which implied that no ethane (C_2H_6) was being produced during activation. The isotope C_2D_4 was not even detected with CD_4 (not shown).

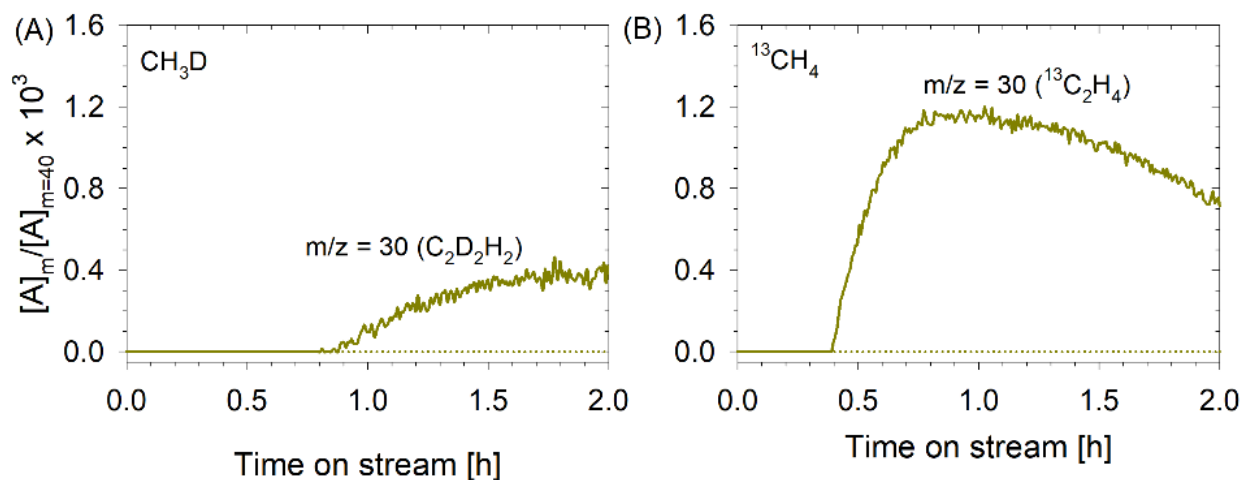


Fig. 6-12 Normalized MS signals for the products of methane activation from the ethylene group (A) $\text{C}_2\text{D}_2\text{H}_2$, $m/z = 30$ from CH_3D , and (D) $^{13}\text{C}_2\text{H}_4$, $m/z = 30$, over partially oxidized commercial GaN powder with CH_4 isotopes (experiments were done at 700 °C and 1 bar).

It can be seen from Fig. 6-11B inset and Fig. 6-12 that the C_2H_4 isotopes were 50% lower (steady-state rates) than C_2H_4 produced by CH_4 on non-oxidized GaN (refer to Chapter 5). However, as more deuterium D gets incorporated for the formation of ethylene isotopes, the yield dropped by another half order of magnitude (Fig. 6-12). Additionally, there was a delay (more than the residence time delay of 5 min) due to KIE on the formation of ethylene isotope as more D was incorporated in the molecule (compare the onset of formation of $\text{C}_2\text{H}_3\text{D}$ ($m/z = 29$) vs. $\text{C}_2\text{H}_2\text{D}_2$ ($m/z = 30$), Fig. 6-11 and 11). In the case of CH_3D feed, $\text{C}_2\text{H}_2\text{D}_2$ ($m/z = 30$; not shown), and C_2D_4 ($m/z = 32$) were not detected). For the CD_4 feed, no C_2D_4 ($m/z = 32$) was observed. These observations support the presence of the KIE. The cleavage of the C-H ($^{13}\text{C-H}$ and C-D) bond is the primary step for the methane activation. However, this is not the rate determining step because H_2 , HD, and D_2 appeared immediately after the residence time delay (Fig. 6-9).

The delay in the formation of higher ethylene isotopes (Fig. 6-12) could be because of a slow formation of CH_2^* , CHD^* , $^{13}\text{CH}_2^*$, and slow dimerization of adsorbed CH_2 (Ga-CH_2) to form C_2H_4 ($\text{CH}_2^* + \text{CHD}^* \rightarrow \text{C}_2\text{H}_3\text{D}$ and $\text{CHD}^* + \text{CHD}^* \rightarrow \text{C}_2\text{H}_2\text{D}_2$). The ion-current intensity for CH_3^* ($m/z = 15$, which formed CH_2^*) from CH_4 was >50% than that of CHD^* ($m/z=15$) from CH_3D (Fig. 6-10). Ethylene formation consists of three elementary steps: (1) formation of CH_2^* (or CHD , $^{13}\text{CH}_2$)

from CH_3^* , (2) dimerization of CH_2^* (or CHD , $^{13}\text{CH}_2$) to form C_2H_4 (or $\text{C}_2\text{H}_2\text{D}_2$, $^{13}\text{CH}_2$), and (3) desorption of ethylene. The first step is the rate determining step, as predicted by the DFT calculations and supported by experiments. A similar KIE was observed for the isotopes of the minor component benzene (C_6H_6 , Fig. 6–13).

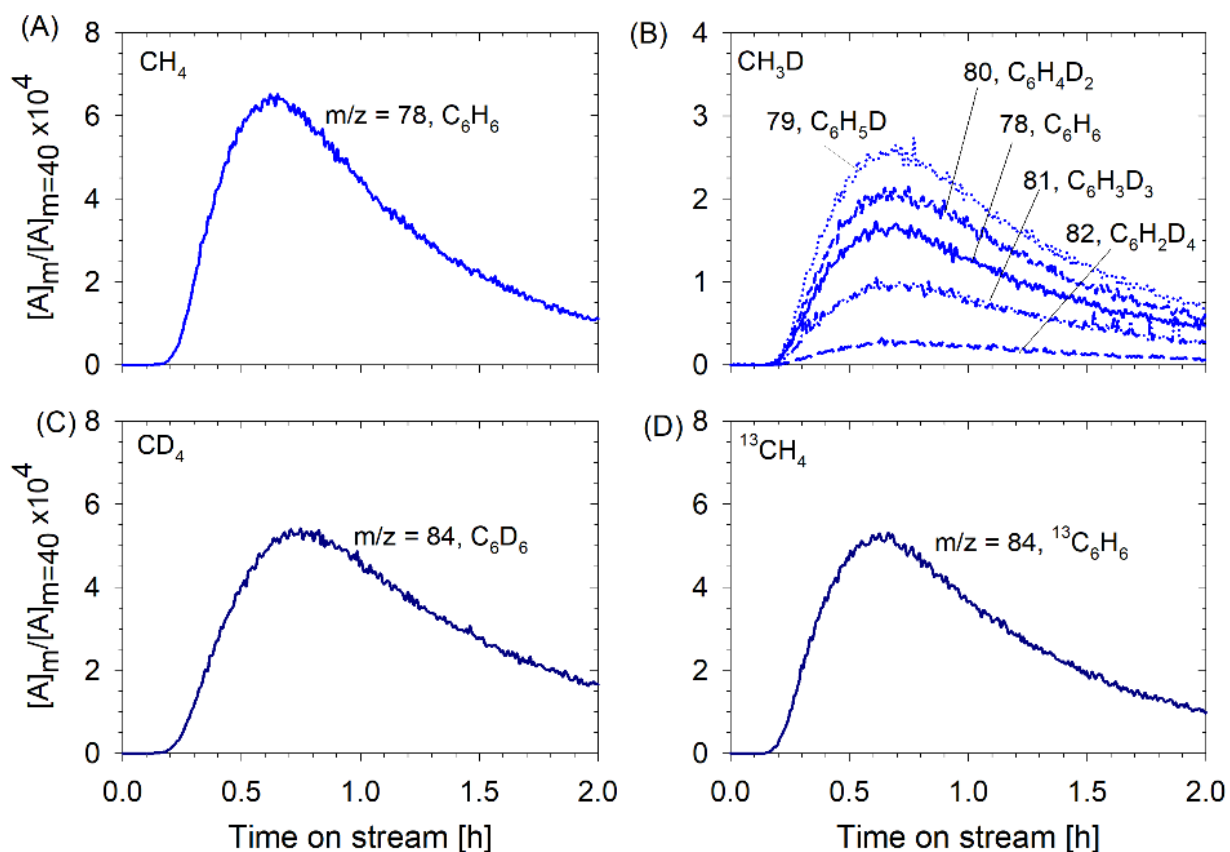


Fig. 6–13 Normalized MS signals for the benzene isotopes over partially oxidized commercial GaN powder with (A) CH_4 , (B) CH_3D , (C) CD_4 , and (D) $^{13}\text{CH}_4$. (experiments were done at 700 °C and 1 bar).

The onset of benzene formation was also delayed by about 5 min after the delay due to residence time. The benzene isotopes yields from $^{13}\text{CH}_4$ ($^{13}\text{C}_6\text{H}_6$) and CD_4 (C_6D_6) were similar and slightly lower than from CH_4 (Fig. 6–13). As discussed above, the slower dimerization to form C_2H_4 (higher adsorption time) favored the formation of higher hydrocarbon species. The benzene formation rates with CH_4 were similar (lower for CD_4 and $^{13}\text{CH}_4$ by 25–30%) to what was seen on unsupported non-oxidized GaN (refer to Chapter 5).

6.3.1.2 Supported GaN/SBA15

The supported catalyst (GaN/SBA15), produced by in-situ nitridation, did not have any exposed Ga₂O₃. Like the unsupported GaN (partially oxidized), they also did not produce any deuterium-containing isotopes of ethylene with CD₄ as well as with CH₃D. However, the dihydrogen isotopes (Fig. 6–14, H₂, HD, and D₂), ethylene (Fig. 6–16, C₂H₄ with CH₄ and CH₃D, and ¹³C₂H₄ with ¹³CH₄), and all benzene isotopes were detected. Similar to commercial GaN (Fig.6–9B), a ratio of $k_{C-H}/k_{C-D} = 2.01$ was calculated based on the CH₃D experiments as illustrated in Fig.6–14B, which shows H₂ (m/z = 2) and HD (m/z = 3) formation rates.

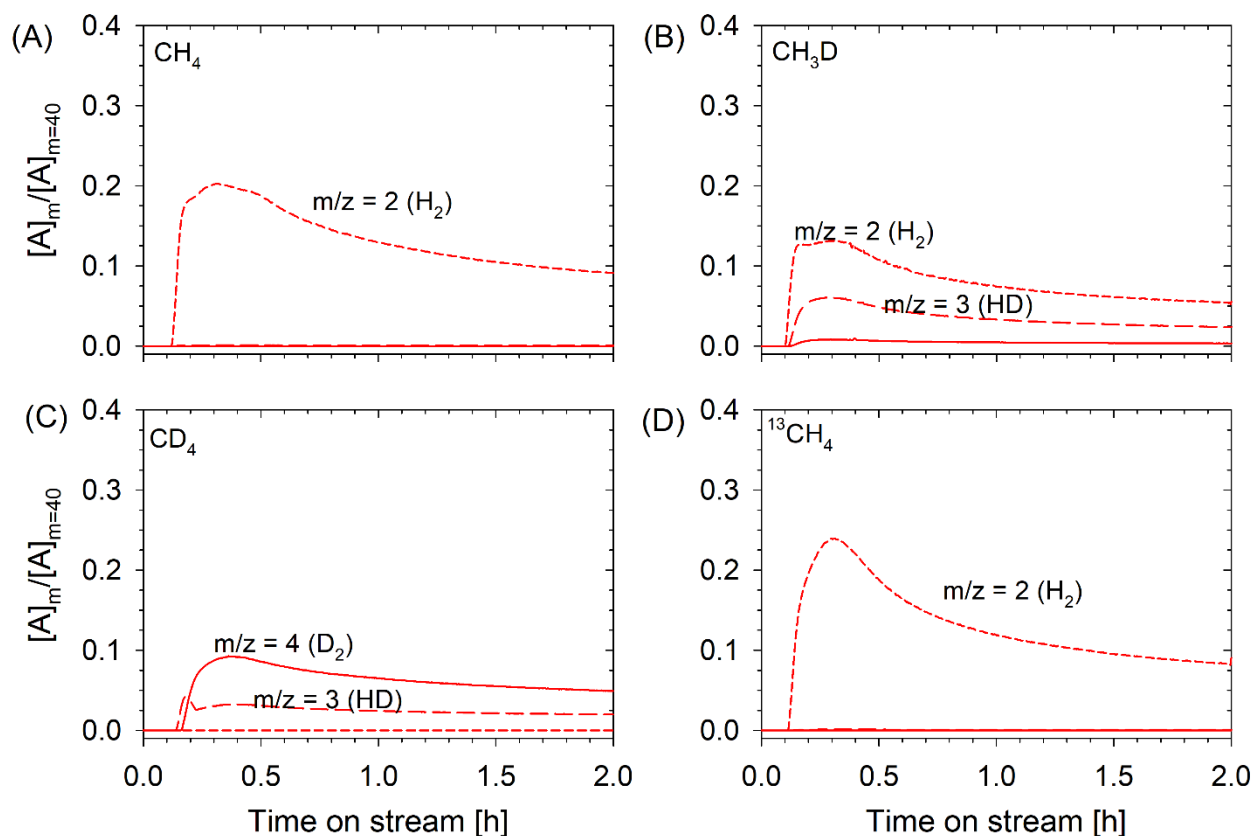


Fig. 6–14 Normalized MS signals for the products of methane activation from the hydrogen group (H₂, m/z = 2, HD, m/z = 3, and D₂, m/z = 4), over supported GaN/SBA15 with CH₄ isotopes (A) CH₄, (B) CH₃D, (C) CD₄, and (D) ¹³CH₄ (experiments were done at 700 °C and 1 bar).

Since HD and D₂ (20 times lower than H₂, and 10 times lower than HD) were produced, the following mechanism was hypothesized based on our DFT (Fig. 6–9 and 14):





The feed gas MS ions on GaN/SBA15 showed a similar trend (Fig. 6-15) as observed over partially oxidized GaN catalysts (Fig. 6-10). This again affirms the KIE due to D or ^{13}C in methane. However, unlike CH_3D over GaN, the intensities for the $m/z = 15$, 18, and 19 stabilized at values higher than that in the feed (grey shaded area in Fig. 6-15B). The intensity for the $m/z = 17$ stabilized lower than the feed $m/z = 17$ intensity. It seems that all reactions represented by equations 6-12 to 17 have attained equilibrium.

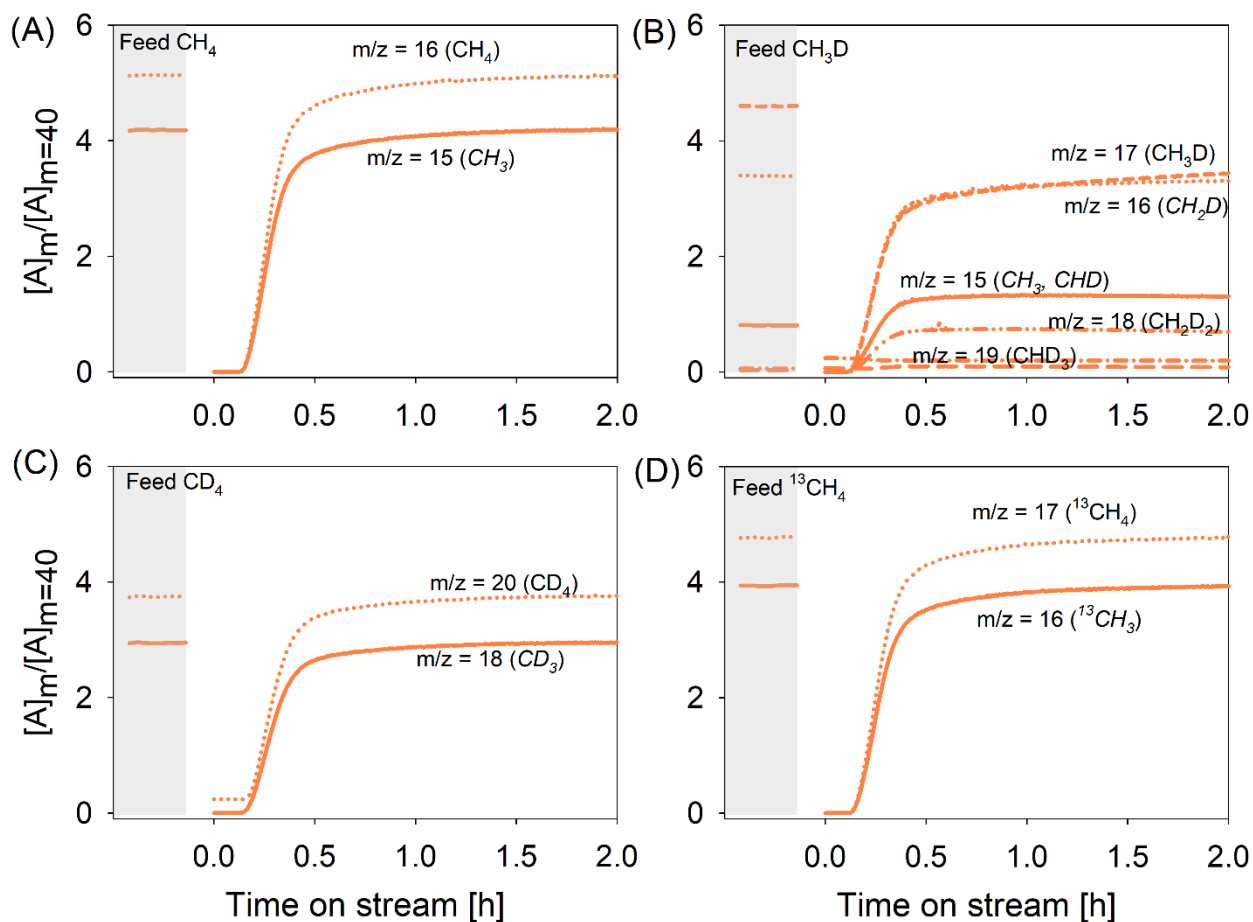


Fig. 6–15 Normalized MS signals for the characteristic feed ions of different CH₄ isotopes during activation over supported GaN/SBA15 (A) CH₄, (B) CH₃D, (C) CD₄, and (D) ¹³CH₄. The shaded area on the left represents the plot without any catalysts.

In-situ nitridation for producing GaN/SBA15 prevented the unwanted oxidation of GaN/SBA15. This is reflected in $m/z = 28$ (Fig. 6–16); only CH₄ and CH₃D had $m/z = 28$ product molar flow rates. The $m/z = 28$ signal was not observed for CD₄, and the one seen for ¹³CH₄ was because of CO (not ¹³CO) produced from the >700 ppmV CO₂ (present as an impurity in ¹³CH₄ gas, refer to appendix A5–1). The possibility of the reverse water-gas shift reaction has already been discussed (refer to Chapter 5). The CO₂ content in the product was zero (not shown). Also, the initial (maximum) rate of C₂H₄ formation from CH₃D was 50% of that from CH₄ (Fig. 6–16A and B). This is because of the involvement of C–D bond cleavage in CH₃D for the formation of CH₃^{*}, which forms CH₂^{*}, and then C₂H₄ by dimerization.

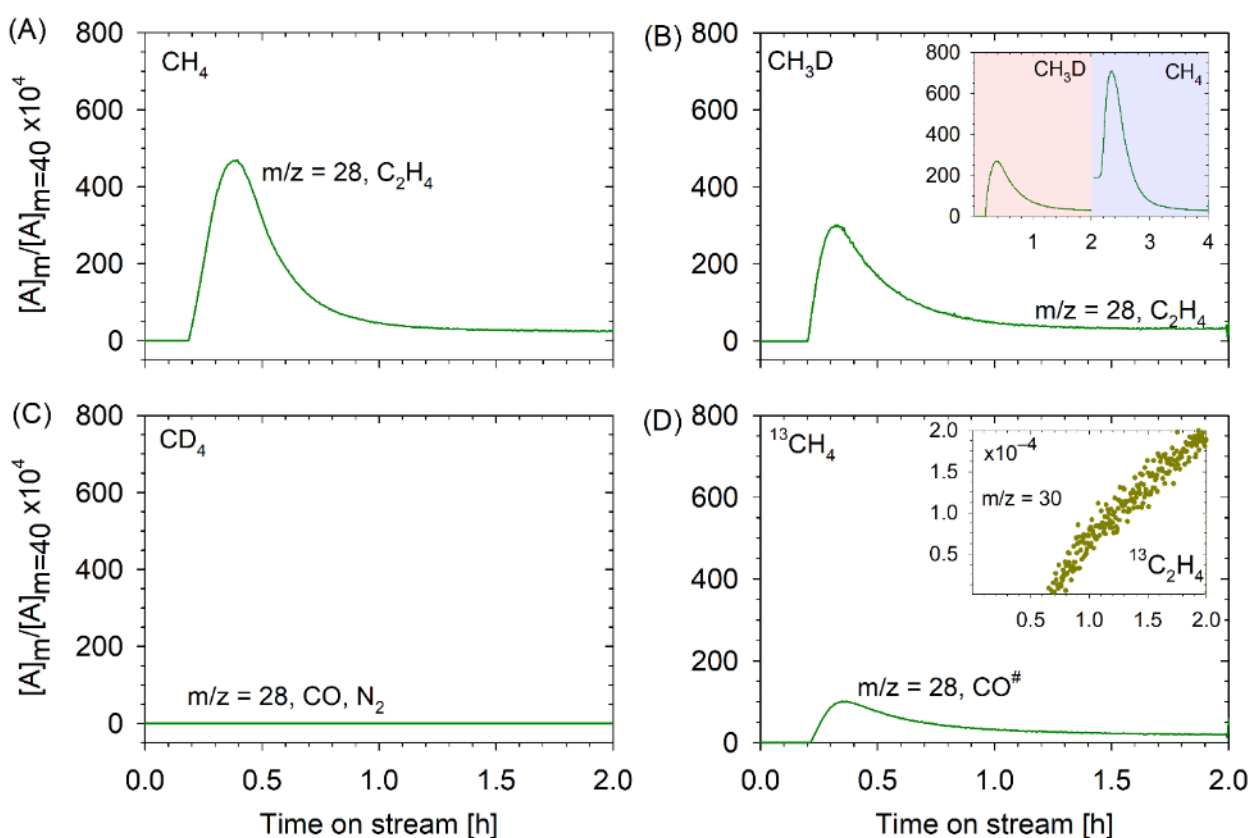


Fig. 6–16 Normalized MS signals for C₂H₄ isotopes produced by methane activation over supported GaN/SBA15 with CH₄ isotopes (A) CH₄, (B) CH₃D, (C) CD₄, and (D) ¹³CH₄ (experiments were done at 700 °C and 1 bar). #CO was produced from the impurity CO₂ in ¹³CH₄ by the RWGS reaction.

The initial rates were reverified by another experiment, where the feed gas was switched to CH_4 after 2 h of CH_3D over GaN/SBA15 (Fig. 6–16B inset). The C_2H_4 rates were of the same order of magnitude as over GaN/SBA15–700 discussed in Chapter 5. The only C_2H_4 isotope seen was with $^{13}\text{CH}_4$ (Fig. 6–16D inset). The $^{13}\text{C}_2\text{H}_4$ isotope rate was one order magnitude lower than the C_2H_4 steady-state flow rate, and the formation of $^{13}\text{C}_2\text{H}_4$ started late (the probable cause has been discussed above). Non-detection of C_2D_4 over GaN/SBA15 (and also over GaN) indicates that the adsorbed CD_x had high negative adsorption energy, and the desorption was also very high (positive). Some of the mixed ethylene isotopes observed over partially oxidized GaN catalysts with CH_3D ($m/z = 29$ and 30 , Fig. 6–11B inset and 6–11) were not seen with GaN/SBA15. Iglesia et al. [92] also reported the non-detection of any labeled products during non-oxidative methane-propane ($^{13}\text{CH}_4\text{--C}_3\text{H}_8$) conversion over ZSM5 at 500°C . They suggested that the non-oxidative conversion of CH_4 to higher hydrocarbons on solid acids was limited by elementary steps that occur after the initial activation of C–H bonds, which was also true for our system (formation of CH_2^* , CHD^* , dimerization, and C_2H_4 desorption).

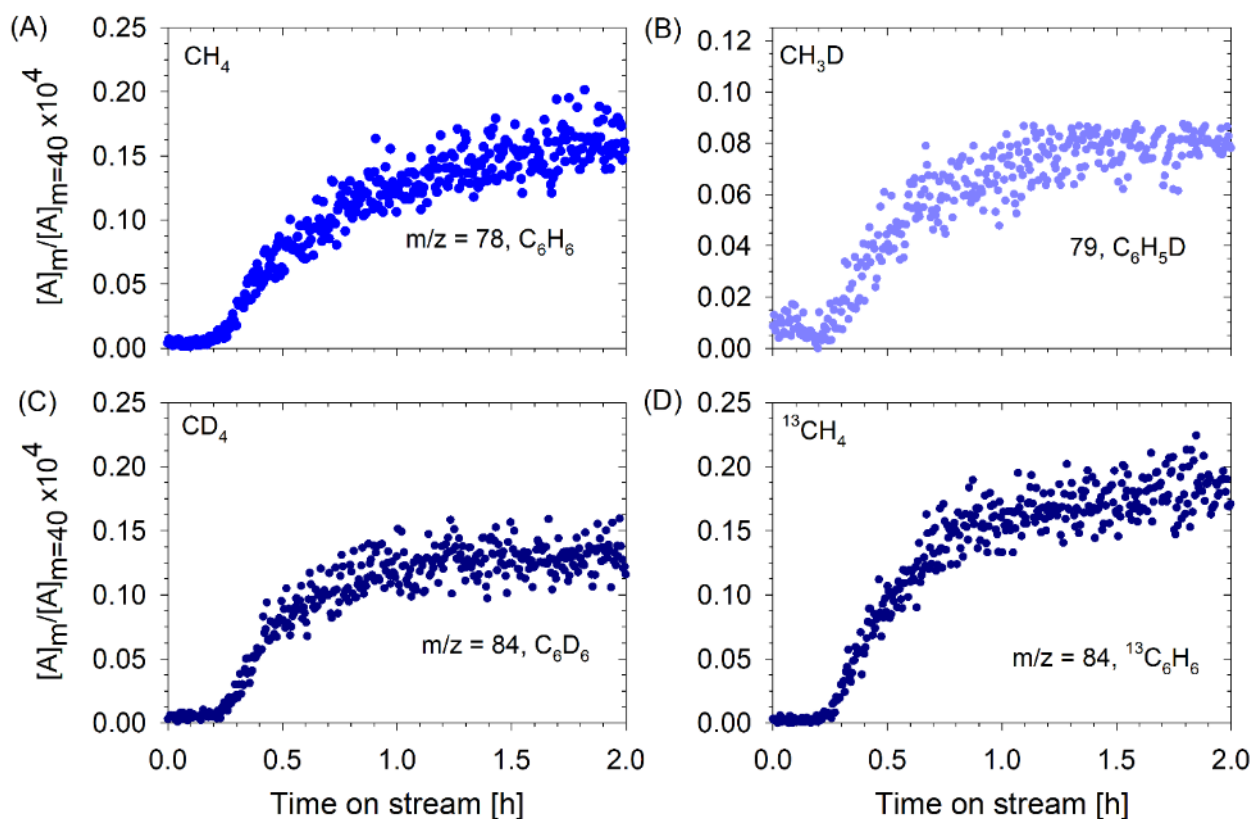


Fig. 6–17 Normalized MS signals for C_6H_6 isotopes produced by methane activation over supported GaN/SBA15 with CH_4 isotopes (A) CH_4 , (B) CH_3D , (C) CD_4 , and (D) $^{13}CH_4$ (experiments were done at 700 °C and 1 bar).

Fig. 6–17 illustrates various benzene isotopes formed over GaN/SBA15. They were at least two orders of magnitude lower than what was produced over the partially oxidized GaN catalyst. As discussed in the ^{13}C SS-NMR section (section 6.3.3), supported catalysts favor the formation of alkenes, while unsupported catalyst produced a significant amount of aromatics besides the alkenes.

If H_2 , DH , D_2 , and C_6D_6 are being formed over the supported catalysts, the adsorbed CD_x species should be present because the first step of activation is the formation of $H_3C-Ga-N-H$. It was observed and also been reported in [90] that the C–H bond cleavage was easier than the cleavage of the C–D bond. Two experiments were performed: one discussed above where the catalyst GaN/SBA15 was first fed with CH_3D for 2 h, and then the feed gas was switched to CH_4 for 2 h. The second experiment was with CD_4/CH_4 (Fig. 6–18).

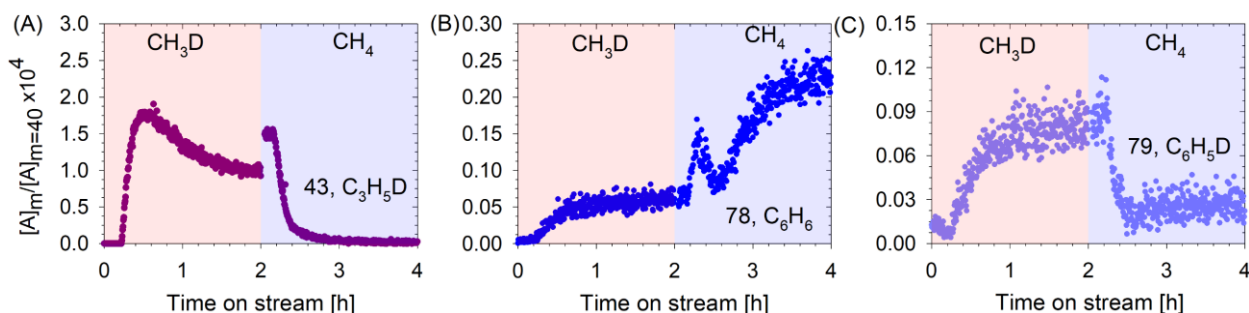


Fig. 6–18 Normalized MS signals for (A) C_3H_5D , $m/z = 43$, (C) C_6H_6 , $m/z = 78$, and (D) C_6H_5D , $m/z = 79$, on supported GaN/SBA15 with 2 h of CH_3D (80 vol% in Ar) followed by 2 h of CH_4 (80 vol% in Ar). The experiments were done at 700 °C and 1 bar.

With CH_3D/CH_4 , no D containing C_2H_4 (C_2H_3D to C_2D_4) isotopes were seen either with CH_3D or with CH_4 after CH_3D . Interestingly, the D containing C_3H_6 isotope C_3DH_5 ($m/z = 43$) was observed with CH_3D (Fig. 6–18A), but not with CH_4 (after CH_3D). This indicates that in CH_3D , the C–H bonds are broken rather than the single C–D bond. As discussed earlier, higher residence times (stronger surface-species interaction) of adsorbed species like CD^* , CD_2^* , and CD_3^* are needed for forming higher hydrocarbons. Similar behavior was observed with D containing C_6H_6 isotopes, where the major products were C_6DH_5 (1 C–D and 5 C–H bonds) and $C_6D_2H_4$ (2 C–D and 4 C–H bonds). Anything above $C_6D_2H_4$ (i.e., $C_6D_3H_3$, C_6DH_5 , and C_6D_6) was not detected. Fig. 6–19 illustrates the

mixed C₂ isotopes produced during the CH₄ cycle, preceded by a 2 h CD₄ cycle. Several C₂ isotopes were seen from mass 28 to 33, except mass 29.

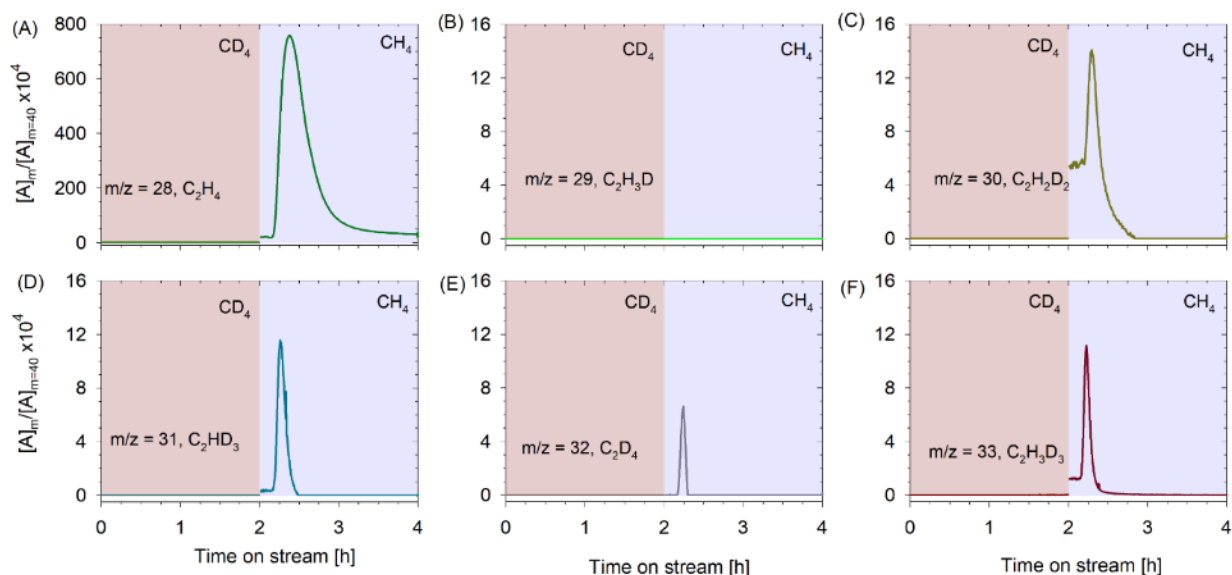


Fig. 6-19 Normalized MS signals for C₂ isotopes produced during CD₄/CH₄ cycle on supported GaN/SBA15 with 2 h of CD₄ (80 vol% in Ar) followed by 2 h of CH₄ (80 vol% in Ar). The experiments were done at 700 °C and 1 bar.

Fig. 6-19 reveals which adsorbed species might have been present on the catalyst surface when switched to from CD₄ to CH₄. Just like the single isotope runs, no C₂ isotope species were observed in the CD₄ cycle. Based on this, most possible surface species are listed in Table 6-2. The absence of C₂H₃D (m/z = 29 in Fig. 6-19B) indicates that CD* surface species was absent, which is not surprising given that the C-D bond cleavage is more difficult than C-H bond. While no ethane (C₂H₆) or deuterated ethane (C₂D₆) was seen with single isotope gas runs, the formation of C₂H₃D₃ was observed (Fig. 6-19F), formed by CH₃* and CD₃*.

Table 6-2 Possible mixed C₂ isotopes from CD₄/CH₄ on GaN/SBA15.

Possible species (CD ₄)	Possible species (CH ₄)		
	CH ₃ *	CH ₂ *	CH*
CD ₃ *	C ₂ H ₃ D ₃ (m = 33)	–	C ₂ HD ₃ (m = 31)
CD ₂ *	–	C ₂ H ₂ D ₂ (m = 30)	–
CD*	C ₂ H ₃ D (m = 29)	–	–

Based on the above observations, a multi-cycle experiment was conducted with CH₄/CD₄. The catalyst GaN/SBA15 was first fed with CH₄ for 30 min, and then the feed gas was switched to CD₄ for 30 min. This cycle was repeated three times. However, the feeding sequence has been reversed (CH₄ first, and then CD₄) to see whether similar observations could be made, as illustrated in Fig. 6–20. The motivation behind this was to observe the formation of any deuterium incorporated alkene isotope when the CH_x replaces CD_x and vice-versa. Fig. 6–20 illustrates that HD and D₂ were not produced in the first CH₄ cycle (0–0.5 h), but they started appearing from the first CD₄ cycle (2nd cycle) onwards. Previously, no HD or D₂ was seen in the 2 h run with CH₄ only, on both GaN and GaN/SBA15. Also, no H₂ was seen with CD₄ (no CH₄ cycle) only runs. This again provides direct evidence for C–H (C–D) bond cleavage, adsorption of H (D), and exchange between adsorbed H (D). Not only the product of interest C₂H₄ (m/z = 28) and C₂D₄ (m/z = 32) were now detected, but also the mixed ethylene isotopes (m/z = 30, and 31) were also detected. These are illustrated in Fig. 6–21. However, during the CD₄ cycle, the highest ethylene isotope C₂D₄ (m/z = 32) was not detected, which is consistent with the observation made with non-cyclic run discussed above. It was as if adsorbed CD_x were replaced (facilitated desorption, e.g., [93]) by CH_x (replacement adsorption, defined in [94]) during the CH₄ activation cycle, which led to the formation of mixed C₂H₄ isotopes.

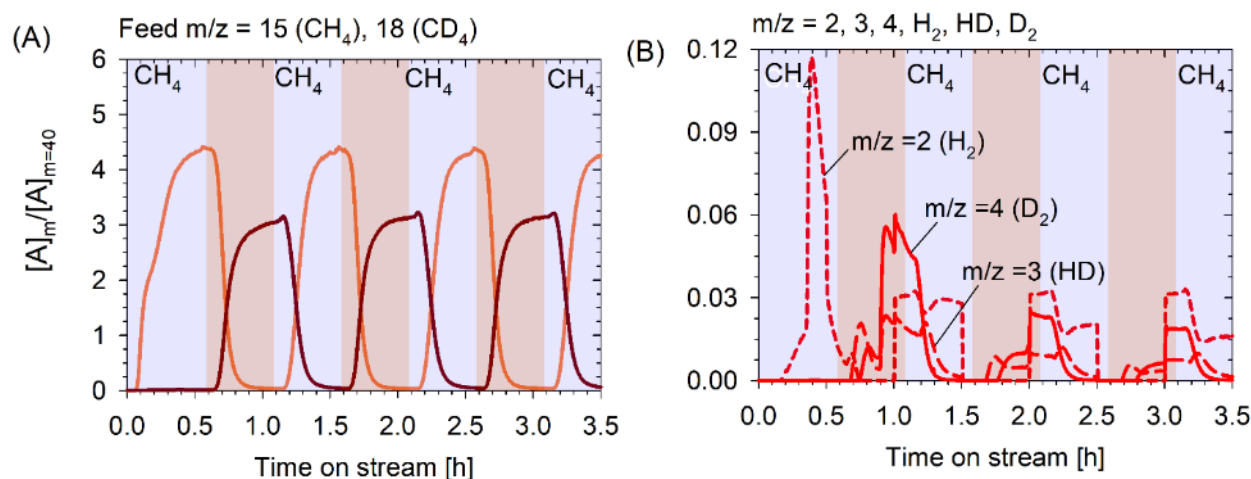


Fig. 6–20 Normalized MS signals for (A) feed CH₄ (m/z = 15) and CD₄ (m/z = 18), (B) H₂, m/z = 2, (C) HD, m/z = 3, and (D) D₂, m/z = 4, on supported GaN/SBA15 (experiments were done at 700 °C and 1 bar).

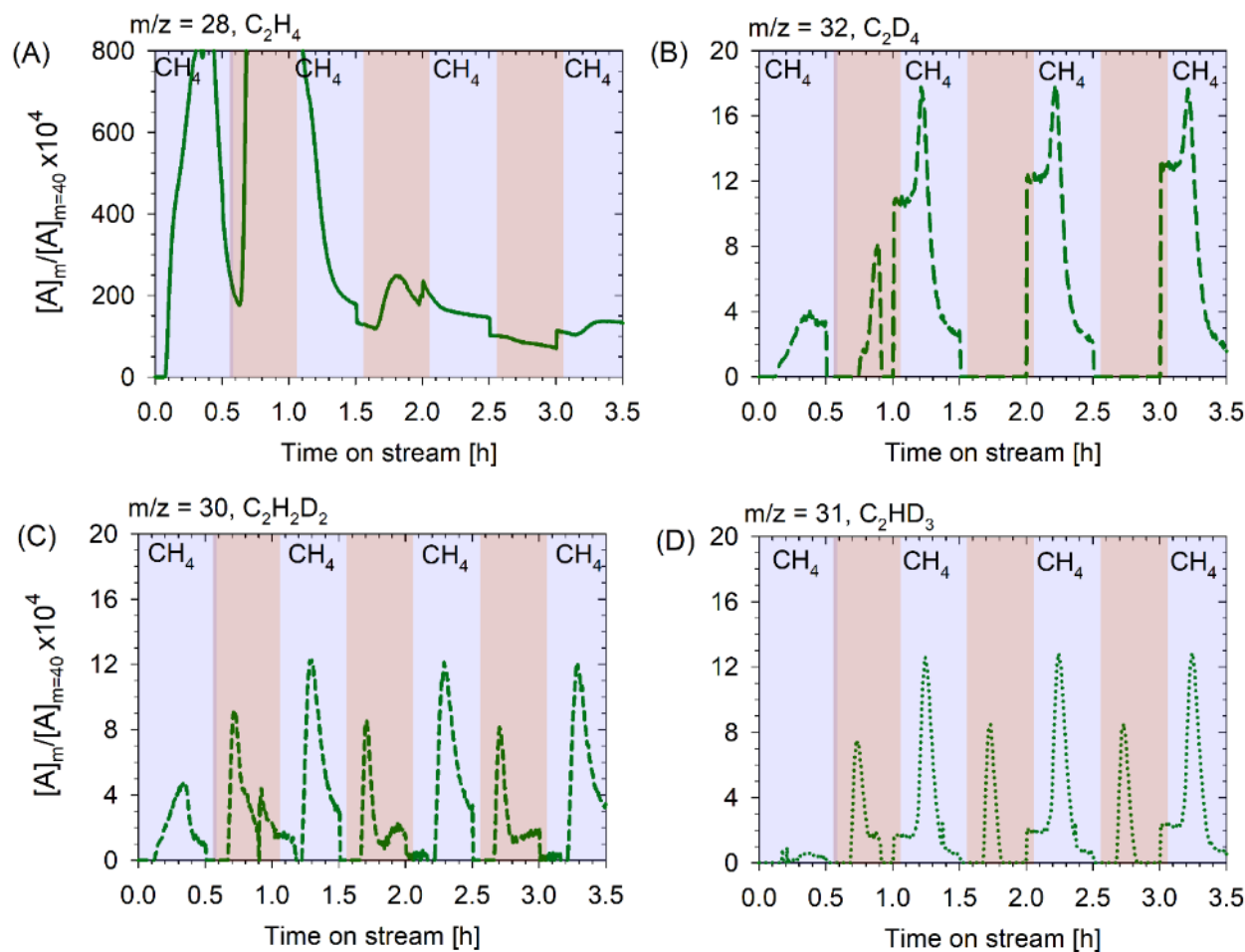


Fig. 6-21 Normalized MS signals for ethylene isotopes (A) C_2H_4 ($m/z = 28$), (B) C_2D_4 , $m/z = 2$, (C) $C_2H_2D_2$, $m/z = 3$, and (D) C_2HD_3 , $m/z = 4$, on supported GaN/SBA15 (experiments were done at 700 °C and 1 bar).

Some contribution to $m/z = 30$ was also made by C_2D_4 at $m/z = 32$ (60.8% [95]), and Fig. 6-21 includes the correction from this contribution by C_2D_4 . Mass 30 seen in the first CH_4 cycle (Fig. 6-21C) could be due to the 0.1% contribution [96] of C_2H_4 ($m/z = 28$) to $m/z = 30$. Similarly, the minor components isotopes for propylene and benzene were also detected, as illustrated in Fig. 6-22. C_3D_6 ($m/z = 48$) was not detected in the non-cyclic run, and it took one cycle (CH_4-CD_4) for its appearance in the cyclic run (Fig. 6-22B). The delay (KIE) in the appearance of D incorporated isotopes (C_3D_6 , C_6D_6) reaffirms that the rate-limiting step is a step after the first C-H (or C-D) bond cleavage and adsorption (ethylene formation). However, the study did not establish which of the three steps for ethylene formation is rate-limiting.

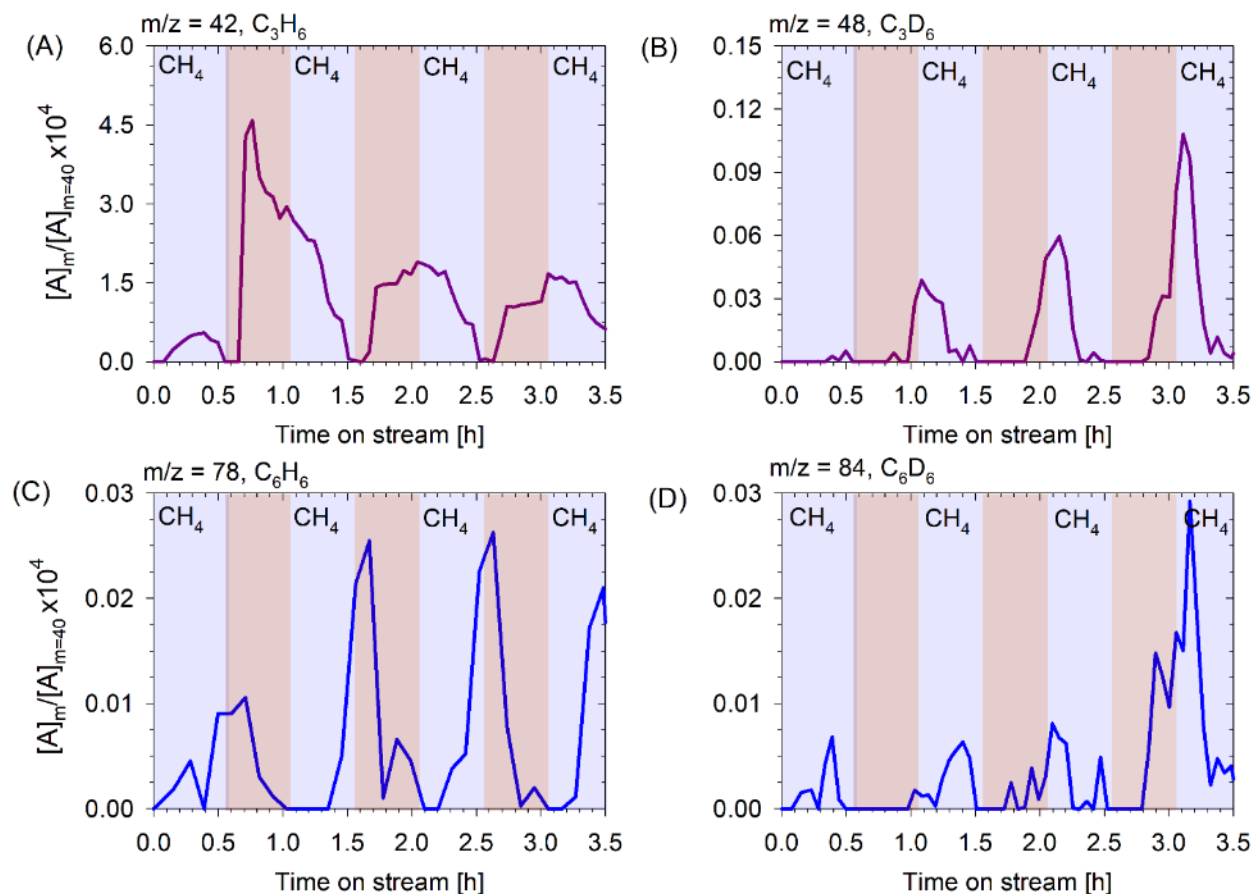


Fig. 6–22 Normalized MS signals for minor components' isotopes (A) C₃H₆ ($m/z = 42$), (B) C₃D₆, $m/z = 48$, (C) C₆H₆, $m/z = 78$, and (D) C₆D₆, $m/z = 84$, on supported GaN/SBA15 (experiments were done at 700 °C and 1 bar).

6.3.2 Nuclear magnetic resonance (NMR)

The spent catalysts, which were obtained after ¹³CH₄ activation experiments (section 6.3.2), were analyzed via ¹³C solid-state NMR (SS-NMR) to identify adsorbed carbonaceous species. Fig. 6–23A illustrates that methyl species (–CH₃), indicated by a chemical shift at –9 ppm [32], were the predominant adsorbed carbon intermediate on the GaN/SBA15 catalyst. A peak at –9 ppm could also be associated with trapped ¹³CH₄ in the pores of the catalyst [32]. However, in the current work, this can be neglected as the catalyst was flushed with Ar for 12 h (overnight) that removed all trapped methane, which was also confirmed by in-situ DRIFTS measurement (refer to chapter 6.3.3, it took around 30 min for CH₄ FTIR peaks to disappear).

For the unsupported GaN catalyst, aromatic surface species, indicated by a broad peak around 125 ppm [32], were observed. These species are known to form polynuclear species or coke, which explains

the higher amount of coke per gram of catalyst, as reported in chapters 5 (see Tables 5-5 and 5-6). The chemical shift observed between 112–140 ppm can be assigned to aromatic C–C and aromatic C–H bonds [97]. For the supported GaN/SBA15 catalyst, the intensity for these species was much smaller (Fig. 6–23B, eight times zoomed), which explains the higher C₂H₄ and lower C₆H₆ selectivities observed for the methane activation experiments conducted over supported than unsupported catalysts (i.e., per gram of Ga; refer to Chapter 5). Unsupported catalysts are nearly non-porous. The surface GaN on these are readily accessible to CH₄, and they also form the active sites for C–C bond coupling to form higher hydrocarbons above C₂H₄. This C–C coupling beyond C₃ becomes limited in GaN/SBA15 due to the dispersion of GaN inside SBA–15 pores (refer to Chapter 5). Fig. 6–23C shows four times zoomed spectrum in the shift range –15 to 20 ppm that could be assigned to alkyl carbons (CH₃, CH₂, CH) [97] as well as to –CH₃ of toluene [32].

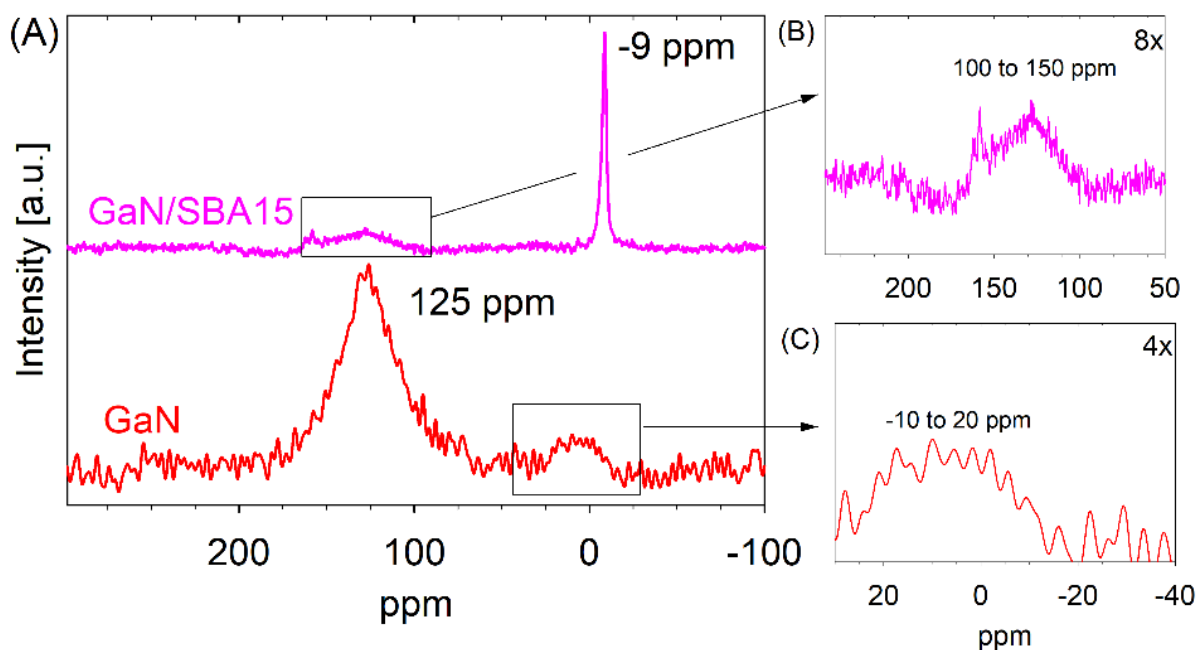


Fig. 6–23 ¹³C CP/MAS NMR spectra of products formed from ¹³CH₄ on (A) GaN and GaN/SBA15 at 700 °C for 120 min: (B) Zoomed (4x) in section (–20 to 20 ppm shift) for GaN and (C) Zoomed (8x) in section (100 to 150 ppm shift) for GaN/SBA15.

6.3.3 Diffuse reflectance infrared Fourier transform spectroscopy (DRIFTS)

6.3.3.1 Effect of dilution with KBr

The effect of dilution on the DRIFT spectra is illustrated in Fig. 6–24. Under the same experimental conditions, the characteristic peaks for the undiluted GaN were inconspicuous, while the 12.5 wt% GaN showed several peaks, as discussed in detail below. Undiluted GaN/SBA15, which was pre-

diluted due to dispersion in SBA-15 (Fig. 5-6, 15 wt% Ga, 18 wt% GaN), showed some of the peaks, but the signal to noise was very low at low wavenumbers ($< 2000 \text{ cm}^{-1}$). Once diluted (40 wt% in KBr), the noise disappeared for GaN/SBA15, and a new peak near 1400 cm^{-1} appeared, which is common to both GaN and GaN/SBA15. Unless otherwise specified, the subsequent discussion on results is based on diluted catalysts. For unsupported GaN, the catalyst content in the catalyst-KBr mixture was 12.5 wt%. For the supported GaN/SBA15, it was 40 wt% catalyst in KBr (around 8 wt% GaN in the catalyst-KBr mixture).

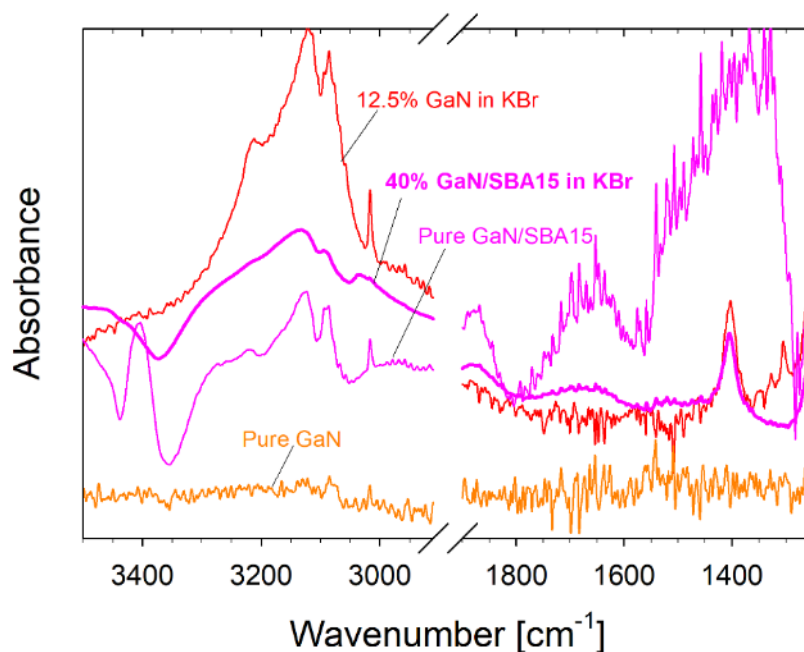


Fig. 6-24 Effect of dilution on the DRIFT spectra for the methane activation catalysts. The spectra were collected during Ar purge ($15 \text{ mL}_N \text{ min}^{-1}$) after 1 h CH_4 activation at $700 \text{ }^\circ\text{C}$ ($80\% \text{ CH}_4$, $2.0 \text{ mL}_N \text{ min}^{-1} \text{ CH}_4$). All spectra are corrected for the background spectrum under Ar at $700 \text{ }^\circ\text{C}$.

6.3.3.2 The masking effect of CH_4 on the spectra for the adsorbed species

During CH_4 adsorption, very strong absorption peaks referring to the $\nu\text{C-H}$ and $\delta\text{C-H}$ bands of the gaseous CH_4 appeared at 3015 cm^{-1} and 1305 cm^{-1} (see brown spectra in Fig. 6-25) [98], which masked the spectra of the adsorbed surface species (very high CH_4 concentration). A similar masking effect was also reported by Guo et al. [98]. Therefore, the sample was purged with Ar after methane exposure to remove the gaseous methane as well as the physisorbed surface species leaving the strongly chemisorbed surface intermediates that are illustrated with the pink spectra for the GaN/SBA15 catalyst in Fig. 6-25. The subsequent discussion on the DRIFTS results is based on the adsorbed species observed during the Ar purge, which lasted for around 0.5 h.

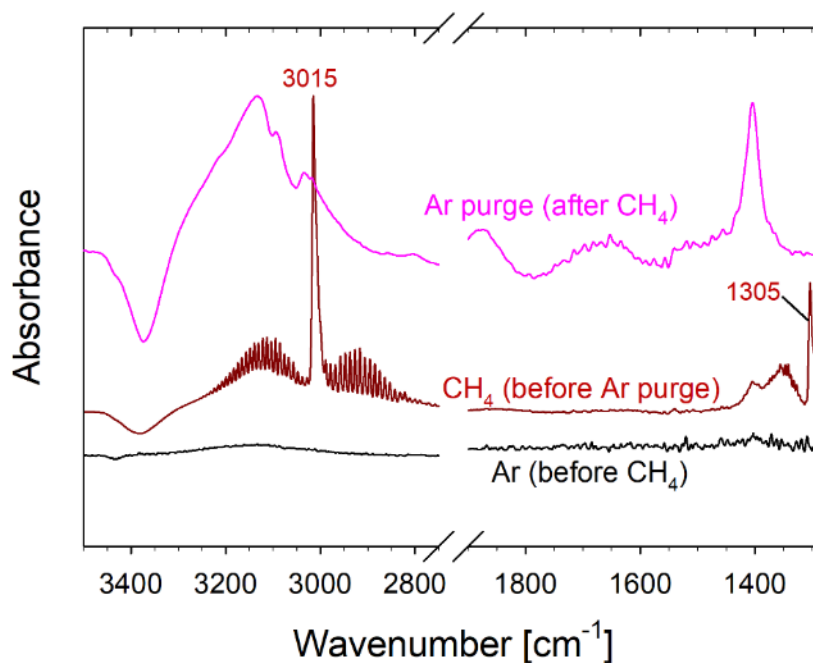


Fig. 6–25 Masking effect of CH_4 on the DRIFT spectra for GaN/SBA15 at 700 °C (80% CH_4 in Ar with 2.0 $\text{mL}_N \text{min}^{-1} \text{CH}_4$). All spectra were corrected for the background spectrum under Ar at 700 °C.

6.3.3.3 Influence of support

SBA–15 and N–SBA–15 (nitridated support) did not exhibit characteristic peaks associated with adsorbed carbon species such as CH_3 , C–H, aromatic, and alkene C=C bonds, which were only visible for the GaN containing catalysts (Fig. 6–26). The broad peak at around 3400 cm^{-1} corresponds to N–H of nitridated supported (N–SBA–15) and is also visible as a shoulder for GaN/SBA15 sample. The parent SBA–15 sample did not exhibit any peaks corresponding to the N–H bond, which are formed during the high-temperature nitridation process. As discussed earlier, during the CH_4 activation, N–H bonds are formed over GaN as $\text{H}_3\text{C–Ga}\cdot\text{N–H}$. This N–H stretch could be assigned to 3400 cm^{-1} and 3210 cm^{-1} . Peaks between 1350 and 1400 cm^{-1} are due to the inorganic structure of SBA–15, which is inconspicuous in GaN/SBA15.

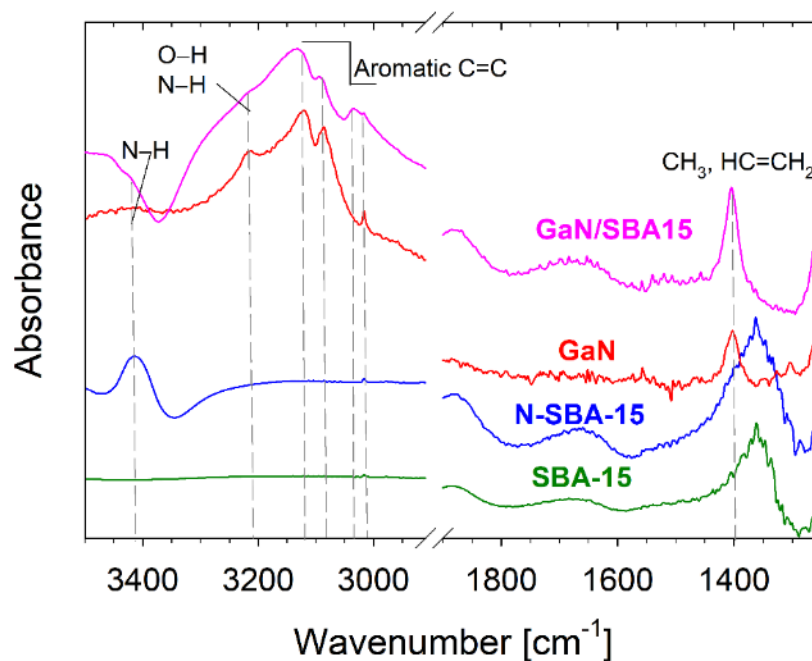


Fig. 6-26 Comparison of the DRIFT spectra for the supports (SBA-15 and N-SBA-15) with the supported GaN/SBA15 and the unsupported GaN. The spectra were collected during Ar purge (0.5 h at $15 \text{ mL}_N \text{ min}^{-1}$) after 1 h CH_4 activation at 700°C (80% CH_4 in Ar with $2.0 \text{ mL}_N \text{ min}^{-1}$ CH_4). All spectra were corrected for the background spectrum under Ar at 700°C .

6.3.3.4 Adsorbed species detected on GaN and GaN/SBA15

Fig. 6-27 illustrates and compares the spectra observed over GaN and GaN/SBA15 catalysts after exposing them to 80% CH_4 for 1 h, followed by Ar purge and cool down. Both GaN and GaN/SBA15 showed characteristic peaks around the same wavenumbers ($\pm 15 \text{ cm}^{-1}$). From left to right: As discussed above, the band at $3450\text{--}3400 \text{ cm}^{-1}$ (appearing as a shoulder for both GaN and GaN/SBA15) could be assigned to secondary amine N-H stretching vibrations (medium intensity) [99]. The peak at 3215 cm^{-1} (as a peak in GaN, and broad shoulder in GaN/SBA15) could be attributed to N-H stretch. The band $3105\text{--}3000 \text{ cm}^{-1}$ is attributed to aromatic (sp^2) =C-H stretching, with medium intensity [99]. This band is well defined and has sharper peaks for the unsupported GaN (Fig. 6-27). Symmetric bending vibration in CH_3 could be assigned to 1402 cm^{-1} (medium-strong, [99]). The vinyl hydrocarbons ($-\text{CH}=\text{CH}_2$) also exhibit a medium intensity around 1400 cm^{-1} for CH_2 in-plane deformation vibration, scissoring [99]. Also, $-\text{C}=\text{C}-$ stretching vibrations in the aromatic ring have a medium intensity band of $1470\text{--}1430 \text{ cm}^{-1}$ [99]. The wavenumbers from $1600\text{--}1740 \text{ cm}^{-1}$ are typical for alkenes (isolated C=C, vinyl), with weak to strong intensities [99]. Methylene ($>\text{CH}_2$) also has the characteristic band at $1500\text{--}1400 \text{ cm}^{-1}$ (deformation with medium intensity) and $1380\text{--}1160$

cm^{-1} (wagging with medium intensity) [99]. The wavenumber near 1240 cm^{-1} could be attributed to C–H in-plane bending in aromatics [99]. A weaker intensity in the band $1250\text{--}1230 \text{ cm}^{-1}$ could also be assigned to $=\text{C}\text{--H}$ in-plane deformation vibrations in monosubstituted benzenes (e.g., toluene) [99]. McKean et al. [100] assigned 1200 cm^{-1} for vibration in $\text{Ga}(\text{CH}_3)_3$. Socrates [99] assigned a medium to weak intensity for $\text{Ga}\text{--CH}_3$ at 1220 cm^{-1} . This could also be assigned to N–H deformation [99], the formation of which is the first step during dissociative chemisorption of CH_4 on GaN via the alkyl adsorption pathway. The intensity for both functional groups around 1240 cm^{-1} is medium and variable [99].

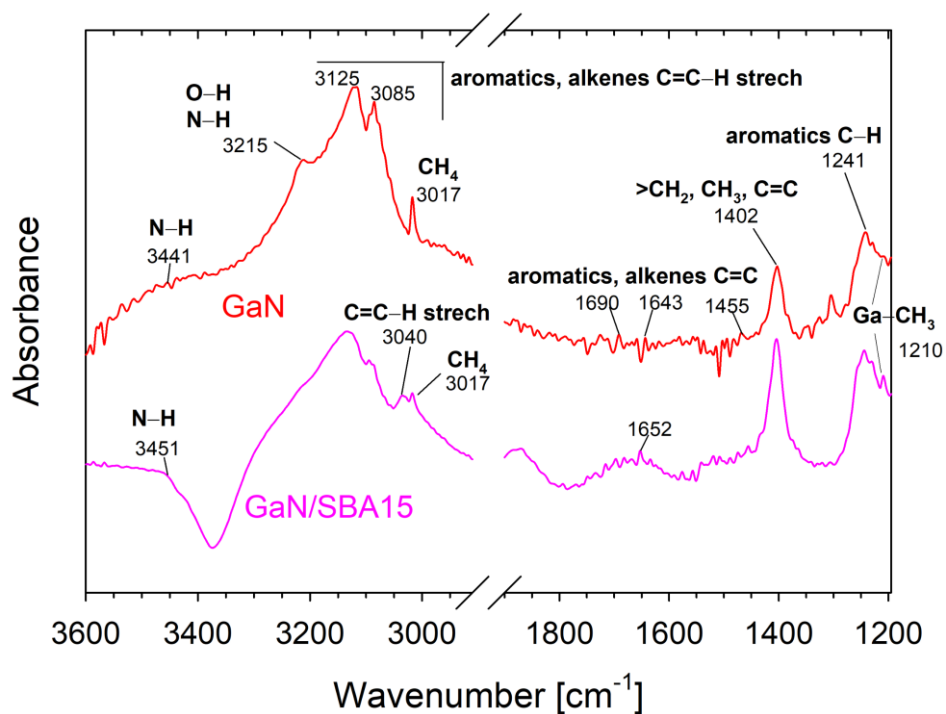


Fig. 6–27 DRIFT spectra for unsupported GaN and supported GaN/SBA15 collected under Ar purge, after 1 h exposure to CH_4 (80% in Ar) at $700 \text{ }^\circ\text{C}$. The peak corresponding to 3017 cm^{-1} is due to free CH_4 . All spectra are corrected for the background spectrum under Ar at $700 \text{ }^\circ\text{C}$.

These adsorbed species substantiate the mechanism proposed by DFT calculations. The first step is the formation of $\text{Ga}\text{--CH}_3$ and N–H. This is followed by the formation of $\text{Ga}\text{--CH}_2$; the two CH_2 combine to form C_2H_4 and H_2 (the rate determining step, Fig. 6–8).

The results illustrated in Fig. 6–27 was obtained by the interaction of CH_4 with the catalysts at $700 \text{ }^\circ\text{C}$. Li et al. [24] obtained benzene at $450 \text{ }^\circ\text{C}$ in a batch reactor (res. time 2–4 h), and Dutta et al. [54] did not see any hydrocarbon formation before $650 \text{ }^\circ\text{C}$ in a continuous reactor (residence time $< 2 \text{ s}$). What

is the minimum temperature required for the formation of these adsorbed species? To establish this, temperature-programmed DRIFTS (TP-DRIFTS) were performed (refer to the methodology Chapter 3). Fig. 6–28 and 29 illustrate the results of TP-DRIFTS. These figures compare the spectra observed for the supported and the unsupported catalysts. The characteristic peaks for both catalysts are around the same wavenumber ($\pm 15 \text{ cm}^{-1}$) and have been discussed above. The DRIFT spectra indicated the formation of adsorbed species from 400 °C for both supported and unsupported catalysts. The olefinic species (1400–1700 cm^{-1}) started from 400 °C indicating that C_2H_4 forms first, which was also discussed in DFT [46] and other mechanisms [36,37]. The appearance of aromatic species (3000–3150 cm^{-1}) started from 450 °C onwards. Table 6–3 summarizes the adsorbed species indicated in Fig. 6–28 and 6–29.

Table 6–3 Summary of adsorbed species seen on GaN/SBA15 and GaN

Adsorbed species wavenumber [cm^{-1}]		Assignment [99]
GaN/SBA15	GaN	
2853, 2797	2926, 2887, 2791	C–H stretching alkane, medium
3131, 3089, 3031	3104, 3070	Aromatic and alkene =C–H stretching, medium C–H stretching alkane, medium
–	3205	N–H stretch, O–H (silanol)
3451	3451 (broad shoulder)	N–H stretch
1402	1398	CH_2 in-plane deformation vibration
1513	1508	Methylene ($>\text{CH}_2$) deformation, medium
1692–1571	1701–1576	C=C stretching, weak to strong

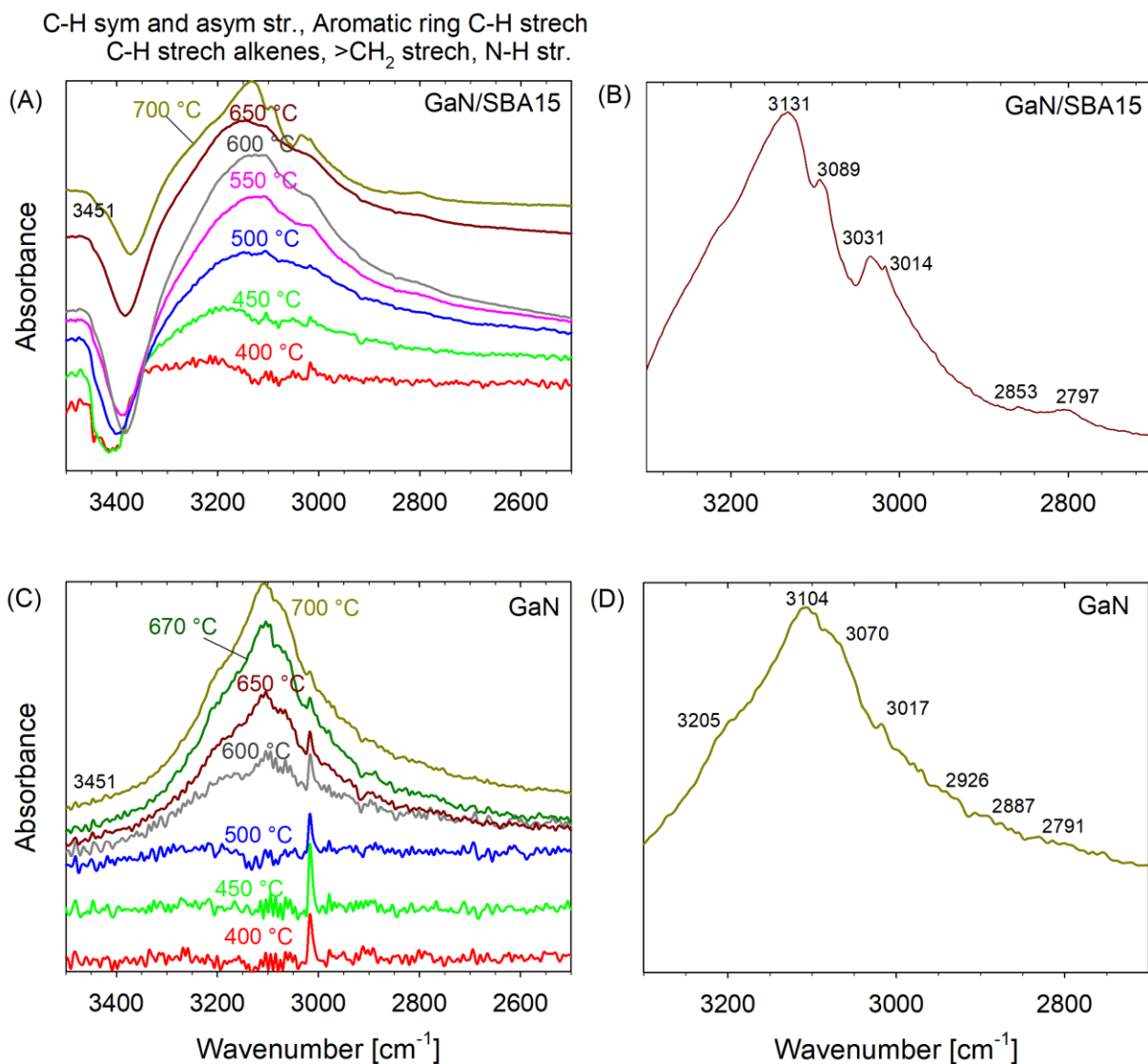


Fig. 6–28 Evolution of surface adsorbed species (between 3500–2500 cm⁻¹) over supported GaN/SBA15 (A) as a function of temperature and (B) at 700 °C; for unsupported GaN (C) as a function of temperature and (D) at 700 °C. The spectra were collected during Ar purge (15 mL_N min⁻¹) after 30 min CH₄ activation (80% CH₄ in Ar with 2.0 mL_N min⁻¹ CH₄). All spectra are corrected for the background spectrum under Ar at 400 °C. The species assignment is based on Socrates [88].

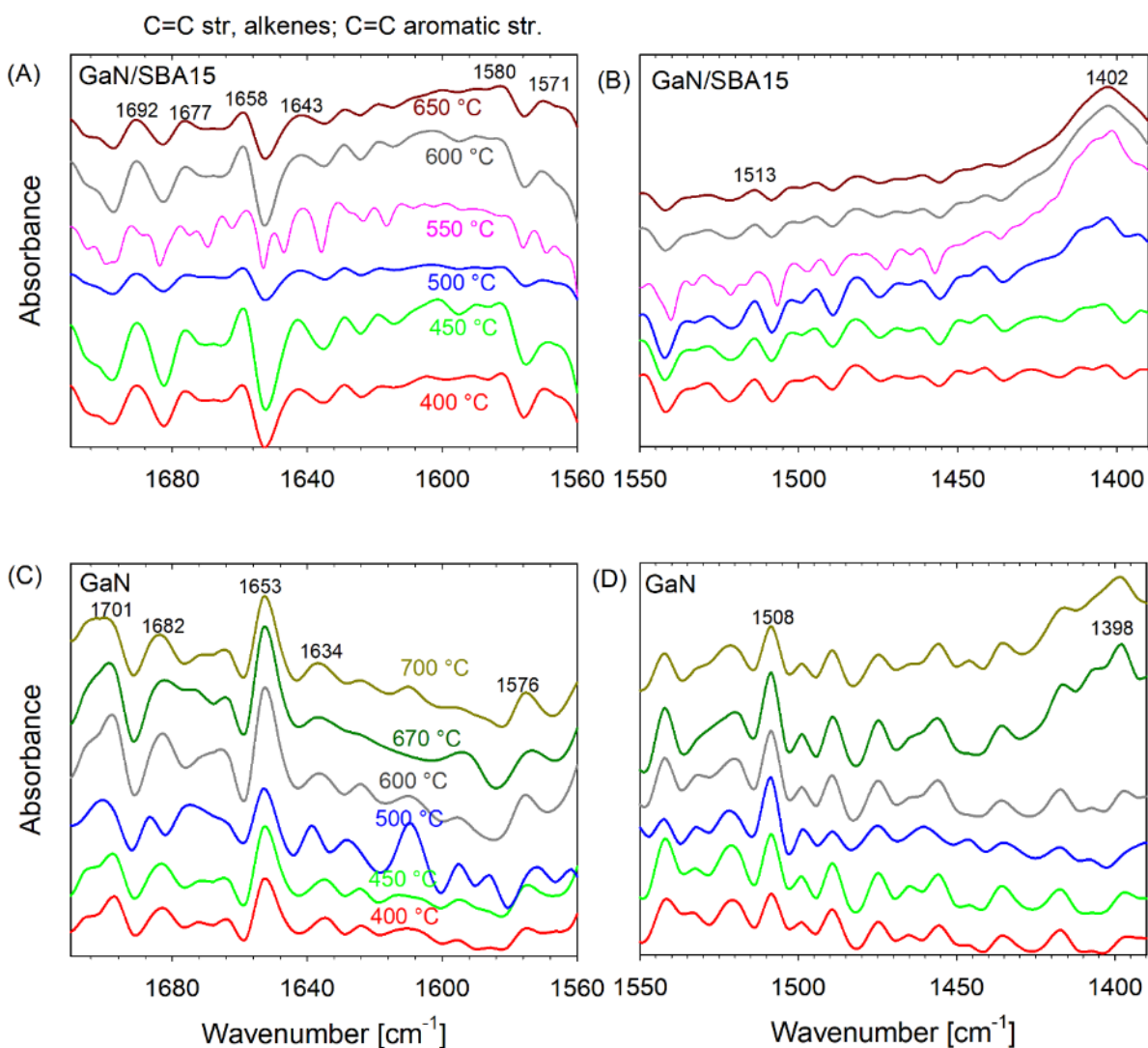


Fig. 6-29 Evolution of surface adsorbed species as a function of temperature on supported GaN/SBA15 (A) between 1600–1400 cm^{-1} and (B) between 1600–1400 cm^{-1} ; for unsupported GaN (C) between 1600–1400 cm^{-1} and (D) between 1600–1400 cm^{-1} . The spectra were collected during Ar purge (15 $\text{mL}_N \text{ min}^{-1}$) after 30 min CH_4 activation (80% CH_4 in Ar with 2.0 $\text{mL}_N \text{ min}^{-1}$ CH_4). All spectra are corrected for the background spectrum under Ar at 400 °C. The species assignment is based on Socrates [88].

6.3.3.5 CD_4 and CH_4 on GaN/SBA15

DRIFTS measurements were carried out on GaN/SBA15 at 700 °C with CH_4 and CD_4 . First, CH_4 was passed over the catalyst for 1 h, then purged with Ar. The spectrum was recorded. This was followed by feeding CD_4 for 1 h, and the spectrum was collected after Ar purge. The second spectrum had peaks contributed by the adsorbed species formed by both CH_4 and CD_4 . Fig. 6-30 illustrates the

two spectra. The spectra with CH₄ was the usual one, as discussed in section 6.3.3.4. With CD₄, some new peaks appeared. The peak at 2750 cm⁻¹ corresponds to O–D formed by the exchange between SBA–15’s silanol group’s (Si–OH) with D of CD₄ [101]. This interaction, however, depends on the acidic nature of the OH group, where silanol has the lowest interaction [101]. However, SBA–15 practically does not have any Brønsted acid sites (<0.1 μmol g⁻¹ [48]). The three new peaks between 2650–2400 cm⁻¹ are due to N–D [102] formed by alkyl adsorption of D₃C^{δ-}D^{δ+} on Ga³⁺N³⁻. The new shoulder appearing between 2300–2200 cm⁻¹ corresponds to ν_s and ν_{as} (CD₃) [103,104]. Absorbances for the other alkyl intermediates like CH₃D, CH₂D₂, CHD₃ overlaps with that of CH₄ above 2900 cm⁻¹ [104], they might have been masked by already adsorbed CH₄ on the catalyst.

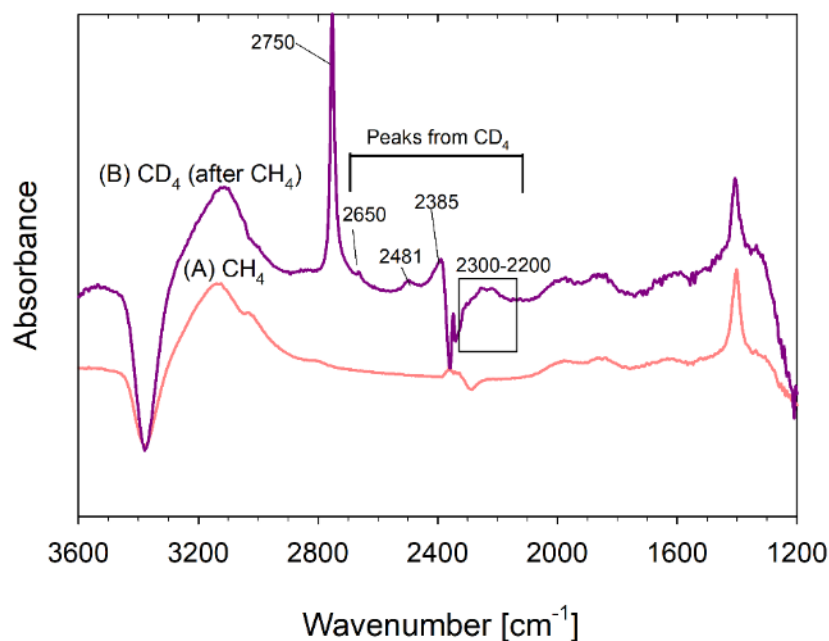


Fig. 6–30 DRIFT spectra for supported GaN/SBA15 collected under Ar purge (0.5 h at 15 mL_N min⁻¹) (A) after 1 h exposure to CH₄ (80% in Ar), (B) preceded by CH₄ adsorption, followed by Ar purge and CD₄ adsorption (80% in Ar), at 700 °C.

To observe the peaks that are contributed only by CD₄, the spectra in Fig. 6–30B was used as background (all the peaks were removed). Then CD₄ was passed over the catalyst for another hour, then purged with Ar to remove CD₄. A spectrum was collected under Ar purge illustrated in Fig. 6–31, which shows new peaks corresponding adsorbed species from CD₄. The approximate assignment to these peaks was made based on the work by Chapados et al. [104]. It is approximate because [104] reports spectra for solid (–267 to –190 °C) CH₄, CD₄, CDH₃, CH₂D₂. The shift in wavenumber from the gas phase to the solid phase was within 20 cm⁻¹. The peaks from 3058–3000 cm⁻¹ could be assigned

to vibrational frequencies of CH_4 ; note that the CH_x may still be present on the surface from the previous CH_4 exposure. The band $2258\text{--}2237\text{ cm}^{-1}$ to CD_4 (C–D stretching [105]), 2115 cm^{-1} could be assigned to CHD_3 , 2988 , 2915 , and 2135 cm^{-1} could be assigned to CHD_3 and CH_2D_2 , 3089 cm^{-1} to CDH_3 [104]. The peak at 3089 cm^{-1} could be due to the C–D bond in $\text{C}_6\text{H}_5\text{D}$ or C_6H_6 [106].

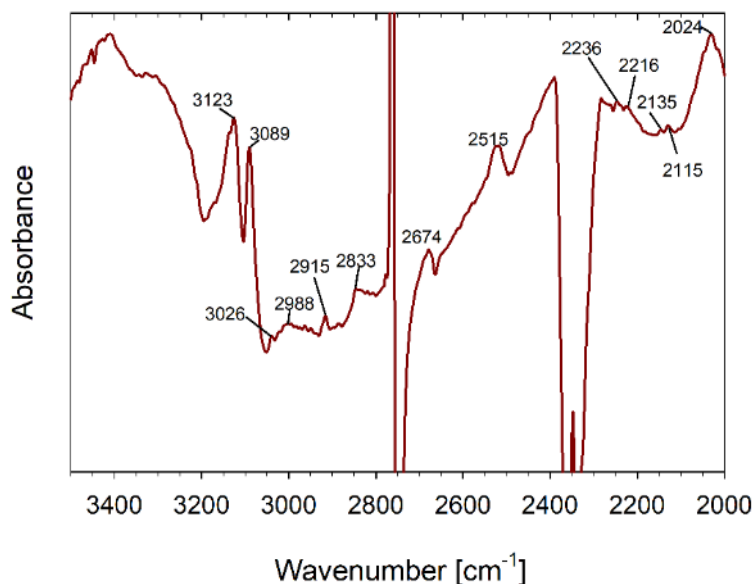


Fig. 6–31 DRIFT spectra for supported GaN/SBA15 collected under Ar purge (0.5 h at $15\text{ mL}_N\text{ min}^{-1}$) after 1 h exposure to CD_4 (80% in Ar) at $700\text{ }^\circ\text{C}$.

6.4 Kinetic study

As stated in chapter 5, the supported GaN/SBA15 is the catalyst of interest, due to higher ethylene yield and lower coke formation. CH_4 activation consists of several steps; (1) diffusion of CH_4 from the bulk gas phase to the GaN surface inside the pores, (2) chemisorption of CH_4 on GaN as $\text{H-N}\cdot\text{Ga-CH}_3$, (3) the formation of Ga-CH_2 from Ga-CH_3 (rate-determining), (4) the formation of C_2H_4 from the two adjacent Ga-CH_2 species, (5) desorption of C_2H_4 , and (6) diffusion of C_2H_4 into the bulk. The detailed elementary steps for C_2H_4 formation on GaN have been reported in chapter 6.2.2 and published by Chaudhary et al. [46]. Overall, ethylene selectivity was $>60\%$, and the CH_4 conversion can be calculated either in terms of C_2H_4 (equation 3–4) or the coke (selectivity $< 40\%$). In general, the reaction rate could be expressed as simple Power-law expressions or as a more complex Langmuir-Hinshelwood (LH) rate expressions. The former only consist of a kinetic term (k_p) and driving force (p_{CH_4}), while the later LH rates include an adsorption term taking into account the possible adsorbed surface species. The power law can be expressed as:

$$r_{obs} = k_r \cdot p_{CH_4}^n \quad 6-25$$

$$r = \frac{k_r \cdot (K_x \cdot p_{CH_4})^\alpha}{[1 + (K_x \cdot p_{CH_4})^\beta]^\gamma} \quad 6-26$$

With $k_r = k_0 \cdot \exp\left\{\frac{-E_A}{\mathcal{R} \cdot T}\right\}$ and $K_x = K_0 \cdot \exp\left\{\frac{-\Delta H}{\mathcal{R} \cdot T}\right\}$, where E_A is the apparent activation energy in kJ mol^{-1} , ΔH is the heat of adsorption in kJ mol^{-1} , T is the temperature of the reaction in K, p is the partial pressure of methane in bar, n is the apparent order of the reaction, k_0 and K_0 are the pre-exponential factors, and \mathcal{R} is the universal gas constant, $8.314 \text{ J K}^{-1} \text{ mol}^{-1}$. α , β , and γ are the exponents, which are varied to observe the fit between the experimental and predicted rates. The rates could be associated with either C_2H_4 ($rate_{\text{C}_2\text{H}_4}$) or coke ($rate_c$) formation in $\text{mol min}^{-1} \text{ g}_{\text{cat}}^{-1}$.

6.4.1 Approach to equilibrium

As the overall reaction is thermodynamically limited (i.e., at $700 \text{ }^\circ\text{C}$, the maximum methane conversion is 4.1 %), the forward rate should be determined based on the approach to equilibrium η . This value indicates how far away or how close the observed rate was from the chemical equilibrium [107]. The forward rate and approach to equilibrium are defined by equations 6-27 and 6-28.

$$r = \frac{r_{obs}}{1-\eta} \quad 6-27$$

$$\eta = \frac{p_{\text{C}_2\text{H}_4}^{1/3} \cdot p_{\text{H}_2}^{4/3}}{p_{\text{CH}_4}} \cdot \frac{1}{K_{eq}} \quad 6-28$$

A value of $\eta = 1$ indicates chemical equilibrium, whereas a value of η close to zero shows that the observed reaction (i.e., measured conversion) was far away from the equilibrium, which is preferred for the estimation of kinetic parameters. The equilibrium constant K_{eq} refers to the chemical reaction expressed in equation 6-28, in which the stoichiometric coefficients of 1/3 for C_2H_4 and C were based on the experimentally determined selectivities of 67% and 33% (Table 5-4), respectively.



In the current case, the approach to equilibrium values were always smaller than $\eta < 0.04$ (maximum η with 0.1 bar CH_4 and 0.9 bar Ar, at $700 \text{ }^\circ\text{C}$), indicating that for all experiments, the calculated methane conversions and ethylene formation rates were far away from the chemical equilibrium. Thus, it can be assumed that the observed rate is equal to the forward rate.

6.4.2 Influence of the pore diffusion

The observed rates reported throughout this thesis could be influenced by pore diffusion. To determine kinetic parameters, the intrinsic rates should be measured with the absence of any mass transfer limitation. For that purpose, the Thiele modulus is usually calculated, which describes the ratio of the intrinsic reaction rate to the rate of diffusive mass transfer through the particle, in the absence of mass transfer limitation. For a spherical catalyst particle and a first-order irreversible reaction, the Thiele modulus is defined as:

$$\Phi_i = l_{CH} \sqrt{\frac{k_0}{D_{eff,i}}} \quad 6-30$$

where l_{CH} is the characteristic length (radius, height), $D_{eff,i}$ is the effective diffusion coefficient in $\text{m}^2 \text{s}^{-1}$, and k_0 is the intrinsic rate constant. In most cases, the intrinsic rate constant is unknown, and the reaction mechanism is rather complex. Therefore, the approach proposed by Weisz uses the observed rate of reaction, which includes the effectiveness factor η_{eff} [108].

$$\Psi = \eta_{eff} \cdot \Phi^2 \quad 6-31$$

$$\Psi_i = \frac{l_{CH}^2 \cdot R_{i,observed}}{D_{eff,i} \cdot c_{s,i}} \quad 6-32$$

where $R_{i,observed}$ ($\text{mol m}^{-3} \text{cat s}^{-1}$) is the observed reaction rate of species i . Pore diffusion limitation can be neglected if $\Psi_i < 0.15$ [108]. The effective diffusion coefficient $D_{eff,i}$ is estimated by:

$$D_{eff,i} = \frac{\varepsilon}{\tau} \left(\frac{1}{D_{i,mix}} + \frac{1}{D_{K,i}} \right)^{-1} \quad [\text{m}^2 \text{s}^{-1}] \quad 6-33$$

where the Knudsen diffusion coefficient $D_{K,i}$ ($\text{m}^2 \text{s}^{-1}$) is given by [109]:

$$D_{K,i} = 97 \cdot \frac{d_{pore}}{2} \cdot \sqrt{\frac{T_{cat}}{M_i}} \quad [\text{m}^2 \text{s}^{-1}] \quad 6-34$$

In eq. 6-34, the pore diameter d_{pore} is defined in m, and the molar weight M_i is defined in g mol^{-1} . The values for the porosity and the tortuosity were calculated as $\varepsilon = 0.92$ and $\tau = 1.26$, respectively, for GaN/SBA15. Rottreau et al. [110] reported $\tau = 1.26$ for heptane and cyclohexane within the pores of SBA-15 with a pore diameter of 6.3 nm. Liu et al. [111] reported a bed porosity (ε) of 0.882 for SBA-15 with $S_{BET} = 876 \text{ m}^2 \text{ g}^{-1}$ and $d_{pore} = 7 \text{ nm}$. Using these equations, the effective diffusion coefficient and Weisz moduli for each gas species were calculated. The characteristic length is defined

as the ratio of volume to surface. The particle size was between 90–120 μm (d_p). A sphericity (φ_p) of 0.72 was used, based on [112] for modified SBA-15. The characteristic length l_{ch} was calculated as:

$$l_{ch} = \frac{d_p}{6} \cdot \varphi_p \quad 6-35$$

Fig. 6-32 illustrates Weisz moduli calculated for CH_4 (diffusion from bulk to catalyst) and C_2H_4 (diffusion from catalyst to bulk) at different reaction temperatures (0.8 bar CH_4 , Fig. 6-32A) and CH_4 feed partial pressures (at 700 $^\circ\text{C}$, Fig. 6-32B). Since determined Weisz moduli were always much smaller than 0.15 (of the order of 10^{-5}), the pore diffusion limitation can be neglected.

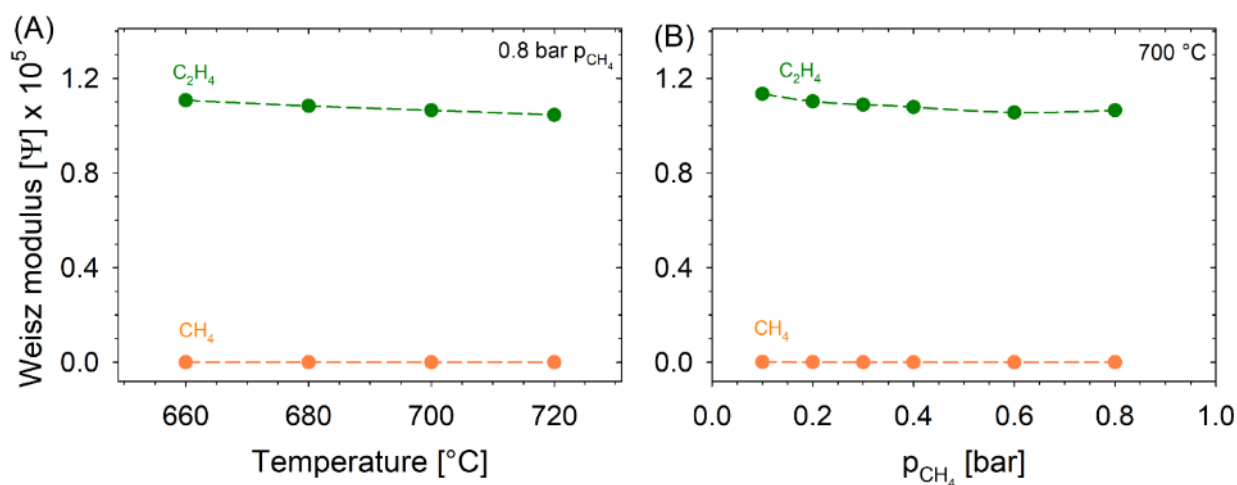


Fig. 6-32 Weisz moduli for C_2H_4 and CH_4 as a function of (A) catalyst temperatures (0.8 bar p_{CH_4}) and (B) p_{CH_4} (700 $^\circ\text{C}$).

6.4.3 Apparent activation energy

Fig. 6-33 illustrates the Arrhenius plot based on the C_2H_4 formation rates as a function of reaction temperature for 2 different CH_4 partial pressures. For 0.8 bar CH_4 , the apparent activation energy of $E_A = 25.5 \pm 5.0 \text{ kJ mol}^{-1}$ was estimated, whereas for 0.2 bar CH_4 a slightly higher value of $E_A = 28.7 \pm 5.0 \text{ kJ mol}^{-1}$ was estimated. These values are 15 times smaller than predicted by DFT (Table 6-1). Similar observed activation energies ($25\text{--}37 \text{ kJ mol}^{-1}$) were reported in the literature for the CH_4 activation over silica-supported Ru catalysts and NiO/Ni(100) systems [113,114].

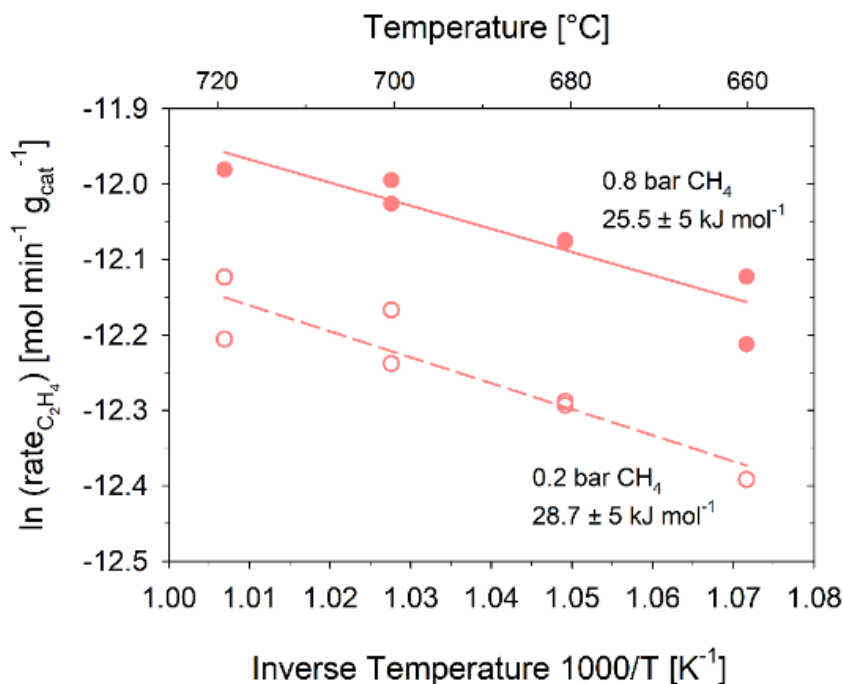


Fig. 6–33 Arrhenius plot based on methane partial pressure in the feed gas for CH₄ activation to C₂H₄ on the supported GaN/SBA15 catalyst. This does not include carbon deposited on the catalyst.

For the rate of coke formation, an apparent activation energy of $402 \pm 47 \text{ kJ mol}^{-1}$ was estimated (Fig. 6–34A), which is within the range of reported values for the thermal decomposition of methane, $347\text{--}430 \text{ kJ mol}^{-1}$ [115]. The apparent activation energy for the C₂H₄ formation rate was 15 times lower, indicating that the overall methane conversion rate (Fig. 6–34B) is governed by the C₂H₄ formation, which is typically observed for parallel reactions. Fig. 6–34C illustrates that the selectivity of coke increases with the increase in temperature. As expected, at higher temperatures, the reaction with the higher activation energy starts gaining prominence.

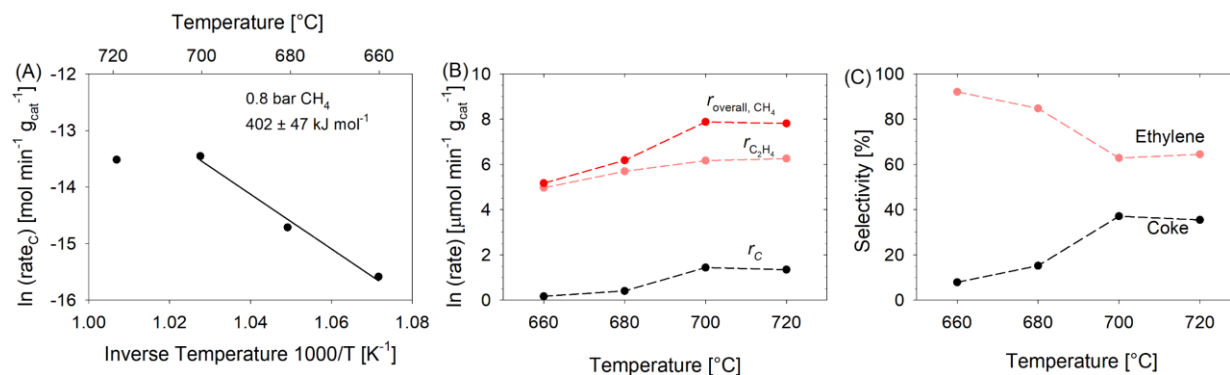


Fig. 6–34 (A) Arrhenius plot based on the rate of methane conversion to coke (B) Overall rate, and rates of methane conversion based on C_2H_4 and C as a function of temperature, and (C) Selectivity of C_2H_4 and Coke as a function of temperature. Experiments were carried out at 1 bar using 80% CH_4 feed (in Ar). The dashed lines are for guidance only.

6.4.4 Apparent reaction order

Fig. 6–35 illustrates the rate and conversion as the function of methane partial pressure (0.1 to 0.8 bar) at 700 °C and 1 bar total pressure. The conversion decreases with the partial pressure, which was also predicted by thermodynamic calculations (Fig. 6–35A). Even though the minor components (C_3H_6 and C_6H_6) were 100–1000 lower than C_2H_4 , their yields also had the same trend (Fig. 6–35A, using equation 3–4). Interestingly, when the minimization of free energy calculations included C_6H_6 , and it predicted C_6H_6 as the main product (not shown). The equilibrium CH_4 conversion to C_6H_6 was still decreasing with the CH_4 partial pressure (not shown).

The apparent order of the reaction was estimated to be close to zero-order ($-0.1 < n \leq 0.05$), as depicted in Fig. 6–35B). The fast dissociative chemisorption of methane leads to faster occupancy of the active sites. The amount of unoccupied active sites is inversely proportional to the methane partial pressure, which means a higher rate at lower partial pressures. To set the context, it was assumed that all 16 wt% Ga (equivalent to 18.6 wt% GaN) are active and accessible to CH_4 . The number of unoccupied (free) active sites (in 100 mg GaN/SBA15), in the first minute of CH_4 flow, is around 10 times at 0.1 bar CH_4 partial pressure ($0.5 \text{ mL}_N \text{ min}^{-1} \text{ CH}_4$ and $4.5 \text{ mL}_N \text{ min}^{-1} \text{ Ar}$). Higher surface coverage of Ga– CH_2 results in a competition for the formation of new Ga– CH_2 (preceded by the formation of Ga– CH_3). It is also possible that a lower surface coverage of adsorbed Ga– CH_3 lowers the carbon deposition by preventing long-chain, cyclic, aromatic C–C coupling. This was also reported by Guo et al. [9], where single site separated Fe atoms prevented C–C coupling from forming coke. At higher p_{CH_4} , the rate is dependent on the availability of unoccupied active sites, which apparently have been saturated with

adsorbed species (Ga-CH₃ and Ga-CH₂). The X_{CH_4} is 10% of X_{eqm, CH_4} at 0.8 bar p_{CH_4} , while it is ~50% of X_{eqm} at 0.1 bar, Fig. 6-35A).

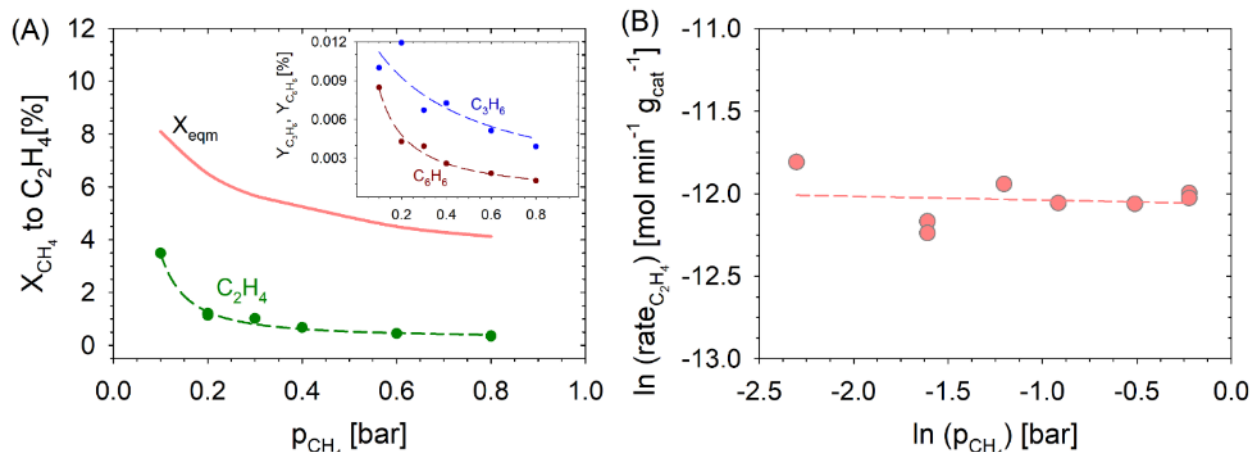


Fig. 6-35 (A) CH₄ conversion based on C₂H₄, and yields of C₃H₆, and C₆H₆ and (B) Reaction rate based on C₂H₄ formation as a function of CH₄ partial pressure for methane activation over GaN/SBA15 at 700 °C and 1 bar. The solid line is the equilibrium X_{CH_4} to C₂H₄ (X_{eqm}), and the dotted lines are for guidance only. The CH₄ conversion to hydrocarbon has been calculated using equation 3-4.

6.4.5 Effect of space velocity

The contact time could be changed either by flow rate (for catalyst mass) or the catalyst mass (for a fixed flow rate). Fig. 6-36 illustrates the effect of contact time modified by total flow rate (including Ar flow rate, equation 6-37), and by catalyst mass (equation 6-38 or 6-39). The contact time was calculated using equation 6-36.

$$\text{Contact time} = \frac{1}{GHSV} \quad 6-36$$

$$GHSV = \frac{V_{cat}}{\dot{V}_{CH_4, in} + \dot{V}_{Ar, in}} \quad 6-37$$

$$V_{cat} = \frac{m_{cat}}{\rho_{Bulk}} \quad 6-38$$

$$\rho_{Bulk} = \frac{m_{cat}}{\pi \cdot \frac{ID^2}{4} \cdot h_{Bed}} \quad 6-39$$

Where m_{cat} is the mass of catalyst used in g, h_{Bed} is the height of the catalyst bed in cm, ID is the quartz reactor inner diameter in cm, ρ_{Bulk} is the bulk density of the catalyst in 0.17 g mL⁻¹, V_{cat} is the volume of the catalyst bed in mL, $\dot{V}_{CH_4, in}$ is the normal inlet volumetric flow rate of CH₄ in

$\text{mL}_N \text{ min}^{-1}$, and $\dot{V}_{Ar,in}$ is the normal inlet volumetric flow rate of Ar in $\text{mL}_N \text{ min}^{-1}$. Here, the GHSV is based on the total inlet gas flow rate at normal conditions (1.013 bar and 0 °C), and not based on the CH_4 flow rate only (as used in Chapters 4, 5, and 7).

Both ethylene formation rate ($\text{rate}_{C_2H_4}$) and methane conversion (X_{CH_4} , based on ethylene) increased with the increasing contact time. The conversion (X_{CH_4}) became constant, and the rate ($\text{rate}_{C_2H_4}$) reached a maximum and then decreased. Similar behavior was reported by Xiao et al. [17] for CH_4 conversion on PtSn catalysts at 650 °C and 0.1 atm CH_4 partial pressure. The yields minor components (C_3H_6 and C_6H_6) increased with contact time. This was expected (higher residence time increases C–C coupling to higher hydrocarbons), and also observed by Dutta et al. (effect of mass, refer to Chapter 4 [54]), and Xiao et al. [17].

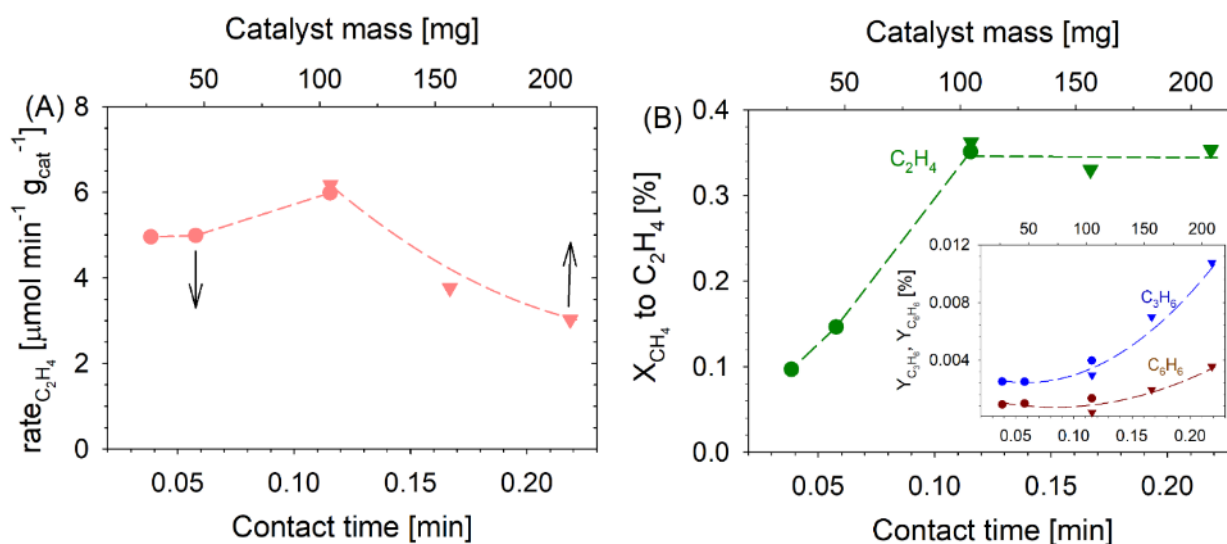


Fig. 6–36 (A) Reaction rate based on C_2H_4 formation and (B) CH_4 conversion based on C_2H_4 , and yields of C_3H_6 , and C_6H_6 as a function of contact time and catalyst mass for methane activation over GaN/SBA15 at 700 °C and 1 bar. The dashed lines are for guidance only. The circles (●) are the data obtained by changing the total gas flow rate (for a fixed catalyst mass of 100 mg GaN/SBA15), and the triangles (▼) are the data obtained by changing catalyst mass (for a fixed total gas flow rate of $5 \text{ mL}_N \text{ min}^{-1}$).

6.4.6 Kinetic modeling

The results of the above experiments (18 events) were used for kinetic parameter estimation and model discrimination. Table 6–4 lists the 18 events of CH_4 activation over GaN/SBA15.

Table 6-4 Event details for kinetic modeling for CH₄ activation over GaN/SBA15.

Event number	Methane partial pressure p_{CH_4} [bar]	Temperature T [°C]
1	0.20	700.0
2*	0.20	700.0
3	0.40	700.0
4	0.60	700.0
5	0.80	700.0
6*	0.80	700.0
7	0.80	660.0
8	0.80	680.0
9*	0.80	700.0
10	0.80	720.0
11*	0.80	660.0
12*	0.80	680.0
13*	0.80	700.0
14	0.20	660.0
15	0.20	680.0
16*	0.20	680.0
17*	0.20	700.0
18	0.20	720.0

* repeat runs

Two Power Law models (#1 and #2) and five Langmuir-Hinshelwood (LH) models (#3-7) were evaluated. The general form for the LH model can be expressed by equation 6-26.

$$r_{C_2H_4} = \frac{k_r(K_x p_{CH_4})^\alpha}{[1+(K_x p_{CH_4})^\beta]^\gamma} \quad 6-26$$

Refer to appendix A5-2 for the derivation of the above expression with all the assumptions. Using generic power law and based on the values of α , β , and γ , the following seven models have been proposed:

Model 1

Zero-order: the order was close to zero (section 6.4.4, from $\ln r_{C_2H_4}$ vs. $\ln p_{CH_4}$ plot, Fig. 6-35B)

$$r_{obs} = k_r \quad 6-40$$

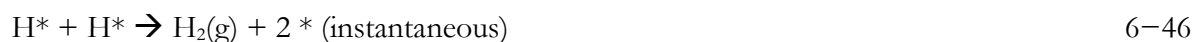
Model 2

Generic power law was also assumed to estimate the reaction order α .

$$r_{obs} = k_r \cdot p_{CH_4}^{\alpha} \quad 6-41$$

Model 3

Based on our DFT results, the elementary steps are proposed:

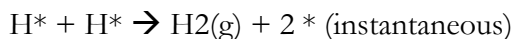


$\alpha = \beta = \frac{1}{2}$ and $\gamma = 2$ (Refer to appendix A5-2 for the derivation)

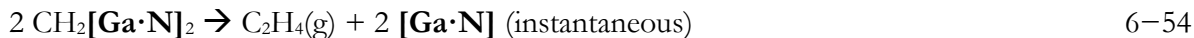
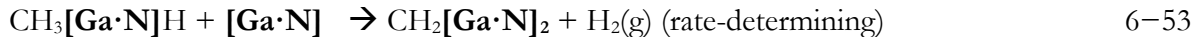
$$r_{obs} = \frac{k_r \cdot \sqrt{K_x \cdot p_{CH_4}}}{(1 + \sqrt{K_x \cdot p_{CH_4}})^2} \quad 6-47$$

Model 4

Two sets of elementary steps may be considered for this model.



Instead of assuming a generic $*$ as the active site, $[Ga \cdot N]$ can also be used as one active site containing two different entities Ga^{3+} and N^{3-} . If the DFT mechanism I (refer to Fig. 6-5) was used as the basis:



$\alpha = \beta = 1$ and $\gamma = 2$ (Refer to appendix A5-2 for the derivation)

$$r_{obs} = \frac{k_r \cdot K_x \cdot p_{\text{CH}_4}}{(1 + K_x \cdot p_{\text{CH}_4})^2} \quad 6-55$$

Model 5

Again, as above, $[\text{Ga}\cdot\text{N}]$ was used as one active site containing. If the DFT mechanism III (refer to Fig. 6-5) was used as the basis:



$\alpha = \beta = \gamma = 1$ (Refer to appendix A5-2 for the derivation)

$$r_{obs} = \frac{k_r \cdot K_x \cdot p_{\text{CH}_4}}{1 + K_x \cdot p_{\text{CH}_4}} \quad 6-59$$

Model 6

The following elementary steps were assumed:



$\alpha = \gamma = 2$ and $\beta = 1$ (Refer to appendix A5-2 for the derivation)

$$r_{obs} = \frac{k_r \cdot (K_x \cdot p_{\text{CH}_4})^2}{(1 + K_x \cdot p_{\text{CH}_4})^2} \quad 6-63$$

Model 7

$\alpha = \frac{1}{2}$, $\beta = 2$, and k_r and K_x have been lumped as k_r' in the numerator. Lumping parameters are common in LH kinetic modeling [116–119]. In general, it has been observed that the lumped parameters led to high correlation coefficients between parameters [120].

$$r_{obs} = \frac{k_r' \cdot \sqrt{p_{CH_4}}}{(1 + \sqrt{K_x p_{CH_4}})^2} \quad 6-64$$

The kinetic parameter estimation and model discrimination was done using the software package Athena Visual Studio v14.2. The results of the model discrimination for the GaN/SBA15 catalyst are summarized in Table 6–5. Refer to the methodology chapter (section 3.5) for definitions of the parameters in Table 6–5. The table also shows the optimal estimated values with the highest posterior density (HDP) interval and the normalized covariance matrix. Based on the posterior probability share (17%, Table 6–5), the models 2, 3, 5, 6 and 7 were statistically similar and gave the best fit to the experimental data over the temperature range from 660 to 720 °C, and methane partial pressure (p_{CH_4}) range from 0.2 to 0.8 bar. Model 3 has the best rank (17.8 % posterior probability share, Table 6–5), and model 1 has the worst (2.5% posterior probability share, Table 6–5). The best fit could also be ascertained from the objective function, which is the sum of squares of the residuals (SSR, Table 6–5). Model 3 has the lowest objective function (3.16×10^{-13} , Table 6–5). The K_x value in equation 6–47 is the same as that calculated from the lumped parameter k_r' (equation 6–64). The HPD interval defines the region in which 95% of the potential values of the parameters are found [52]. The covariance matrix in multi-parameter estimation is an important criterion to evaluate the quality of the parameters and the model. The elements in the normalized covariance matrix E_{ij} are within, where a value of +1 (–1) indicates a strong correlation (anti-correlation) between parameter i and j . A correlation coefficient of +1 means a perfect direct (increasing) linear correlation, and a coefficient of –1 is inverse (decreasing) linear anticorrelation. For the models mentioned above (2, 3, 5, and 6), K_x and k_r have strong anti-correlation with a greater degree of linear dependence (the correlation coefficients are close to –1, –0.8 to –0.9). For model 7, the correlation is positive (close to 1) because K_x is lumped inside k_r' . This is expected because a strong adsorption means a slower rate of reaction. The reaction involves the interaction of two adsorbed species (adjacent), followed by the formation of adsorbed products and desorption of the product. The effect of strong adsorption has been observed in the isotope

labeling experiments (refer to section 6.3.1), where strong adsorption of CD_x species might have led to non-formation of lower hydrocarbon products like C_2D_4 .

Table 6–5 Kinetic parameters and HPD interval estimated for all the models (first column). $T_{ref} = 700$ °C.

#	Objective function (SSR)	Posterior probability share [%]	Parameters	95% HPD interval	Normalized covariance matrix			
1	4.55×10^{-12}	2.5	$k_r(T_{ref})^*$	$5.64 \pm 2.95 \times 10^{-6}$	1			
			E_A , kJ mol ⁻¹	27.61 ± 21.55	0.364	1		
2	4.55×10^{-13}	17.4	$k_r(T_{ref})$	$6.29 \pm 0.16 \times 10^{-6}$	1			
			E_A , kJ mol ⁻¹	29.24 ± 7.03	0.291	1		
			α	0.14 ± 0.02	0.734	0.057	1	
3	3.16×10^{-13}	17.8	$k_r(T_{ref})$	$2.44 \pm 0.06 \times 10^{-5}$	1			
			E_A , kJ mol ⁻¹	18.96 ± 11.93	0.158	1		
			$K_x(T_{ref})$, bar ⁻¹	0.87 ± 0.18	-0.807	-0.141	1	
			ΔH , kJ mol ⁻¹	87.39 ± 84.47	-0.169	-0.851	0.301	1
4	5.99×10^{-13}	9.4	$k_r(T_{ref})$	$2.51 \pm 0.05 \times 10^{-5}$	1			
			E_A , kJ mol ⁻¹	26.8 ± 8.45	0.372	1		
			$K_x(T_{ref})$, bar ⁻¹	1.91 ± 0.13	-0.114	-0.045	1	
			ΔH , kJ mol ⁻¹	16.77 ± 28.36	-0.044	-0.063	0.351	1
5	3.20×10^{-13}	17.6	$k_r(T_{ref})$	$6.48 \pm 0.19 \times 10^{-6}$	1			
			E_A , kJ mol ⁻¹	19.15 ± 11.97	0.375	1		
			$K_x(T_{ref})$, bar ⁻¹	18.24 ± 4.11	-0.864	-0.363	1	
			ΔH , kJ mol ⁻¹	77.52 ± 80.90	-0.410	-0.854	0.516	1
6	3.20×10^{-13}	17.6	$k_r(T_{ref})$	$6.45 \pm 0.18 \times 10^{-6}$	1			
			E_A , kJ mol ⁻¹	20.05 ± 11.23	0.391	1		
			$K_x(T_{ref})$, bar ⁻¹	39.46 ± 8.22	-0.849	-0.370	1	
			ΔH , kJ mol ⁻¹	69.47 ± 73.79	-0.417	-0.833	0.531	1
7	3.16×10^{-13}	17.8	$k_r(T_{ref})$	$2.29 \pm 0.19 \times 10^{-5}$	1			
			E_A , kJ mol ⁻¹	62.44 ± 32.77	0.366	1		
			$K_x(T_{ref})$, bar ⁻¹	0.87 ± 0.18	0.983	0.338	1	
			ΔH , kJ mol ⁻¹	86.83 ± 84.85	0.320	0.982	0.303	1

* unit of k_r depends on the rate expression

The pre-exponential factors are based on the reference temperature ($T_{ref} = 973.15 \text{ K} = 700 \text{ }^\circ\text{C}$). The best fit model (#3) considers the formation of CH_2^* from CH_3^* as the slowest step. This reaffirms that the formation of CH_2^* is the rate-determining step as predicted by DFT. The intrinsic activation energy (Table 6–5) is closer to the apparent activation energy (Fig. 6–33). Wen et al. [121], using DFT modeling, reported activation energies for $\text{CH}_3^* \rightarrow \text{CH}_2^* + \text{H}^*$ over $\text{Pt}_3/\text{Ce}_{1-x}\text{Pt}_x\text{O}_{2-\delta}(111)$ (97 kJ mol^{-1}), $\text{Pt}_1/\text{Ce}_{1-x}\text{Pt}_x\text{O}_{2-\delta}(111)$ (35 kJ mol^{-1}), and $\text{Pt}_{10}/\text{Ce}_{1-x}\text{Pt}_x\text{O}_{2-\delta}(111)$ (68 kJ mol^{-1}). These activation energies have the same order of magnitude as determined for CH_4 activation over GaN/SBA15 by kinetic modeling. The HPD interval was rather broad due to the small data size. The measured concentrations are in good agreement with the predicted data for models except model 1, for all the kinetic data points. Fig. 6–37 illustrates the results for the best fit model 3.

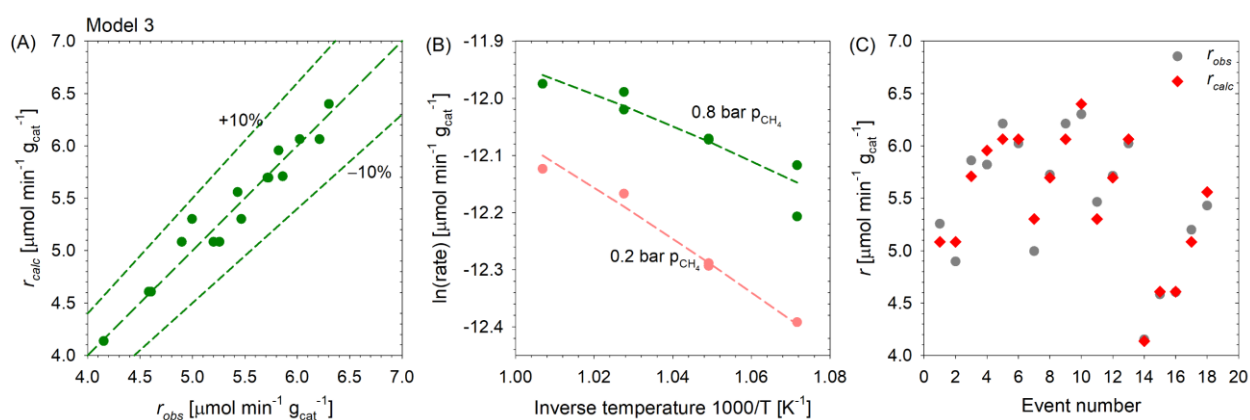


Fig. 6–37 (A) Parity plot for the rate of reaction based on C_2H_4 formation, (B) Arrhenius plot, and (C) Comparison between the observed (r_{obs}) and the calculated (r_{calc}) rates of C_2H_4 formation for all events for the best fit model 3.

The results for the other models are depicted in Fig. A5–1, and Fig. A5–2. The parity plot (Fig. 6–37A) depicts that all the rates are within the $\varepsilon = 10\%$ region except for model 1. The Arrhenius plots are also in good agreement between the experimental and predicted values (Fig. 6–37B). For all events (660 to 720 $^\circ\text{C}$ and 0.2 to 0.8 bar p_{CH_4}), the observed rates are in good agreement with the rates calculated by the model (Fig. 6–37C).

6.5 Conclusions

A theoretical study using DFT showed that gallium nitride is produced through the oxynitride intermediate during nitridation. The two main rate-limiting steps were NH_2^* dissociation to NH^* and the desorption of the last H_2O^* . The experimental verification of the mechanism has not been done

yet. The DFT study also concludes that methane activation on GaN begins with fast dissociative adsorption of methane on GaN to form $\text{H}_3\text{C}-\text{Ga}\cdot\text{N}-\text{H}$. The rate determining step was the formation of CH_2^* from CH_3^* followed by the formation of C_2H_4 by dimerization of CH_2^* . The presence of surface intermediates proposed by the DFT ($\text{Ga}-\text{CH}_3$, CH_2), aromatic species, vinylidene ($\text{H}_2\text{C}=\text{CH}-$) species has been observed by the DRIFTS experiment. Surface intermediates start forming between 400–450 °C. ^{13}C SSNMR reaffirms the presence of $\text{Ga}-\text{CH}_3$ species. The NMR study also confirms that supported GaN/SBA15 has higher aliphatic surface intermediates ($\text{Ga}-\text{CH}_3$) and hence higher C_2H_4 than unsupported (higher aromatics intermediates and coke). The isotope labeling experiments established the kinetic isotope effect (KIE) on both supported and unsupported GaN catalysts. Either there was a delay (over and above residence time) in the formation of mixed isotope products (formed by $^{13}\text{CH}_4$ and CD_4) or facilitated desorption (by CH_4) was required. However, the formation of H_2 isotopes was delayed only by residence time. This confirms that $\text{H}-\text{CH}_3$ bond cleavage was not rate-determining, but C_2H_4 formation was, as proposed by DFT. Parametric study on GaN/SBA15 at different activation temperatures showed that the apparent activation energy for coke formation is around 15 times the activation energy for C_2H_4 formation. Thus, the formation rate of C_2H_4 governs the overall rate of methane activation. The apparent order of the reaction is practically zero for CH_4 partial pressure, which indicates that active sites are always covered with adsorbed species (faster coverage), and it is the formation of C_2H_4 that decides the rate. The C_2H_4 formation has three elementary steps as per DFT; the formation of CH_2^* from CH_3^* , dimerization of CH_2^* , and desorption of C_2H_4 . While isotope labeling and parametric studies confirmed the formation of C_2H_4 as rate-determining, but none of the experimental methods tells which of the three steps is rate-determining. The results of 18 experimental runs were used for kinetic modeling and parameter determination. Power law and generalized Langmuir-Hinshelwood rate expression were used for the kinetic parameter estimation. The pore-diffusion limitation on the reaction rate was negligible, as concluded from a very low Weisz modulus ($\Psi \ll 0.15$). The intrinsic activation energy predicted from the best fit model was 19 kJ mol^{-1} . This intrinsic activation energy is close to the apparent activation energy ($25-28 \text{ kJ mol}^{-1}$), determined by fitting the Arrhenius equation on the experimental data. The order predicted by model 2 was 0.14 (close to zero). The most probable kinetic models considered the formation of CH_2^* from CH_3^* as the RDS. The same elementary step was also projected as the RDS by the DFT study. The models predicted the observed rates in excellent agreement with the experimental data.

Chapter 7

7 Catalyst regeneration

As discussed in chapters 4 and 5, coking and hence, catalyst deactivation is one of the obstacles for direct methane activation. In this work, the regeneration capability and reusability of gallium nitride (GaN) catalysts for the direct non-oxidative methane activation with subsequent coupling to ethylene were studied. Unsupported GaN as well as silica-supported GaN/SBA15 catalysts were synthesized and evaluated. Each catalyst was subjected to two different regeneration methods. In the first method, the spent catalysts were regenerated with air at 500–550 °C and reused several times. Due to the slight oxidation of the surface GaN to Ga₂O₃, the ethylene yield decreased by 16% after 5 cycles. The second method included an intermediate re-nitridation step after air regeneration to convert the surface Ga₂O₃ back to GaN. By doing so, the ethylene yield remained constant over multiple cycles.

The results presented in this chapter have been published: ‘Dutta, K., Shahryari, M., Kopyscinski, J., *Direct nonoxidative methane coupling to ethylene over gallium nitride: A catalyst regeneration study*. Ind. Eng. Chem. Res. 59 (2020) 4245–4256 [80]. Kanchan Dutta developed the regeneration strategies, designed and conducted the experiments, analysis and wrote the manuscript, while Mohsen Shahryari (Master’s student) assisted in carrying out the TGA experiments and proofreading. Jan Kopyscinski provided feedback on the methodology, analysis, and manuscript, and was responsible for funding.

7.1 Introduction

Generally, two approaches exist to improve methane conversion and product selectivity and to deal with the coking: (1) catalyst development and (2) reaction engineering. Catalyst performance has been improved by support optimization for suppressing coking [11,13]. Dealumination of the zeolite support or silanation methods were used to reduce the number of acid sites that facilitate coking. Adding promoters was another way; transition metals in Period 4 (Fe, Co, Ni, Cr, Cu, Zn) and metals in Group 13 (Ga and Al) show improvement in terms of methane conversion and catalyst stability [122–124]. In another approach, the inhibition of coking was achieved by preparing an isolated monoatomic iron site embedded in a silica matrix [9]. It was hypothesized that the absence of an adjacent iron site hinders catalytic C–C coupling and thus catalyst deactivation. However, a reaction temperature of more than 1000 °C was required that produced ethylene (40–48%), naphthalene (20–30%), and benzene (25–30%).

From the process design standpoint, the addition of co-reactants, coupling methane activation with other reactions (e.g., methane reforming, oxidative coupling), changing residence time, and the introduction of regeneration cycles have been explored to reduce coking or remove coke deposition to extend the catalyst lifetime [6,14]. Coking is unavoidable, which makes catalyst regeneration a crucial step. Besides fixed bed reactors, various fluidized bed reactors with and without regeneration cycles have been applied. It is common to regenerate the catalysts with air at high temperature to burn off the carbon deposition [6,11]. Hydrogen at 900 °C has also been used for the regeneration process [125].

In this work, we present an experimental study on various regeneration procedures for unsupported and supported GaN/SBA15 catalysts. Additionally, we report an effective protocol consisting of activation/regeneration/re-nitridation cycles that extend the catalyst life. The re-nitridation step allows restoring the active surface gallium-nitride after each regeneration step in air in which surface gallium-oxides are formed. We hypothesize that we can regenerate the catalysts using an optimum regeneration agent (e.g., air, H₂, and CO₂). We also hypothesize that we can use temperatures lower than 550 °C to prevent overoxidation of GaN during regeneration. We have already seen that GaN/SBA15 attained steady-state rather quickly after a higher initial rate, and the catalyst was stable. We think that the catalyst would be stable over an extended period.

7.2 Regeneration cycles

7.2.1 Regeneration medium

Hydrogen, carbon dioxide, and air have been tested as possible regeneration agents. Hydrogen was not suitable as temperatures over 800 °C were needed to remove carbon in the form of CH₄ (Fig. 7–1). Moreover, under the reducing H₂ atmosphere, GaN decomposed into NH₃ and N₂ above 720 °C and 900 °C, respectively (Fig. 7–1B and C). As a result, gallium metal was produced, which appeared as a shiny metallic coating on the quartz reactor (Fig. 7–1D). A blank experiment conducted with an empty reactor did not produce any CH₄, NH₃, and N₂ (not shown).

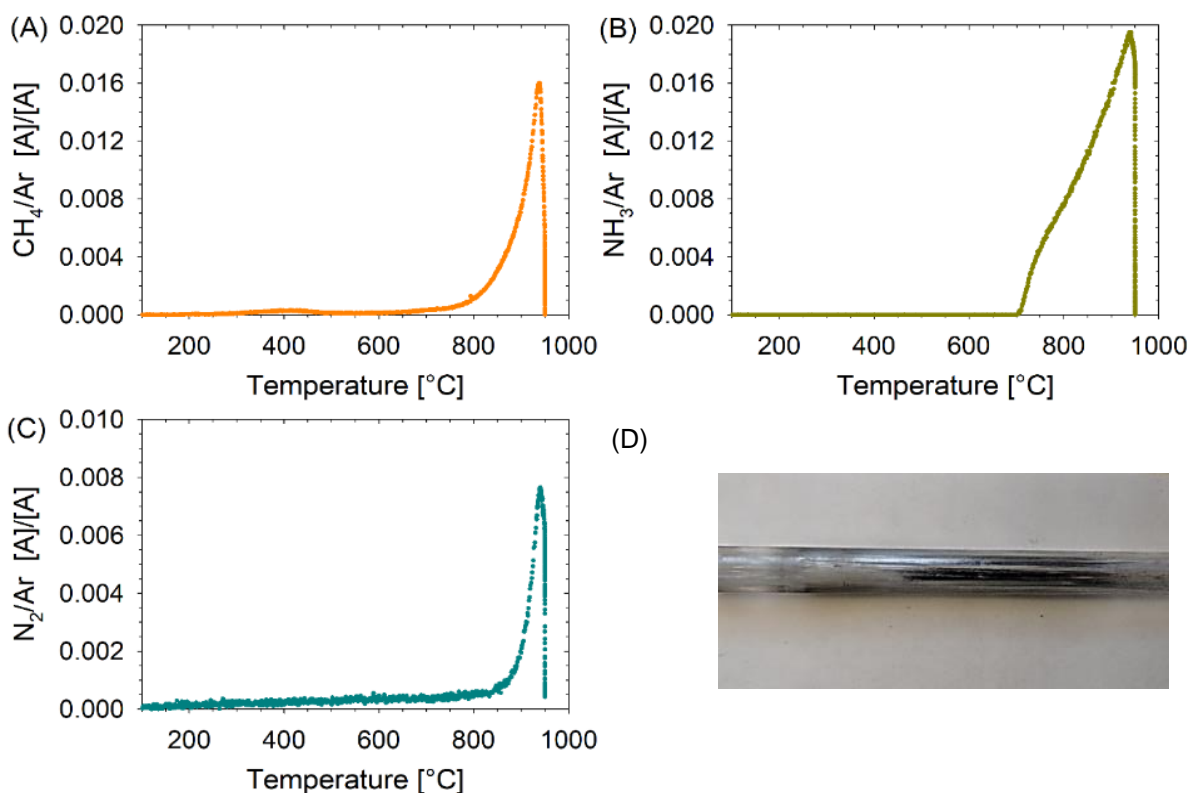


Fig. 7–1 Normalized (with internal standard Ar) MS signal for (A) CH₄ ($m/z = 15$), (B) NH₃ ($m/z = 17$), (C) N₂ ($m/z = 28$) during TPR of spent GaN with 40% H₂ in Ar from 40–950 °C (at 2.5 °C min⁻¹); (D) Shiny metallic Ga coating on the outer surface of the cold quartz reactor after TPR.

Carbon dioxide was also not a suitable regeneration agent. Again, temperatures over 800 °C were needed to remove carbon in the form of CO (i.e., $\text{CO}_2 + \text{C} \rightarrow 2 \text{CO}$), as illustrated in Fig. 7–2. Furthermore, GaN decomposed at temperatures higher than 850 °C (Fig. 7–2A and C). Thermodynamically, GaN decomposition to Ga₂O₃ and N₂ ($m/z = 28$) is favored in the presence of CO₂ at temperatures higher than 850 °C. Both N₂ and CO ($m/z = 28$) were produced at 1000 °C,

indicated by a higher peak intensity at $m/z = 28$ (Fig. 7–2C) for the spent GaN sample when compared with the blank run, and the spent Ga_2O_3 (no N). The peak at 900 °C corresponds to the removal of carbon from the GaN surface, which was about 100 °C higher than that of the Ga_2O_3 catalyst. This might indicate a stronger carbon-gallium interaction on the GaN sample.

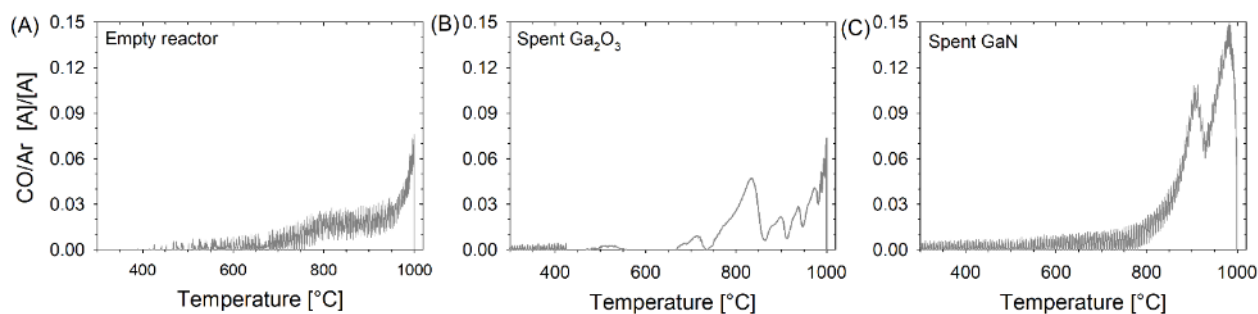


Fig. 7–2 Normalized (with internal standard Ar) MS signal for CO ($m/z = 28$) during temperature-programmed reaction with CO_2 for (A) empty reactor (B) spent unsupported Ga_2O_3 and (C) spent unsupported GaN.

Air as a regeneration agent was very suitable as the carbon deposition was removed at temperatures between 450 to 500 °C for GaN and between 550 to 600 °C for GaN/SBA15. TPO-TGA (weight change) and TPO-MS (CO_2 and H_2O formation) experiments yielded the same temperatures as depicted in Fig. 7–3. The confinement effect [84] can explain the higher temperature required to regenerate the supported catalyst as the SBA–15 support has an average pore diameter of 7 to 8 nm. At higher temperatures, GaN started to oxidize, which is indicated by a significant weight increase. For pure GaN, an increase of the weight by 12 wt% would be achieved for complete oxidation to Ga_2O_3 . Since the unsupported catalyst contained 14.4 wt% Ga_2O_3 and 85.6 wt% GaN, the increase of 9.5 wt% was very close to the theoretical value of 10.2 wt% (Fig. 7–3A). Based on these results, GaN and GaN/SBA15 catalysts were regenerated at 500 °C and 550 °C, respectively.

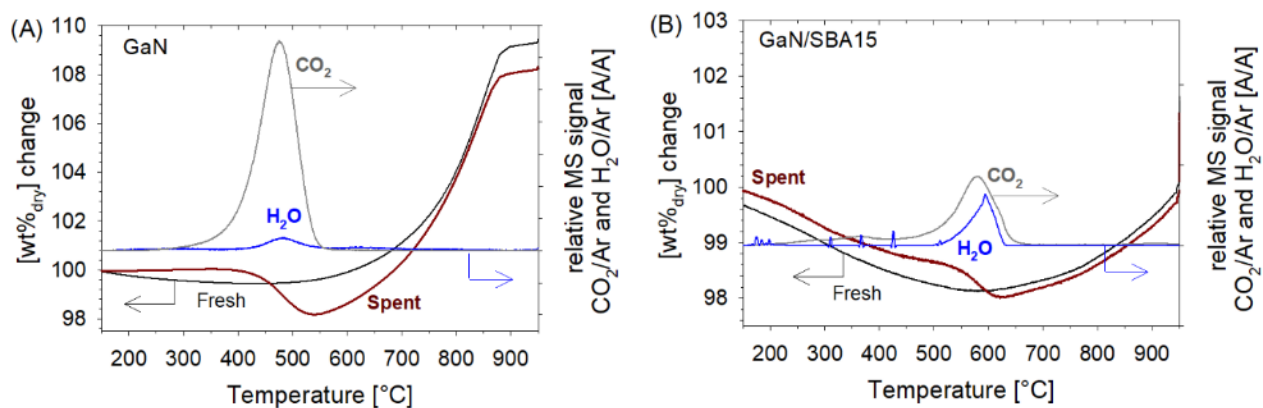


Fig. 7–3 TPO (MS and TGA) results for fresh and used (A) unsupported GaN and (B) supported GaN/SBA15 catalyst.

7.2.2 Reference activation/regeneration cycle

The reference activation/regeneration cycle refers to method 1, in which the catalyst was subjected to 8 h (18 h for GaN/SBA15) activation at 700 °C followed by regeneration in air at 500 °C for 4.25 h (550 °C for 3.25 h for GaN/SBA15) for 5 cycles. For the unsupported GaN catalyst, the results in terms of CH₄ conversion and product formation rate is illustrated in Fig. 7–4.

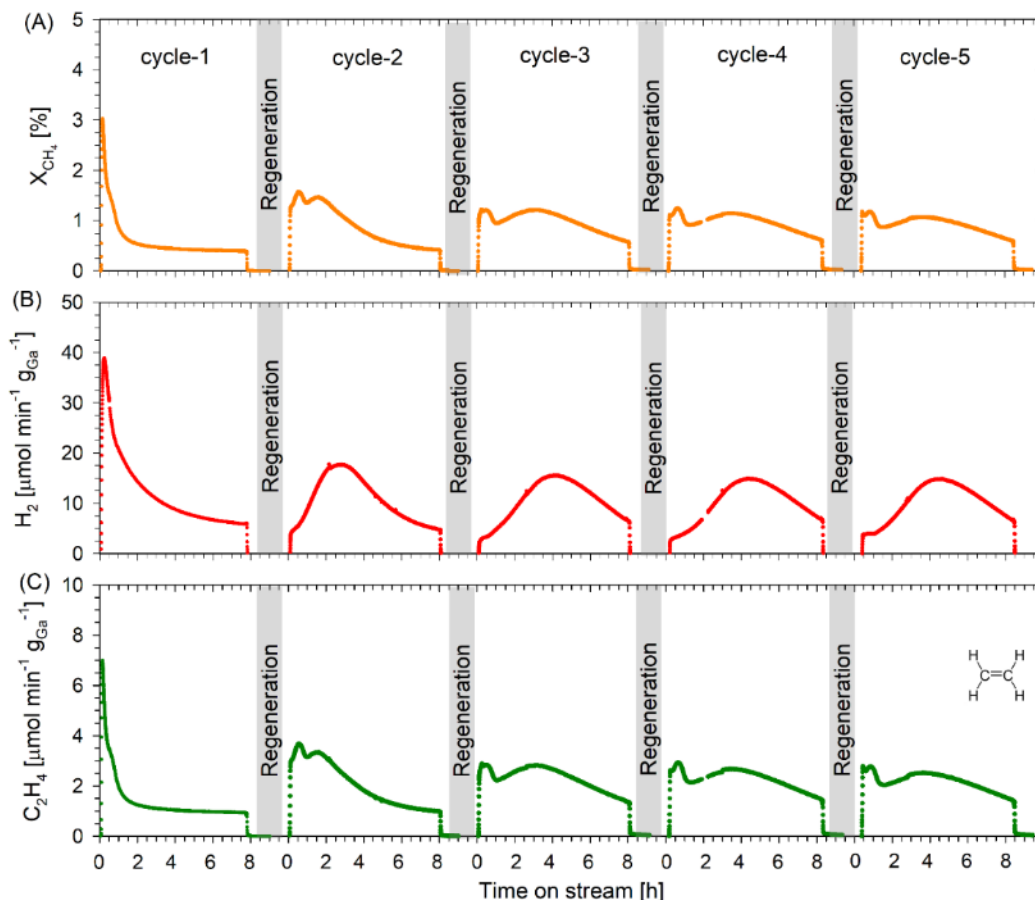


Fig. 7-4 (A) CH_4 conversion and product formation rate of (B) H_2 and (C) C_2H_4 as a function of time on stream over unsupported GaN used in 5 activation cycles with 4 intermediate regeneration steps in air (GaN-R). Activation: $700\text{ }^\circ\text{C}$ with 567 h^{-1} , regeneration: air at $500\text{ }^\circ\text{C}$.

The methane activation behavior changed significantly from the 2nd cycle onwards. In detail, the maximum CH_4 conversion, as well as product formation rates, shifted to later times (Fig. 7-4). The reason for this change was the slight surface oxidation of GaN to Ga_2O_3 during the regeneration in air, which had its unique CH_4 activation behavior (refer to chapter 5). During the initial CH_4 adsorption onto Ga_2O_3 , the hydrogen in CH_4 reacts with lattice oxygen to form CO_2 (Fig. A6-1A) as well as H_2O and CO (not shown), which has been confirmed via our DFT modeling [46].

The higher the amount of Ga_2O_3 formed during the regeneration process, the more H_2O and CO_2 (and CO) were produced, resulting in a shift of the H_2 and C_2H_4 formation rates. Note, the nominal mass to charge ratio ($m/z = 28$) corresponds to C_2H_4 as well as to CO and N_2 . GaN material is stable under reaction conditions and does not decompose (releasing N_2). A significant part of the first peak

in Fig. 7-4C for cycles 2 to 5 could be associated with CO formed on surface Ga_2O_3 , while the second peak could be attributed to C_2H_4 .

In terms of the minor products propylene (C_3H_6), benzene (C_6H_6), and toluene (C_7H_8), their formation rates decreased and shifted with each cycle (Fig. A6-2). Moreover, after 6 h on stream, no benzene, toluene, and naphthalene were produced as the catalyst seemed to deactivate rather fast.

The supported GaN/SBA15 catalysts were stable (despite a low CH_4 conversion) and active (per gram of gallium) when compared to the unsupported catalysts, as illustrated in Fig. 7-5 and A6-3. Even after 4 regeneration cycles with air, both the CH_4 conversion and C_2H_4 formation rates were steady throughout each methane activation cycle of 17 h each ($X_{\text{CH}_4} = 0.4$; $r_{\text{C}_2\text{H}_4} = 20 \mu\text{mol min}^{-1} \text{g}_{\text{Ga}}^{-1}$). As before, the formation rates of C_3H_6 , C_6H_6 , and C_7H_8 were over 100 times lower than that of the desired C_2H_4 and were decreasing with each new cycle (Fig. A6-3).

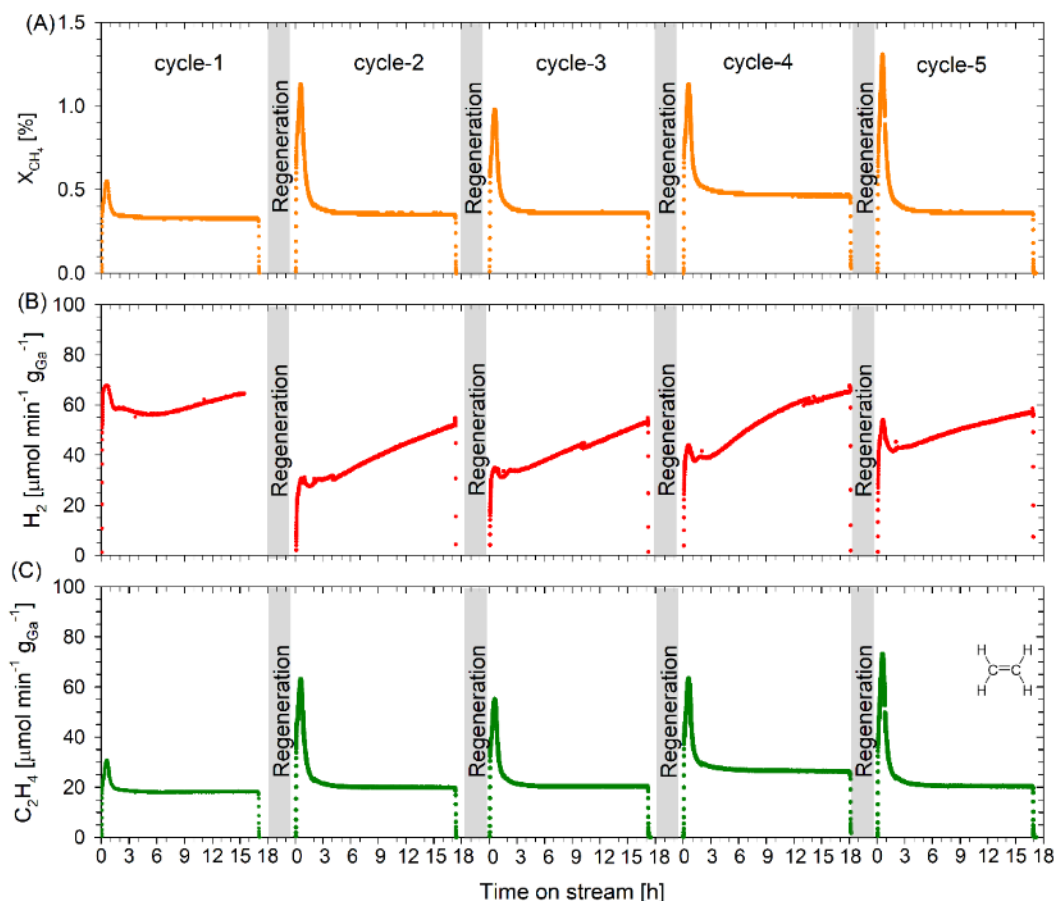


Fig. 7-5 (A) CH₄ conversion and product formation rates for (B) H₂ and (C) C₂H₄ as a function of time on stream over supported GaN/SBA15 used in 5 activation cycles with 4 intermediate regeneration steps in air (GaN/SBA15-R). Activation: 700 °C with 567 h⁻¹, regeneration: air at 550 °C.

The higher CH₄ conversion at the beginning of each activation cycle can be explained by the fact that CH₄ adsorbed on free active sites. It is hypothesized that the dissociative methane adsorption on Ga (i.e., first C-H bond cleavage and formation of CH₃^{*}) is rather fast, while the second C-H bond cleavage and formation of a CH₂^{*} surface complex over a Ga-N hollow site is the rate-determining step [46]. Additionally, at the onset of the 2nd to 5th activation cycle, an elevated CO₂ concentration was measured due to the reaction of the lattice oxygen from Ga₂O₃ with CH₄, as described above (Fig. A6-1B). In the first cycle, no CO₂ was formed as the gallium catalyst was in nitride form.

The product selectivity after each cycle is summarized in Table 7-1. For both GaN and GaN/SBA15, ethylene selectivities of 97% were achieved in the first cycle, which slightly increased to 99% for the subsequent cycles as the selectivities of the minor product species decreased. Also, as mentioned

before, the amount of produced CO (same nominal mass to charge ratio as C₂H₄) in the 2nd to 5th cycle was unknown but contributed to the increase in the calculated observed C₂H₄ selectivity value as well. Thus, the real C₂H₄ selectivities might decrease with each cycle.

Table 7-1 Product selectivity for GaN and GaN/SBA catalyst (activation/regeneration).

Catalyst	Product selectivity* [mol%]						
	C ₂ H ₄	C ₃ H ₆	C ₆ H ₆	C ₇ H ₈	C ₁₀ H ₈	CO ₂	
GaN-R	GaN (cycle 1)	97.3	0.65	1.88	0.11	0.02	0.05
	GaN (cycle 2)#	97.4	0.32	1.82	0.18	0.04	0.26
	GaN (cycle 3)	98.0	0.24	1.27	0.14	0.03	0.31
	GaN (cycle 4)	98.3	0.21	1.05	0.11	0.02	0.30
	GaN (cycle 5)	98.7	0.17	0.86	0.04	0.00	0.24
GaN/SBA15-R	GaN/SBA15 (cycle 1)	97.4	2.04	0.37	0.12	0.01	0.03
	GaN/SBA15 (cycle 2)#	97.9	0.55	0.13	0.04	0.03	1.37
	GaN/SBA15 (cycle 3)	98.3	0.41	0.11	0.03	0.03	1.11
	GaN/SBA15 (cycle 4)	99.0	0.14	0.06	0.02	0.01	0.81
	GaN/SBA15 (cycle 5)	98.3	0.28	0.06	0.02	0.01	1.37

* based on gaseous carbon species (C₂H₄, C₃H₆, C₆H₆, C₇H₈, C₁₀H₈, CO₂) without adsorbed carbon species.

from 2nd cycle onwards, actual C₂H₄ selectivity is lower because of the contribution by CO to mass 28.

7.2.3 Optimized activation/regeneration cycle

To decrease the amount of surface Ga₂O₃, a re-nitridation of the regenerated catalyst was carried out. Thus, the subsequent activation cycles displayed similar behavior as the first cycle (Fig. 7-6 and 7-7). After the regeneration in air and subsequent re-nitridation with NH₃, the initial CH₄ conversion was ~2.5%. Just like the fresh catalyst (cycle 1), the conversion declined to 0.4% after 7 h, which was reproducible. Also, the catalyst appeared to be more stable when both regeneration and re-nitridation were performed.

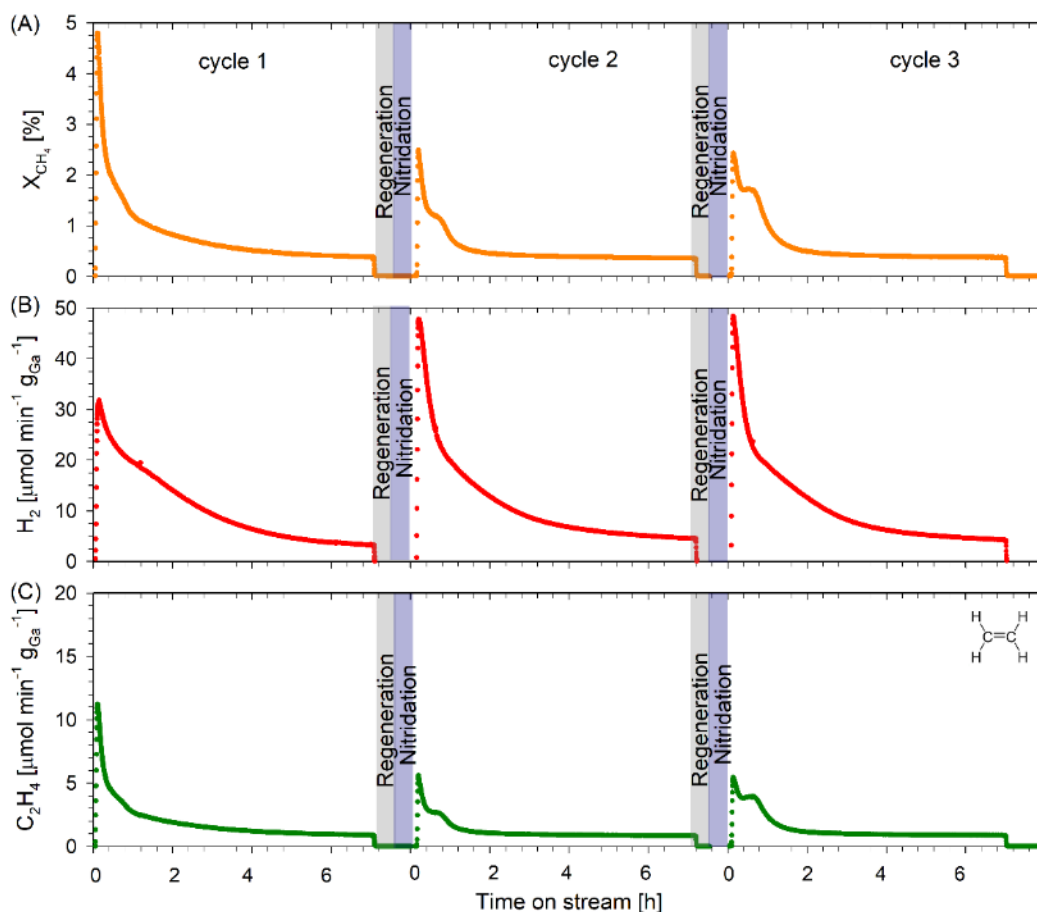


Fig. 7-6 (A) CH₄ conversion and product formation rates for (B) H₂ and (C) C₂H₄ as a function of time on stream over unsupported GaN catalyst with 3 activation cycles and 2 intermediate regeneration and re-nitridation steps (GaN-RN). Activation: 700 °C with 567 h⁻¹, regeneration with air at 500 °C, and re-nitridation with NH₃ at 750 °C.

The maximum H₂ rate reached in cycle 1 was 32 μmol min⁻¹ g_{Ga}⁻¹. This rate increased by 45% to 48 μmol min⁻¹ g_{Ga}⁻¹ during cycle 2 and remained steady throughout cycle 3. After 7 h on stream, the H₂ production rate decreased steadily to 4 μmol min⁻¹ g_{Ga}⁻¹. The C₂H₄ formation in the second and third cycles reached steady state at a rate of about 1 μmol min⁻¹ g_{Ga}⁻¹, corresponding to a CH₄ conversion of 0.4%. Aromatic compounds such as benzene and toluene were only produced at the beginning of each cycle when the active GaN surface was free. Once CH₄ conversion and C₂H₄ formation reached a steady-state, the aromatic species molar rates became zero (Fig. A6-4).

Again, the supported GaN/SBA15 catalyst was more active and stable compared to the unsupported GaN catalyst (Fig. 7-7). After regeneration in air and subsequent re-nitridation in NH₃, the active

surface sites (GaN) were empty, enabling a high CH₄ conversion in the first hour of each activation cycle. Ethylene formation rates were about the same for each cycle, with a steady-state value of 20 $\mu\text{mol min}^{-1} \text{g}_{\text{Ga}}^{-1}$. However, the H₂ formation rates in the 2nd and 3rd cycles were lower than in the first cycle but constant with time on stream. Also, the formation of minor species (C₃H₆, C₆H₆, and C₇H₈) decreased slightly with each cycle (Fig. A6–5).

CO₂ formation for the re-nitridated catalysts (GaN–RN and GaN/SBA15–RN) was much smaller when compared to that of the catalyst that was only regenerated (GaN–R and GaN/SBA15–R) as depicted in Fig. A6–1.

The main difference between the two regeneration methods was the H₂ and CO₂ formation rates. The samples that underwent re-nitridation formed H₂O (not shown) and CO₂ (Fig. A6–1) at the beginning of each cycle, resulting in a slower H₂ formation rate at the start. The same trend was also shown for supported Ga₂O₃/SBA–15 catalysts, as discussed in chapter 5 and [58].

The product selectivities did not change significantly with each cycle. The selectivity of 97 to 98% was achieved for C₂H₄ with both types of catalysts (Table 7–2). The unsupported catalyst exhibited a slightly higher C₆H₆ selectivity than the supported sample, whereas the opposite was observed for C₃H₆.

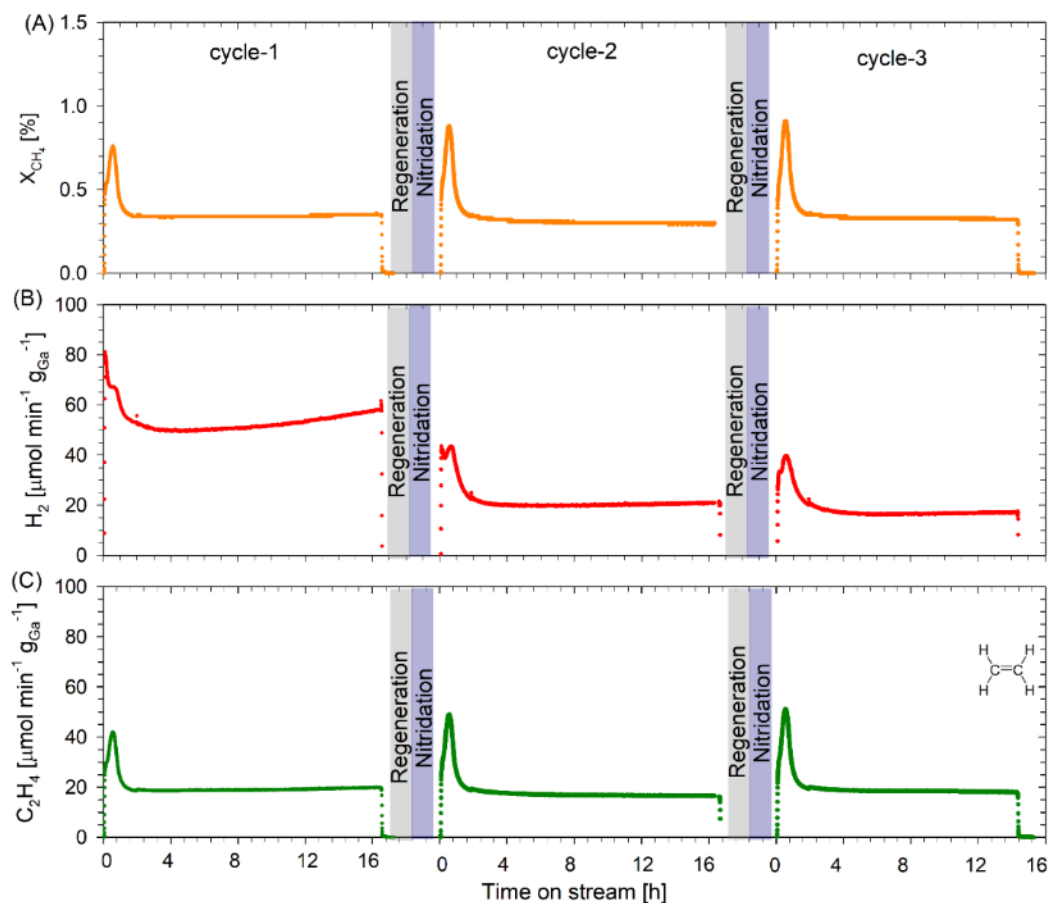


Fig. 7-7 CH_4 conversion and product formation rates for (B) H_2 and (C) C_2H_4 as a function of time on stream over supported GaN catalysts with 3 activation cycles and 2 intermediate regenerations and re-nitridation steps (GaN/SBA15-RN). Activation: 700 °C with 567 h^{-1} , regeneration with air at 550 °C, and re-nitridation with NH_3 at 700 °C.

Table 7–2 Product selectivity for GaN–RN, and GaN/SBA15–RN catalysts (activation/regeneration/re-nitridation).

Catalyst		Gas selectivity [mol%]					
		C ₂ H ₄	C ₃ H ₆	C ₆ H ₆	C ₇ H ₈	C ₁₀ H ₈	CO ₂
GaN–RN	GaN (cycle 1)	97.7	0.43	1.57	0.13	0.03	–
	GaN (cycle 2)	97.1	1.01	1.68	0.09	0.03	–
	GaN (cycle 3)	97.5	0.85	1.32	0.07	0.02	–
GaN/SBA15–RN	GaN/SBA15 (cycle 1)	98.0	1.49	0.21	0.06	0.01	–
	GaN/SBA15 (cycle 2)	97.7	1.52	0.15	0.10	0.01	–
	GaN/SBA15 (cycle 3)	98.2	0.98	0.07	0.05	0.00	–

7.3 Thermogravimetric analysis for carbon deposition

Fig. 7–8 visualizes the increase of adsorbed carbon as a function of time on stream during the methane activation at 700 °C. In the first cycle, the rate of carbon deposition increased from 2 to 4.5 $\mu\text{mol min}^{-1} \text{g}_{\text{Cat}}^{-1}$ within 24 h. In the second and third cycles, the rate increased faster and achieved a value of 6 $\mu\text{mol min}^{-1} \text{g}_{\text{Cat}}^{-1}$ after 24 h. After 24 h on stream, a total carbon deposition of 60 $\text{mg g}_{\text{Cat}}^{-1}$ for the 1st cycle and 80 $\text{mg g}_{\text{Cat}}^{-1}$ for the 2nd and 3rd cycles were determined. This was by a factor of 3–4 larger compared to the carbon deposition reported from the packed-bed reactor experiments above with 18 $\text{mg g}_{\text{Cat}}^{-1}$ for the last run (GaN/SBA15–R). This was expected because TGA experiments were diffusion-limited due to the absence of a convective flow that constantly removes the products from the catalyst bed. After the last activation cycle, the regeneration in air at 550 °C was conducted for more than 12 h, even though 4.25 h were sufficient to remove all carbon surface species. In that extra 8 h, a slight increase in the sample weight of 0.02 mg was detected (<0.13% of the initial mass), indicated a very small surface gallium nitride oxidation.

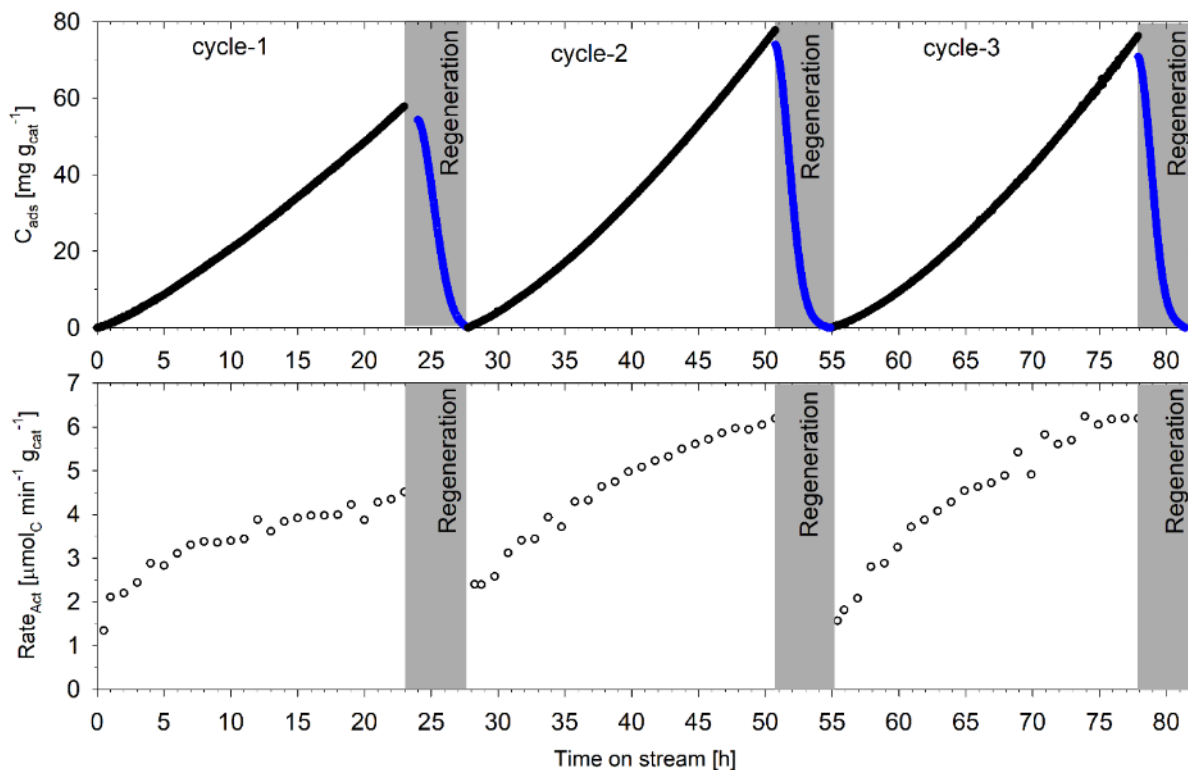


Fig. 7–8 TGA results for three methane activation and regeneration cycles. Activation: 700 °C with 20 mg GaN/SBA15, regeneration: air at 550 °C.

7.4 Long-term test

The supported catalysts displayed greater stability and larger hydrogen and ethylene yields per gram of gallium. Therefore, a long-term run (150 h) was completed using the GaN/SBA15 catalyst (nitridated at 700 °C). The activation temperature was initially maintained at 700 °C for 100 h, then increased (at 5 °C min⁻¹) to and held constant at 750 °C for 24 h, before finally being decreased (at 5 °C min⁻¹) to and maintained at 700 °C for another 24 h. The yields of the major (H₂ and C₂H₄, Fig. 7–9) and minor products (C₃H₆, C₆H₆, and C₇H₁₀, 3–4 orders of magnitude lower than C₂H₄, Fig. A6–6) were nearly stable with a small increase observed for H₂ at 100 h and 700 °C. This change in H₂ yield was probably because of the increased carbon deposition. The production rate of H₂ was steady around 75 μmol min⁻¹ g_{Ga}⁻¹, while that of C₂H₄ was constant at 15–16 μmol min⁻¹ g_{Ga}⁻¹ with C₂H₄ selectivity of 98% (based on gas phase species).

When the temperature was raised to 750 °C, all of the product yields initially increased, but rapidly declined after that. They continued decreasing as the temperature was lowered to 700 °C (after 24 h at

750 °C) and the catalyst lost nearly all its activity. Around half of all the H₂ formed was produced in the first 100 h at 700 °C. Another 40% of the total H₂ yield was achieved in the subsequent 24 h at 750 °C. This represents around a 250% increase in H₂ production at 750 °C, an indication of rapid carbon deposition. This was further supported by a modest 24% increase of C₂H₄ output. The loss of stability and decrease in yield, which occurred within the first 30 min at 750 °C, also supports rapid catalyst coking. TPO-MS of the spent catalyst exhibited the CO₂, and H₂O peaks, both at approximately 600 °C (Fig. A6–7). A total carbon deposition of 237 mg_C g_{Cat}⁻¹ was determined, which was around 10 times greater than for the catalysts discussed in the previous sections. Temperatures of lower than 750 °C are recommended for the non-oxidative methane dehydrogenation and subsequent coupling to ethylene.

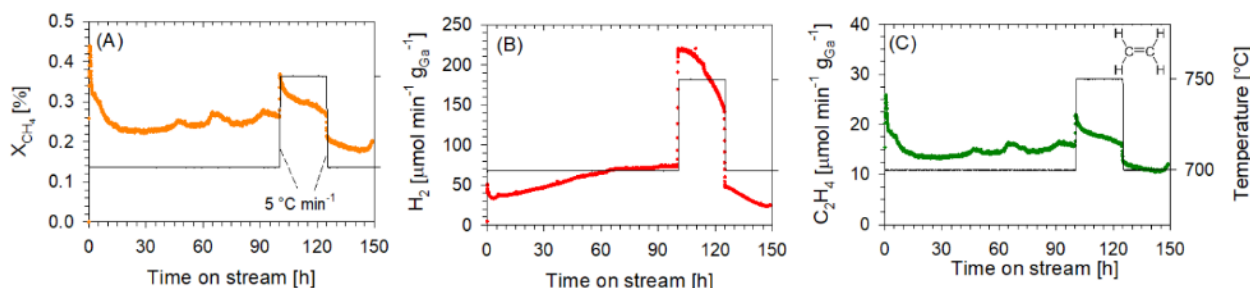


Fig. 7–9 (A) CH₄ conversion and product formation rates for (B) H₂ and (C) C₂H₄ as a function of time on stream for supported GaN/SBA15 for long term run (150 h).

7.5 Catalyst characterization: fresh and spent

XRD patterns of the fresh and spent catalysts are illustrated in Fig. 7–10. The reference pattern of β -Ga₂O₃ ($2\theta = 31.7^\circ, 35.2^\circ, 38.4^\circ, 64.7^\circ$; PDF# 04–013–1733) and GaN ($2\theta = 32.5^\circ, 36.9^\circ, 57.9^\circ$; PDF #00–006–0523) were taken from the International Centre for Diffraction Data (ICDD). The unsupported non-nitridated sample exhibited a pattern for β -Ga₂O₃ only, whereas all of the nitridated samples (fresh and used) showed only diffraction patterns corresponding to GaN (Fig. 7–10A). The nitridated gallium-containing supported catalysts showed signs of crystalline GaN but did not exhibit any peaks corresponding to β -Ga₂O₃ (Fig. 7–10B). Even for the Ga₂O₃/SBA15 samples, no diffraction patterns for β -Ga₂O₃ were observed, indicating non-crystalline particles. This was further confirmed with TEM [58]. During the nitridation of the supported samples, the amorphous Ga₂O₃ was converted to crystalline GaN, which exhibited sharp peaks corresponding to this nitride.

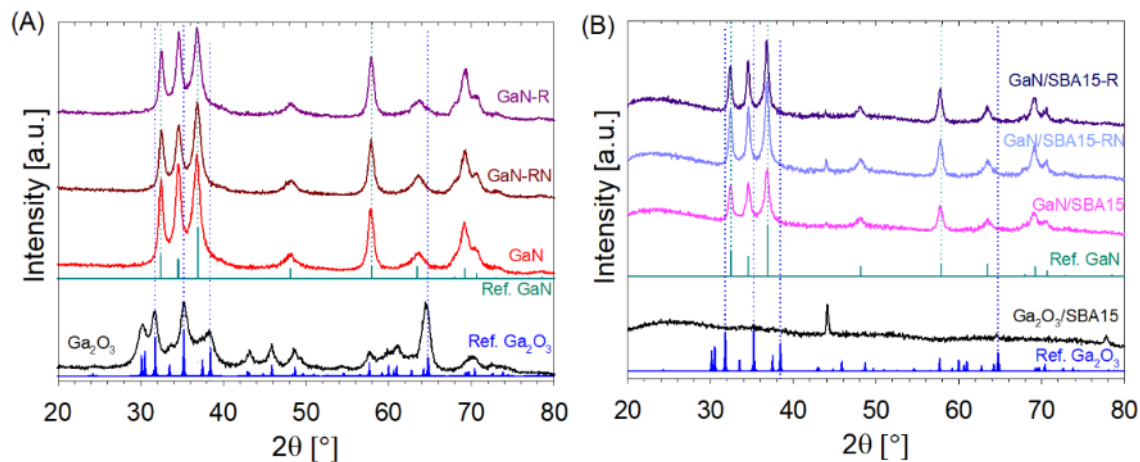


Fig. 7–10 XRD pattern for (A) unsupported and (B) supported catalysts in comparison with references.

The sample regenerated with air (GaN–R) did not show any diffraction pattern for Ga_2O_3 , indicating that the GaN in the bulk phase was not oxidized during the regeneration at 500 °C. However, slight surface oxidation forming amorphous Ga_2O_3 is plausible and also explains the formation of CO_2 and H_2O in the subsequent activation cycle. The used, regenerated (GaN/SBA15–R) and regenerated/re-nitridated (GaN/SBA15–RN) catalysts only showed a GaN diffraction pattern. The XRD peak around $2\theta = 44^\circ$ (Fig. 7–10B) corresponds to the XRD aluminum sample holder.

ICP–OES was used to confirm the presence of gallium in GaN/SBA15. Results showed that the actual Ga loading was 15.0 ± 1.0 wt%, which is very close to the theoretical loading of 16 wt%. The difference of around 1 wt% from the target loading due to gallium loss during catalyst synthesis.

SEM–EDS analysis for the fresh GaN catalysts is illustrated in the supporting information Fig. 7–11. Fresh GaN had an almost equimolar Ga ($38.2 \pm 1.5\%$) and N ($40.7 \pm 4.7\%$) content, with a balance of C ($9.7 \pm 2.8\%$) and O ($11.3 \pm 1.8\%$). The spent GaN catalyst also exhibited an equimolar Ga and N content, but with a larger C content ($20.1 \pm 3.8\%$) due to adsorbed carbon (Fig. A6–8). The compositions for the GaN–R (Fig. A6–9), GaN–RN (Fig. A6–10), and fresh GaN samples were indistinguishable from one another, which proves that the oxidation in air (at 500 °C) was only superficial and not significant. On the other hand, the spent catalyst treated with 40% H_2 lost 50–80 atomic% N (Fig. A6–11), which was also visible from the evolution of NH_3 and N_2 (Fig. 7–1).

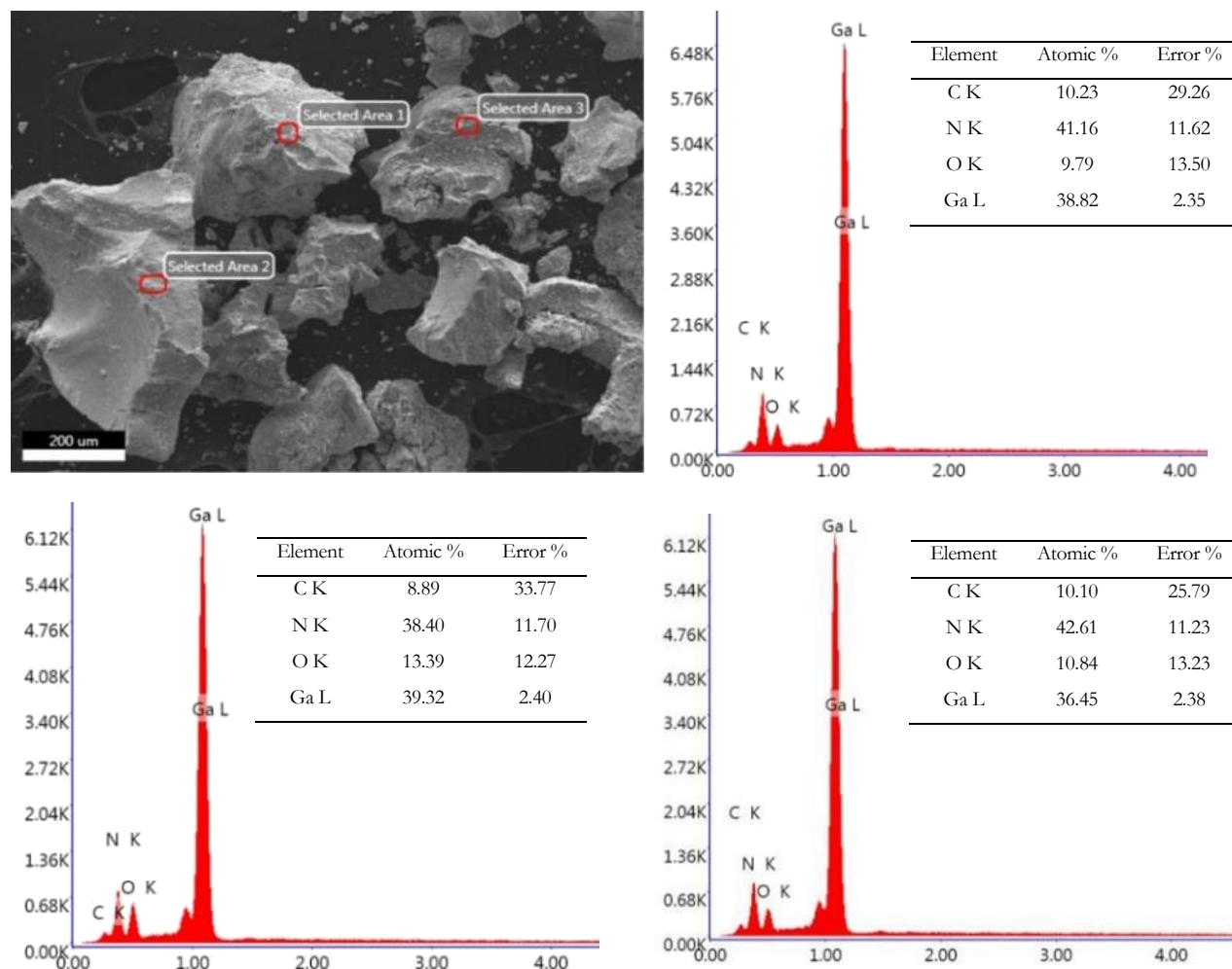


Fig. 7-11 SEM-EDS for fresh GaN.

Table 7-3 summarizes the results of the N₂ adsorption/desorption measurements for the fresh and spent catalyst samples. The unsupported samples had a much smaller total surface area and pore volume than the supported samples (i.e., by a factor of 20). Moreover, they exhibited a bimodal pore size distribution at around 9 and 30 nm, whereas the SBA-15 supported nitride catalyst had a narrow pore size distribution of 7–8 nm (Table 7-3). Nitrogen adsorption and desorption isotherms, along with the pore size distributions are illustrated in Fig. 7-12.

After the impregnation of the support with gallium, the total surface area decreased by more than 50% from 912 to 426 m² g⁻¹. After the nitridation step, the BET surface area was further reduced for both the unsupported and supported samples. The reduction in the area was most likely due to a collapse of the pore structure as well as GaN crystallization above the calcination temperature [70].

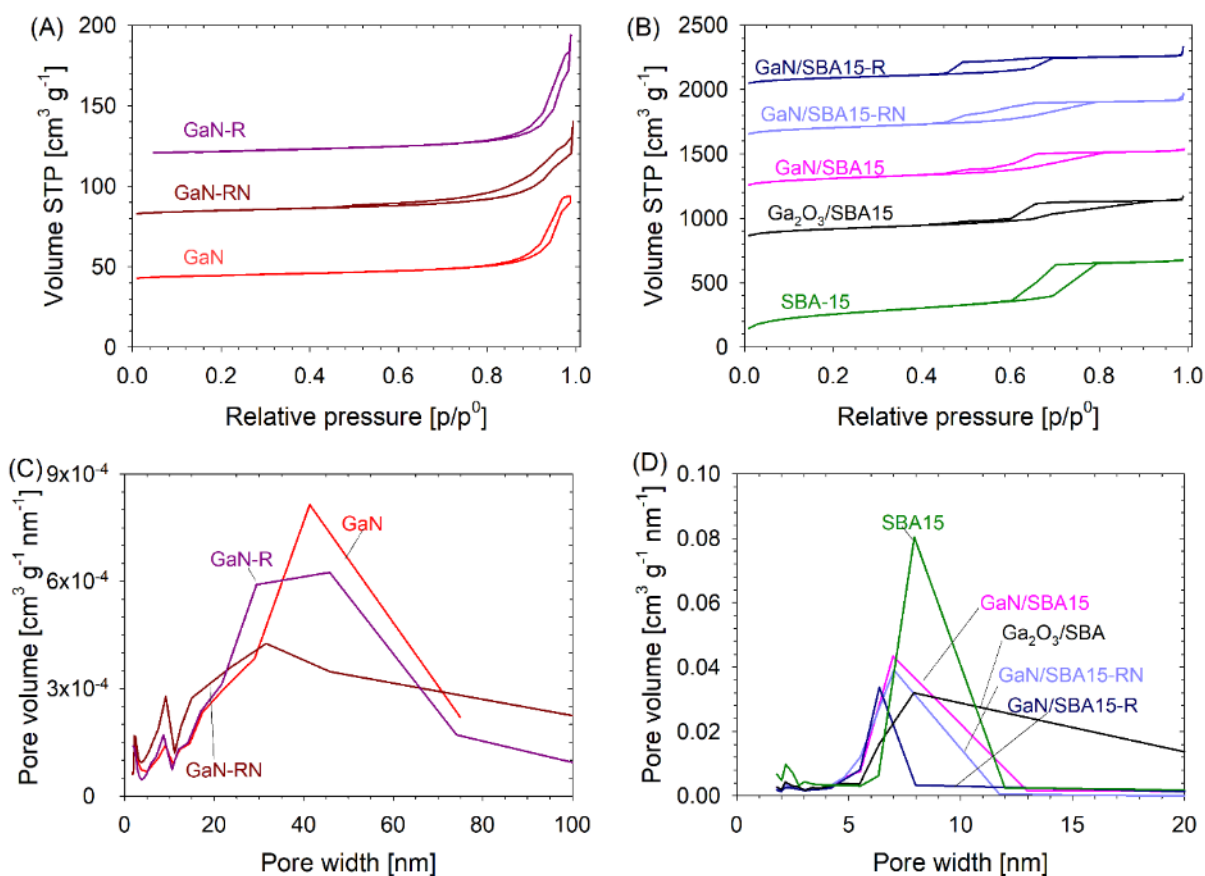


Fig. 7–12 N₂ adsorption-desorption isotherms for (A) unsupported catalysts, fresh (GaN) and spent (GaN–RN, and GaN–R), and (B) for supported catalysts, fresh (Ga₂O₃, GaN/SBA15) and spent (GaN/SBA15–RN and GaN/SBA15–R). Pore size distribution for (C) for unsupported catalysts and (D) for supported catalysts.

For the spent catalyst GaN–RN, the total surface area remained practically unchanged within the accuracy of the instrument ($\pm 4 \text{ m}^2 \text{ g}^{-1}$); however, it dropped to $8 \text{ m}^2 \text{ g}^{-1}$ for the GaN–R catalyst (Table 7–3). For the latter, the decrease in the area might be caused by the continued oxidation of GaN to Ga₂O₃. The total surface area of the spent supported catalyst GaN/SBA15–RN decreased slightly from 398 to 376 $\text{m}^2 \text{ g}^{-1}$. The decrease in surface area for the GaN/SBA15–R catalyst was more significant (398 to 329 $\text{m}^2 \text{ g}^{-1}$) at 12% (Table 7–3).

Table 7–3 Nitrogen adsorption and desorption results for unsupported and supported fresh and spent catalysts.

Sample	S_{BET}^a [m ² g ⁻¹]	V_{Pore}^b [cm ³ g ⁻¹]	D_{Pore}^c [nm]
Ga ₂ O ₃	35	0.13	9.4, 29.3
GaN (fresh)	17	0.06	9.2, 29.6
GaN–RN (3 cycles)	18	0.09	9.2, 29.6
GaN–R (5 cycles)	8	0.11	8.7, 47.8
SBA15	912	0.89	7.9
Ga ₂ O ₃ /SBA15	426	0.53	7.9
GaN/SBA15 (fresh)	398	0.49	7.0
GaN/SBA15–RN (3 cycles)	376	0.54	7.0
GaN/SBA15–R (5 cycles)	329	0.49	6.4

^a S_{BET} = BET total specific surface area obtained from adsorption data in the p/p^0 range from 0.06–0.2; all reported data are within ± 4 m² g⁻¹ for unsupported and ± 10 m² g⁻¹ for supported samples based on the repeated analysis.

^b V_{Pore} = pore volume was obtained at $p/p^0 = 0.9$

^c D_{Pore} = calculated using the Barrett-Joyner-Halenda (BJH) method;

Temperature programmed oxidation - mass spectrometry (TPO-MS) was performed on the fresh and spent catalysts to estimate the amount of adsorbed carbon produced during the methane activation. For both the supported and unsupported catalysts, only the spent catalysts after the final (3rd or 5th) activation cycle was used. TPO-MS of all the spent unsupported catalysts (GaN–R and GaN–RN) exhibited a single CO₂ peak around 500 °C, as illustrated in Fig. 7–13A, which was very similar to the results presented in Fig. 7–3. The results indicate that the adsorbed carbon was most likely in amorphous rather than graphitic form. However, the precise type and stoichiometry of the adsorbed carbon (C_xH_y*) are unknown.

Quantitative analyses of the spent catalysts yielded a relative carbon amount of 14 mg_C g_{cat}⁻¹ for the GaN–R and 19 mg_C g_{cat}⁻¹ for the GaN–RN catalyst. Approximately 1.1 % of the total CH₄ fed for 8 h was converted to surface carbon in the last activation cycle for the GaN–RN catalyst, while 0.7% was converted to surface carbon in the last activation cycle for the GaN–R catalyst.

The supported catalysts exhibited a single CO₂ peak around 600 °C (Fig. 7–13B), which is 100 °C above the peak displayed by the unsupported ones with 18 and 14 mg_C g_{cat}⁻¹ for the GaN/SBA15–R and GaN/SBA15–RN (Table 7–4), respectively. Both supported and unsupported catalysts adsorbed around 15–20 mg_C g_{cat}⁻¹, which was much smaller than the 43–120 mg_C g_{cat}⁻¹ reported over PtSn–zeolite [16]. Considering only the Ga sites, the supported catalysts had around 5 times more surface carbon than the unsupported catalysts (i.e., in mg carbon per gram of Ga). This indicates a better dispersion of the active Ga–N centers. This adsorbed surface carbon is a necessary carbon intermediate (i.e., CH₂* or CH₃*) for the formation of C₂H₄; it also contributes to catalyst deactivation.

Based on the results of the TPO analysis, the overall product selectivities and CH₄ conversions were determined (Table 7–4). The supported samples were superior due to their higher C₂H₄ selectivity and their tendency to adsorb less carbon. It was also noted that a mild re-nitridation helped suppress GaN oxidation limiting CO₂ and H₂O formation. The unsupported catalyst had a higher CH₄ conversion; however, it also contained 20 times more gallium. Therefore, the supported catalyst was much more active and selective on a per gram gallium.

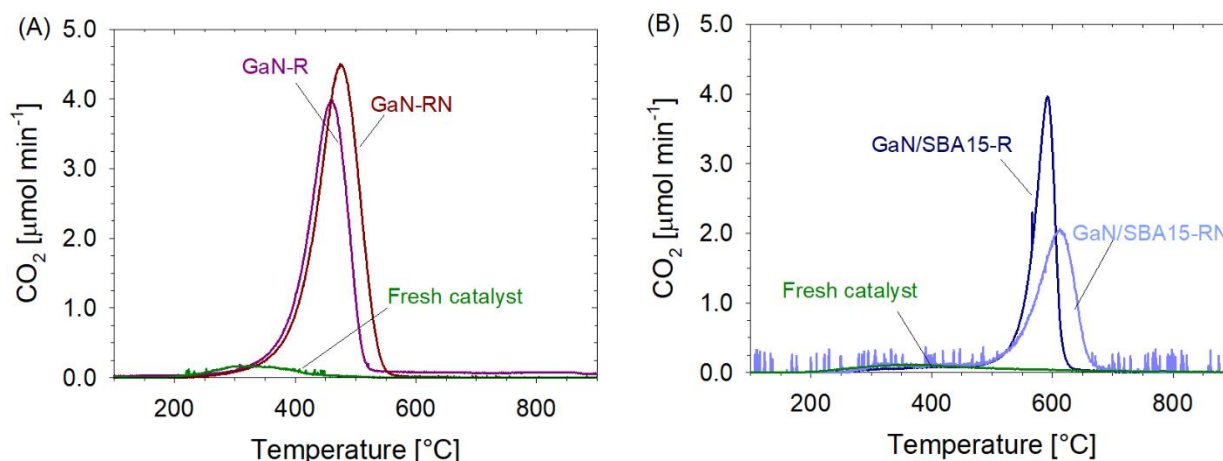


Fig. 7–13 TPO for (A) spent unsupported (GaN–R and GaN–RN) and (B) spent supported (GaN/SBA15–R and GaN/SBA15–RN) catalysts used for methane activation at 700 °C.

Table 7-4 Overall product selectivity and methane conversion for all catalysts.

Catalyst	Overall selectivity [mol%]						X_{CH_4} [%] ^a	C_{ads} [mg _C g _{cat} ⁻¹]	
	C ₂ H ₄	C ₃ H ₆	C ₆ H ₆	C ₇ H ₈	C ₁₀ H ₈	CO ₂			
GaN-R	54.7*	0.09	0.47	0.02	0.00	0.13	44.6	1.64	13.99
GaN-RN	34.8	0.30	0.47	0.02	0.01	–	64.4	1.70	19.37
GaN/SBA15-R	81.2*	0.24	0.05	0.01	0.01	1.13	17.4	0.51	18.02
GaN/SBA15-RN	81.3	0.81	0.06	0.04	0.00	–	17.2	0.44	13.76

*C₂H₄ selectivity could be lower (by up to 15% points) due to contribution by CO to m/z = 28.

The regenerated and re-nitridated supported catalysts (GaN/SBA15-RN) produced less adsorbed carbon per gram of the catalyst (Table 7-4) and had a constant C₂H₄ yield. In supported catalysts, GaN is dispersed as 3–5 nm nanoparticles inside SBA-15 pores. Unsupported catalysts (>80% GaN) have lower porosity (Table 7-3) and poor dispersion of GaN (only the surface GaN are catalytic while the bulk remained inaccessible to CH₄). The dispersion of the active sites in GaN/SBA15 resulted in lower coke and higher C₂H₄ yields. A similar observation was made for isolated well-dispersed active Fe sites inside SiO₂ for CH₄ conversion to C₂H₄ [9].

7.6 Conclusions

Both supported (GaN/SBA15) and unsupported (GaN) catalysts were synthesized for methane activation studies. The supported GaN/SBA15 catalysts had a 20–40 times higher activity towards C₂H₄ per gram of gallium than the unsupported catalysts. For the unsupported catalyst, a slight reduction in methane activation was observed. All the supported catalysts exhibited excellent and reproducible stability (for >100 h). Even though the CH₄ conversion was low ($X = 0.4$ – 0.5), no significant deactivation was observed for the supported samples.

In terms of catalyst regeneration, air was the best regeneration agent as it only required temperatures of 450 to 550 °C to remove the carbon deposition without oxidizing the bulk of the gallium nitride catalyst. Regeneration with H₂ or CO₂, on the other hand, required temperatures of higher than 850 °C at which GaN started to decompose.

GaN and GaN/SBA15 catalysts were used in multiple activation/regeneration and activation/regeneration/re-nitridation cycles. Without a re-nitridation step after regeneration with air, surface

Ga_2O_3 was formed, which led to the formation of CO_2 , CO , and H_2O at the beginning of each activation cycle. A re-nitridation after the catalyst regeneration is highly recommended as the surface Ga_2O_3 is converted to GaN , which keeps the ethylene yield constant over multiple cycles.

Chapter 8

8 Conclusion and future work

The project was started with four distinct objectives, as discussed in section 1.2. Several experimental and theoretical studies were assigned to each objective. The conclusion for each objective are summarized below:

8.1 Proof of concept with commercial GaN

Using commercial GaN, it was proven that in a packed-bed reactor, CH_4 is converted mostly to C_2H_4 at 700 °C, while aromatics (e.g., benzene, toluene) were two to three orders of magnitude smaller. This was in contrast to the batch reactor experiments, where benzene had 89% selectivity at 450 °C without any carbon deposition. The residence time in the batch reactor was around 3000 times than the continuous reactor, which was the reason behind much lower benzene yields.

8.2 Catalyst development and influence of nitridation

Unsupported GaN was not only commercially unviable, but also, the ethylene yield was at least 10 times lower than the yield from the supported GaN (on mesoporous high surface area silica, SBA-15). Supported catalysts also produced less coke per gram of catalyst than the unsupported catalyst. Nitridation, which increased the basicity of the catalyst and the support, lowered carbon deposition (GaN/SBA15-650 had the highest coke among all supported nitride catalysts). Nitridation improved

the selectivity for ethylene when compared to the selectivity from the oxide precursor. Ga_2O_3 and $\text{Ga}_2\text{O}_3/\text{SBA15}$ produced water and carbon oxides (CO and CO_2), which reduced the ethylene yield. However, complete bulk nitridation was not required for eliminating water and CO_x formation; only the surface nitridation was enough, which was accessed by methane for activation. To summarize, compared to the oxide precursors, the nitrides exhibited a higher atom conversion efficiency for the CH_4 carbon leading to higher C_2H_4 selectivity (71 % for $\text{GaN}/\text{SBA15}$, <58 % for $\text{Ga}_2\text{O}_3/\text{SBA15}$) and lower coke selectivity (27 % for $\text{GaN}/\text{SBA15}$, 40 % for $\text{Ga}_2\text{O}_3/\text{SBA15}$). Fig. 8–1 summarizes the conclusion of nitride catalyst development.

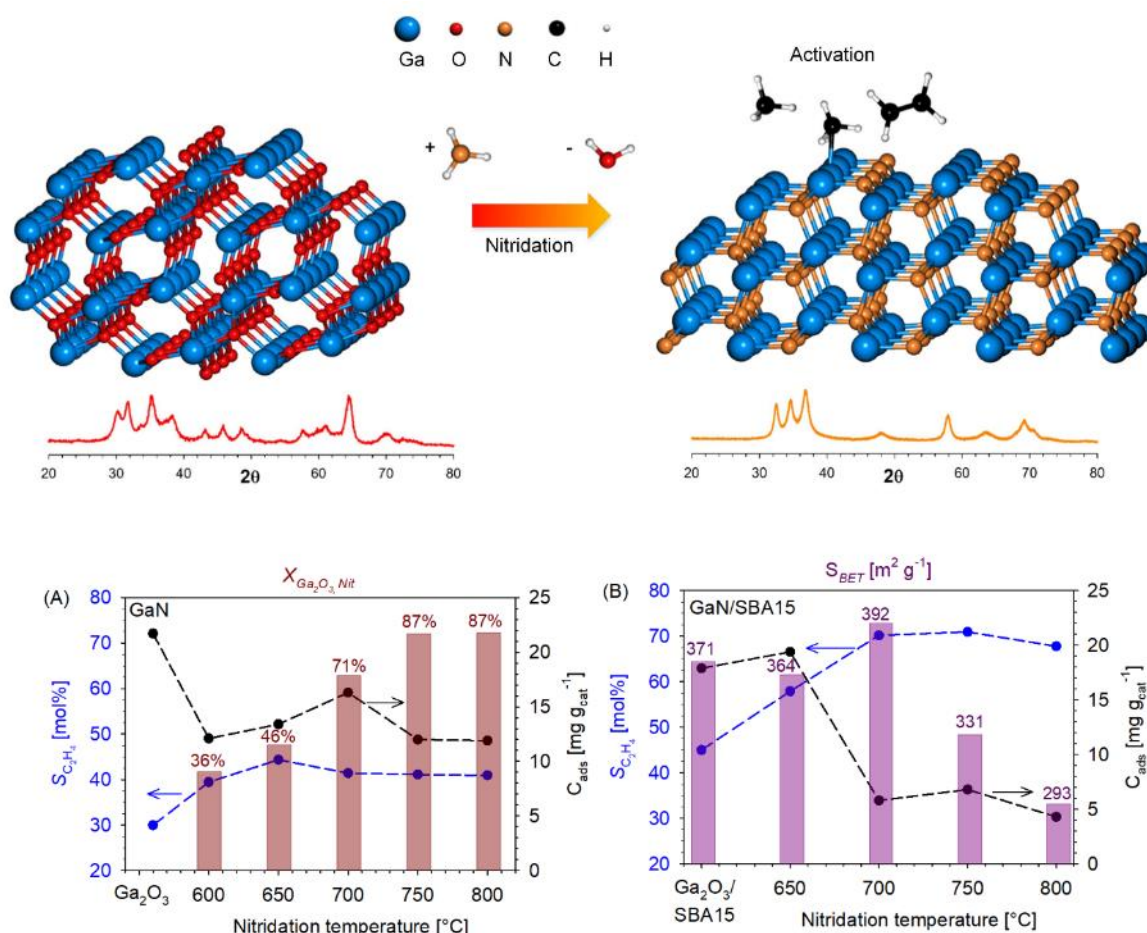


Fig. 8–1 Top: morphological change during nitridation; Bottom: Product selectivity (C_2H_4 and coke) as a function of nitridation temperatures, nitrogen content, and surface area.

8.3 Reaction mechanism and kinetics

DFT calculations showed that the reaction is initiated by dissociative adsorption of CH_4 , followed by the formation of $\text{H}_3\text{C}-\text{Ga}\cdot\text{N}-\text{H}$. The adsorbed species $\text{H}_3\text{C}-\text{Ga}$ forms $\text{H}_2\text{C}-\text{Ga}$ and H_2 gas. The rate

determining step is the dimerization of $\text{H}_2\text{C}-\text{Ga}$ releasing C_2H_4 as the product (Fig. 8–2A). The presence of adsorbed intermediates was confirmed via DRIFTS and NMR studies. The DRIFTS experiments identified the surface intermediates predicted by the DFT study (CH_3 , CH_2 , $\text{HC}=\text{CH}_2$, C_6H_5). The NMR study showed that the deposited carbon on the unsupported catalysts are mostly aromatic, while they are $\text{Ga}-\text{CH}_3$ on the supported catalysts. The coke formation has around 15 times higher apparent activation energy than C_2H_4 formation. The parametric study concludes that the C_2H_4 formation governs the methane conversion. The apparent order of reaction for methane conversion is zero, which experimentally proves that methane adsorption (dissociative) is fast and covers the active sites rapidly. The surface species ($\text{Ga}-\text{CH}_2$, $\text{Ga}-\text{CH}_3$) then either form C_2H_4 by dimerization or form coke. A kinetic modeling study was carried out using 18 experiments. The best model considered the formation of CH_2^* from CH_3^* as the rate-determining step, which was also predicted by the DFT study. The intrinsic activation energy predicted by the kinetic modeling was 19 kJ mol^{-1} (compare with the apparent activation energy by fitting the Arrhenius equation on the observed rates 25 kJ mol^{-1}).

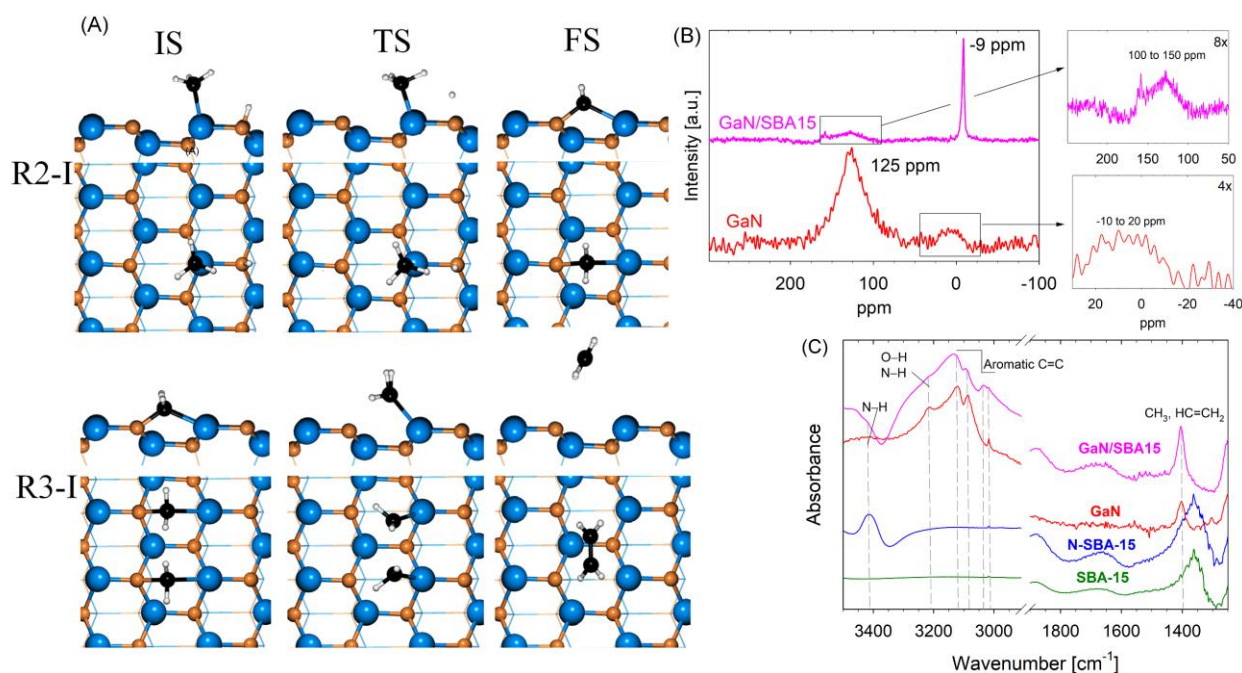


Fig. 8–2 (A) DFT model for C_2H_4 formation over GaN, (B) ^{13}C NMR spectra for spent GaN and GaN/SBA15 catalysts (C) DRIFTS results for the supports and catalysts [$-\text{NH}_2$ and $-\text{NH}$ at 3400 cm^{-1} ; $-\text{CH}=\text{CH}_2$ at 1400 cm^{-1} , C–H stretching alkene between $3000\text{--}3100 \text{ cm}^{-1}$, O–H stretching: $3550\text{--}3200 \text{ cm}^{-1}$].

8.4 Catalyst stability and regeneration

Both unsupported and supported GaN catalysts can be regenerated and reused, maintaining the same C₂H₄ yield and selectivity in all cycles. The regeneration was carried out by burning carbon deposited using air followed by replenishing the lost nitrogen (due to oxidation) by a mild re-nitridation. This was the optimized regeneration method for the catalysts. Air was found to be the best regenerating agent, which required temperature less than 550 °C for regeneration while avoiding bulk oxidation of the catalyst. Without the re-nitridation step, the thin layer of oxide on the air-regenerated nitride catalyst produced H₂O and CO_x, which reduced the C₂H₄ yield. The supported GaN/SBA15 had stable C₂H₄ yield and conversion over 100 h, reducing the requirement of frequent regeneration and re-nitridation. Fig. 8–3 summarizes the mechanistic aspect of regeneration through a schematic and results of methane activation over GaN/SBA15 using the optimized regeneration cycle.

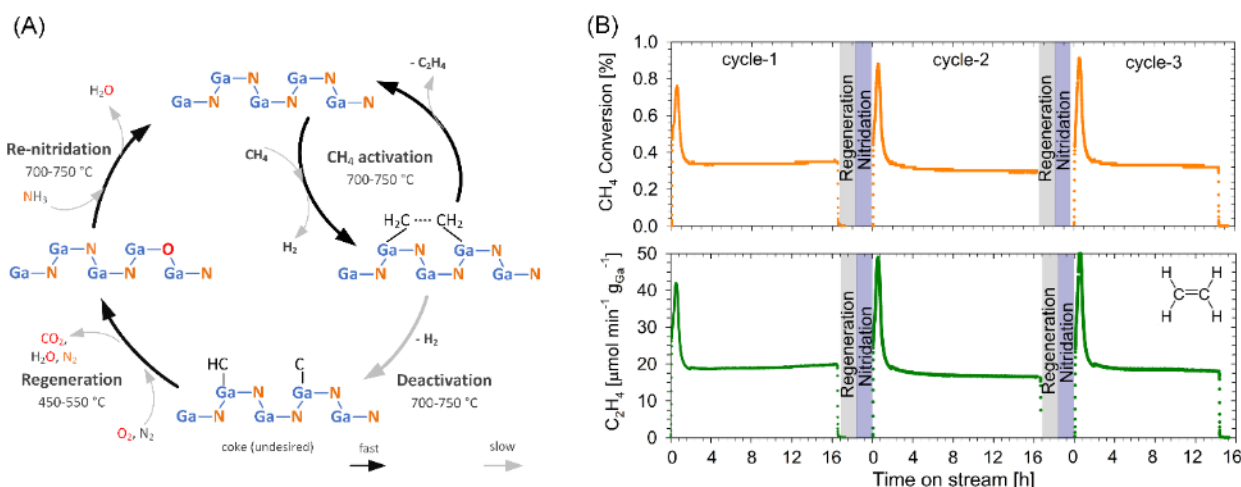


Fig. 8–3 (A) Schematic of the mechanism for methane activation and catalyst regeneration (B) results for GaN/SBA15 (product molar rates) used three times with the optimized regeneration method.

8.5 Future work

8.5.1 Other metal nitrides

Preliminary testing was also carried out with two more metal nitrides, molybdenum (Mo) and tungsten (W). These catalysts were synthesized by impregnating the aqueous solutions of metal precursors into SBA–15 using incipient impregnation. Ammonium heptamolybdate and paratungstate were used as the precursors for Mo and W, respectively. The loading for both the catalysts was 4 wt% (zerovalent metal basis). The impregnated SBA–15 sample was dried at 80 °C for 8 h and then calcined for 5 h at 550 °C (at a ramping rate of 1 °C min⁻¹). The supported oxide catalysts were nitridated using 99.99% NH₃ in a fixed bed reactor at 700 °C for 8 h (at a ramping rate of 1.5 °C min⁻¹). The supported nitrides

were used immediately after the synthesis. Fig. 8–4 depicts the molar flow rates of the products for MoN, WN, and GaN, respectively. The catalysts start deactivation within 2 h, with methane achieving a maximum conversion of 3% (based on hydrocarbon products without coke). While the maximum C_2H_4 rate (initial) over MoN was $550 \mu\text{mol min}^{-1} \text{g}_{\text{metal}}^{-1}$, it attained a steady rate of around $100 \mu\text{mol min}^{-1} \text{g}_{\text{metal}}^{-1}$, which was 5 times larger than for the GaN/SBA15 catalyst.

While benzene had the highest molar rate for MoN, it attained the same steady rate of around $1 \mu\text{mol min}^{-1} \text{g}_{\text{metal}}^{-1}$ for both. At the steady-state, the H_2 to C_2H_4 ratio attained a value close to 2.6 for MoN, while it is around 18 for WN, which indicates higher coking for WN/SBA15 catalyst.

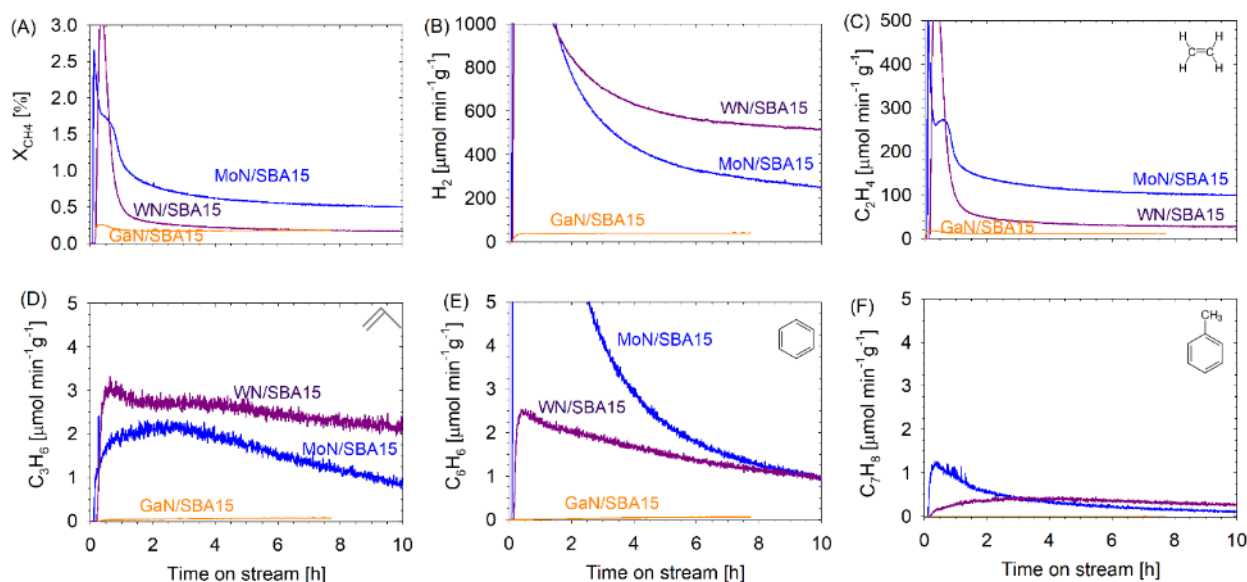


Fig. 8–4 Comparison between (A) Methane conversion and product flow rates of (B) hydrogen, (C) ethylene, (D) propylene, (E) benzene, and (F) toluene formation rates as a function of time on stream over supported MoN/SBA15, WN/SBA15, and GaN/SBA15 catalysts. Methane activation conditions: 700 °C and 1 bar.

Apparently, MoN seems superior in terms of both ethylene and benzene, when compared with GaN and WN. This gives us the flexibility to design a catalyst with maximum ethylene or benzene yields by combining the metals in a bi or trimetallic catalyst.

8.5.2 Effect of catalyst supports and support parameters

A catalyst development work is not limited to one support, one metal loading, and one metal only. We plan to test and compare different metal nitrides (discussed above), mixed metal nitrides, supports, and support with different characteristics. There is still much room for developing the nitride catalyst. It has been shown by researchers that varying those parameters mentioned above can better the results

in terms of CH_4 conversion and C_2H_4 (or C_6H_6) selectivity. A few considerations: (1). One cannot develop a catalyst solely based on Ga; it falls under the category of endangered elements. It should be used as a promoter or co-metal, (2) The Brønsted acid sites in zeolites promote coking, and reducing these sites can suppress coking. These acid sites may get nitrated to $-\text{NH}_2$ (during *in-situ* nitridation of metal oxides supported on zeolites), which might automatically act as coke suppressor, (3) lower metal nitride loading in a higher pore width (separated active sites, higher dispersion) might result in lower coke, which means a higher amount of lower hydrocarbons like C_2H_4 , C_3H_6 , and (4) with the same concept one can improve higher hydrocarbons like C_6H_6 (with of course higher coke deposition). Currently, bimetallic and trimetallic nitride catalysts are under development using different supports like zeolite (ZSM-5) and γ -alumina; different pore width SBA-15 (12 nm); different metal loadings used single or in combination with other metals (2–16 wt% Ga, 1–5 wt% Mo, 1–5 wt% W). Other metals like Fe, Co, Ni could also be included.

8.5.3 Kinetics study

A preliminary kinetics study was presented in chapter 6. As seen in chapters 5 and 7, the methane conversion was less than 0.5% at 700 °C (equilibrium conversion was 4% at 700 °C), which essentially makes our reactor a differential reactor. A more rigorous kinetic modeling with large data (>100 events) set should be carried out. The experiments would be performed on the best performing catalyst(s) discussed so far and in section 8.4.2. Modeling would be based on the mechanisms predicted by DFT calculations for deriving the intrinsic rate equation and the parameters (order and activation energy, equilibrium constants for adsorption, desorption, and other processes). A detailed study (both experimental and DFT) should be carried out to understand the mechanism of coke deposition and catalyst deactivation. The experimental results for catalyst deactivation should be used for kinetic modeling of deactivation.

8.5.4 Other metal pnictogenides (group 15 anions) catalysts

While it is recommended to evaluate different metal nitrides (cations), the effect of some other group 15 anions (pnictogenides) should be explored. These include the addition of phosphorus (phosphides) and bismuth (bismuthides) to Ga, Mo, and W. Hydrogen that is produced by methane conversion is a reduction reaction of H in CH_4 from +1 state to zerovalent state. Group 15 elements are typically used as the electron donor (e.g., donors for n-type semiconductors). It is envisaged that the addition of the electron donor will facilitate the H^+ reduction reaction, and hence methane activation.

Chapter 9

9 Originality

In contrast to precious metal and metal oxide catalysts utilized for the direct non-oxidative methane activation, metal nitrides are an emerging class of catalysts. The metal-nitride catalysts for methane activation itself represent the novelty of the work. No further catalyst development study was carried out for thermal non-oxidative methane activation, after discovering the methane aromatization capability of GaN in a batch reactor. So, every additional work around the GaN catalyst has been original and unique.

9.1 Proof of concept with commercial GaN

Results reported in chapter 4 (and the associated publication [54]), was the first study of the catalytic properties of commercial GaN in a continuous flow reactor. This work established that the residence time plays an important role in determining the major product (a shift from C_6H_6 in a batch reactor to C_2H_4 in a continuous reactor). Lower residence time (<2s) necessitated higher temperatures (>650 °C), which led to catalyst deactivation by carbon deposition. This work established the optimum operating conditions and product profile; it was the steppingstone to a comprehensive nitride catalyst development study.

9.2 Catalyst development and structure-activity relationship

After identifying the methane activation capability of commercially available GaN, it was important to develop and optimize supported GaN catalysts because using pure GaN is not economically viable. Nitride catalyst development, discussed in Chapter 5 (and associated publication [58]), was a unique study where supported GaN catalysts were developed for the first time. The catalysts were developed from scratch, including the support SBA-15 (using standard published procedure). In addition to the supported catalysts, unsupported catalysts were developed. Unsupported catalysts synthesis provided insight into the extent of nitridation and also aided in making a quantitative comparison for concluding why supported catalysts were better not just in terms of economic viability but also in terms of activity and carbon deposition. Nothing was known on how the nitride content could affect the methane activation, and also, the nitridation reaction is itself thermodynamically hindered. We devised experiments with varying nitridation conditions. These synthesis parameters did influence the surface area, nitride content, desired product (C_2H_4) selectivity, and carbon deposition. A detailed catalyst (fresh and used) characterization also provided insight into the structure of the supported catalyst and activity (and unsupported as well). We compared our GaN catalyst with other catalysts (PtSn, PtBi, Fe@SiO₂, catalysts, which focused on converting methane directly to ethylene) used for the direct non-oxidative methane coupling to ethylene. The low methane conversion was common to all, but we had lower coke and more than 90% ethylene selectivity in the gas phase.

A preliminary DFT study established the alkyl-adsorption mechanism for methane activation on GaN. A detailed DFT study was carried out and established the elementary steps (with activation energies) for methane activation on both GaN and Ga₂O₃, for the first time. A summary of the results is given in Chapter 6 (and associated publication [58]). Another unique work was to verify the DFT mechanism by identifying the surface species (predicted by the DFT study) experimentally. DRIFTS study, ¹³C SS-NMR, and isotope labeling study were carried out for experimental verification. These experimental studies were unprecedented, as is the GaN catalyst itself. Kinetics study was carried out based on the observed rates of reaction (effect of temperature, methane partial pressure, and contact time) on GaN/SBA15, yet another study carried out for the first time.

9.3 Optimized catalyst activation/regeneration cycle

Another important industrial aspect for a fast deactivating catalyst is its regeneration capability. Chapter 7 (and the associated publication [80]), was the inceptive study about regeneration and long term use

of GaN catalysts. After establishing the methane conversion and ethylene yield, and looking into the mechanistic and kinetic aspects, we also established an optimum regeneration method for the GaN catalysts. The optimized route maintained the conversion and yield. A circulating fluidized bed with separate activation and regeneration reactors (like the fluidized catalytic cracking reactor system) could be a viable option for a continuous CH₄ activation process. Additionally, we demonstrated the long-term stability of the supported GaN catalyst over 100 h.

Nomenclature

Latin symbols

$c_{S,i}$	mol m^{-3}	concentration of the i^{th} species on the surface
C_{ads}	$\text{mg g}_{\text{cat}}^{-1}$	adsorbed carbonaceous surface intermediates
d_{pore}	μm	particle diameter
d_{pore}	nm	pore diameter
$D_{i,j}$	$\text{m}^2 \text{s}^{-1}$	binary diffusion coefficient of species i and j
$D_{i,\text{mix}}$	$\text{m}^2 \cdot \text{s}^{-1}$	molecular diffusion coefficient of species i
$D_{K,i}$	$\text{cm}^2 \text{s}^{-1}$	Knudsen diffusion coefficient of species i
$D_{\text{eff},i}$	$\text{m}^2 \text{s}^{-1}$	effective diffusion coefficient of species i
E_A	kJ mol^{-1}	activation energy
ΔG_R^0	kJ mol^{-1}	standard free energy of reaction at 298.15 K
GHSV	differ	gas hourly space velocity
h_{Bed}	cm	catalyst bed height
ΔH_R^0	kJ mol^{-1}	standard heat of reaction at 298.15 K

ID	cm	inner diameter of the quartz reactor
k_0	differ	pre-exponential factor for Arrhenius equation
k_r	differ	intrinsic rate constant
K_x	bar ⁻¹	adsorption equilibrium constant
l_{CH}	m	characteristic length
m_{cat}	g	mass of catalyst loaded
M_i	g mol ⁻¹	molar mass of the i^{th} component
MFC	–	mass flow controller (for gases)
n	–	order of the reaction
n_i^0	mol	number of moles of the i^{th} component at time $t = 0$
$\dot{n}_{i,in}$	mol min ⁻¹	inlet molar flow rate of the i^{th} component
$\dot{n}_{i,out}$	mol min ⁻¹	outlet molar flow rate of the i^{th} component
n_N	mol	number of moles of nitrogen in the nitride catalyst
p_i	bar	partial pressure of the i^{th} gas species
r	mol min ⁻¹ g _{cat} ⁻¹	rate of reaction
r_{obs}	mol min ⁻¹ g _{cat} ⁻¹	observed rate of reaction
\mathcal{R}	J K ⁻¹ mol ⁻¹	universal gas constant = 8.314
S_i	–	selectivity of the i^{th} species
T	K	temperature
V_{cat}	mL	volume of the catalyst bed
$\dot{V}_{i,in}$	mL _N min ⁻¹	volumetric flow rate of the i^{th} gas species at normal conditions
$WHSV$	differ	weight hourly space velocity
X_{CH_4}	–	methane conversion
Y_i	–	product yield

Greek symbols

ε	–	bed porosity
η	–	approach to equilibrium
η_{eff}	–	effectiveness factor
Ψ_i	–	Weisz modulus for the i^{th} component

φ_P	–	sphericity
Φ	–	Thiele modulus
ν_i	–	number of carbon atoms in the i^{th} hydrocarbon species
ρ_{Bulk}	g mL^{-1}	bulk density of the catalyst
τ	–	tortuosity

Other

*	–	empty active site
CH_3^*		occupied site (e.g., methyl group)

Subscripts and superscripts

ads	adsorbed
<i>Bed</i>	catalyst bed
<i>Bulk</i>	catalyst bulk property
<i>c</i>	carbon
<i>cat</i>	catalyst
<i>eqm</i>	equilibrium
N	normal conditions, 273.15 K and 1.013 bar
tot	total

Abbreviation

CP	cross-polarization
DFT	density functional theory
DRIFTS	diffuse reflectance infrared Fourier transform spectroscopy
EDS	energy-dispersive X-ray spectroscopy
EISA	evaporation induced self-assembly
FBR	fixed bed reactor
FID	flame ionization detector
FTIR	Fourier transform infrared
GC	gas chromatography
GHSV	gas hourly space velocity

HRTEM	high-resolution transmission electron microscopy
ICDD	International Centre for Diffraction Data
ICP	inductively coupled plasma
IR	infrared
MAS	magic angle spinning (in NMR)
MS	mass spectrometry
OCM	oxidative coupling of methane
SEM	scanning electron microscopy
SEM	secondary electron multiplier (in MS)
SS-NMR	solid-state nuclear magnetic resonance
STEM	scanning transmission electron microscopy
TCD	thermal conductivity detector
TEM	transmission electron microscopy
TEOS	tetraethyl orthosilicate
TGA	thermogravimetric analysis
TI	temperature indicator
TIC	temperature indicator controller
TPD	temperature-programmed desorption
TP-DRIFTS	temperature-programmed DRIFTS
TPO	temperature-programmed oxidation
TPR	temperature-programmed reduction
TPSR	temperature-programmed surface reaction
XRD	X-ray diffraction

Gas species (mass-to-charge ratio, m/z)

	Name	m/z
H ₂	hydrogen	2
HD	hydrogen isotope	3
D ₂	hydrogen isotope (deuterium)	4
CO	carbon monoxide	28
CO ₂	carbon dioxide	44

CH ₄	methane	15, 16
¹³ CH ₄	carbon labeled methane	16, 17
CH ₃ D	methane isotope	16, 17
CD ₄	methane isotope	18, 20
C ₂ H ₄	ethylene	28
C ₂ D ₄	ethylene isotope	32
C ₂ H ₆	ethane	30
C ₂ D ₆	ethane isotope	36
C ₃ H ₆	propylene	42
C ₆ H ₆	benzene	78
C ₆ D ₆	benzene isotope	84
C ₇ H ₈	toluene	91
C ₁₀ H ₈	naphthalene	120
H ₂ O	water	18
N ₂	nitrogen	28
NH ₃	ammonia	17
Ar	argon	40, 20

References

- [1] S. McGrath, IBISWorld Industry Report 32521CA Plastic & Resin Manufacturing in Canada, 2019. <https://clients1.ibisworld.com>.
- [2] N. Leach, IBIS World Industry Report 32511CA Petrochemical Manufacturing in Canada, 2019. <https://clients1.ibisworld.com> (accessed November 2, 2019).
- [3] Natural Gas Facts, Natural Resources Canada, (n.d.). <https://www.nrcan.gc.ca/science-data/data-analysis/energy-data-analysis/energy-facts/natural-gas-facts/20067> (accessed January 13, 2020).
- [4] Quebec Oil and Gas association QOGA, Natural Gas in Quebec, (n.d.). <http://www.apgq-qoga.com/en/natural-gas/history/> (accessed January 13, 2020).
- [5] J. Baltrusaitis, I. Jansen, J.D. Schuttlefield Christus, Renewable energy based catalytic CH₄ conversion to fuels, *Catal. Sci. Technol.* 4 (2014) 2397–2411. doi:10.1039/C4CY00294F.
- [6] C. Karakaya, R.J. Kee, Progress in the direct catalytic conversion of methane to fuels and chemicals, *Prog. Energy Combust. Sci.* 55 (2016) 60–97. doi:10.1016/j.peccs.2016.04.003.
- [7] P. Schwach, X. Pan, X. Bao, Direct Conversion of Methane to Value-Added Chemicals over Heterogeneous Catalysts: Challenges and Prospects, *Chem. Rev.* 117 (2017) 8497–8520. doi:10.1021/acs.chemrev.6b00715.
- [8] P. Tang, Q. Zhu, Z. Wu, D. Ma, Methane activation: the past and future, *Energy Environ. Sci.* 7 (2014) 2580–2591. doi:10.1039/C4EE00604F.
- [9] X. Guo, G. Fang, G. Li, H. Ma, H. Fan, L. Yu, C. Ma, X. Wu, D. Deng, M. Wei, D. Tan, R. Si, S. Zhang, J. Li, L. Sun, Z. Tang, X. Pan, X. Bao, Direct, nonoxidative conversion of methane to ethylene, aromatics, and hydrogen., *Science*. 344 (2014) 616–9. doi:10.1126/science.1253150.
- [10] N. Kosinov, F.J.A.G. Coumans, G. Li, E. Uslamin, B. Mezari, A.S.G. Wijkema, E.A. Pidko, E.J.M. Hensen, Stable Mo/HZSM-5 methane dehydroaromatization catalysts optimized for high-temperature calcination-regeneration, *J. Catal.* 346 (2017) 125–133. doi:10.1016/J.JCAT.2016.12.006.

- [11] S. Ma, X. Guo, L. Zhao, S. Scott, X. Bao, Recent progress in methane dehydroaromatization: From laboratory curiosities to promising technology, *J. Energy Chem.* 22 (2013) 1–20. doi:10.1016/S2095-4956(13)60001-7.
- [12] H. Sheng, E.P. Schreiner, W. Zheng, R.F. Lobo, Non-oxidative Coupling of Methane to Ethylene Using Mo₂C/[B]ZSM-5, *ChemPhysChem.* 19 (2018) 504–511. doi:10.1002/cphc.201701001.
- [13] J.J. Spivey, G. Hutchings, Catalytic aromatization of methane, *Chem. Soc. Rev.* 43 (2014) 792–803. doi:10.1039/C3CS60259A.
- [14] K. Sun, D.M. Ginosar, T. He, Y. Zhang, M. Fan, R. Chen, Progress in Nonoxidative Dehydroaromatization of Methane in the Last 6 Years, *Ind. Eng. Chem. Res.* 57 (2018) 1768–1789. doi:10.1021/acs.iecr.7b04707.
- [15] I. Vollmer, B. van der Linden, S. Ould-Chikh, A. Aguilar-Tapia, I. Yarulina, E. Abou-Hamad, Y.G. Sneider, A.I. Olivos Suarez, J.-L. Hazemann, F. Kapteijn, J. Gascon, On the dynamic nature of Mo sites for methane dehydroaromatization, *Chem. Sci.* 9 (2018) 4801–4807. doi:10.1039/C8SC01263F.
- [16] D. Gerceker, A. Hussain Motagamwala, K.R. Rivera-Dones, J.B. Miller, G.W. Huber, M. Mavrikakis, J.A. Dumesic, Methane Conversion to Ethylene and Aromatics on PtSn Catalysts, *ACS Catal.* 7 (2017) 2088–2100. doi:10.1021/acscatal.6b02724.
- [17] Y. Xiao, A. Varma, Highly Selective Nonoxidative Coupling of Methane over Pt-Bi Bimetallic Catalysts, *ACS Catal.* 8 (2018) 2735–2740. doi:10.1021/acscatal.8b00156.
- [18] A. Sridhar, M. Rahman, S.J. Khatib, Enhancement of Molybdenum/ZSM-5 Catalysts in Methane Aromatization by the Addition of Iron Promoters and by Reduction/Carburization Pretreatment, *ChemCatChem.* 10 (2018) 2571–2583. doi:10.1002/cctc.201800002.
- [19] B.L. Farrell, V.O. Igenegbai, S. Linic, A Viewpoint on Direct Methane Conversion to Ethane and Ethylene Using Oxidative Coupling on Solid Catalysts, *ACS Catal.* 6 (2016) 4340–4346. doi:10.1021/acscatal.6b01087.
- [20] C. Hammond, S. Conrad, I. Hermans, Oxidative Methane Upgrading, *ChemSusChem.* 5 (2012) 1668–1686. doi:10.1002/cssc.201200299.
- [21] I. Hermans, E.S. Spier, U. Neuenschwander, N. Turrà, A. Baiker, Selective oxidation catalysis: Opportunities and challenges, *Top. Catal.* 52 (2009) 1162–1174. doi:10.1007/s11244-009-9268-3.
- [22] J.S.J. Hargreaves, D. McKay, Catalysis with Nitrides and Oxynitrides, in: J.J. Spivey, K.M. Dooley (Eds.), *Catal.* Vol. 19, 2006: pp. 84–108. doi:10.1039/9781847555229-00084.
- [23] J.S.J.S.J. Hargreaves, Heterogeneous catalysis with metal nitrides, *Coord. Chem. Rev.* 257 (2013) 2015–2031. doi:10.1016/j.ccr.2012.10.005.
- [24] L. Li, X. Mu, W. Liu, X. Kong, S. Fan, Z. Mi, C.-J.J. Li, Thermal non-oxidative aromatization of light alkanes catalyzed by gallium nitride, *Angew. Chemie - Int. Ed.* 53 (2014) 14106–14109. doi:10.1002/anie.201408754.
- [25] S. Pimputkar, Gallium nitride, in: *Single Cryst. Electron. Mater.*, Elsevier, 2019: pp. 351–399. doi:10.1016/b978-0-08-102096-8.00011-2.
- [26] Z.-G. Zhang, Process, reactor and catalyst design: Towards application of direct conversion of methane to aromatics under nonoxidative conditions, *Carbon Resour. Convers.* 2 (2019) 157–174. doi:10.1016/j.crcon.2019.07.001.
- [27] K. Huang, C.T. Maravelias, Synthesis and Analysis of Nonoxidative Methane Aromatization Strategies, *Energy Technol.* (2019) 1900650. doi:10.1002/ente.201900650.
- [28] A. Galadima, O. Muraza, Advances in Catalyst Design for the Conversion of Methane to Aromatics: A Critical Review, *Catal. Surv. from Asia.* 23 (2019) 149–170. doi:10.1007/s10563-018-9262-5.

- [29] Y. Chen, X. Mu, X. Luo, K. Shi, G. Yang, T. Wu, Catalytic Conversion of Methane at Low Temperatures: A Critical Review, *Energy Technol.* (2019) 1900750. doi:10.1002/ente.201900750.
- [30] E.D. Glendening, R. Faust, A. Streitwieser, K.P.C. Vollhardt, F. Weinhold, The Role of Delocalization in Benzene, *J. Am. Chem. Soc.* 115 (1993) 10952–10957. doi:10.1021/ja00076a061.
- [31] E. Mansoor, M. Head-Gordon, A.T. Bell, Computational Modeling of the Nature and Role of Ga Species for Light Alkane Dehydrogenation Catalyzed by Ga/H-MFI, *ACS Catal.* 8 (2018) 6146–6162. doi:10.1021/acscatal.7b04295.
- [32] M. V. Luzgin, A.A. Gabrienko, V.A. Rogov, A. V. Toktarev, V.N. Parmon, A.G. Stepanov, The “Alkyl” and “Carbenium” Pathways of Methane Activation on Ga-Modified Zeolite BEA: 13 C Solid-State NMR and GC-MS Study of Methane Aromatization in the Presence of Higher Alkane, *J. Phys. Chem. C* 114 (2010) 21555–21561. doi:10.1021/jp1078899.
- [33] D. Bajec, A. Kostyniuk, A. Pohar, B. Likozar, Nonoxidative methane activation, coupling, and conversion to ethane, ethylene, and hydrogen over Fe/HZSM-5, Mo/HZSM-5, and Fe–Mo/HZSM-5 catalysts in packed bed reactor, *Int. J. Energy Res.* 43 (2019) 6852–6868. doi:10.1002/er.4697.
- [34] B.J. Lee, Y.G. Hur, D.H. Kim, S.H. Lee, K.-Y.Y. Lee, Non-oxidative aromatization and ethylene formation over Ga/HZSM-5 catalysts using a mixed feed of methane and ethane, *Fuel*. 253 (2019) 449–459. doi:10.1016/j.fuel.2019.05.014.
- [35] A.L. Dipu, S. Ohbuchi, Y. Nishikawa, S. Iguchi, H. Ogihara, I. Yamanaka, Direct Nonoxidative Conversion of Methane to Higher Hydrocarbons over Silica-Supported Nickel Phosphide Catalyst, *ACS Catal.* 10 (2020) 375–379. doi:10.1021/acscatal.9b03955.
- [36] K.S. Wong, J.W. Thybaut, E. Tangstad, M.W. Stoecker, G.B. Marin, Methane aromatisation based upon elementary steps: Kinetic and catalyst descriptors, *Microporous Mesoporous Mater.* 164 (2012) 302–312. doi:10.1016/j.micromeso.2012.07.002.
- [37] C. Karakaya, H. Zhu, R.J. Kee, Kinetic modeling of methane dehydroaromatization chemistry on Mo/Zeolite catalysts in packed-bed reactors, *Chem. Eng. Sci.* 123 (2015) 474–486. doi:10.1016/j.ces.2014.11.039.
- [38] A.M. Champagnie, T.T. Tsotsis, R.G. Minet, A.I. Webster, A high temperature catalytic membrane reactor for ethane dehydrogenation, *Chem. Eng. Sci.* 45 (1990) 2423–2429. doi:10.1016/0009-2509(90)80124-W.
- [39] Z. Ziaka, R. Minet, Propane Dehydrogenation in a Packed-Bed Membrane Reactor, *AIChE J.* 39 (1993). doi:10.1002/aic.690390317.
- [40] T. Okubo, K. Haruta, K. Kusakabe, S. Morooka, H. Anzai, S. Akiyama, Equilibrium shift of dehydrogenation at short space-time with hollow fiber ceramic membrane, *Ind. Eng. Chem. Res.* 30 (1991) 614–616. doi:10.1021/ie00052a002.
- [41] Y.M. Sun, S.J. Khang, Catalytic membrane for simultaneous chemical reaction and separation applied to a dehydrogenation reaction, *Ind. Eng. Chem. Res.* 27 (1988) 1136–1142. doi:10.1021/ie00079a008.
- [42] S. Natesakhawat, N.C. Means, B.H. Howard, M. Smith, V. Abdelsayed, J.P. Baltrus, Y. Cheng, J.W. Lekse, D. Link, B.D. Morreale, Improved benzene production from methane dehydroaromatization over Mo/HZSM-5 catalysts via hydrogen-permeable palladium membrane reactors, *Catal. Sci. Technol.* 5 (2015) 5023–5036. doi:10.1039/C5CY00934K.
- [43] M.C. Iliuta, F. Larachi, B.P. a Grandjean, I. Iliuta, A. Sayari, Methane Nonoxidative Aromatization over Ru–Mo/HZSM-5 in a Membrane Catalytic Reactor, *Ind. Eng. Chem. Res.* 41 (2002) 2371–2378. doi:10.1021/ie010977s.
- [44] F. Larachi, H. Oudghiri-Hassani, M.C. Iliuta, B.P.A. Grandjean, P.H. McBreen, Ru-Mo/HZSM-5 catalyzed methane aromatization in membrane reactors, *Catal. Letters.* 84 (2002) 183–192.

- doi:10.1023/A:1021475819517.
- [45] J.J. Caro, Catalytic membrane reactors - Lab curiosity or key enabling technology?, *Chemie-Ingenieur-Technik*. 86 (2014) 1901–1905. doi:10.1002/cite.201400069.
- [46] V. Chaudhari, K. Dutta, C.-J. Li, J. Kopyscinski, Mechanistic insights of methane conversion to ethylene over gallium oxide and gallium nitride using density functional theory, *Mol. Catal.* 482 (2020) 110606. doi:10.1016/j.mcat.2019.110606.
- [47] D. Zhao, J. Feng, Q. Huo, N. Melosh, G.H. Fredrickson, B.F. Chmelka, G.D. Stucky, Triblock Copolymer Syntheses of Mesoporous Silica with Periodic 50 to 300 Angstrom Pores, *Science* (80-.). 279 (1998) 548–552. doi:10.1126/science.279.5350.548.
- [48] P.J. Larkin, *Infrared and Raman Spectroscopy*, 2nd ed., Elsevier, 2018. doi:10.1016/C2015-0-00806-1.
- [49] W.E. Stewart, M. Caracotsios, *Computer-Aided Modeling of Reactive Systems*, 2007. doi:10.1002/9780470282038.
- [50] S.-H. Hsu, S.D. Stamatidis, J.M. Caruthers, W.N. Delgass, V. Venkatasubramanian, G.E. Blau, M. Lasinski, S. Orcun, Bayesian Framework for Building Kinetic Models of Catalytic Systems, *Ind. Eng. Chem. Res.* 48 (2009) 4768–4790. doi:10.1021/ie801651y.
- [51] W.E. Stewart, M. Caracotsios, J.P. Sørensen, Parameter estimation from multiresponse data, *AIChE J.* 38 (1992) 641–650. doi:10.1002/aic.690380502.
- [52] J. Kopyscinski, J. Choi, J.M. Hill, Comprehensive kinetic study for pyridine hydrodenitrogenation on (Ni)WP/SiO₂ catalysts, *Appl. Catal. A Gen.* 445–446 (2012) 50–60. doi:10.1016/j.apcata.2012.08.027.
- [53] W.E. Stewart, Y. Shon, G.E.P. Box, Discrimination and goodness of fit of multiresponse mechanistic models, *AIChE J.* 44 (1998) 1404–1412. doi:10.1002/aic.690440618.
- [54] K. Dutta, L. Li, P. Gupta, D.P. Gutierrez, C.-J. Li, J. Kopyscinski, Direct non-oxidative methane aromatization over gallium nitride catalyst in a continuous flow reactor, *Catal. Commun.* 106 (2018) 16–19. doi:10.1016/j.catcom.2017.12.005.
- [55] C.-J. Li, Z. Mi, L. Li, Process for producing aromatic compounds using light alkanes, PCT/CA2014/050864, 2015. <https://patents.google.com/patent/WO2015035518A1/en?q=WO2015035518> (accessed March 28, 2019).
- [56] V. Fila, M. Bernauer, B. Bernauer, Z. Sobalik, Effect of addition of a second metal in Mo/ZSM-5 catalyst for methane aromatization reaction under elevated pressures, *Catal. Today*. 256 (2015) 269–275. doi:10.1016/j.cattod.2015.02.035.
- [57] C. Guizani, F.J. Escudero Sanz, S. Salvador, The nature of the deposited carbon at methane cracking over a nickel loaded wood-char, *Comptes Rendus Chim.* 19 (2016) 423–432. doi:10.1016/j.crci.2015.10.009.
- [58] K. Dutta, V. Chaudhari, C.-J. Li, J. Kopyscinski, Methane conversion to ethylene over GaN catalysts. Effect of catalyst nitridation, *Appl. Catal. A Gen.* 595 (2020) 117430. doi:10.1016/j.apcata.2020.117430.
- [59] A.J.J. Koekkoek, J.A.R. Van Veen, P.B. Gerritsen, P. Giltay, P.C.M.M. Magusin, E.J.M. Hensen, Brønsted acidity of Al/SBA-15, *Microporous Mesoporous Mater.* 151 (2012) 34–43. doi:10.1016/j.micromeso.2011.11.019.
- [60] W. Han, S. Fan, Q. Li, Y. Hu, Synthesis of Gallium Nitride Nanorods Through a Carbon Nanotube-Confined Reaction, *Science* (80-.). 277 (1997) 1287–1289. doi:10.1126/science.277.5330.1287.
- [61] U. Rizal, B.P. Swain, Raman characterization of gallium nitride nanowires deposited by chemical vapor deposition, in: *Lect. Notes Electr. Eng.*, Springer Verlag, 2017: pp. 47–61. doi:10.1007/978-981-10-

- 4394-9_6.
- [62] S. Yu, H. Li, H. Yang, D. Li, H. Sun, G. Zou, Microanalysis of wurtzite-GaN single crystals prepared by d.c. arc discharge, *Mater. Lett.* 26 (1996) 77–80. doi:10.1016/0167-577X(95)00201-4.
- [63] T.J. Goodwin, V.J. Leppert, S.H. Risbud, I.M. Kennedy, H.W.H. Lee, Synthesis of gallium nitride quantum dots through reactive laser ablation, *Appl. Phys. Lett.* 70 (1997) 3122–3124. doi:10.1063/1.119109.
- [64] J. Meng, S. Wong, Y. Jaluria, Fabrication of gallium nitride films in a chemical vapor deposition reactor, *J. Therm. Sci. Eng. Appl.* 7 (2015). doi:10.1115/1.4029353.
- [65] R.J. Molnar, T.D. Moustakas, Growth of gallium nitride by electron-cyclotron resonance plasma-assisted molecular-beam epitaxy: The role of charged species, *J. Appl. Phys.* 76 (1994) 4587–4595. doi:10.1063/1.357293.
- [66] T. Sasaki, T. Matsuoka, Substrate-polarity dependence of metal-organic vapor-phase epitaxy-grown GaN on SiC, *J. Appl. Phys.* 64 (1988) 4531–4535. doi:10.1063/1.341281.
- [67] I. Barin, O. Knacke, O. Kubaschewski, Thermochemical properties of inorganic substances, Springer Berlin Heidelberg, Berlin, Heidelberg, 1977. doi:10.1007/978-3-662-02293-1.
- [68] W.-S. Jung, Reaction intermediate(s) in the conversion of β -gallium oxide to gallium nitride under a flow of ammonia, *Mater. Lett.* 57 (2002) 110–114. doi:10.1016/S0167-577X(02)00713-9.
- [69] A.-H. Lu, F. Schüth, Nanocasting: A Versatile Strategy for Creating Nanostructured Porous Materials, *Adv. Mater.* 18 (2006) 1793–1805. doi:10.1002/adma.200600148.
- [70] S.N. Talapaneni, D. Park, J. Choy, K. Ramadass, A. Elzatahry, A.S. Al Balawi, A.M. Al-Enizi, T. Mori, A. Vinu, A.S. Al Balawi, A.M. Al-Enizi, T. Mori, A. Vinu, Facile Synthesis of Crystalline Nanoporous GaN Templated by Nitrogen Enriched Mesoporous Carbon Nitride for Friedel-Crafts Reaction, *ChemistrySelect.* 1 (2016) 6062–6068. doi:10.1002/slct.201601545.
- [71] S. Geller, Crystal Structure of β -Ga₂O₃, *J. Chem. Phys.* 33 (1960) 676–684. doi:10.1063/1.1731237.
- [72] E. Auer, A. Lugstein, S. Löffler, Y.J. Hyun, W. Brezna, E. Bertagnolli, P. Pongratz, Ultrafast VLS growth of epitaxial β -Ga₂O₃ nanowires, *Nanotechnology.* 20 (2009) 434017. doi:10.1088/0957-4484/20/43/434017.
- [73] P. Ravadgar, R.-H. Horng, S.-D. Yao, H.-Y. Lee, B.-R. Wu, S.-L. Ou, L.-W. Tu, Room-temperature ultraviolet nanowire nanolasers, *Appl. Phys. Lett.* 67 (1995) 2914–2919. doi:10.1364/OE.21.024599.
- [74] S.S. Masiero, N.R. Marcilio, O.W. Perez-Lopez, Aromatization of methane over Mo-Fe/ZSM-5 catalysts, *Catal. Letters.* 131 (2009) 194–202. doi:10.1007/s10562-009-0032-x.
- [75] H.Y. Chen, S. Tang, Z.Y. Zhong, J. Lin, K.L. Tan, XPS and FTIR studies of Mo/ZSM-5 catalysts for nonoxidative conversion of methane to aromatics, *Surf. Rev. Lett.* 8 (2001) 627–632. doi:10.1142/S0218625X0100152X.
- [76] X. Chen, T. Zhang, L. Xia, T. Li, M. Zheng, Z. Wu, X. Wang, Z. Wei, Q. Xin, C. Li, Catalytic decomposition of hydrazine over supported molybdenum nitride catalysts in a monopropellant thruster, *Catal. Letters.* 79 (2002) 21–25. doi:10.1023/A:1015343922044.
- [77] P.A. Aegerter, W.W.C. Quigley, G.J. Simpson, D.D. Ziegler, J.W. Logan, K.R. McCrea, S. Glazier, M.E. Bussell, Thiophene hydrodesulfurization over alumina-supported molybdenum carbide and nitride catalysts: Adsorption sites, catalytic activities, and nature of the active surface, *J. Catal.* 164 (1996) 109–121. doi:10.1006/jcat.1996.0367.
- [78] N. Chino, T. Okubo, Nitridation mechanism of mesoporous silica: SBA-15, *Microporous Mesoporous Mater.* 87 (2005) 15–22. doi:10.1016/j.micromeso.2005.07.034.

- [79] B. Xu, B. Zheng, W. Hua, Y. Yue, Z. Gao, Support effect in dehydrogenation of propane in the presence of CO₂ over supported gallium oxide catalysts, *J. Catal.* 239 (2006) 470–477. doi:10.1016/j.jcat.2006.02.017.
- [80] K. Dutta, M. Shahryari, J. Kopyscinski, Direct Nonoxidative Methane Coupling to Ethylene over Gallium Nitride: A Catalyst Regeneration Study, *Ind. Eng. Chem. Res.* 59 (2020) 4245–4256. doi:10.1021/acs.iecr.9b05548.
- [81] J. Van Doorn, J.A. Moulijn, Carbon deposition on catalysts, *Catal. Today.* 7 (1990) 257–266. doi:10.1016/0920-5861(90)85024-I.
- [82] M. Huo, L. Li, X. Zhao, Y. Zhang, J. Li, Synthesis of Ni-based catalysts supported on nitrogen-incorporated SBA-16 and their catalytic performance in the reforming of methane with carbon dioxide, *J. Fuel Chem. Technol.* 45 (2017) 172–181. doi:10.1016/S1872-5813(17)30012-9.
- [83] N. Kosinov, E.A. Uslamin, F.J.A.G. Coumans, A.S.G. Wijkema, R.Y. Rohling, E.J.M. Hensen, Structure and Evolution of Confined Carbon Species during Methane Dehydroaromatization over Mo/ZSM-5, *ACS Catal.* 8 (2018) 8459–8467. doi:10.1021/acscatal.8b02491.
- [84] N. Kosinov, A.S.G. Wijkema, E. Uslamin, R. Rohling, F.J.A.G. Coumans, B. Mezari, A. Parastayev, A.S. Poryvaev, M. V. Fedin, E.A. Pidko, E.J.M. Hensen, Confined Carbon Mediating Dehydroaromatization of Methane over Mo/ZSM-5, *Angew. Chemie Int. Ed.* 57 (2018) 1016–1020. doi:10.1002/anie.201711098.
- [85] A.D. Mayernick, M.J. Janik, Methane oxidation on Pd-Ceria: A DFT study of the mechanism over Pd xCe_{1-x}O₂, Pd, and PdO, *J. Catal.* 278 (2011) 16–25. doi:10.1016/j.jcat.2010.11.006.
- [86] A. Trincherro, A. Hellman, H. Grönbeck, Methane oxidation over Pd and Pt studied by DFT and kinetic modeling, *Surf. Sci.* 616 (2013) 206–213. doi:10.1016/j.susc.2013.06.014.
- [87] N. Ghazali, K. Yasui, A. Hashim, Synthesis of gallium nitride nanostructures by nitridation of electrochemically deposited gallium oxide on silicon substrate, *Nanoscale Res. Lett.* 9 (2014) 685. doi:10.1186/1556-276X-9-685.
- [88] G. Gougeon, Master's thesis, Ecole Polytechnique Federale de Lausanne, Switzerland and McGill University, Canada, 2019.
- [89] P. Giannozzi, S. Baroni, N. Bonini, M. Calandra, R. Car, C. Cavazzoni, D. Ceresoli, G.L. Chiarotti, M. Cococcioni, I. Dabo, A. Dal Corso, S. de Gironcoli, S. Fabris, G. Fratesi, R. Gebauer, U. Gerstmann, C. Gougoussis, A. Kokalj, M. Lazzeri, L. Martin-Samos, N. Marzari, F. Mauri, R. Mazzarello, S. Paolini, A. Pasquarello, L. Paulatto, C. Sbraccia, S. Scandolo, G. Sclauzero, A.P. Seitsonen, A. Smogunov, P. Umari, R.M. Wentzcovitch, QUANTUM ESPRESSO: a modular and open-source software project for quantum simulations of materials, *J. Phys. Condens. Matter.* 21 (2009) 395502. doi:10.1088/0953-8984/21/39/395502.
- [90] M.A.A. Clyne, R.F. Walker, Absolute rate constants for elementary reactions in the chlorination of CH₄, CD₄, CH₃Cl, CH₂Cl₂, CHCl₃, CCl₃ and CBrCl₃, *J. Chem. Soc. Faraday Trans. 1 Phys. Chem. Condens. Phases.* 69 (1973) 1547. doi:10.1039/f19736901547.
- [91] A. Sattler, Hydrogen/Deuterium (H/D) Exchange Catalysis in Alkanes, *ACS Catal.* 8 (2018) 2296–2312. doi:10.1021/acscatal.7b04201.
- [92] E. Iglesia, J.E. Baumgartner, Hydrogen transfer and activation of propane and methane on ZSM5-based catalysts, *Catal. Letters.* 21 (1993) 55–70. doi:10.1007/BF00767371.
- [93] E.W. Shin, J.H. Kang, W.J. Kim, J.D. Park, S.H. Moon, Performance of Si-modified Pd catalyst in acetylene hydrogenation: the origin of the ethylene selectivity improvement, *Appl. Catal. A Gen.* 223 (2002) 161–172. doi:10.1016/S0926-860X(01)00758-X.
- [94] D. Murzin, Modeling of Adsorption and Kinetics in Catalysis over Induced Nonuniform Surfaces:

- Surface Electronic Gas Model, *Ind. Eng. Chem. Res.* 34 (1995) 1208–1218. doi:10.1021/ic00043a025.
- [95] V.H. Dibeler, F. 1 Mohler, M. De Hemptinne, Mass Spectra of the Deuteroethylenes, *J. Res. Natl. Bur. Stand.* (1934). 53 (1954). https://nvlpubs.nist.gov/nistpubs/jres/53/jresv53n2p107_A1b.pdf (accessed February 26, 2020).
- [96] W.E. Wallace, NIST Chemistry WebBook: NIST Standard Reference Database Number 69, National Institute of Standards and Technology, n.d.
- [97] A. Piterina, J. Barlett, J.T. Pembroke, ¹³C-NMR Assessment of the Pattern of Organic Matter Transformation during Domestic Wastewater Treatment by Autothermal Aerobic Digestion (ATAD), *Int. J. Environ. Res. Public Health.* 6 (2009) 2288–2306. doi:10.3390/ijerph6082288.
- [98] J. Guo, Z. Hou, J. Gao, X. Zheng, DRIFTS Study on Adsorption and Activation of CH₄ and CO₂ over Ni/SiO₂ Catalyst with Various Ni Particle Sizes, *Chinese J. Catal.* 28 (2007) 22–26. doi:10.1016/S1872-2067(07)60009-6.
- [99] G. Socrates, *Infrared and Raman Characteristic Group Frequencies: Tables and Charts*, 3rd Edition, 3rd ed., John Wiley & Sons, Ltd, 2004.
- [100] D.C. McKean, G.P. McQuillan, J.L. Duncan, N. Shephard, B. Munro, V. Fawcett, H.G.M. Edwards, Vibrational spectra of trimethyl gallium species in relation to the force field and methyl group internal rotation, *Spectrochim. Acta - Part A Mol. Spectrosc.* 43 (1987) 1405–1411. doi:10.1016/S0584-8539(87)80019-3.
- [101] L. Chen, L. Lin, Z. Xu, T. Zhang, D. Liang, Q. Xin, P. Ying, Interaction of methane with surfaces of silica, aluminas and HZSM-5 zeolite. A comparative FT-IR study, *Catal. Letters.* 35 (1995) 245–258. doi:10.1007/BF00807180.
- [102] M. Rozenberg, G. Shoham, I. Reva, R. Fausto, Low temperature FTIR spectroscopy and hydrogen bonding in cytosine polycrystals, *Spectrochim. Acta - Part A Mol. Biomol. Spectrosc.* 60 (2004) 463–470. doi:10.1016/S1386-1425(03)00251-8.
- [103] J.-C. Maire, U. Krüerke, M. Mirbach, W. Petz, C. Siebert, *Ga Organogallium Compounds*, Springer Berlin Heidelberg, 1986. doi:10.1007/978-3-662-07374-2.
- [104] C. Chapados, A. Cabana, Infrared Spectra and Structures of Solid CH₄ and CD₄ in Phases I and II, *Can. J. Chem.* 50 (1972) 3521–3533. doi:10.1139/v72-566.
- [105] K. Chakarova, K. Hadjiivanov, Interaction of benzene with hydroxyl groups in zeolites: A FTIR study of C₆H₆ and C₆D₆ adsorption on H-ZSM-5 and D-ZSM-5, *Microporous Mesoporous Mater.* 143 (2011) 180–188. doi:10.1016/j.micromeso.2011.02.025.
- [106] J.F.M. Aarts, N.R.M. Sassen, Vibrational spectra of C₆H₆ and C₆H₅D adsorbed on Pd(111). A comparative study of electron energy loss spectra, *Surf. Sci.* 214 (1989) 257–275. doi:10.1016/0039-6028(89)90422-6.
- [107] W. Tu, M. Ghossoub, C.V. Singh, Y.H.C. Chin, Consequences of Surface Oxophilicity of Ni, Ni-Co, and Co Clusters on Methane Activation, *J. Am. Chem. Soc.* 139 (2017) 6928–6945. doi:10.1021/jacs.7b01632.
- [108] C.N. Satterfield, P.J. Cadle, Diffusion in commercially manufactured pelleted catalysts, *Ind. Eng. Chem. Process Des. Dev.* 7 (1968) 256–260. doi:10.1021/i260026a017.
- [109] J. Kopyscinski, Production of synthetic natural gas in a fluidized bed reactor, (2010) 1–252. doi:10.3929/ethz-a-006031831.
- [110] T.J. Rottreau, C.M.A. Parlett, A.F. Lee, R. Evans, Diffusion NMR Characterization of Catalytic Silica Supports: A Tortuous Path, (2017). doi:10.1021/acs.jpcc.7b02929.
- [111] Y. Liu, Z. Li, X. Yang, Y. Xing, C. Tsai, Q. Yang, Z. Wang, R.T. Yang, Performance of mesoporous

- silicas (MCM-41 and SBA-15) and carbon (CMK-3) in the removal of gas-phase naphthalene: adsorption capacity, rate and regenerability, *RSC Adv.* 6 (2016) 21193–21203. doi:10.1039/C5RA27289K.
- [112] D. Pérez-Quintanilla, A. Sánchez, I. del Hierro, M. Fajardo, I. Sierra, Preconcentration of Zn(II) in water samples using a new hybrid SBA-15-based material, *J. Hazard. Mater.* 166 (2009) 1449–1458. doi:10.1016/j.jhazmat.2008.12.065.
- [113] J.N. Carstens, A.T. Bell, Methane activation and conversion to higher hydrocarbons on supported ruthenium, *J. Catal.* 161 (1996) 423–429. doi:10.1006/jcat.1996.0200.
- [114] T. V. Choudhary, D.W. Goodman, Methane activation on Ni and Ru model catalysts, *J. Mol. Catal. A Chem.* 163 (2000) 9–18. doi:10.1016/S1381-1169(00)00395-2.
- [115] S.J. Han, S. Lee, H.W. Kim, K. Kim, Y.T. Kim, Non-oxidative direct conversion of methane on silica-based iron catalysts: effect of catalytic surface, *ACS Catal.* (2019). doi:10.1021/acscatal.9b01643.
- [116] J. Kopyscinski, T.J. Schildhauer, F. Vogel, S.M.A. Biollaz, A. Wokaun, Applying spatially resolved concentration and temperature measurements in a catalytic plate reactor for the kinetic study of CO methanation, *J. Catal.* 271 (2010) 262–279. doi:10.1016/j.jcat.2010.02.008.
- [117] R. Yadav, R.G. Rinker, Steady-state methanation kinetics over a Ni/Al₂O₃ catalyst, *Can. J. Chem. Eng.* 71 (1993) 202–208. doi:10.1002/cjce.5450710206.
- [118] G.C. Laredo, E. Altamirano, J.A. De los Reyes, Self-inhibition observed during indole and o-ethylaniline hydrogenation in the presence of dibenzothiophene, *Appl. Catal. A Gen.* 242 (2003) 311–320. doi:10.1016/S0926-860X(02)00521-5.
- [119] Z.M. de Pedro, J.A. Casas, L.M. Gomez-Sainero, J.J. Rodriguez, Hydrodechlorination of dichloromethane with a Pd/AC catalyst: Reaction pathway and kinetics, *Appl. Catal. B Environ.* 98 (2010) 79–85. doi:10.1016/j.apcatb.2010.05.007.
- [120] A.C.A. Monteiro-Gezork, R. Natividad, J.M. Winterbottom, Hydrogenation of naphthalene on NiMo-Ni- and Ru/Al₂O₃ catalysts: Langmuir-Hinshelwood kinetic modelling, *Catal. Today.* 130 (2008) 471–485. doi:10.1016/j.cattod.2007.10.102.
- [121] J.-H. Wen, G.-C. Wang, Methane Non-Oxidative Direct Conversion to C₂ Hydrogenations over CeO₂-Supported Pt Catalysts : A DFT Study, *J. Phys. Chem. C.* (2020) acs.jpcc.0c03494. doi:10.1021/acs.jpcc.0c03494.
- [122] R. Fricke, H. Kosslick, G.G. Lischke, M. Richter, Incorporation of Gallium into Zeolites: Syntheses, Properties and Catalytic Application, *Chem. Rev.* 100 (2000) 2303–2405. doi:10.1021/cr9411637.
- [123] B. Liu, Y. Yang, A. Sayari, Non-oxidative dehydroaromatization of methane over Ga-promoted Mo/HZSM-5-based catalysts, *Appl. Catal. A Gen.* 214 (2001) 95–102. doi:10.1016/S0926-860X(01)00470-7.
- [124] V.R. Choudhary, A.K. Kinage, T. V. Choudhary, Low-Temperature Nonoxidative Activation of Methane over H-Galloaluminosilicate (MFI) Zeolite, *Science* (80-.). 275 (1997) 1286–1288. doi:10.1126/science.275.5304.1286.
- [125] Y. Lu, Z. Xu, Z. Tian, T. Zhang, L. Lin, Methane aromatization in the absence of an added oxidant and the bench scale reaction test, 1999. doi:https://doi.org/10.1023/A:1019063425801.

Appendix

Appendix A1 for Chapter 5: HRTEM images of unsupported catalysts (Fig. A1–1 to A1–5).

Darkfield HRTEM images of fresh Ga_2O_3 and fresh GaN–650 nanoparticles; The HRTEM image of fresh Ga_2O_3 nanoparticle; The HRTEM image of fresh GaN–650 nanoparticle showing GaN and Ga_2O_3 phases; The HRTEM image of fresh GaN–650 nanoparticle showing the c-plane of the GaN phase; Micrograph of fresh GaN–650 nanoparticle, HRTEM image GaN phase and corresponding Inverse Fast Fourier Transform (IFFT), HRTEM image of GaN– Ga_2O_3 phase and corresponding IFFT.

Appendix A2 for Chapter 5: HRTEM images of supported catalysts (Fig. A2–1).

The HRTEM image of spent GaN/SBA15–650, agglomerated particles in spent GaN/SBA15–650 with STEM image (inset), HRTEM images of spent GaN/SBA15–800, and STEM image of spent GaN/SBA15–800.

Appendix A3 for Chapter 5: Activity measurements of the synthesized catalysts (Fig. A3–1 to A3–9).

Molar flow rates of CO_2 and H_2O as a function of time on stream for the methane activation at 700 °C and 1 bar over unsupported Ga_2O_3 and GaN–600 catalysts; SEM-EDS for fresh and spent unsupported Ga_2O_3 ; XRD pattern for fresh and spent unsupported Ga_2O_3 ; Molar flow rate for

naphthalene for unsupported catalysts synthesized at different nitridation temperatures and at 750 °C at different NH₃ exposure durations; images of fresh and spent unsupported and supported catalysts; The ratio of H₂ to C₂H₄ as a function of time on stream for unsupported and supported catalysts; Molar flow rates of CO₂ and H₂O as a function of time on stream for the methane activation at 700 °C and 1 bar over supported Ga₂O₃/SBA15 and GaN/SBA15-650 catalysts; Reproducibility and repeatability of runs with unsupported (GaN-750) and supported catalysts (GaN/SBA15-700).

Appendix A4 for Chapter 5: Temperature-programmed oxidation (TPO-MS) of spent catalysts (Fig. A4-1).

Water evolution during TPO of spent catalysts GaN-750 and GaN/SBA15-700.

Appendix A5 for Chapter 6: Certificate of Analysis (COA) for methane isotope gases (Sigma-Aldrich).

Appendix A5 for Chapter 6: Forward rate expressions for CH₄ activation to C₂H₄ and H₂, and results for kinetic modeling (Fig. A5-1 and A5-2).

Appendix A6 for Chapter 7: Catalyst regeneration (Fig. A6-1 to A6-11).

CO₂ formation rate during activation cycles over GaN-R, GaN/SBA15-R, GaN-RN, and GaN/SBA15-RN; Product molar flow rates for C₃H₆, C₆H₆, and C₇H₈ as a function of time on stream over GaN-R, GaN/SBA15-R, GaN-RN, GaN/SBA15-RN, and supported GaN/SBA15 for long term run (150 h); TPO-MS for spent supported GaN/SBA15 catalyst used for methane activation for 150 h; CO₂ molar flow rate as a function of time, and qualitative water signal (m/z = 18, normalized with internal standard Ar with m/z = 40) during the TPO; SEM-EDS for spent GaN (1 cycle); SEM-EDS for GaN-R (1 cycle); SEM-EDS for GaN-RN (1 cycle, regeneration + re-nitridation); SEM-EDS for the sample obtained by H₂ TPR of spent GaN.

A1 HRTEM images of unsupported catalysts

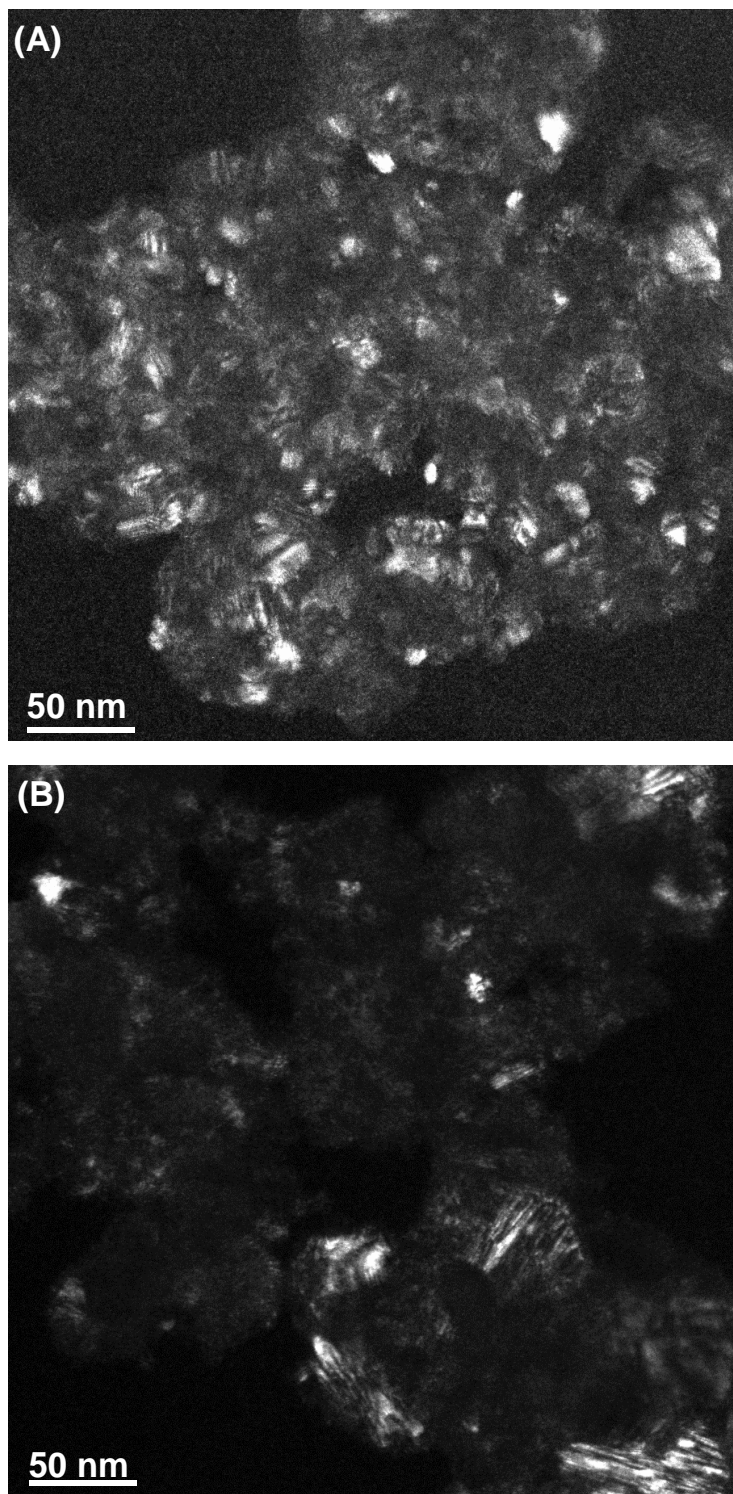


Fig. A1-1 Darkfield HRTEM images of (A) fresh Ga_2O_3 and (B) fresh GaN-650 nanoparticles.

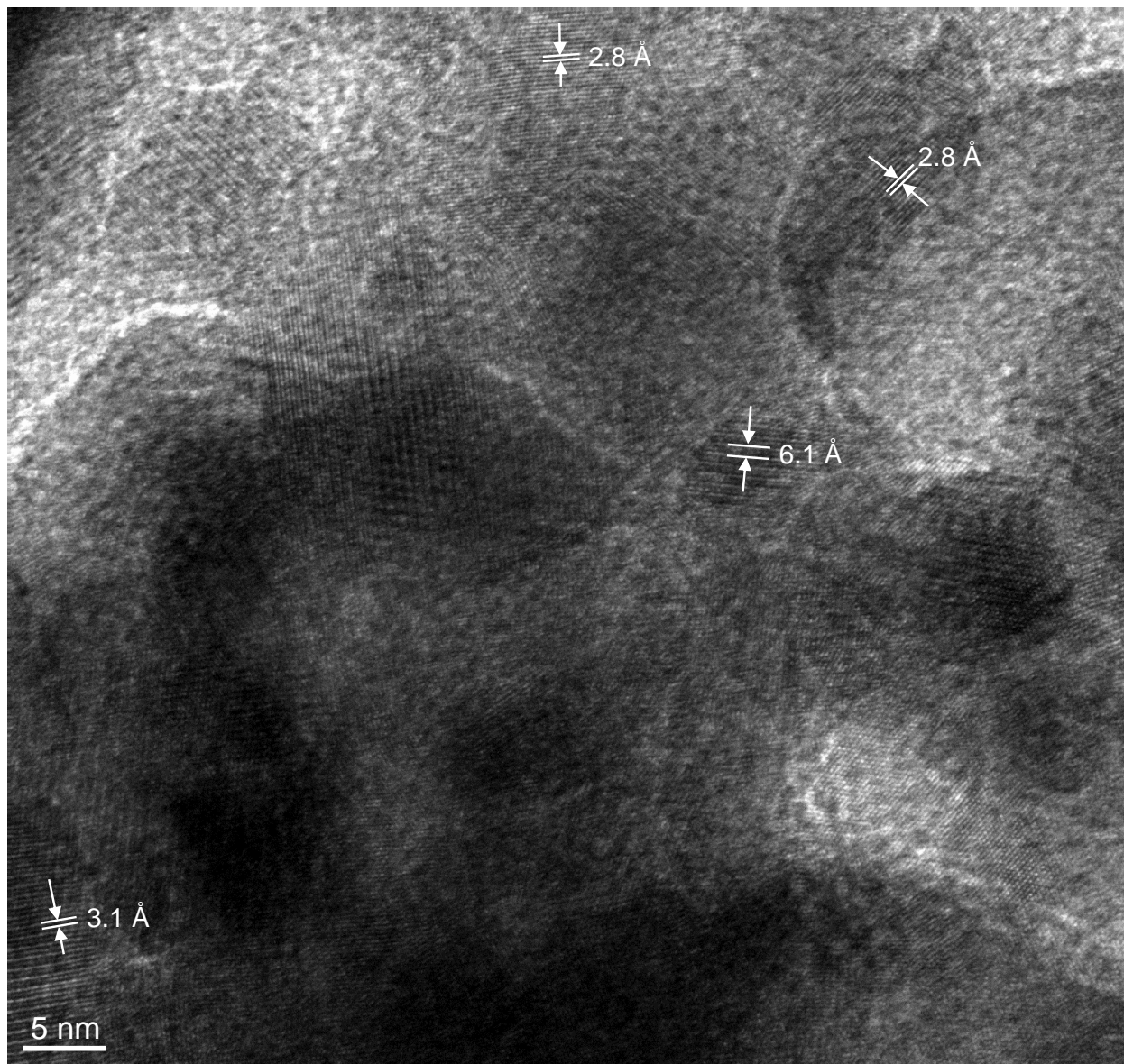


Fig. A1-2. The HRTEM image of fresh Ga₂O₃ nanoparticle.

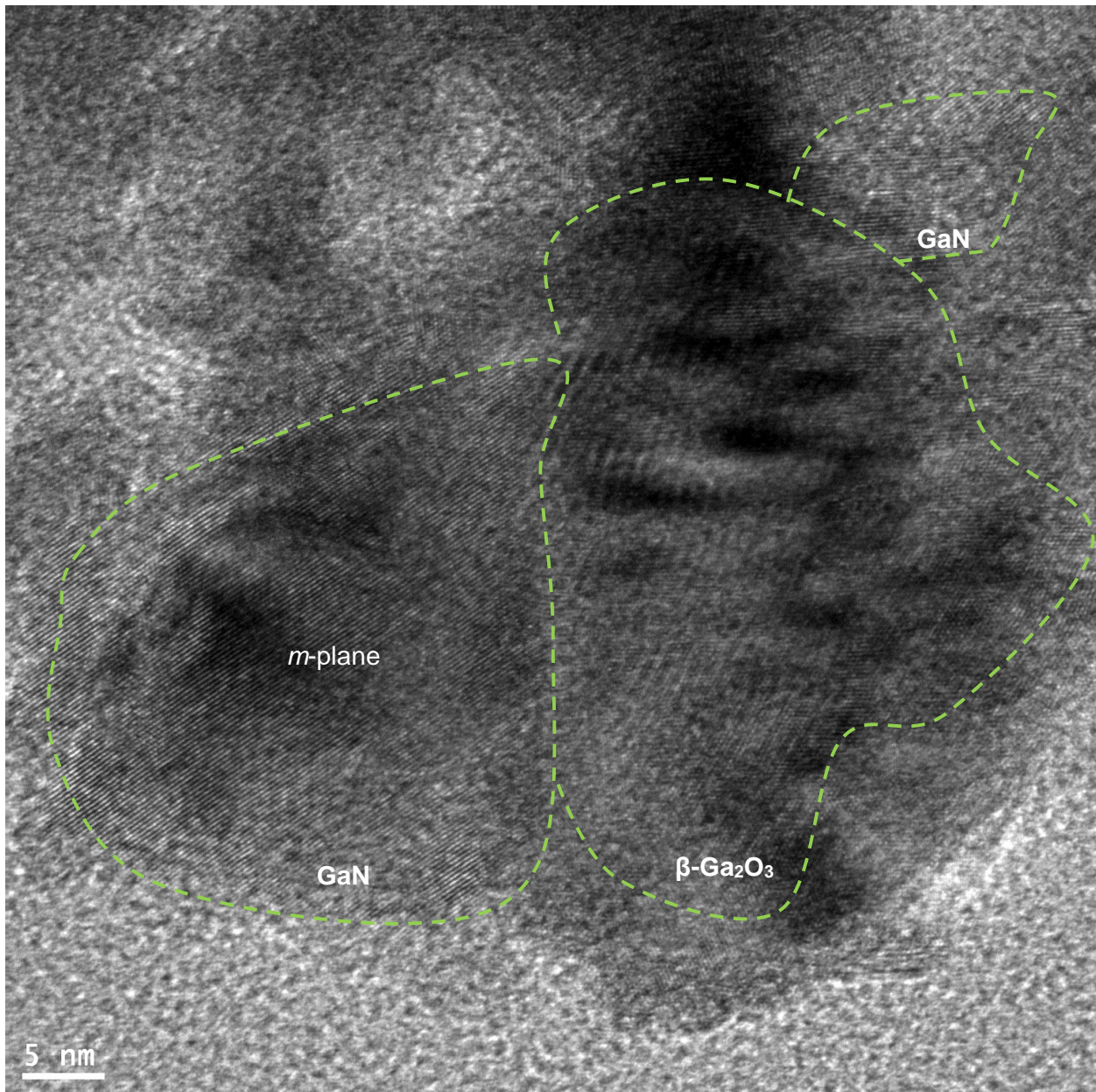


Fig. A1-3. The HRTEM image of fresh GaN-650 nanoparticle showing GaN and Ga₂O₃ phases.

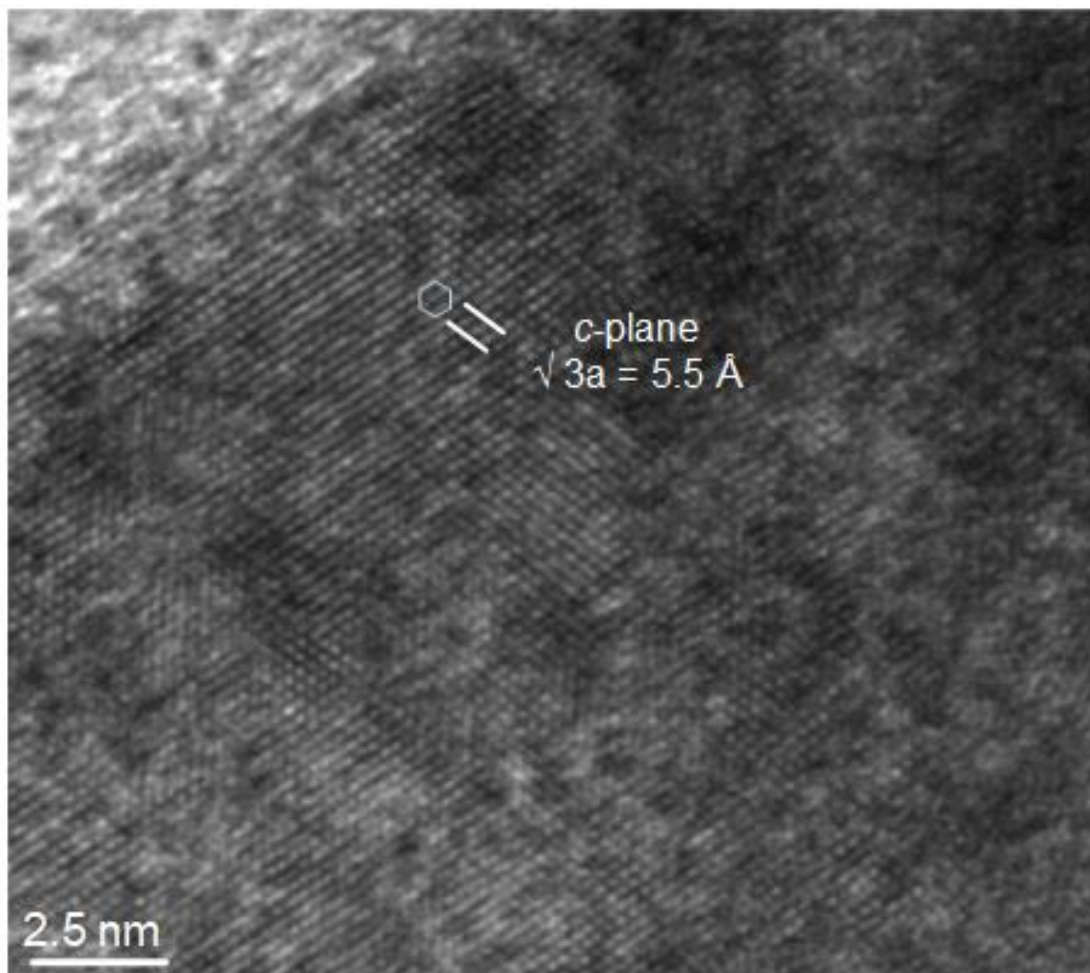


Fig. A1-4. The HRTEM image of fresh GaN-650 nanoparticle showing the c -plane of the GaN phase.

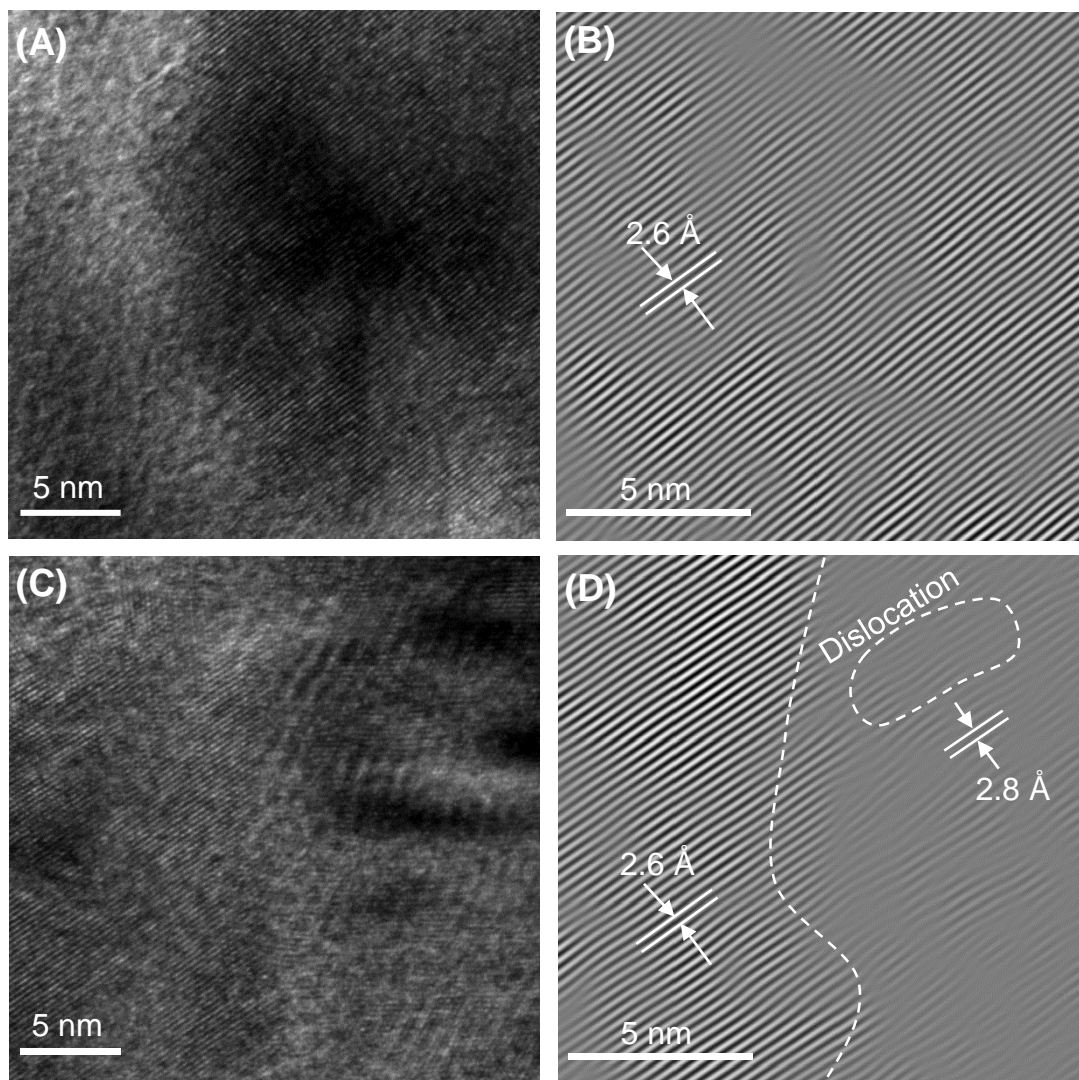


Fig. A1-5. Micrograph of fresh GaN-650 nanoparticle (A) HRTEM image GaN phase and (B) corresponding Inverse Fast Fourier Transform (IFFT), (C) HRTEM image of GaN-Ga₂O₃ phase and (D) corresponding IFFT.

A2 HRTEM images of supported catalysts

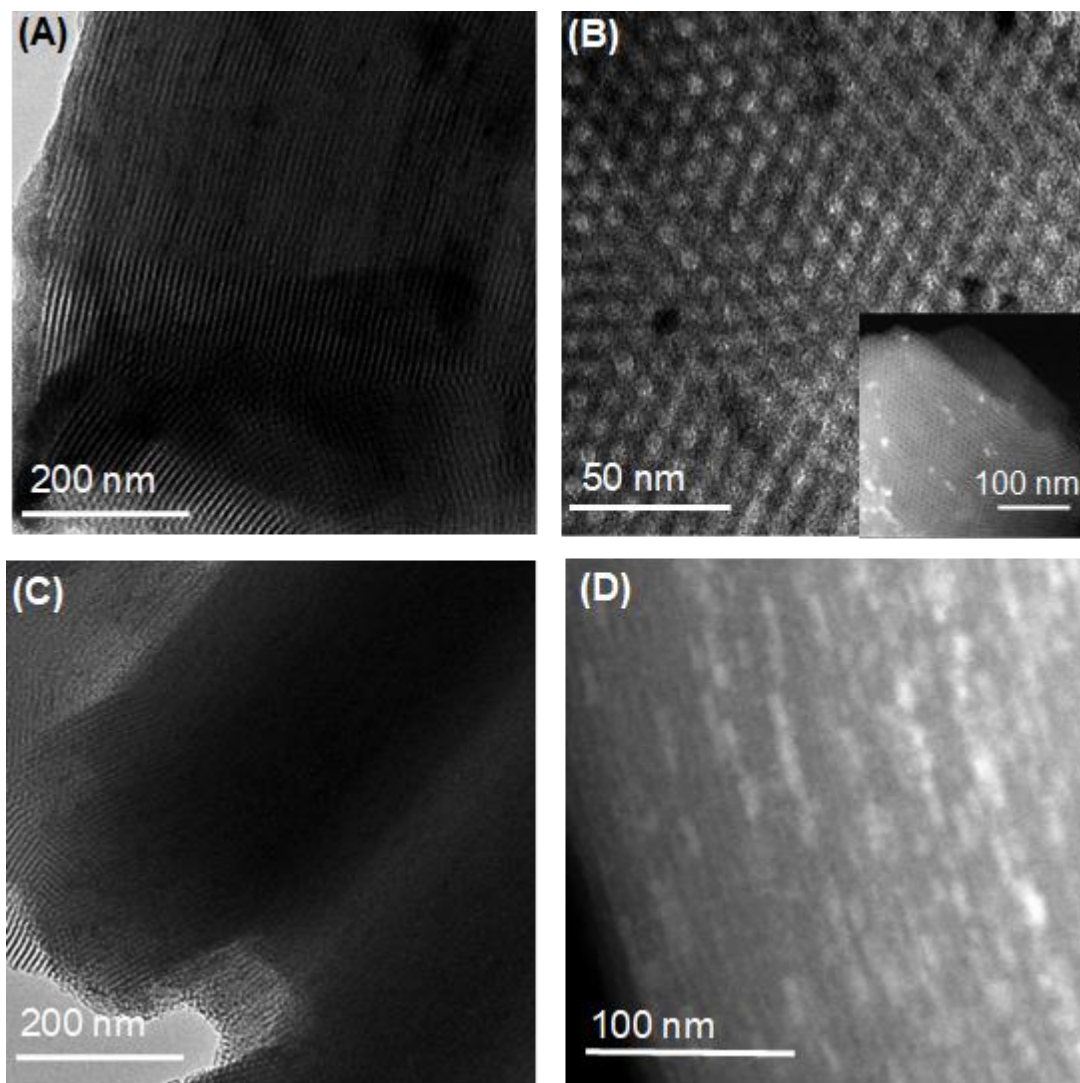


Fig. A2-1. (A) The HRTEM image of spent GaN/SBA15-650 (B) agglomerated particles in spent GaN/SBA15-650 with STEM image (inset) (C) HRTEM images of spent GaN/SBA15-800 and (D) STEM image of spent GaN/SBA15-800.

A3 Activity measurements of the synthesized catalysts

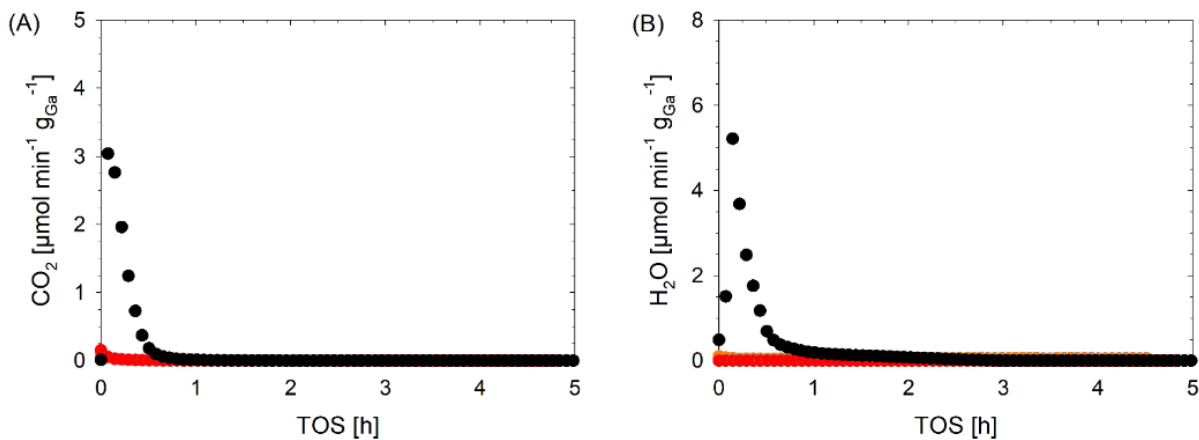
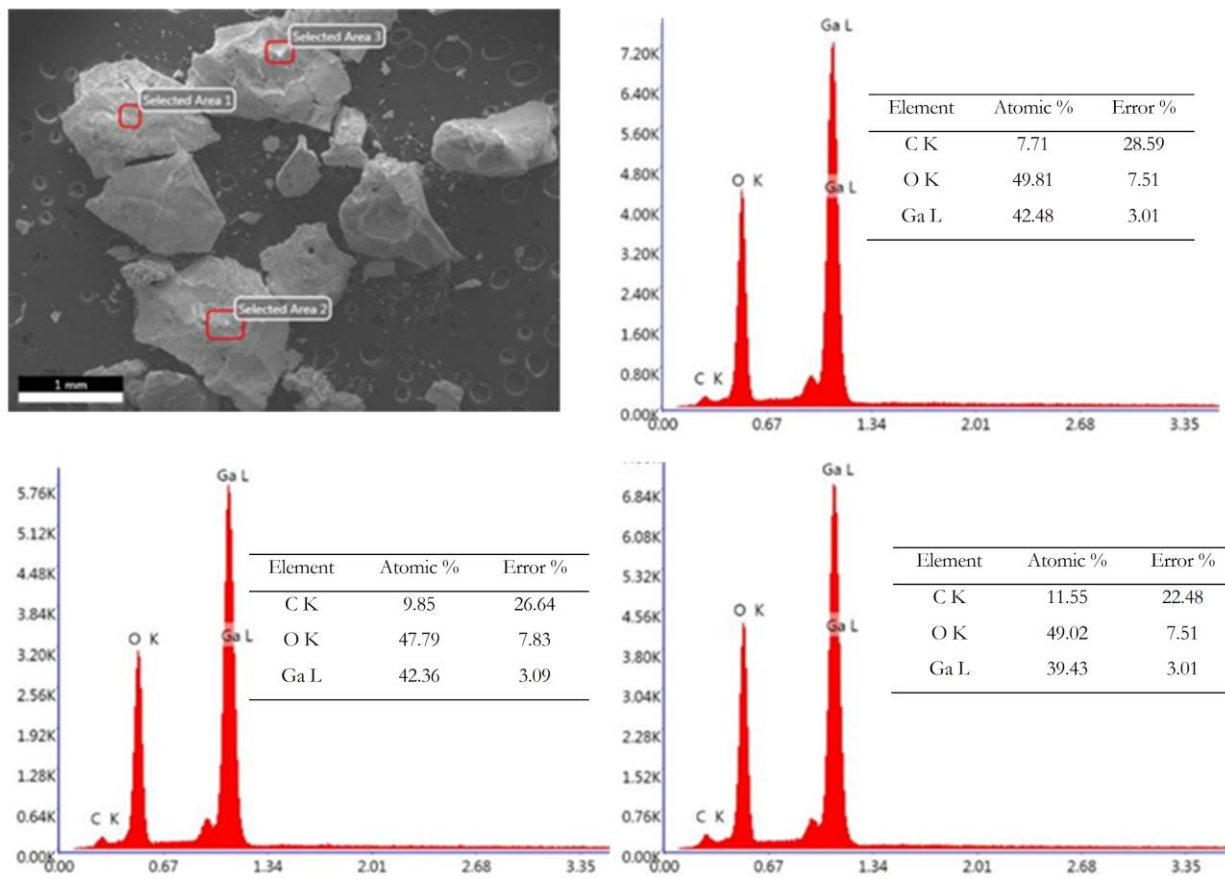
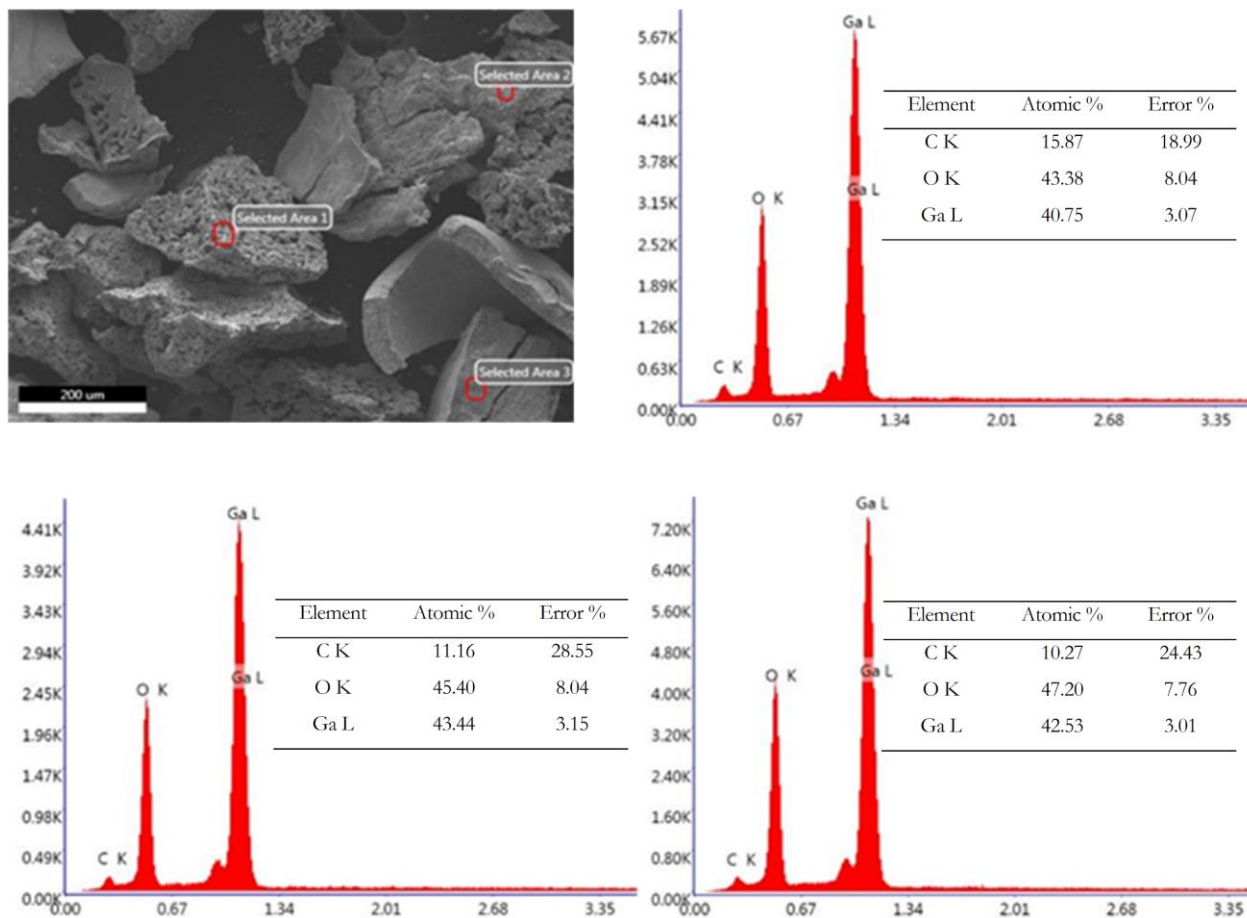
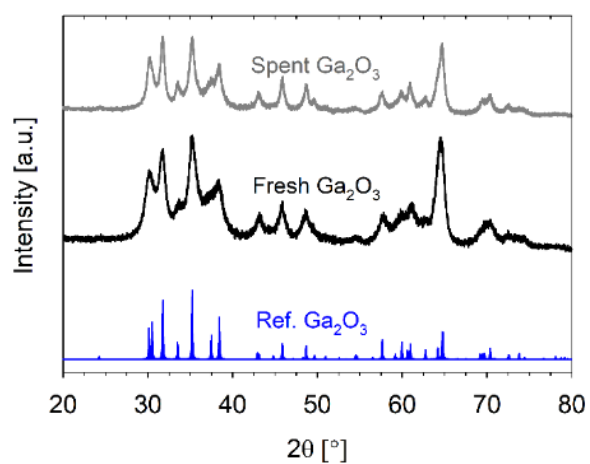


Fig. A3-1. Molar flow rates of (A) CO₂ and (B) H₂O as a function of time on stream for the methane activation at 700 °C and 1 bar over unsupported Ga₂O₃ (black) and GaN-600 catalysts (red).

Fig. A3-2. SEM-EDS for fresh unsupported Ga_2O_3 .

Fig. A3-3. SEM-EDS for spent unsupported Ga_2O_3 .Fig. A3-4. XRD pattern for fresh and spent unsupported Ga_2O_3 .

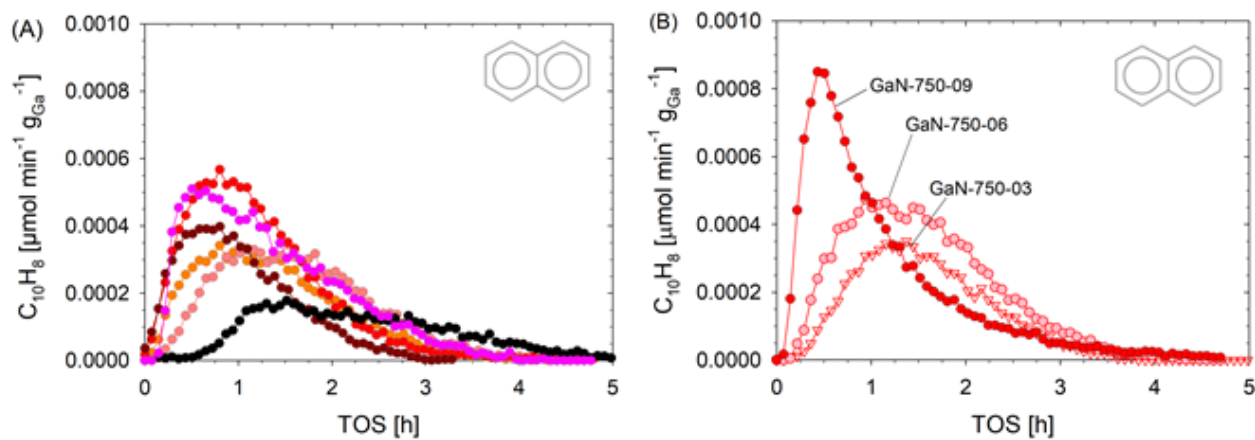


Fig. A3-5. Molar flow rate for naphthalene for unsupported catalysts synthesized (A) at different nitridation temperatures and (B) at 750 °C at different NH_3 exposure durations.

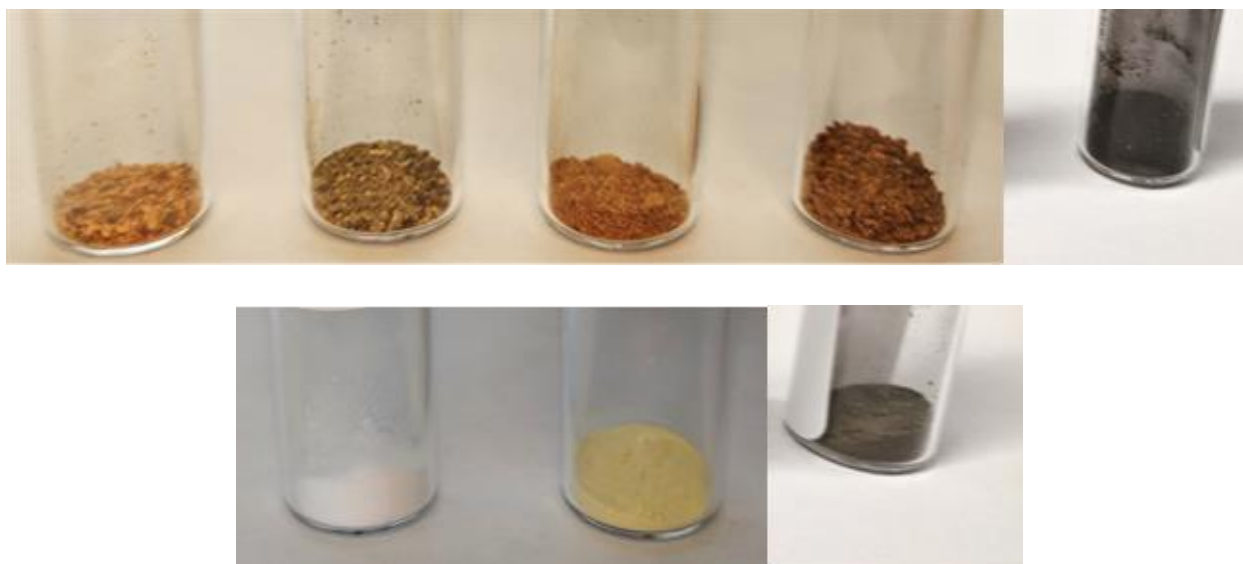


Fig. A3-6. **Top:** from left to right, fresh unsupported GaN-650, GaN-700, GaN-750, GaN-800, and spent GaN-750 catalysts; **Bottom:** from left to right, fresh supported $\text{Ga}_2\text{O}_3/\text{SBA15}$, GaN/SBA15-800 (all GaN/SBA15 were light yellow in color), and spent GaN/SBA15-700 catalysts.

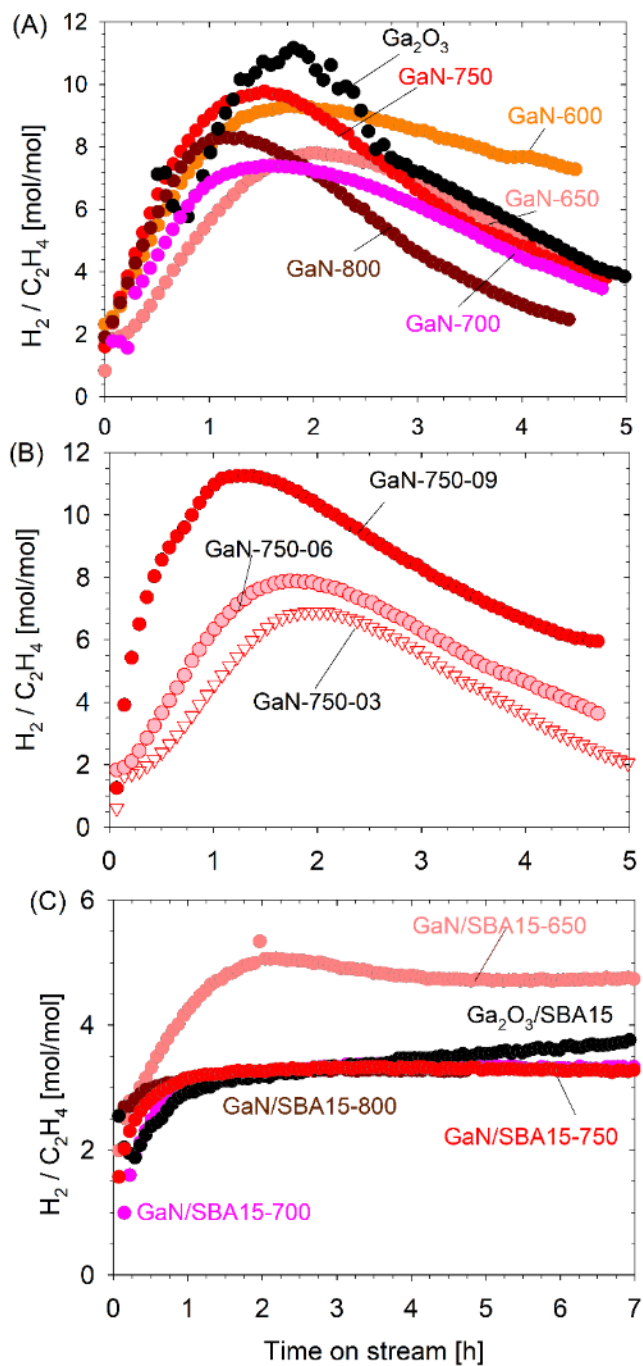


Fig. A3-7. The ratio of H_2 to C_2H_4 as a function of time on stream for unsupported and supported catalysts

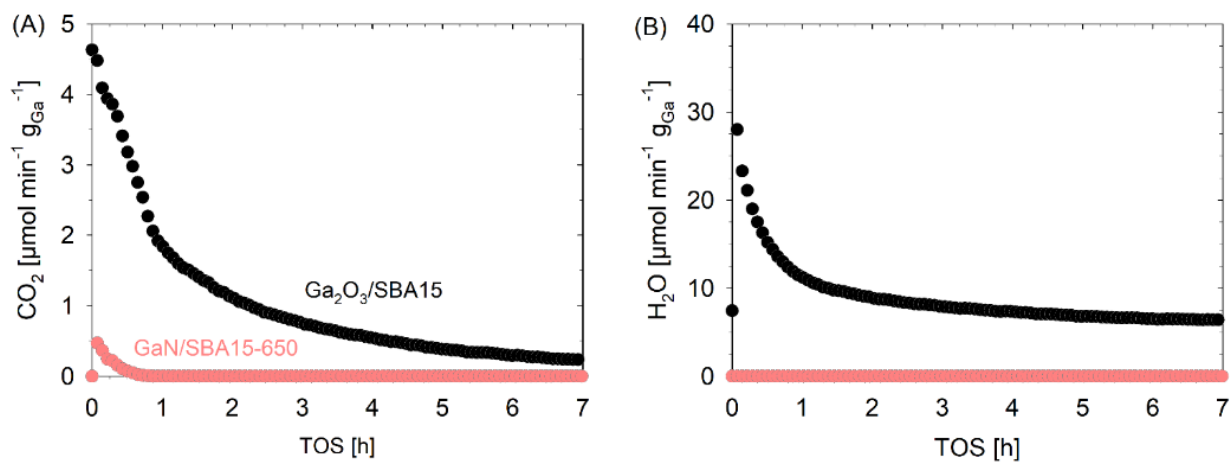


Fig. A3–8. Molar flow rates of (A) CO₂ and (B) H₂O as a function of time on stream for the methane activation at 700 °C and 1 bar over supported Ga₂O₃/SBA15 and GaN/SBA15–650 catalysts.

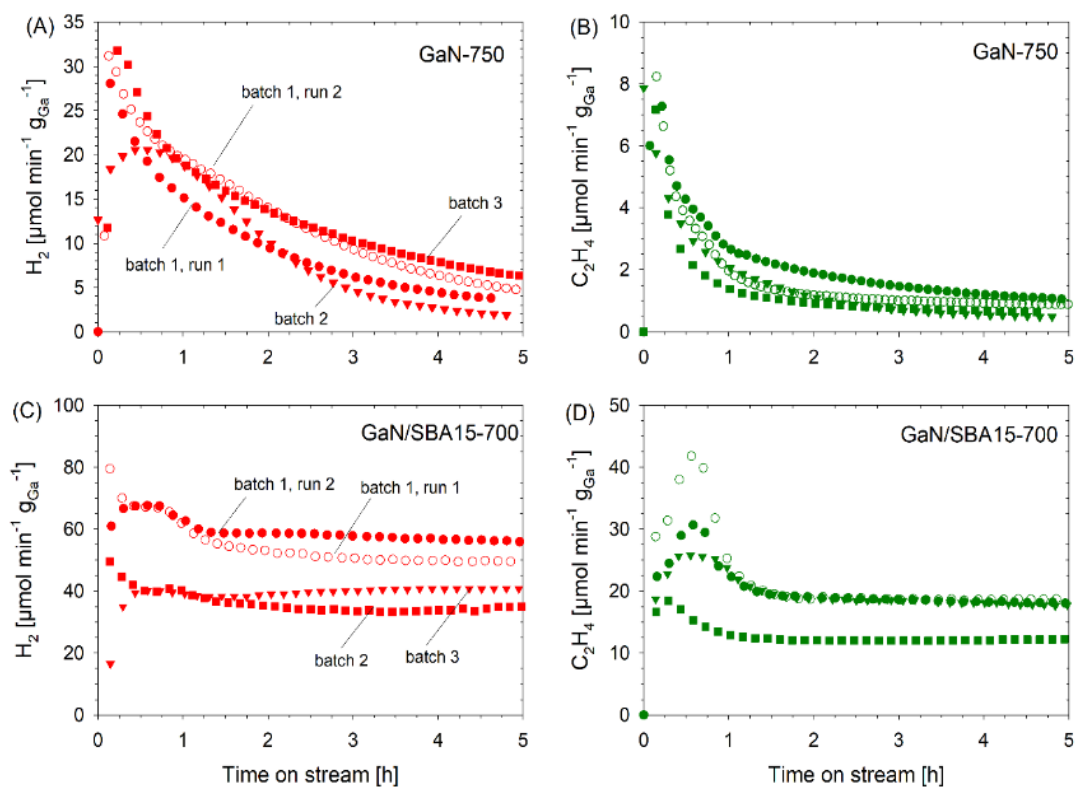


Fig. A3–9. Reproducibility and repeatability of runs with unsupported (GaN–750) and supported catalysts (GaN/SBA15–700). The symbols (●) and (○) represent run 1 and 2 from catalyst batch 1, while (▼) and (■) refer to batch 2 and 3, respectively. All catalysts were synthesized using the same methodology.

A4 Temperature-programmed oxidation (TPO-MS) of spent catalysts

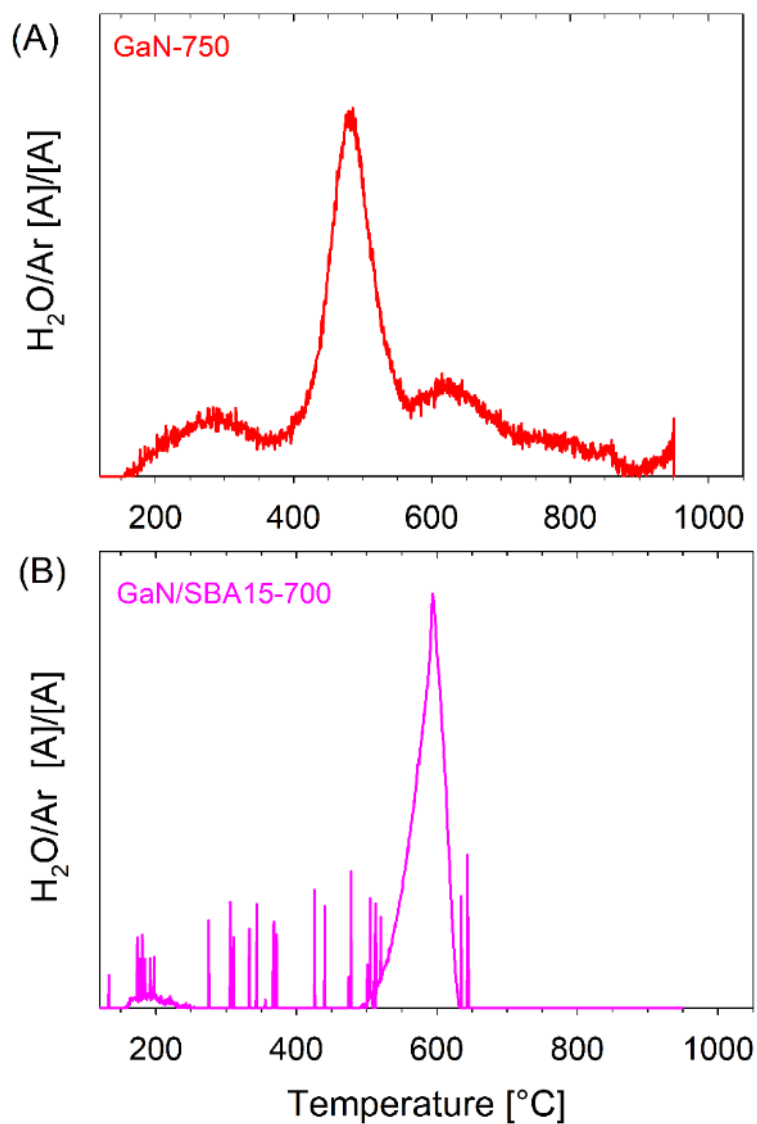


Fig. A4-1. Water evolution during TPO of spent catalysts (A) GaN-750 and (B) GaN/SBA15-700. Ion-current [A] for $m/z = 18$ was normalized with internal standard Ar ion current ($m/z = 40$).

A5-1 Certificate of analysis (COA) for methane isotope gases (Sigma-Aldrich)

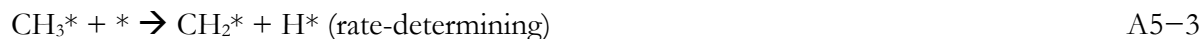
Parameters	CH ₃ D	CD ₄	¹³ CH ₄	
Purity	≥ 98*	≥ 99	≥ 99	%
Air	3845	-	-	ppmV
Ar / O ₂	-	<50	<30	ppmV
CO ₂	15	<15	713	ppmV
N ₂	-	50	50	ppmV
C ₂ H ₆	112	30	-	ppmV
CO	-	-	57	ppmV
THC	-	-	<20	ppmV

* D enrichment

A5-2 Forward rate expressions for CH₄ activation to C₂H₄ and H₂

Model 3

Based on our DFT results, the elementary steps are



From equation A5-1

$$K_1 = \frac{\theta_{\text{CH}_4}}{p_{\text{CH}_4} \theta_v}$$

The subscript v is for the vacant sites.

$$\theta_{\text{CH}_4} = K_1 p_{\text{CH}_4} \theta_v \quad \text{A5-6}$$

From equation A5-2

$$K_2 = \frac{\theta_{\text{CH}_3} \theta_{\text{H}}}{\theta_{\text{CH}_4} \theta_v}$$

$$\theta_{\text{CH}_3} \theta_{\text{H}} = K_2 \theta_{\text{CH}_4} \theta_v$$

$$\theta_{\text{CH}_3} \theta_{\text{H}} = K_1 K_2 p_{\text{CH}_4} \theta_v^2$$

Assuming $\theta_{\text{CH}_3} \approx \theta_{\text{H}}$

$$\theta_{\text{CH}_3}^2 = K_1 K_2 p_{\text{CH}_4} \theta_v^2$$

$$\theta_{\text{CH}_3} = \theta_v \sqrt{K_1 K_2 p_{\text{CH}_4}} \quad \text{A5-7}$$

From equation A5-3, no backward reaction (approach to equilibrium, η is less than 2%)

$$r = k_3 \theta_{\text{CH}_3} \theta_v \quad \text{A5-8}$$

From equation A5-7 and A5-8

$$r = k_3 \theta_v^2 \sqrt{K_1 K_2 p_{CH_4}}$$

Site balance gives, $\theta_{CH_3} + \theta_v = 1$ (note that H and CH₃ do not adsorb on the same type of site)

$$\theta_{CH_3} + \theta_v = 1$$

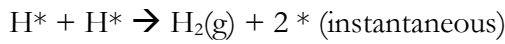
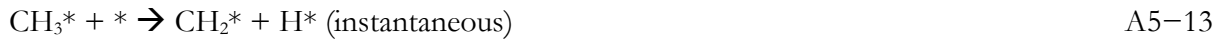
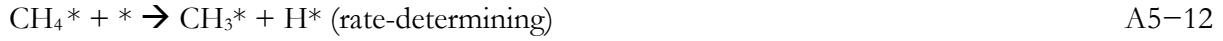
From equation A5-7

$$\theta_v \sqrt{K_1 K_2 p_{CH_4}} + \theta_v = 1$$

$$\theta_v = \frac{1}{1 + \sqrt{K_1 K_2 p_{CH_4}}} \quad \text{A5-9}$$

$$r = \frac{k_3 \sqrt{K_1 K_2 p_{CH_4}}}{\left(1 + \sqrt{K_1 K_2 p_{CH_4}}\right)^2} \quad \text{A5-10}$$

Model 4



From equation A5-11

$$K_1 = \frac{\theta_{CH_4}}{p_{CH_4} \theta_v} \quad \text{A5-15}$$

The subscript v is for the vacant sites.

$$\theta_{CH_4} = K_1 p_{CH_4} \theta_v \quad \text{A5-16}$$

From equation A5-12 and A5-16

$$r = k_2 \theta_{CH_4} \theta_v = k_2 K_1 p_{CH_4} \theta_v^2 \quad \text{A5-17}$$

Site balance:

$$\theta_{CH_4} + \theta_v = 1$$

From equation A5-16

$$K_1 p_{CH_4} \theta_v + \theta_v = 1$$

$$\theta_v = \frac{1}{1 + K_1 p_{CH_4}} \quad A5-18$$

From equations A5-17 and A5-19

$$r = \frac{k_2 K_1 p_{CH_4}}{(1 + K_1 p_{CH_4})^2} \quad A5-19$$

Model 5 (and Model 4)

In model 5, instead of assuming a generic * as the active site, $[Ga \cdot N]$ has been used as one active site containing two different entities Ga^{3+} and N^{3-} . If the DFT mechanism III (refer to Fig. 6-5) is used as the basis:



From equation A5-20

$$K_1 = \frac{\theta_{CH_3[Ga \cdot N]H}}{p_{CH_4} \theta_v}$$

$$\theta_{CH_3[Ga \cdot N]H} = K_1 p_{CH_4} \theta_v \quad A5-23$$

From equation A5-21

$$r = k_2 \theta_{CH_3[Ga \cdot N]H} \quad A5-24$$

From equations A5-23 and A5-24

$$r = k_2 K_1 p_{CH_4} \theta_v \quad A5-25$$

Site balance:

$$\theta_{CH_3[Ga \cdot N]H} + \theta_v = 1$$

From equation A5-23

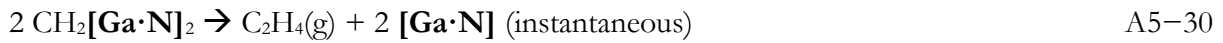
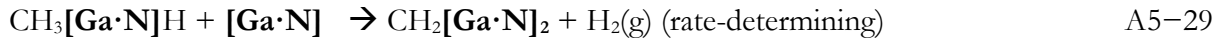
$$K_1 p_{CH_4} \theta_v + \theta_v = 1$$

$$\theta_v = \frac{1}{1+K_1 p_{CH_4}} \quad \text{A5-26}$$

From equations A5-25 and A5-26

$$r = \frac{k_2 K_1 p_{CH_4}}{1+K_1 p_{CH_4}} \quad \text{A5-27}$$

If Mechanism I (refer to Fig. 6-5) is used as the basis:



From equation A5-28

$$K_1 = \frac{\theta_{CH_3[Ga \cdot N]H}}{p_{CH_4} \theta_v}$$

$$\theta_{CH_3[Ga \cdot N]H} = K_1 p_{CH_4} \theta_v \quad \text{A5-31}$$

From equation A5-29

$$r = k_2 \theta_{CH_3[Ga \cdot N]H} \theta_v \quad \text{A5-32}$$

From equations A5-31 and A5-32

$$r = k_2 K_1 p_{CH_4} \theta_v^2 \quad \text{A5-33}$$

Site balance:

$$\theta_{CH_3[Ga \cdot N]H} + \theta_v = 1$$

From equation A5-31

$$K_1 p_{CH_4} \theta_v + \theta_v = 1$$

$$\theta_v = \frac{1}{1+K_1 p_{CH_4}} \quad \text{A5-34}$$

From equations A5-33 and A5-34

$$r = \frac{k_2 K_1 p_{CH_4}}{(1+K_1 p_{CH_4})^2} \quad \text{A5-35}$$

The equation A5–35 is similar to the equation derived for **Model 4** (equation A5–19).

Model 6

In model 6, the following elementary steps were assumed:



From equation A5–36

$$K_1 = \frac{\theta_{\text{CH}_4}}{p_{\text{CH}_4} \theta_v}$$

$$\theta_{\text{CH}_4} = K_1 p_{\text{CH}_4} \theta_v \quad \text{A5-39}$$

From equation A5–37 and A5–39

$$r = k_2 \theta_{\text{CH}_4}^2 = k_2 K_1^2 p_{\text{CH}_4}^2 \theta_v^2 \quad \text{A5-40}$$

Site balance:

$$\theta_{\text{CH}_4} + \theta_v = 1$$

From equation A5–39

$$K_1 p_{\text{CH}_4} \theta_v + \theta_v = 1$$

$$\theta_v = \frac{1}{1 + K_1 p_{\text{CH}_4}} \quad \text{A5-41}$$

From equations A5–40 and A5–41

$$r = \frac{k_2 K_1^2 p_{\text{CH}_4}^2}{(1 + K_1 p_{\text{CH}_4})^2} \quad \text{A5-42}$$

Based on equations A5–10, A5–19, A5–27, A5–35, and A5–42, the generic equation could be written as:

$$r = \frac{k_r (K_x p_{\text{CH}_4})^\alpha}{[1 + (K_x p_{\text{CH}_4})^\beta]^\gamma} \quad \text{A5-43}$$

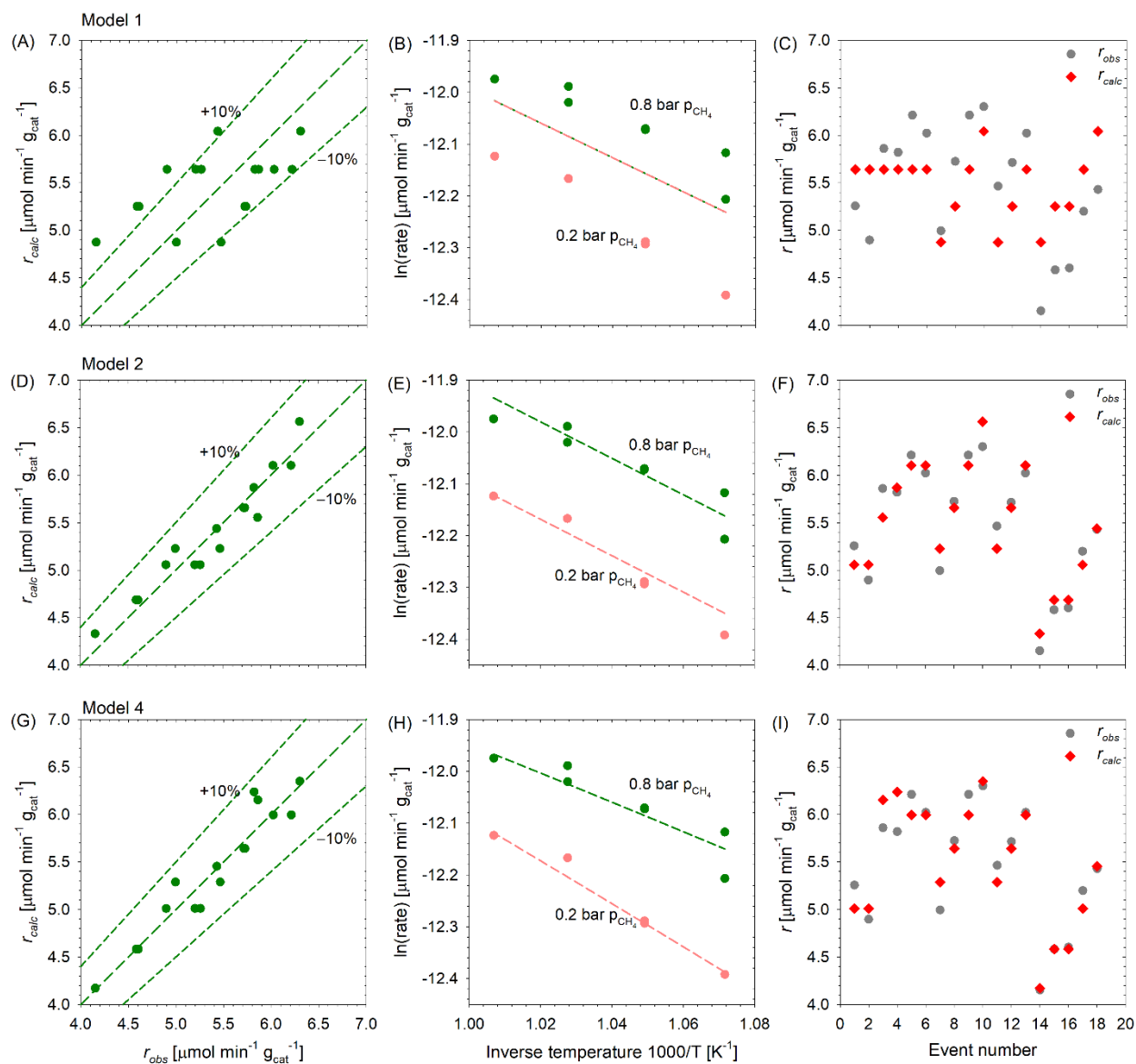


Fig. A5-1 Parity plot for the rate of reaction based on C_2H_4 formation, Arrhenius plot, and Comparison between the observed (r_{obs}) and the calculated (r_{calc}) rates of C_2H_4 formation for (A), (B), (C) Model 1, (D), (E), (F) Model 2, and (G), (H), (I) Model 4.

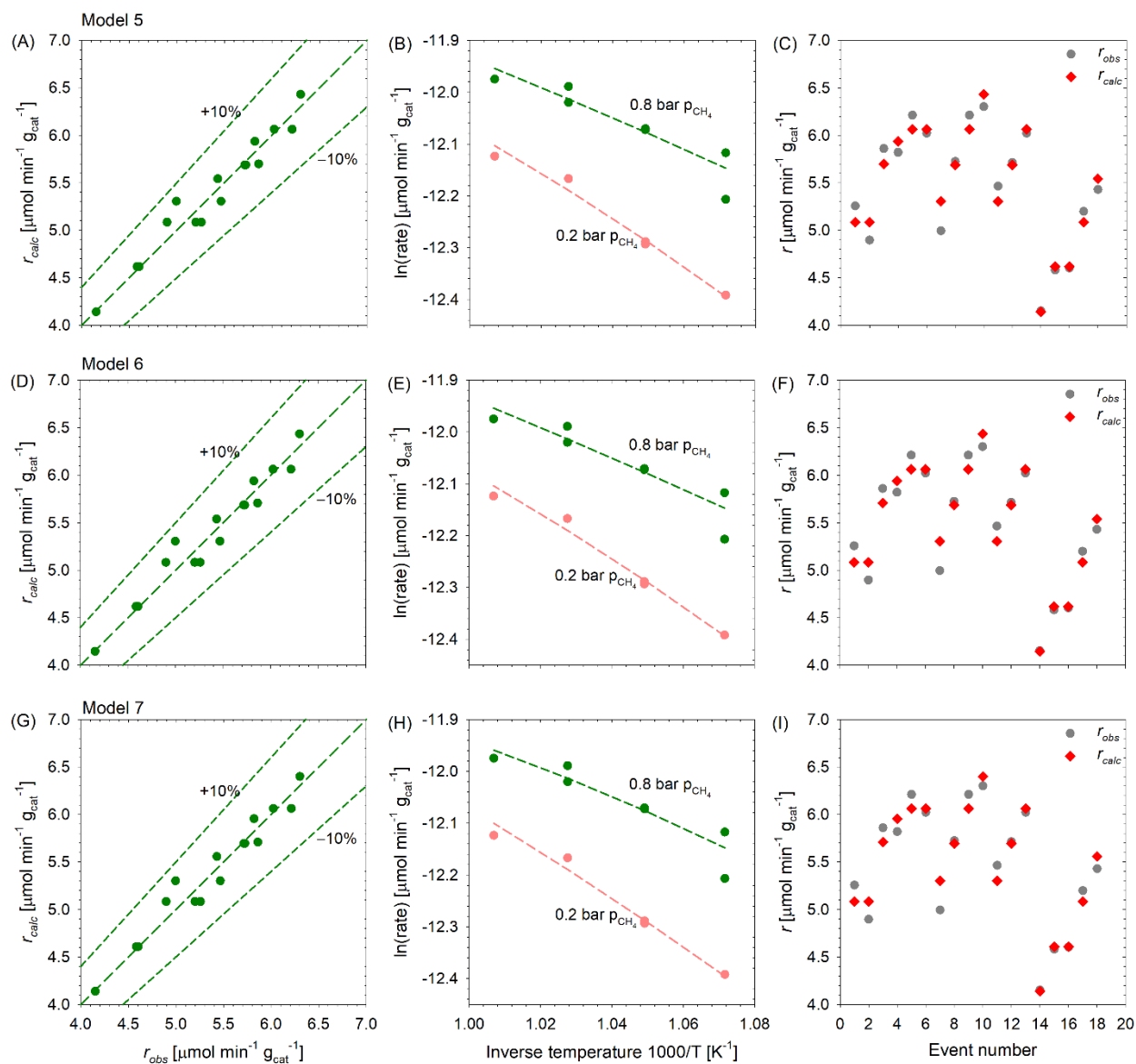


Fig. A5-2 Parity plot for the rate of reaction based on C_2H_4 formation, Arrhenius plot, and Comparison between the observed (r_{obs}) and the calculated (r_{calc}) rates of C_2H_4 formation for (A), (B), (C) Model 5, (D), (E), (F) Model 6, and (G), (H), (I) Model 7.

A6 Catalyst regeneration

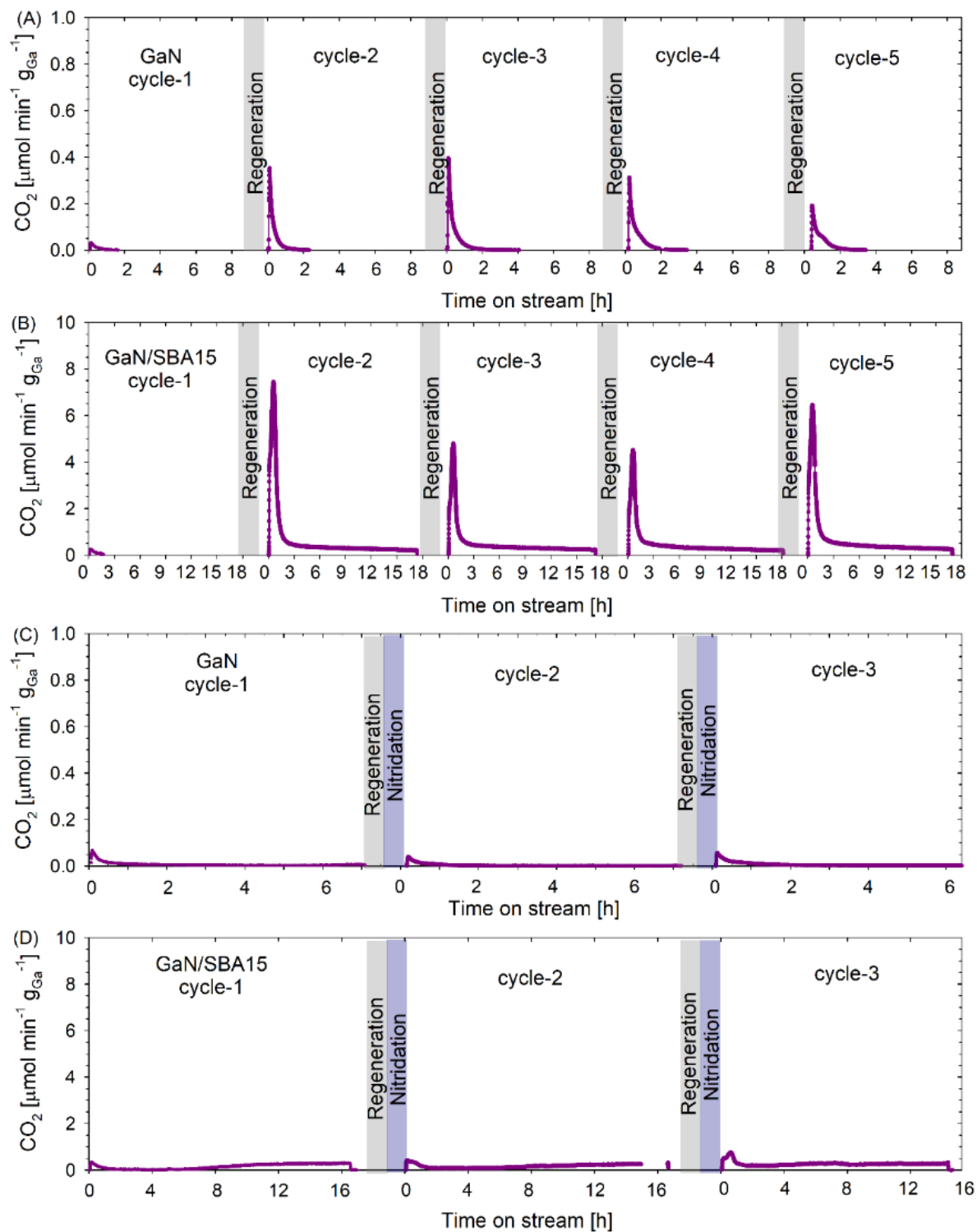


Fig. A6-1 CO_2 formation rate during activation cycles (A) GaN-R (B) GaN/SBA15-R, (C) GaN-RN, and (D) GaN/SBA15-RN.

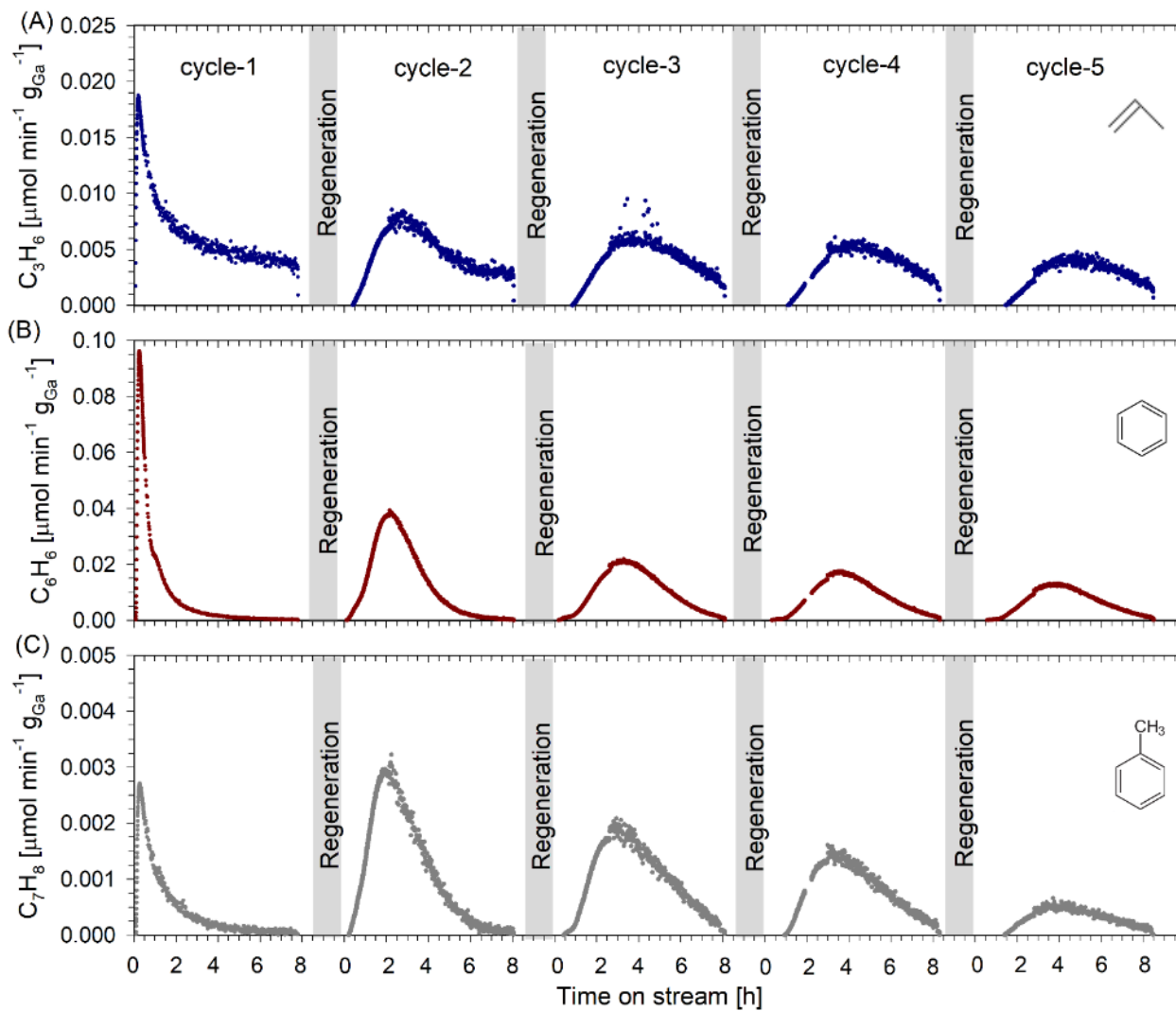


Fig. A6-2 Product molar flow rates for (A) C_3H_6 , (B) C_6H_6 , and (C) C_7H_8 as a function of time on stream for unsupported GaN used in 5 activation cycles with 4 intermediate regeneration steps in air (GaN-R).

Activation: $700\text{ }^\circ\text{C}$ at 567 h^{-1} , regeneration: Air at $500\text{ }^\circ\text{C}$.

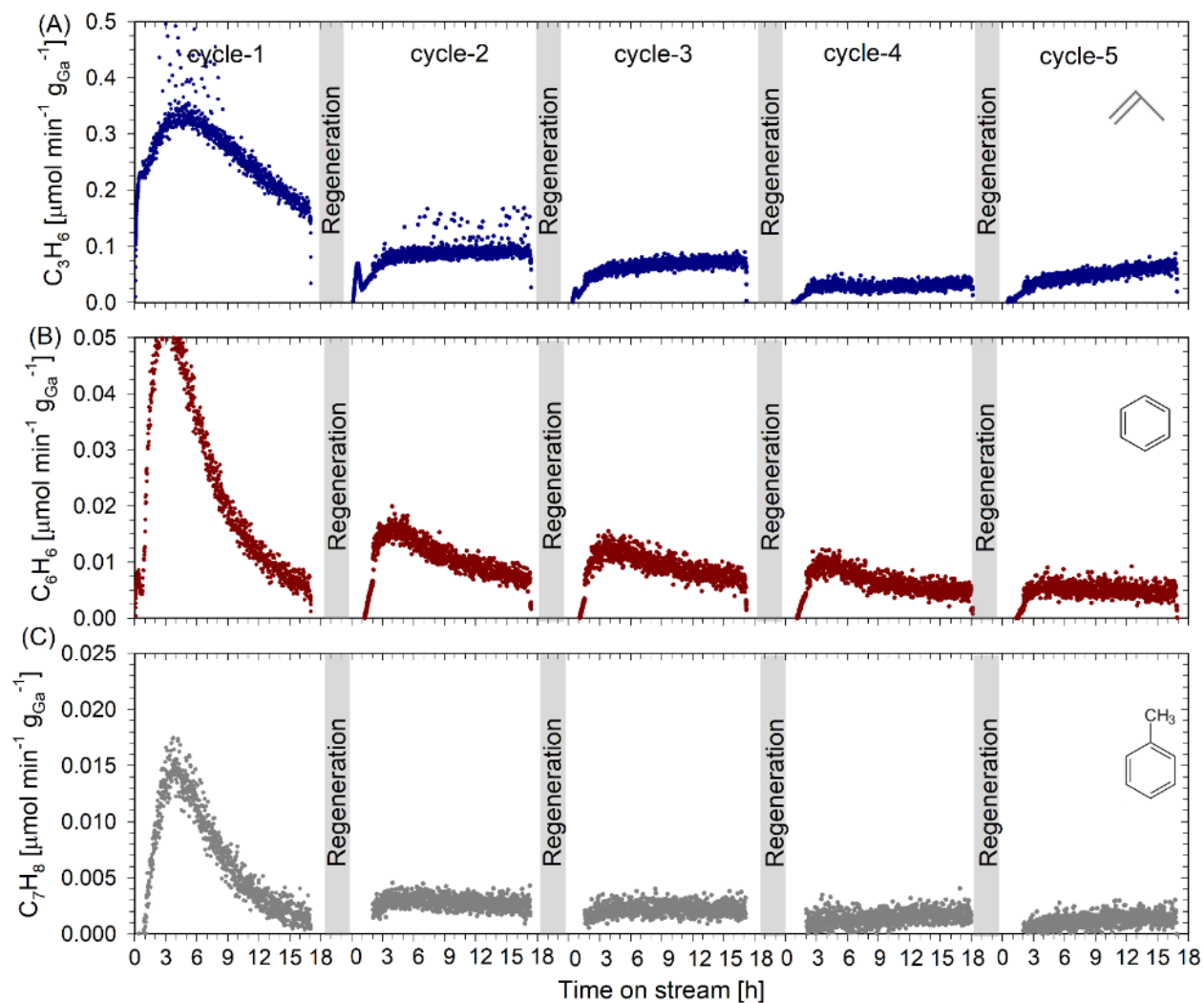


Fig. A6-3 Product formation rates for (A) C_3H_6 , (B) C_6H_6 , and (C) C_7H_8 as a function of time on stream for supported GaN/SBA15 used in 5 activation cycles with 4 intermediate regeneration steps in air (GaN/SBA15-R). Activation: $700\text{ }^\circ\text{C}$ at 567 h^{-1} , regeneration: Air at $550\text{ }^\circ\text{C}$.

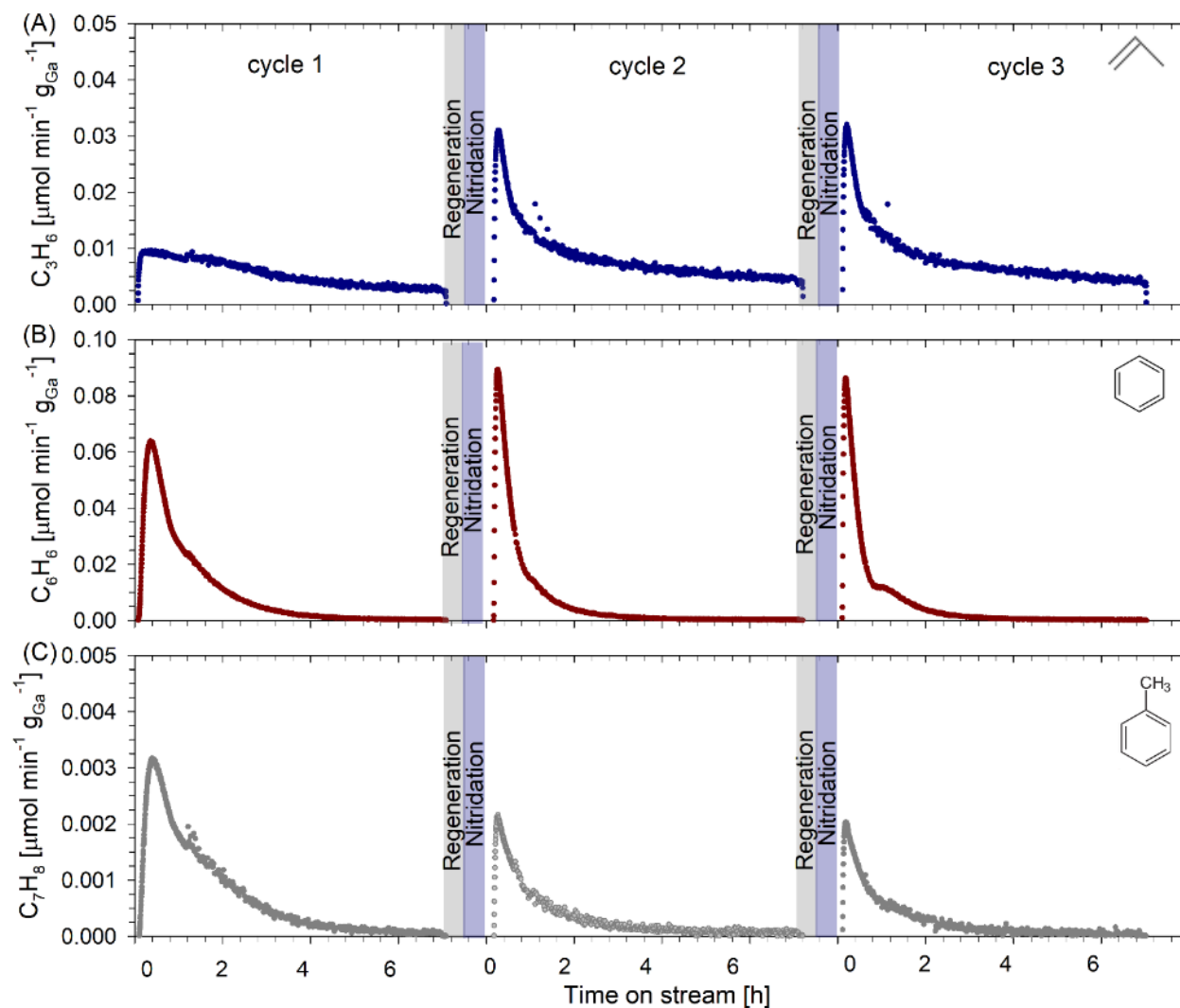


Fig. A6-4 Product formation rates for (A) C_3H_6 , (B) C_6H_6 , and (C) C_7H_8 as a function of time on stream over unsupported GaN catalyst with 3 activations and 2 intermediate regeneration and re-nitridation steps (GaN-RN).

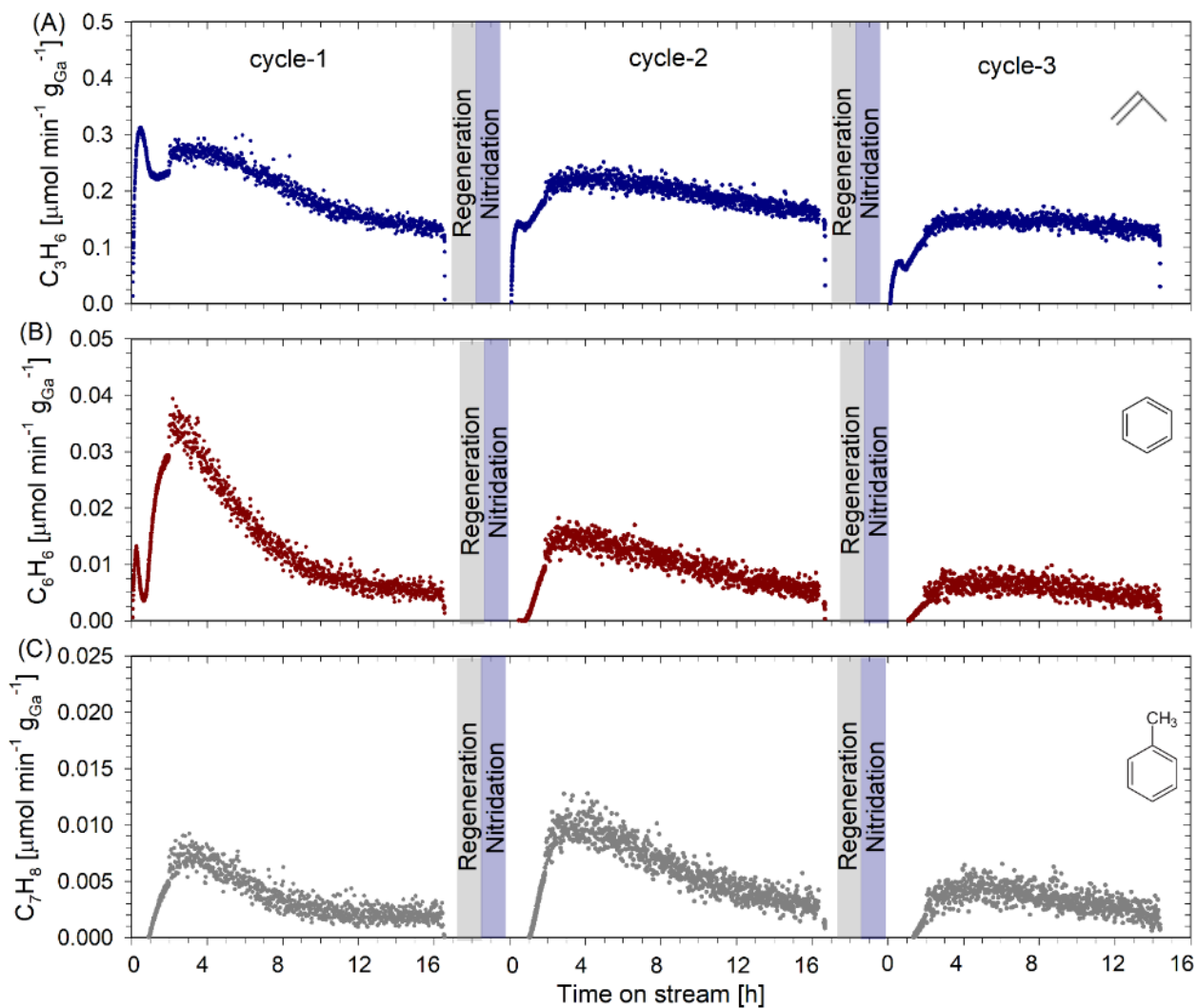


Fig. A6-5 Product formation rates for (A) C_3H_6 , (B) C_6H_6 , and (C) C_7H_8 as a function of time on stream over supported GaN/SBA15 catalyst with 3 activations and 2 intermediate regeneration and re-nitridation steps (GaN/SBA15-RN).

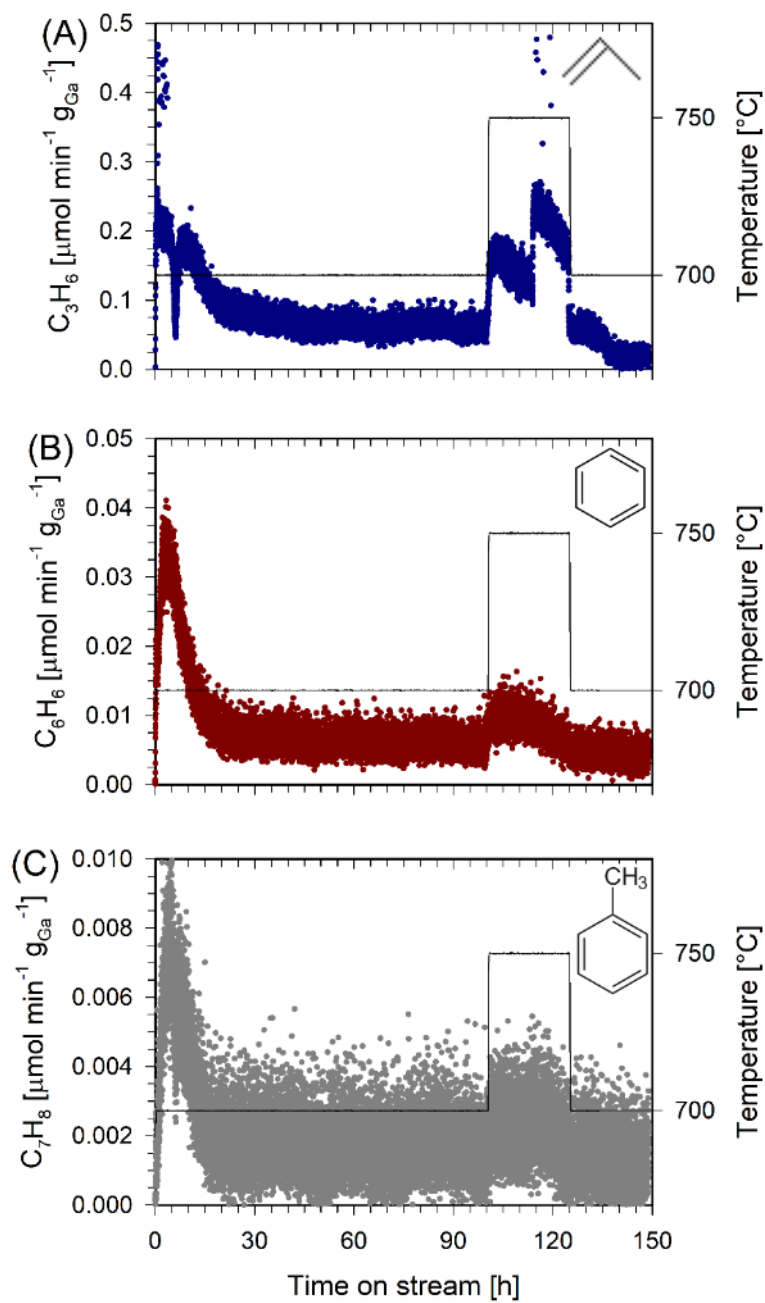


Fig. A6-6 Product molar flow rates for (A) C_3H_6 , (B) C_6H_6 , and (C) C_7H_8 as a function of time on stream for supported GaN/SBA15 for long term run (150 h).

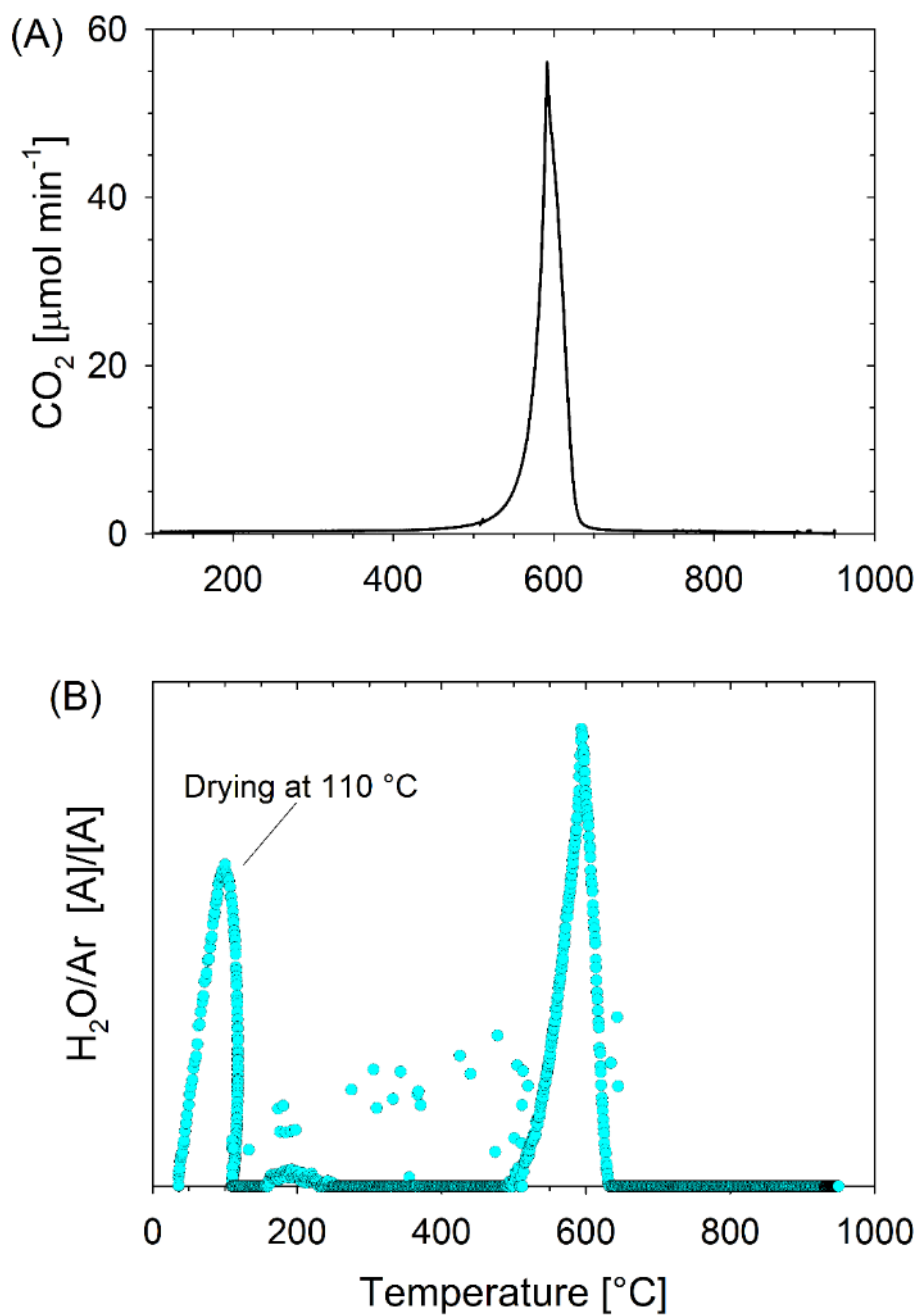


Fig. A6-7 TPO-MS for spent supported GaN/SBA15 catalyst used for methane activation for 150 h; (A) CO₂ molar flow rate as a function of time, and (B) qualitative water signal ($m/z = 18$, normalized with internal standard Ar with $m/z = 40$) during the TPO.

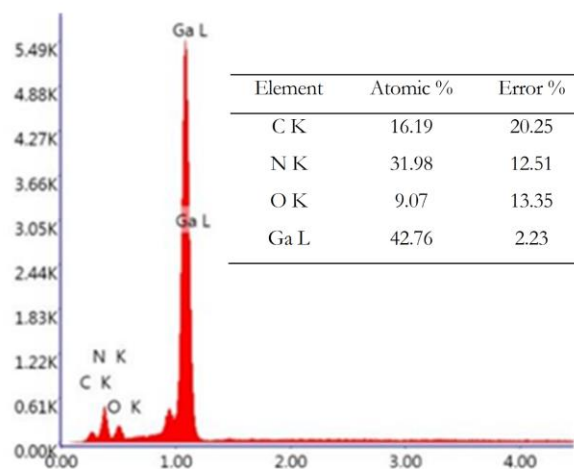
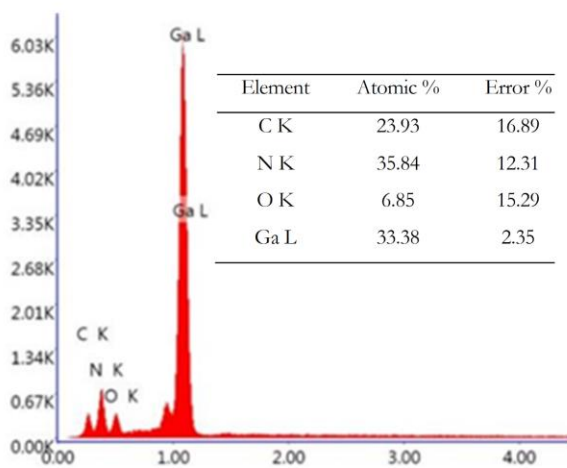
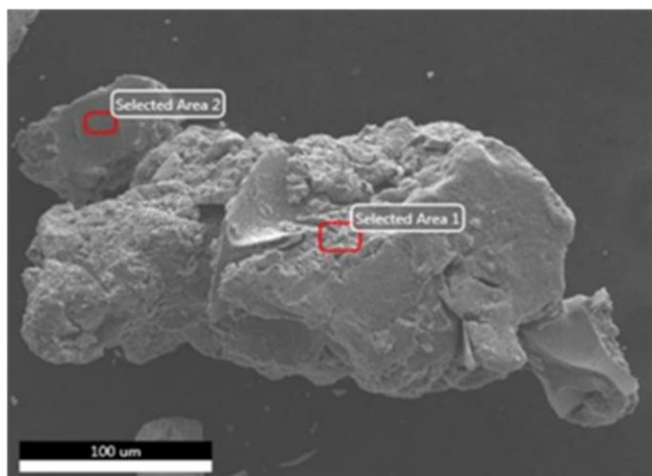


Fig. A6-8 SEM-EDS for spent GaN (1 cycle).

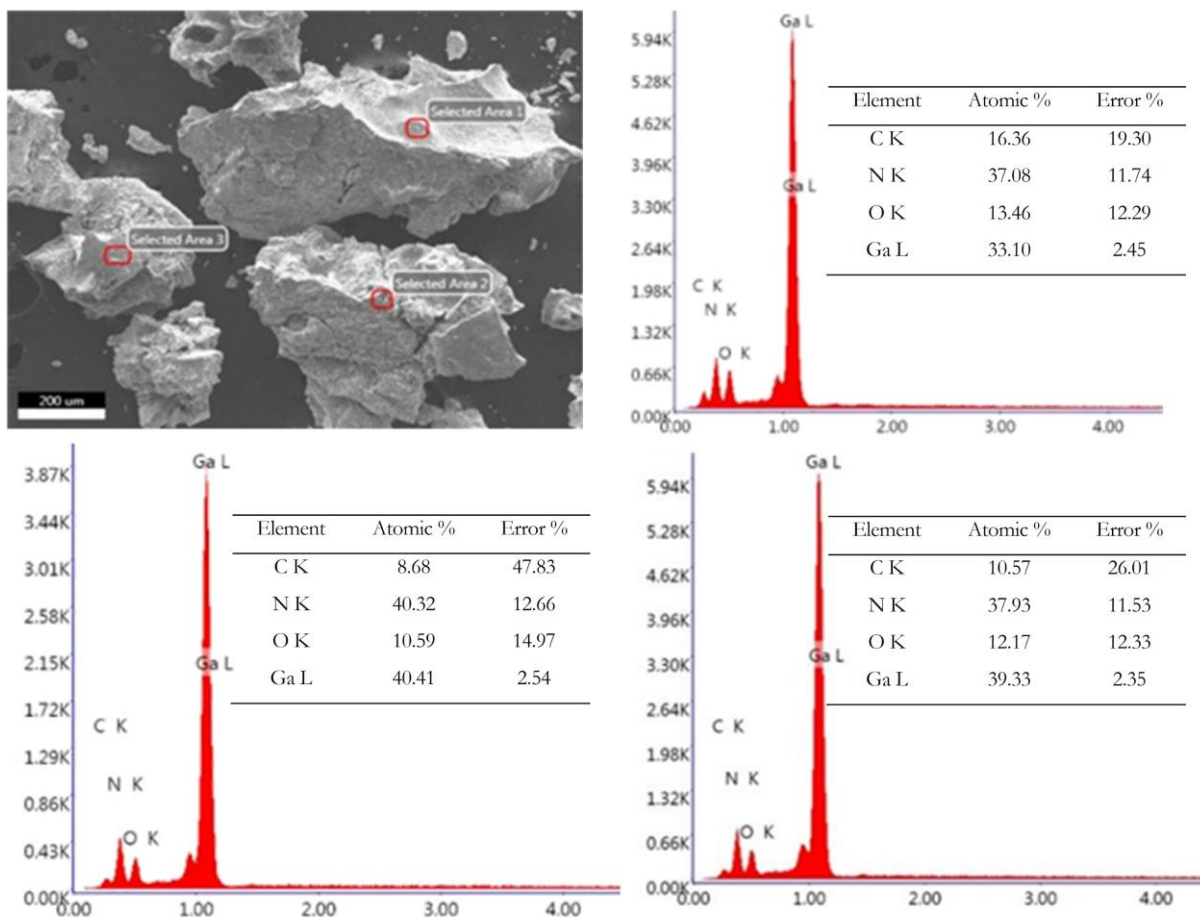


Fig. A6-9 SEM-EDS for GaN-R (1 cycle).

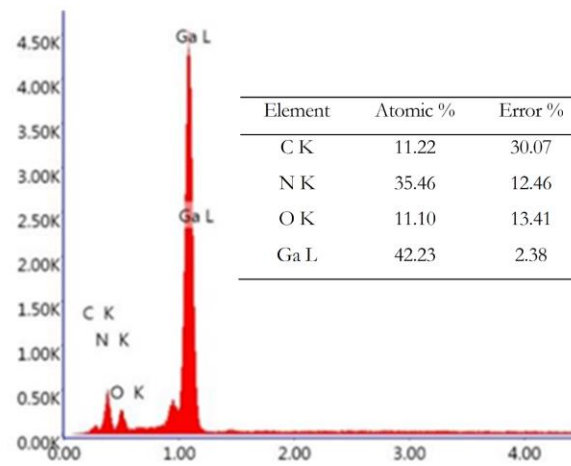
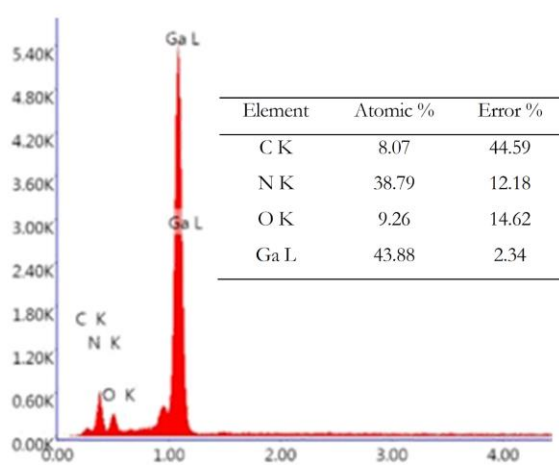
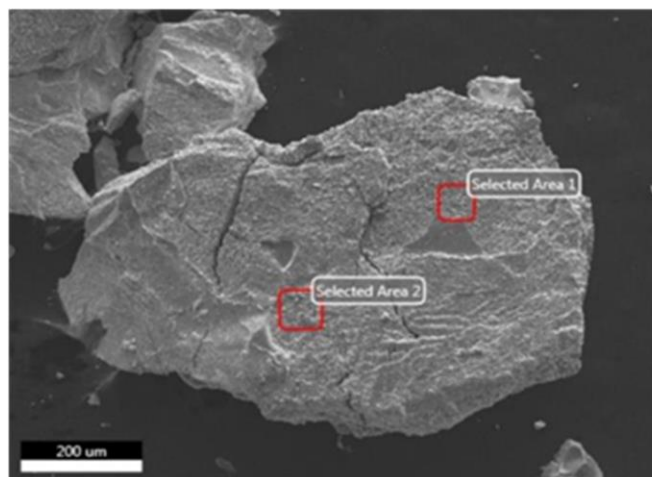


Fig. A6-10 SEM-EDS for GaN-RN (1 cycle, regeneration + re-nitridation).

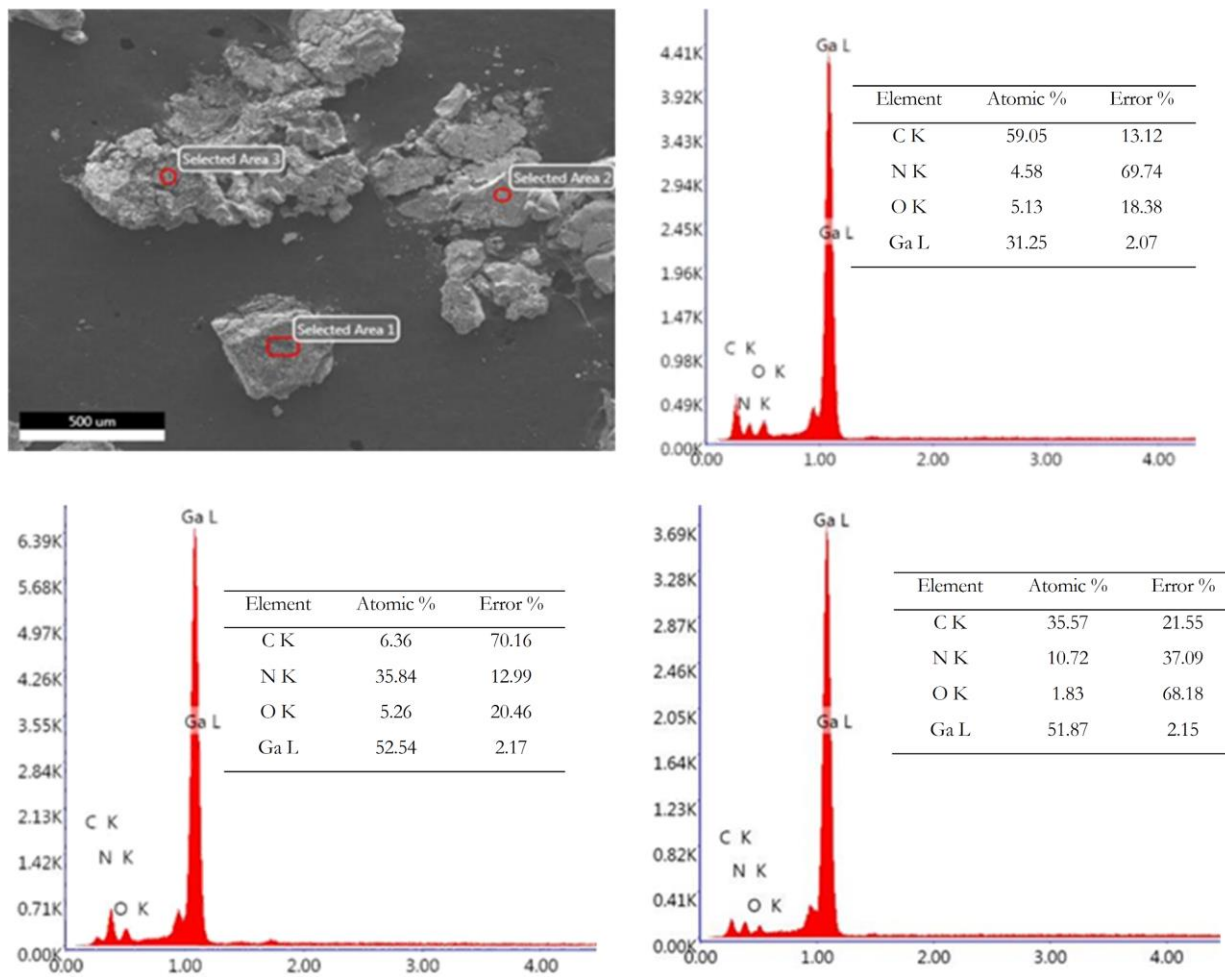


Fig. A6-11 SEM-EDS for the sample obtained by H₂ (40% in Ar) TPR of spent GaN (40–950 °C at 2.5 °C min⁻¹).

Published contributions

1. **K. Dutta**, L. Li, P. Gupta, D.P. Gutierrez, C.-J. Li, J. Kopyscinski, *Direct non-oxidative methane aromatization over gallium nitride catalyst in a continuous flow reactor*, Catal. Commun. 106 (2018) 16–19.
2. V. Chaudhari, **K. Dutta**, C.-J. Li, J. Kopyscinski, *Mechanistic insights of methane conversion to ethylene over gallium oxide and gallium nitride using density functional theory*, Mol. Catal. 482 (2020) 110606.
3. **K. Dutta**, M. Shahryari, J. Kopyscinski, *Direct nonoxidative methane coupling to ethylene over gallium nitride: A catalyst regeneration study*, Ind. Eng. Chem. Res. 59 (2020) 4245–4256.
4. **K. Dutta**, V. Chaudhari, C.-J. Li, J. Kopyscinski, *Methane conversion to ethylene over GaN catalysts. Effect of catalyst nitridation*, Appl. Catal. A Gen. 595 (2020) 117430.

Provisional patent application

5. Kopyscinski, J., **Dutta, K.**, Li C.-J., *Gallium nitride catalysts for the selective thermal non-oxidative conversion of C1–4 acyclic alkanes to C2–6 acyclic alkenes*, USPTO 62/897,500, September 9, 2019.

Oral contributions

1. *Methane activation and coupling to olefins over GaN catalysts*, presented at the 69th Canadian Chemical Engineering Conference, Halifax, NS, Canada, 20–23 October 2019.
2. *Supported and unsupported GaN for the direct non-oxidative methane aromatization*, presented at the 68th Canadian Chemical Engineering Conference, Toronto, ON, Canada, 28–31 October 2018.
3. *Development of mesoporous GaN catalysts for the direct non-oxidative methane aromatization*, presented at the 25th Canadian Catalysis Symposium, Saskatoon, SK, Canada, 08–11 May 2018.

Curriculum Vitae**Kanchan Dutta**

Catalytic Process Engineering (CPE) Lab, McGill University

kanchan.dutta@mail.mcgill.ca

Education and qualifications

2016 – present	Ph.D. candidate, McGill University, Montreal, Canada <i>Catalyst development for direct non-oxidative methane conversion</i>
2003–2005	Master of Technology, Indian Institute of Technology, India <i>Monte Carlo simulation of nanoparticles formation in reverse micelle</i>
2000–2003	Bachelor of Technology, Calcutta University, India
1997–2000	Bachelor of Science (Chemistry Hons.), Calcutta University, India

Career summary

2007 – 2015	UOP India Private Ltd. (A Honeywell Company), India
2010 – 2015	Senior Research and Development Engineer
2007 – 2010	Design Engineer
2005 – 2007	Air Liquide Global E&C Solutions, India Pvt. Ltd., Formerly Lurgi India Company Pvt. Ltd., New Delhi, India, Process Engineer

Publications and patents

1. K. Dutta, V. Chaudhari, C.-J. Li, J. Kopyscinski, Methane conversion to ethylene over GaN catalysts. Effect of catalyst nitridation, *Appl. Catal. A Gen.* 595 (2020) 117430.
2. K. Dutta, M. Shahryari, J. Kopyscinski, Direct Nonoxidative Methane Coupling to Ethylene over Gallium Nitride: A Catalyst Regeneration Study, *Ind. Eng. Chem. Res.* 59 (2020) 4245–4256.
3. V. Chaudhari, K. Dutta, C.-J. Li, J. Kopyscinski, Mechanistic insights of methane conversion to ethylene over gallium oxide and gallium nitride using density functional theory, *Mol. Catal.* 482 (2020) 110606.

4. Kanchan Dutta, Lu Li, Pranjal Gupta, Daniel Pacheco Gutierrez, Jan Kopyscinski. Direct non-oxidative methane aromatization over gallium nitride catalyst in a continuous flow reactor, *J. Catal. Commun.* 2018, 106, 16–19.
5. Processes for producing a transportation fuel from a renewable feedstock (US9914883B2).
6. Processes for producing biomass-derived pyrolysis oils (US20170096605A1).
7. Processes for producing a fuel from a renewable feedstock (US10240099B2).
8. Ethayaraja, Mani, Kanchan Dutta, Devarajan Muthukumar, and Rajdip Bandyopadhyaya. "Nanoparticle Formation in Water-in-oil Microemulsions: Experiments, Mechanism, and Monte Carlo Simulation." *Langmuir* 23.6 (2007): 3418–23.
9. Ethayaraja, M., C. Ravikumar, D. Muthukumar, K. Dutta, and R. Bandyopadhyaya. "CdS-ZnS Core-Shell Nanoparticle Formation: Experiment, Mechanism, and Simulation." *Journal of Physical Chemistry C* 111.8 (2007): 3246–252.
10. Ethayaraja, M., Kanchan Dutta, and Rajdip Bandyopadhyaya. "Mechanism of Nanoparticle Formation in Self-Assembled Colloidal Templates: Population Balance Model and Monte Carlo Simulation." *The Journal of Physical Chemistry B* 110.3 (2006): 16471–6481.

Scholarship and awards

1. Alexander Graham Bell Canada Graduate Scholarships – CGSD: Apr 2017 (Natural Sciences and Engineering Research Council of Canada).
2. Concours : B2, Comite: 05F: Apr 2017 (Fonds de recherche du Quebec – Nature et technologies (FRQNT)) (declined).
3. Emil Nenniger Memorial Fellowship: Jan 2017 (Faculty of Engineering, McGill University).
4. Graduate Excellence Fellowship Award: Jan 2017 (Faculty of Engineering, McGill University).
5. Graduate Excellence Fellowship Award: Jan 2016 (Faculty of Engineering, McGill University).
6. Lorne Trottier Engineering Graduate Fellowships: Jan 2016 (Faculty of Engineering, McGill University).

Conference awards

7. First prize, The Canadian Catalysis Division Student Conference Award, 2019.
8. The Canadian Catalysis Foundation (CCF) travel award, 2018.